

**Crystallization and Structure-Property Investigations of Semicrystalline  
Poly(arylene ether) based Polymers**

by  
Srivatsan Srinivas

Dissertation Submitted to the Faculty of the  
Virginia Polytechnic Institute and State University  
in partial fulfillment of the requirements for the degree of  
**DOCTOR OF PHILOSOPHY**  
in  
Materials Engineering and Science

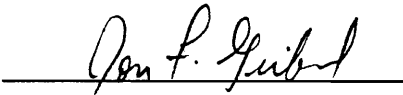
APPROVED:



Dr. Garth L. Wilkes, Chairman



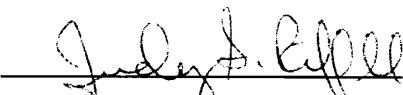
Dr. James E. McGrath



Dr. Jon F. Geibel



Dr. Hervé Marand



Dr. Judy S. Riffle



Dr. Richey M. Davis

June, 1996  
Blacksburg, Virginia

Key words: Crystallization kinetics, morphology, poly(arylene ethers), polyimides

**CRYSTALLIZATION AND STRUCTURE-PROPERTY  
INVESTIGATIONS OF SEMICRYSTALLINE  
POLY(ARYLENE ETHER) BASED POLYMERS**

by

Srivatsan Srinivas

Dr. Garth L. Wilkes, Chairman

Materials Engineering and Science

**ABSTRACT**

This dissertation addresses the crystallization, melting and morphological characteristics of selected high temperature poly(arylene ether) based polymers. The first part deals with the studies carried out on a series of biphenol and hydroquinone based novel poly(ether ether sulfide)s which were investigated with respect to their crystallization and morphological behavior. The biphenol based poly(ether ether sulfide)s ( $T_g = \text{ca. } 142 \text{ }^\circ\text{C}$ ,  $T_m = \text{ca. } 347 \text{ }^\circ\text{C}$ ,  $T_m^\circ = 371 \text{ }^\circ\text{C}$ ), and the hydroquinone based poly(ether ether sulfide)s ( $T_g = \text{ca. } 100 \text{ }^\circ\text{C}$ ,  $T_m = \text{ca. } 243 \text{ }^\circ\text{C}$ ,  $T_m^\circ = 292 \text{ }^\circ\text{C}$ ) were studied to evaluate the crystallization characteristics and to compare the observed behavior with that displayed by commercial polymers like PEEK and PPS. Isothermal melt crystallization kinetic studies of the sulfides were carried out and analyzed using the Avrami formulation. The results were

used to compare the behavior of the polymers at different crystallization temperatures and for the different molecular weights. Non-isothermal crystallization kinetics of the same polymers were investigated from the melt; in all cases, the Ozawa analysis could not describe the evolution of crystallinity. The non-isothermal data were hence analyzed using the conventional form of the Avrami equation, which yielded good fits to the data. The Avrami parameters obtained in this analysis do not, however, have the same physical significance as in the case of isothermal crystallization. Still, this approach is shown to be useful as a means of comparing the rates of crystallization. Spherulitic growth rate and morphological studies were carried out on the hydroquinone based poly(ether ether sulfide)s. At all crystallization temperatures, distinct populations of two kinds of spherulites were formed, with a population of coarse textured spherulites exhibiting a higher growth rate (Type II) than a population of fine textured spherulites (Type I). The morphology of these spherulites have been studied here using a variety of techniques, in conjunction with growth rate studies under a variety of conditions, in order to explain the occurrence of such phenomena. The differences in the growth rate and morphology have been attributed to differences in film thickness; the causes behind such effects, however, still remain unclear.

The second part of this dissertation involves the study of a series of high performance polyimides. Semicrystalline polyimides based on an all para-linked diamine, 1,4-bis(4-aminophenoxy)benzene (TPEQ diamine) and oxydiphthalic dianhydride (ODPA), endcapped with phthalic anhydride (PA) ( $T_g = \text{ca. } 230 \text{ }^\circ\text{C}$ ,  $T_m = \text{ca. } 420 \text{ }^\circ\text{C}$ ), and based on a PA endcapped meta-linked diamine, 1,3-bis(4-aminophenoxy)benzene (TPER

diamine) and 3,3', 4,4'-biphenyltetracarboxylic dianhydride (BPDA), ( $T_g = \text{ca. } 215 \text{ }^\circ\text{C}$ ,  $T_m = \text{ca. } 395 \text{ }^\circ\text{C}$ ) were investigated. The thermal stability of these polymers above  $T_m$  was investigated by studying the effect of time and temperature in the melt on the crystallization, melting and rheological behavior of these polymers. The TPER polyimide was shown to display exceptional thermal stability as evidenced by the fact that residence in the melt at temperatures as high as  $430 \text{ }^\circ\text{C}$  for times up to 30 min did not result in any loss of crystallizability or degree of crystallinity of the sample. The nature of the endgroups was found to play a critical role in determining the thermal stability of these polyimides under extreme conditions. In this investigation, the thermal stability of these polyimides has been compared to that of a commercial polyimide "New TPI". The TPER based polyimide displayed considerably superior stability and crystallizability characteristics compared to New TPI.

The last section of this dissertation deals with the structural changes accompanying cold-crystallization in New TPI, as a function of crystallization temperature and time. The changes in the glass transition, melting behavior and morphology accompanying the crystallization process were followed by a combination of thermal analysis, dynamic relaxation methods, and x-ray scattering. Increasing crystallization temperatures caused a decrease in the glass transition temperature, an increase in the degree of crystallinity, and increases in both the average lamellar and amorphous layer thicknesses. Increasing crystallization time at a given crystallization temperature produced an increase in  $T_g$ , an increase in the degree of crystallinity, and a decrease in the average lamellar thickness.

The results have been rationalized based on secondary crystallization occurring in the polymer leading to the formation of a bimodal distribution of lamellar thicknesses.

*To*

*my parents*

*Vatsala and M. Srinivasan*

*without whose sacrifices none of this would have been possible*

## Acknowledgments

First and foremost, I would like to thank my advisor Dr. Garth L. Wilkes, who has been an outstanding teacher and advisor. He was instrumental in teaching me polymer science through this classes and through the numerous discussions I had with him on my research, both during my Masters as well as during my Ph.D. He also taught a novice like me the art and skill of scientific presentation. All skills developed by me both technical as well as non-technical, as well as the value of thinking for myself, I attribute to his guidance and encouragement over all the years I have been here.

Thanks are due to Dr. Hervé Marand for the discussions I have had with him and for teaching me polymer crystallization as well as the most important lesson I learnt in graduate school - not to believe all that is published. I also wish to thank him for the opportunity to carry out post-doctoral research in his group. I would like to thank Dr. James E. McGrath for being the first to expose me to polymer science through his course on polymer chemistry, and for being responsible for a part of the work presented in this dissertation. Many thanks are due to Dr. Jon Geibel who in spite of his busy schedule was able to fly down on a few occasions to Blacksburg, and for all the discussions I had with him during those times. He was always willing to help with samples, analysis of samples, with getting references and with his constant encouragement. Thanks are due to Dr. Judy

Riffle for supplying the polymers used in part of this study, and to Dr. Richey Davis for being a collaborator in part of this work.

I would like to thank the NSF Science and Technology Center for High Performance Polymeric Adhesives and Composites for financial support through this study. I would also like to acknowledge support through the Phillips Petroleum Fellowship.

Most of the work presented has been interdisciplinary in nature. I would therefore like to acknowledge all my collaborators whose work also appears in this dissertation - Dr. Babu for synthesizing the poly ether sulfides used in the first part of this study, Marvin Graham for synthesizing the polyimides, Dr. Andy Brink for synthesizing PEEK, and Dr. Kent Blizard of Foster Miller Inc. for supplying the New TPI film. I would like to thank Franklin Caputo for all his help during his summer research at Blacksburg, Slade Gardner for extensive rheological work, and Robert Young for some rheological work. Special thanks are due to Steve McCartney for his help on the AFM, and for introducing me to the music of The Band. Thanks are due to Venkat Vasudevan for his help in molecular modelling.

There are numerous students and post-doctoral associates I had the opportunity to know during my rather long tenure in Blacksburg. Almost all of them have had an influence in my research and my acquiring knowledge during my student years. Firstly I would like to thank Ravi Verma with whom I have had countless arguments and discussions, usually heated, on all aspects of polymer science. We disagreed on everything

except the fringed micelle model. He, however, taught me all I know of scattering techniques, a lot of crystallization and structure-property relationships and finally how to provide handwaving explanations for unexplained phenomena. Thanks are also due to Drs. Saikat, Saikumar, Satya, Dilip, and Hemanshu for their friendship and for teaching me various aspects of material science during my graduate years.

I would like to thank past and present members of the Wilkes Lab for their friendship over the past years - David Rodrigues, Don Loveday, Chinmay, Jim Dounis, Pamela, Rob, Kurt, David Shelby (also for improving my golf swing), Jianye, Chris, Ta-Hua and Howard, and now Bryan and Varun. Special mention must be made of Don Brandom with whom I have had a number of quite enthusiastic discussions on polyimides, crystallization and blues music. Thanks are also due to members of Ward's group specially Mark Muggli, Kermit and Dave Porter for their friendship. Other students in the Chemical Engineering Dept. like Slade, Rob Young, Norm, Todd, Fred, Raj and Bala made the department a fun place to work in. Special thanks are due to Sandy for all her help over the years in getting things done.

I would like to thank my roommates (many of them over the years) and friends in Blacksburg, Ravi, Sukhtej, Mahesh, Shanky, Suresh, Sunder, Snag, Milan and Viru for a great time I had in Blacksburg.

The most important acknowledgments I leave for the end. My brothers Mahesh and Ramesh, and sisters-in-law Mythily and Jaya for their constant encouragement over the years and more so during the last few months when needed most. My most important

thanks go to my parents Vatsala and M. Srinivasan, who have constantly inspired and encouraged me in all my endeavors, and for sacrificing so much so I may succeed. To them I dedicate this dissertation.

# Table of Contents

**ABSTRACT**

**ACKNOWLEDGMENTS**

**TABLE OF CONTENTS**

**LIST OF FIGURES**

**LIST OF TABLES**

<b>INTRODUCTION</b>	.....	1
<b>CHAPTER 1</b>	<b>THERMAL CHARACTERIZATION AND CRYSTALLIZATION OF NOVEL POLY(ARYLENE ETHER ETHER SULFIDE)S.</b>	
<b>1.1</b>	Abstract	.....5
<b>1.2</b>	Introduction	.....6
<b>1.3</b>	Experimental	.....10
<b>1.4</b>	Results and Discussion	.....11
<b>1.5</b>	Summary and Conclusions	.....41
	Acknowledgments	
	References	
<b>CHAPTER 2</b>	<b>KINETICS OF ISOTHERMAL AND NON-ISOTHERMAL CRYSTALLIZATION OF NOVEL POLY(ARYLENE ETHER ETHER SULFIDE)S.</b>	

<b>2.1</b>	Abstract	.....	44
<b>2.2</b>	Introduction	.....	46
<b>2.3</b>	Experimental		
	<b>2.3.1</b>	Materials	.....49
	<b>2.3.2</b>	Characterization	.....49
	<b>2.3.3</b>	Data Analysis	.....50
<b>2.4</b>	Results and Discussion		
	<b>2.4.1</b>	Isothermal Crystallization	.....56
	<b>2.4.2</b>	Non-isothermal Crystallization.....	77
<b>2.5</b>	Conclusions	.....	88
	Acknowledgments		
	References		

**CHAPTER 3**            CRYSTALLIZATION AND MORPHOLOGY OF  
POLY(ARYLENE ETHER ETHER SULFIDE)S: DUAL SPHERULITIC  
MORPHOLOGY.

<b>3.1</b>	Abstract	.....	94
<b>3.2</b>	Introduction	.....	95
<b>3.3</b>	Experimental	.....	99
<b>3.4</b>	Results and Discussion	.....	102
<b>3.5</b>	Conclusions	.....	128

Acknowledgments

References

**CHAPTER 4** INFLUENCE OF MELT STABILITY ON THE  
CRYSTALLIZATION BEHAVIOR OF BIS(4-AMINOPHENOXY)BENZENE-  
OXYDIPHTHALIC ANHYDRIDE BASED POLYIMIDES.

<b>4.1</b>	Abstract	.....	133
<b>4.2</b>	Introduction	.....	134
<b>4.3</b>	Experimental		
	<b>4.3.1</b> Materials	.....	136
	<b>4.3.2</b> Polymer Synthesis	.....	137
	<b>4.3.3</b> Characterization	.....	140
<b>4.4</b>	Results and Discussion	.....	142
<b>4.5</b>	Conclusions	.....	172

Acknowledgments

References

**CHAPTER 5** SEMICRYSTALLINE POLYIMIDES BASED ON  
CONTROLLED MOLECULAR WEIGHT PHTHALIMIDE ENDCAPPED 1,3-BIS(4-  
AMINOPHENOXY)BENZENE AND 3,3',4,4'-BIPHENYLTETRACARBOXYLIC  
DIANHYDRIDE: SYNTHESIS, CRYSTALLIZATION, MELTING AND THERMAL  
STABILITY.

5.1	Abstract	176
5.2	Introduction	178
5.3	Experimental	
5.3.1	Materials	183
5.3.2	Polymer Synthesis	184
5.3.3	Characterization	187
5.4	Results and Discussion	189
5.4.1	DSC Studies	191
5.4.2	Melting studies	196
5.4.3	Dynamic Mechanical Studies	214
5.4.4	SAXS Studies	224
5.4.5	Thermal Stability	226
5.4.6	Rheological Studies	242
5.5	Conclusions	248
	Acknowledgments	
	References	

**CHAPTER 6**      **STRUCTURAL AND CRYSTALLIZATION STUDIES OF  
NEW-TPI POLYIMIDE.**

6.1	Abstract	256
6.2	Introduction	257

<b>6.3</b>	Experimental	
<b>6.3.1</b>	Sample Preparation	262
<b>6.3.2</b>	Characterization Techniques	263
<b>6.4</b>	Results and Discussion	
<b>6.4.1</b>	WAXS Studies	264
<b>6.4.2</b>	DSC Studies	272
<b>6.4.3</b>	Dynamic Mechanical Studies	281
<b>6.4.4</b>	SAXS Studies	299
<b>6.5</b>	Conclusions	316
	Acknowledgments	
	References	

<b>CHAPTER 7</b>	<b>SUMMARY AND FUTURE WORK</b>	323
------------------	--------------------------------	-----

**VITA**

## List of Figures

Figure 1.1	Plot of $T_g$ vs $1/M_n$ for poly(ether ether sulfoxide)s	.....14
Figure 1.2	Wide angle x-ray patterns for poly(ether ether sulfoxide)s	.....16
Figure 1.3	First heat DSC scan for poly(phenyl ether ether sulfide)	.....18
Figure 1.4	Second heat DSC scan for poly(phenyl ether ether sulfide)	.....19
Figure 1.5	First heat DSC scan for poly(biphenyl ether ether sulfide)	.....22
Figure 1.6	Second heat DSC scan for poly(biphenyl ether ether sulfide)	.....23
Figure 1.7	Wide angle x-ray patterns for poly(ether ether sulfide)s	.....26
Figure 1.8	Hoffman-Weeks plot for poly(ether ether sulfide)s	.....28
Figure 1.9	Effect of melt temperature on the maximum crystallization temperature for poly(phenyl ether ether sulfide). Time in the melt is 5 min.	.....30
Figure 1.10	Effect of melt temperature on the heat of crystallization for poly(phenyl ether ether sulfide). Time in the melt is 5 min.	.....31
Figure 1.11	Effect of time in the melt on the maximum crystallization temperature for poly(phenyl ether ether sulfide)	.....32
Figure 1.12	Effect of melt temperature on the maximum crystallization temperature for poly(biphenyl ether ether sulfide). Time in the melt is 5 min.	.....34
Figure 1.13	Effect of melt temperature on the heat of crystallization for poly(biphenyl ether ether sulfide). Time in the melt is 5 min.	.....36

Figure 1.14	Effect of melt temperature on the onset of crystallization for poly(biphenyl ether ether sulfide). Time in the melt is 5 min.	.....37
Figure 1.15	Effect of time in the melt on the maximum crystallization temperature for poly(biphenyl ether ether sulfide)	.....38
Figure 1.16	Effect of time in the melt on the heat of crystallization for poly(biphenyl ether ether sulfide)	.....39
Figure 2.1	Relative crystallinity as a function of time for isothermal crystallization from the melt for phenyl sulfide 19.9K.	.....57
Figure 2.2	Avrami plots for isothermal crystallization from the melt for phenyl sulfide 19.9K.	.....58
Figure 2.3	Avrami exponents as a function of undercooling for phenyl sulfide and biphenyl sulfide systems.	.....60
Figure 2.4	Avrami rate constants as a function of undercooling for phenyl sulfide and biphenyl sulfide systems.	.....62
Figure 2.5	Crystallization half-times as a function of undercooling for phenyl sulfide and biphenyl sulfide systems.	.....67
Figure 2.6	Heat of crystallization as a function of undercooling for phenyl sulfide and biphenyl sulfide systems.	.....69
Figure 2.7	Nucleation density as a function of undercooling for phenyl sulfide 19.9K	.....71

Figure 2.8	Hoffman-Weeks plot for various molecular weights of phenyl sulfide polymer.	.....73
Figure 2.9	Kinetic analysis of rate constants from melt isothermal crystallization for phenyl sulfide 34K.	.....75
Figure 2.10	Maximum crystallization temperature as a function of cooling rate for non-isothermal crystallization from the melt for various polymers.	.....78
Figure 2.11	Relative crystallinity as a function of cooling rate for non-isothermal crystallization from the melt for phenyl sulfide 19.9K.	.....81
Figure 2.12	Ozawa plot for non-isothermal crystallization from the melt for phenyl sulfide 19.9K.	.....82
Figure 2.13	Avrami plots for non-isothermal crystallization from the melt for phenyl sulfide 19.9K.	.....84
Figure 2.14	Avrami reduced rate constants as a function of cooling rate for non-isothermal crystallization for various polymers.	.....86
Figure 3.1	Chemical structure of poly(ether ether sulfide).	.....96
Figure 3.2	Schematic of sample preparation for hot stage optical microscopy.	.....101
Figure 3.3	Polarized optical micrographs of (A) Type I and (B) Type II spherulites.	.....103
Figure 3.4	Growth rate plots for Type I and Type II spherulites at 210 °C.	.....105
Figure 3.5	Growth rates as a function of temperature for Type I and Type II spherulites.	.....107

Figure 3.6	Growth rates of Type I spherulites at 200 °C as a function of melt temperature.	.....111
Figure 3.7	Growth rates of Type II spherulites at 210 °C as a function of melt temperature.	.....112
Figure 3.8	Growth rates of Type I spherulites at 210 °C on different substrates.....	114
Figure 3.9	Growth rates of Type II spherulites at 210 °C on different substrates.....	115
Figure 3.10	Phase contrast optical micrographs for (A) Type I and (B) Type II spherulites.	.....118
Figure 3.11	SEM micrographs for (A) Type I and (B) Type II spherulites.	.....120
Figure 3.12	SEM micrographs for (A) Type I and (B) Type II spherulites.	.....121
Figure 3.13	AFM height images for (A) Type I and (B) Type II spherulites.	.....122
Figure 3.14	AFM amplitude images for (A) Type I and (B) Type II spherulites.	.....123
Figure 3.15	H <sub>v</sub> SALS patterns for (A) Type I and (B) Type II spherulites.	.....125
Figure 3.16	V <sub>v</sub> SALS patterns for (A) Type I and (B) Type II spherulites.	.....127
Figure 4.1	TGA scans for 10K samples imidized at different conditions	.....143
Figure 4.2	Temperatures for 5% weight loss by TGA	.....145
Figure 4.3	First heat DSC scans for various molecular weights	.....147
Figure 4.4	Second heat DSC scans for various molecular weights	.....150
Figure 4.5	DSC scans for 15K polyimide	.....153
Figure 4.6	DSC scans for 30K polyimide	.....155

Figure 4.7	Wide angle x-ray scattering patterns for as-received and quenched samples for 15K polyimide	.....157
Figure 4.8	Effect of temperature and time in the melt on the maximum crystallization temperature of 10K polymer	.....159
Figure 4.9	Effect of temperature and time in the melt on the melting temperature of 10K polymer	.....161
Figure 4.10	Effect of temperature and time in the melt on the heat of crystallization of 10K polymer	.....163
Figure 4.11	Effect of temperature and time in the melt on the maximum crystallization temperature of 12.5K polymer	.....165
Figure 4.12	Effect of temperature and time in the melt on the heat of crystallization of 12.5K polymer	.....166
Figure 4.13	Complex viscosity as a function of time for 12.5K polymer	.....168
Figure 4.14	DSC scans for 12.5K polyimide subjected to different melt treatments...	169
Figure 5.1	First heat DSC scans for TPER polyimide and New TPI.	.....192
Figure 5.2	Second heat DSC scans for TPER polyimide and New TPI.	.....194
Figure 5.3	Repeated heating DSC scans for PA endcapped TPER 30K.	.....197
Figure 5.4	DSC scans for PA endcapped TPER 30K subjected to various cooling rates from the melt.	.....198
Figure 5.5	DSC scans for PA endcapped TPER 30K samples isothermally crystallized at various temperatures.	.....201

Figure 5.6	DSC scans for PA endcapped TPER 30K samples crystallized at 345 °C for 5 min.	.....204
Figure 5.7	DSC scans for PA endcapped TPER 30K isothermally crystallized at 345 °C for various times.	.....206
Figure 5.8	DSC scans at different heating rates for PA endcapped TPER 30K isothermally crystallized at 345 °C for 30 min.	.....207
Figure 5.9	Wide angle x-ray scattering patterns for PA endcapped TPER 30K samples exhibiting single melting endotherm and multiple melting endotherms....	210
Figure 5.10	Hoffman-Weeks plot for PA endcapped TPER 30K polyimide.	.....212
Figure 5.11	Dynamic mechanical spectra of as-received and slow cooled samples of PA endcapped TPER 30K.	.....215
Figure 5.12	Arrhenius plots of frequency vs. 1/T based on dynamic mechanical relaxation experiments for as-received and slow cooled samples of PA endcapped TPER 30K.	.....216
Figure 5.13	Schematic representation of spherulitic and lamellar morphology.	.....221
Figure 5.14	Lorentz corrected SAXS plots for PA endcapped TPER 30K.	.....225
Figure 5.15	Effect of time and temperature in the melt on the heat of melting of PA endcapped TPER 30K.	.....227
Figure 5.16	Effect of time and temperature in the melt on the heat of crystallization of PA endcapped TPER 30K.	.....229

Figure 5.17	Effect of time and temperature in the melt on the melting temperature of PA endcapped TPER 30K.	.....232
Figure 5.18	Effect of time and temperature in the melt on the heat of melting of New TPI.	.....234
Figure 5.19	Effect of time and temperature in the melt on the heat of melting of PA endcapped TPEQ/ODPA polyimide.	.....236
Figure 5.20	DSC cooling scans for TPER 30K polyimide samples with different endgroups after a melt history of 430 °C, 30 min.	.....238
Figure 5.21	DSC heating scans for TPER 30K polyimide samples with different endgroups after cooling as shown in Figure 5.20.	.....239
Figure 5.22	Frequency dependence of complex viscosity for PA endcapped TPER 30K polyimide at 420 °C and 3% strain.	.....243
Figure 5.23	Isothermal viscosity sweeps for PA endcapped TPER samples and New TPI at different temperatures.	.....244
Figure 5.24	Isothermal viscosity sweeps for TPER 30K polyimide with different endgroups at 430 °C.	.....249
Figure 6.1	Chemical structure of New TPI.	.....260
Figure 6.2	X-ray profiles for samples crystallized at different temperatures.	.....267
Figure 6.3	X-ray profiles for samples crystallized at 300 °C for different times.	.....270
Figure 6.4	Degree of crystallinity as a function of crystallization time at 300 °C.....	271

Figure 6.5	DSC traces of amorphous and semicrystalline samples of New TPI. ....	273
Figure 6.6	Glass transition temperatures determined from DSC as a function of crystallization temperature. ....	276
Figure 6.7	Melting temperatures determined from DSC as a function of crystallization temperature. ....	277
Figure 6.8	Glass transition temperatures determined from DSC as a function of crystallization time. ....	279
Figure 6.9	Melting temperatures determined from DSC as a function of crystallization time. ....	280
Figure 6.10	Dynamic mechanical storage modulus for representative amorphous sample (crystallized at 300 °C for 2.2 min). ....	282
Figure 6.11	Dynamic mechanical loss factor for representative amorphous sample (crystallized at 300 °C for 2.2 min). ....	283
Figure 6.12	Dynamic mechanical storage modulus for sample crystallized at 300 °C for 135 min. ....	285
Figure 6.13	Dynamic mechanical loss factor for sample crystallized at 300 °C for 135 min. ....	286
Figure 6.14	Dynamic mechanical loss factor for samples crystallized for 135 min at various temperatures. ....	288
Figure 6.15	Arrhenius plots of frequency vs. 1/T from dynamic mechanical experiments for samples crystallized for 135 min at various temperatures. ....	293

Figure 6.16	Dynamic mechanical loss factor for samples crystallized at 300 °C for various times.	.....294
Figure 6.17	Dynamic mechanical loss factor for samples crystallized at 300 °C for various times.	.....295
Figure 6.18	Glass transition temperatures determined from peak of $\tan \delta$ as a function of crystallization time for samples crystallized at 300 °C.	.....297
Figure 6.19	Smearred SAXS data for an amorphous sample and a semicrystalline sample.	.....302
Figure 6.20	Lorentz corrected plots for samples crystallized for 135 min at various temperatures.	.....304
Figure 6.21	Correlation functions for samples crystallized for 135 min at various temperatures.	.....305
Figure 6.22	Long spacings as a function of crystallization temperature.	.....307
Figure 6.23	Lamellar thickness and inter-lamellar amorphous layer thickness as a function of crystallization temperature.	.....310
Figure 6.24	Lorentz corrected plots for samples crystallized at 300 °C for various times.	.....312
Figure 6.25	Long spacings as a function of crystallization time.	.....313
Figure 6.26	Lamellar thickness and inter-lamellar amorphous layer thickness as a function of crystallization time.	.....315

## List of Tables

Table 1.1	Temperatures for 5% weight loss by TGA for poly(ether ether sulfoxide)s and poly(ether ether sulfide)s.	.....12
Table 2.1	Chemical structures and transition temperatures of poly(ether ether sulfide)s.	.....47
Table 5.1	Chemical structures and transition temperatures of TPER/BPDA, TPEQ/ODPA and New TPI polyimides.	.....180
Table 5.2	Temperatures for 2% weight loss by TGA for various polyimides.	.....190
Table 6.1	Degree of crystallinity from WAXS measurements for samples of New TPI isothermally cold-crystallized for 135 min at various temperatures.	.....268
Table 6.2	Average lamellar and amorphous layer thickness obtained from the correlation function and minimum lamellar thickness determined from the Scherrer analysis.	.....309

## Introduction

The growing demand for polymeric materials that possess thermal and dimensional stability has led to the development of high performance polymers. High performance polymers are defined as materials that can be used in applications where the material experiences extreme conditions of load, temperature, and environment. Such polymers, both thermoplastic as well as thermoset systems, are increasingly being considered for applications as replacements for metals and ceramics, due to their ease of processing and high stiffness and/or strength to weight ratio.

Examples of thermoset polymers in use today include epoxy, bismaleimide, and polyimide resins. There has, however, been interest in replacing the thermoset resins by thermoplastic polymers, motivation for such development being based on the fact that thermoplastic polymers are often more ductile and therefore tougher than the brittle thermosets. Other advantages of thermoplastic polymers include a longer shelf life and ease of processability, i.e. unlike thermosets, they can be compression molded, injection molded and extruded using conventional equipment. Thermoplastics can also be recycled or reused, i.e. they can be reformed at higher temperatures, and used again. Even among the thermoplastic polymers in use, semicrystalline polymers have the advantage over their amorphous counterparts in that they possess higher stiffness, greater solvent and moisture resistance, and improved thermal and radiation stability. The disadvantage of using high performance semicrystalline thermoplastics is that often the processing temperatures have to be high enough

that chemical degradation may occur during processing. Therefore improved thermal stability of such polymers is of extreme importance. Due to the combination of the above mentioned advantages, these polymers are being used in a variety of applications such as composite matrix materials, adhesives, and electrical and electronic applications such as cable insulation, packaging and interlayer dielectric applications.

Perhaps the most important category of high performance thermoplastic polymers is the poly(arylene ether) based system. The poly(arylene ether) polymers are tough, rigid, and thermo-oxidatively stable polymers in use in a variety of engineering applications. The basic structure of this polymer is most accurately described by its name; these polymers are comprised of a rigid phenyl (aromatic) backbone and flexible ether linkages, and may include other chemical moieties. The rigid nature of the aromatic group provides these polymers with a stiff backbone leading to relatively high values of transition temperatures ( $T_g$  and  $T_m$ ). Commercially available poly(arylene ether) based polymers include Udel (polysulfone), Ultem (polyether imide) and Victrex (poly ether ether ketone). The application of high performance semicrystalline polymers requires an understanding of the relationship between structure, processing, morphology, and the resulting properties. Since most of the end use properties for which the high performance semicrystalline polymers are designed are critically dependent on the level and type of crystallinity, the study of the parameters governing the crystallization behavior is essential to tailoring the polymers to attain the required properties.

The objective of this study was to investigate the thermal, morphological, and crystallization behavior of high performance poly(arylene ether) based semicrystalline polymers,

and the parameters governing this behavior, both molecular (molecular weight, chain architecture) as well as processing (melt history, crystallization time/temperature etc.). The first three chapters deal with studies carried out on a series of novel poly(ether ether sulfide)s synthesized at VPI. These polymers are synthesized by the reactions of diphenyl sulfoxide based dihalides with diphenols (in this case, hydroquinone and biphenol). The reduction of the resulting amorphous precursor yields the corresponding semicrystalline polymer, leading to a phenyl or biphenyl based poly(ether ether sulfide). Chapter 1 discusses the thermal characterization and preliminary crystallization behavior of these poly(ether ether sulfide) polymers, and their amorphous precursors, the poly(ether ether sulfoxide)s. Chapter 2 details the results of studies on the crystallization behavior of the various molecular weights of the poly(ether ether sulfide)s under isothermal and non-isothermal conditions. Chapter 3 discusses the results of the spherulitic growth rate studies on the poly(ether ether sulfide)s. An interesting feature observed during the course of this study was the appearance of dual spherulitic morphology, the study of which forms a sizable part of this chapter. Chapter 4 deals with the thermal characterization and investigation of the thermal stability of polyimides based on 1,4-bis(4-aminophenoxy)benzene (TPEQ) and oxydiphthalic anhydride (ODPA) utilizing crystallization and rheological studies. Chapter 5 reports on the crystallization, melting, relaxation and rheological behavior of polyimides based on 1,3-bis(4-aminophenoxy)benzene (TPER) and biphenyl dianhydride (BPDA). This study also investigates the thermal stability of this system via crystallizability and rheological studies and compares the results with those of a commercial polyimide, New TPI. Finally in Chapter 6, using thermal analysis in conjunction

with x-ray scattering behavior, this dissertation addresses the effects of crystallization conditions (time and temperature) on the evolution of crystallinity in a commercial thermoplastic polyimide known as New TPI. This material is based on 3,3'-bis(4-aminophenoxy) biphenyl diamine (BAPB) and pyromellitic dianhydride (PMDA). A summary of all the results of chapters 1-6 is given in chapter 7 along with some possible avenues to explore in the future.

The poly(ether ether sulfide)s and the precursor sulfoxides used in this study were synthesized by Dr. J. R. Babu and Dr. J. S. Riffle, and were supplied in powder form. The molecular weight information was supplied along with the materials. Some details of the synthesis of these polymers are presented in Chapter 1. The TPEQ/ODPA polyimide and TPER/BPDA polyimides used in this study were synthesized by Marvin Graham and Dr. J. E. McGrath. Although the syntheses of these polymers have been described in great detail in Chapters 4 and 5, it should be emphasized that this author did not perform the synthesis of these polymers.

The results of these studies have been presented in the form of journal publications, each of which is presented as a separate chapter following the introduction. It should be mentioned that each chapter is presented with an abstract, introduction, experimental section, results and discussion and references. All relevant literature in the areas dealt with in this dissertation have been referred to in the various chapters. Details of the experimental conditions used and data analysis methods utilized have also been explained in the relevant chapters.

# Chapter - 1

## **Thermal Characterization and Crystallization of Novel Poly(arylene ether ether sulfide)s**

### **1.1 Abstract**

Thermal characterization has been carried out on a series of biphenol and hydroquinone based novel poly(arylene ether ether sulfide) polymers. TGA studies of the sulfide systems indicated high thermal stability in air as well as in nitrogen. X-ray studies showed the poly(ether ether sulfoxide) precursor materials to be amorphous and the poly(ether ether sulfide) materials to be semicrystalline. Based on the number average molecular weight of the poly(ether ether sulfoxide) materials, and the glass transition temperatures determined by DSC, the limiting  $T_{g\infty}$  has been determined for both amorphous precursors. The biphenol based precursor sulfoxide had a  $T_{g\infty}$  of 214 °C and the hydroquinone based precursor had a  $T_{g\infty}$  of 179 °C. DSC studies showed the biphenol based poly(ether ether sulfide) to have a  $T_g$  of ca. 142 °C and  $T_m$  of ca. 347 °C, and the hydroquinone based poly(ether ether sulfide) to have a  $T_g$  of ca. 100 °C and a  $T_m$  of ca. 243 °C. The equilibrium melting temperature  $T_m^\circ$  has been determined for both sulfide polymers using the Hoffman-Weeks method. The hydroquinone based poly(ether ether sulfide) exhibited a  $T_m^\circ$  of 278 °C, and the biphenol based poly(ether ether sulfide) showed a  $T_m^\circ$  of 371 °C. The effect of time and temperature in the melt on the subsequent

crystallization behavior of the two sulfide materials has also been investigated as a function of molecular weight.

## 1.2 Introduction

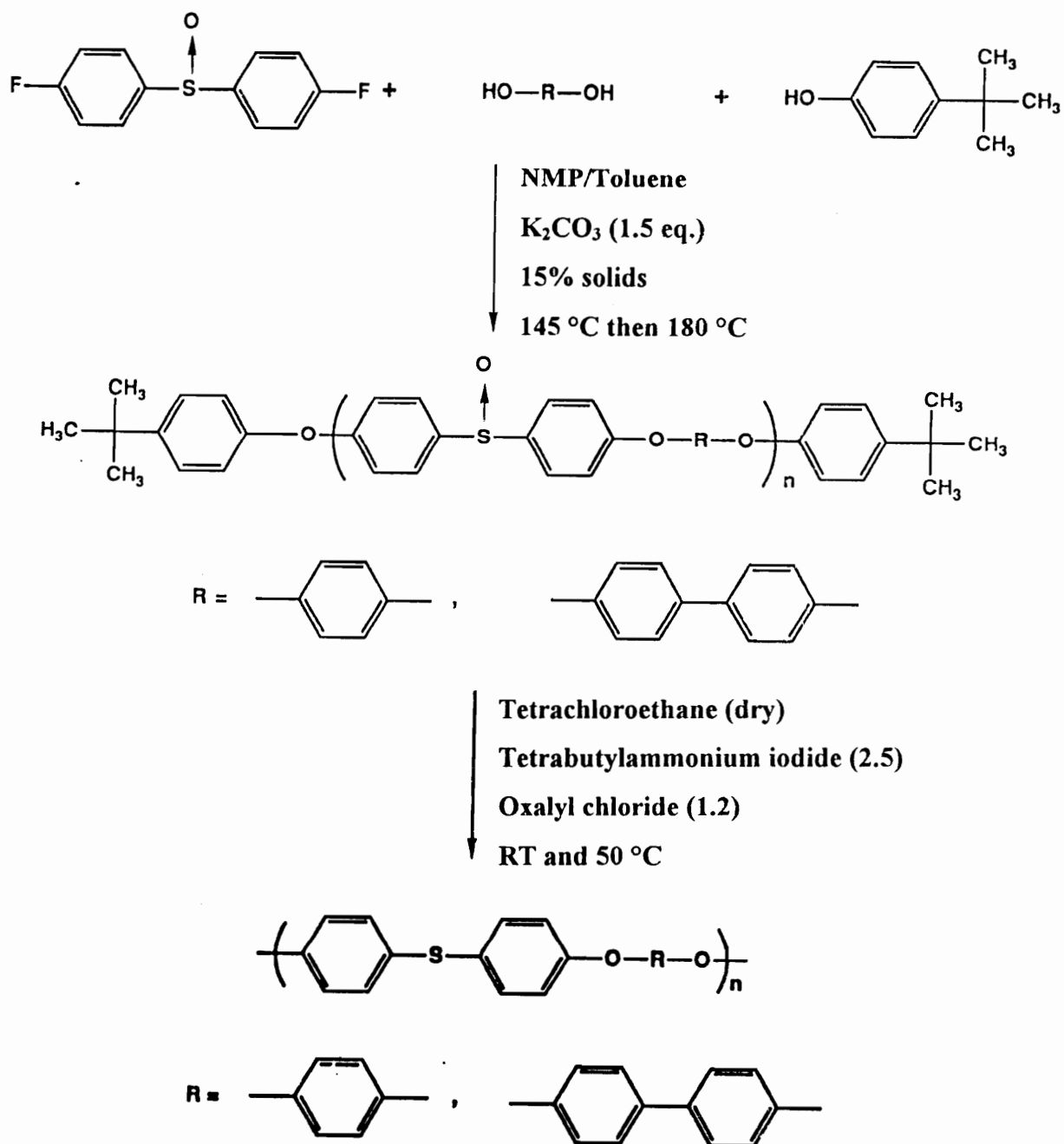
Recently, there has been considerable interest in the development of semicrystalline thermoplastic polymers for use in high performance engineering applications. Such polymers are being developed as potential replacements for conventional thermoset materials, such as the epoxies. Advantages of the thermoplastic polymers include their longer shelf life, their higher solvent and water resistance, and ease of processing. Due to the semicrystalline nature of these thermoplastic resins, their final properties depend greatly on the nature and extent of crystallinity present in the matrix. In order to retain mechanical properties and solvent resistance at temperatures above  $T_g$ , the extent or degree of crystallinity must be substantial. In case the degree of crystallinity is low, the maximum service temperature is limited by the softening or glass transition temperature; a lower degree of crystallinity also lowers the solvent resistance. The nature of the crystalline morphology therefore plays a critical role in determining the performance of the polymer in any engineering application. Both the nature, as well as the degree of crystallinity, depend on the processing conditions utilized, specifically the temperature and residence time in the melt.

Recent efforts have been directed towards developing semicrystalline poly(arylene ether) and poly(arylene thioether) resins. Important members in this class of polymers

include commercially well established polymers like PEEK and PPS, respectively. Efforts in this direction have also led to the development of copolymers based on the incorporation of ketone and sulfone linkages in poly(arylene ether) and poly(arylene thioether) polymers. Recent work of Senn has dealt with the synthesis and characterization of copolymers of poly(arylene sulfide)s with sulfones and ketones<sup>1-5</sup>.

New members in this class of polymers are the poly(arylene ether ether sulfide)s discussed in this work. The synthetic route to these polymers has been reported by Riffle et al.<sup>6</sup>. Briefly, soluble amorphous precursors, poly(arylene ether ether sulfoxide)s are prepared by nucleophilic aromatic substitution reactions between 4,4'-difluorodiphenyl sulfoxide and diphenols. The poly(ether ether sulfoxide)s are subsequently reduced to the corresponding sulfides using oxalyl chloride in conjunction with an iodide salt as shown in the reaction scheme (**Scheme I**). The reduction results in rapid, quantitative conversion of the sulfoxides to the semicrystalline sulfides which precipitate from solvent (tetrachloroethane) as fine particles. For simplicity, the precursor poly(ether ether sulfoxide)s derived from 4,4'-difluorodiphenyl sulfoxide and hydroquinone will be referred to as phenyl sulfoxides and those based on biphenol as biphenyl sulfoxides. Similarly their corresponding poly(ether ether sulfide)s will be referred to as phenyl sulfides and biphenyl sulfides, respectively.

It is now well known that thermal history, specifically the time and temperature in the melt, influence the crystallization behavior of a semicrystalline polymer during isothermal and non-isothermal crystallization<sup>7-15</sup>. Furthermore, due to the presence of a



Scheme I

large distribution of crystal sizes and perfection, semicrystalline polymers do not exhibit sharp melting temperatures, but show broad melting regions. At temperatures just above the experimentally measured melting temperature, complete disordering does not occur, resulting in regions having localized order. These regions of residual order can act as nucleating agents for crystallization when the polymer is subsequently cooled<sup>7</sup>. This process is hence known as self-nucleation. Higher temperatures or longer times in the melt destroy the number of residual nuclei, and therefore decrease the rate of crystallization during isothermal crystallization, or decrease the maximum crystallization temperature during non-isothermal crystallization. For many polymers it has been shown that holding the polymer at temperatures above its equilibrium melting temperature for a sufficient time effectively destroys all residual nuclei. The only nuclei which survive these melt conditions are other heterogeneities such as dirt, catalyst, etc. Such behavior has been reported for a number of materials including PEEK<sup>8-10</sup> and PPS<sup>11</sup>. However, it has also been shown that, for polar polymers such as nylon 66 and poly(tetrafluoroethylene), residual crystallinity persists even at temperatures well above the equilibrium melting temperatures, and that residence at high temperatures for very long times can still fail to destroy all the residual nuclei<sup>12-15</sup>.

This report details the results of initial characterization studies carried out on a series of novel poly(ether ether sulfoxide)s and poly(ether ether sulfide)s, as a function of backbone structure and molecular weight, using thermogravimetric analysis (TGA), differential scanning calorimetry (DSC), and X-ray diffraction (XRD).

### 1.3 Experimental

The phenyl sulfoxide precursors, in powder form had number-average molecular weights (g/mol) of 8.6K, 21K, 36K and 139K as determined by GPC using universal calibration. Similarly the phenyl sulfide polymers had molecular weights of 8.1K, 19.9K and 34K, the difference between these values and the sulfoxide precursors being due to the chemical reduction. The biphenyl sulfoxide precursor polymers had molecular weights ( $M_n$ ) of 8.2K, 15K, 20K, 25K, 30K, and 42K, and the biphenyl sulfide polymers had calculated molecular weights of 7.8K, 14.3K and 19.1K. The details of the molecular weight characterization have been given elsewhere<sup>6</sup>.

Thermogravimetric (TGA) measurements were carried out on a Seiko TG/DTA on 12-14 mg of sample. The experiments were conducted on as-received powder samples at heating rates of 10 °C/min under an air or nitrogen purge of 50 ml/min. Temperature calibration was based on the melting temperatures of indium and zinc. The temperatures for 5% weight loss are reported in this paper.

DSC measurements were made on a Seiko DSC on 7-9 mg of sample. All the experiments were carried out at heating rates of 10 °C/min under a nitrogen purge of 50 ml/min. Temperature and heat flow were calibrated using indium and zinc standards. All DSC traces shown have been normalized to 1 mg. The  $T_g$  measurements on the sulfoxide materials were performed on samples which were heated to 200 °C (phenyl) or 250 °C (biphenyl), quenched to room temperature, and subsequently reheated at 10 °C/min. The temperature at the midpoint of the transition was taken to be the glass transition

temperature. Measurements on the sulfide materials involved heating the samples to 300 °C (phenyl) or 400 °C (biphenyl), holding for 2 min, quenching to room temperature, and subsequently reheating at 10 °C/min. These will be referred to as the first and second heats respectively. The heating and cooling schedules involved in the melt time/temperature studies are described along with the results.

The X-ray diffraction was carried out on a Nicolet diffractometer operating at 40kV and 30mA and equipped with a STOE Bragg-Brentano type goniometer. Cu-K $\alpha$  radiation of wavelength 1.54 Å passed through a graphite monochromator before final collimation. Data were collected at 0.05° increments between angles of 5-60°. X-ray studies on the sulfide polymers were carried out on the as-received powders. The diffraction experiments on the sulfoxide polymers were carried out on films which were formed by hot-pressing the sulfoxides at temperatures 30 °C above their T<sub>g</sub> for 5 min.

## 1.4 Results And Discussion

TGA studies carried out on the sulfoxide precursor polymers indicated a sharp weight loss at ca. 345 °C for the biphenyl sulfoxides and ca. 370 °C for the phenyl sulfoxides. Table 1.1 shows the temperatures for 5% weight loss for the phenyl sulfoxide system and biphenyl sulfoxide polymers as determined by TGA. For the case of the phenyl sulfoxide polymers, the 8.6K polymer had a lower degradation temperature as compared

**Table 1.1** Temperatures for 5% weight loss by TGA for poly(ether ether sulfoxide)s and poly(ether ether sulfide)s.

**Phenyl Sulfoxide**

<b>Molecular weight</b>	<b>Air (°C)</b>	<b>Nitrogen (°C)</b>
8.6K	354	354
21K	377	382
36K	367	372

**Phenyl Sulfide**

<b>Molecular weight</b>	<b>Air (°C)</b>	<b>Nitrogen (°C)</b>
8.1K	513	509
19.9K	515	516
34K	516	513

**Biphenyl Sulfoxide**

<b>Molecular weight</b>	<b>Air (°C)</b>	<b>Nitrogen (°C)</b>
8.2K	341	343
15K	340	341
20K	345	344

**Biphenyl Sulfide**

<b>Molecular weight</b>	<b>Air (°C)</b>	<b>Nitrogen (°C)</b>
7.8K	531	515
14.3K	534	526
19.1K	520	526

to the higher molecular weight polymers. For the biphenyl sulfoxide polymers, the temperatures for 5% weight loss were essentially independent of molecular weight. Interestingly, changing the purge atmosphere from nitrogen to air did not appreciably change the degradation temperatures.

DSC studies on the sulfoxide materials showed only an endothermic transition corresponding to the  $T_g$  and no recrystallization exotherm or melting endotherm, indicating that the sulfoxide polymers were amorphous. It is a well known fact that the  $T_g$  of a polymer increases with molecular weight and eventually reaches an asymptotic value corresponding to the glass transition at infinite molecular weight,  $T_{g\infty}$ . Using free volume arguments, Fox and Flory<sup>16</sup> proposed the following relationship to determine the high molecular weight limit  $T_{g\infty}$

$$T_g = T_{g\infty} - K/M_n \quad (1)$$

where  $K$  is a constant for a given polymer.

As detailed in the experimental section, the  $T_g$ 's of the sulfoxide polymers were determined from the mid-points of the glass transitions using DSC. These data were plotted as a function of number average molecular weight (Figure 1.1). A least-squares analysis of the data yielded  $T_{g\infty} = 179$  °C for the phenyl sulfoxide and  $T_{g\infty} = 214$  °C for the biphenyl sulfoxide.

Wide angle X-ray diffraction (WAXD) studies carried out on the phenyl sulfoxide (21K) and biphenyl sulfoxide (20K) films resulted in characteristic amorphous diffraction

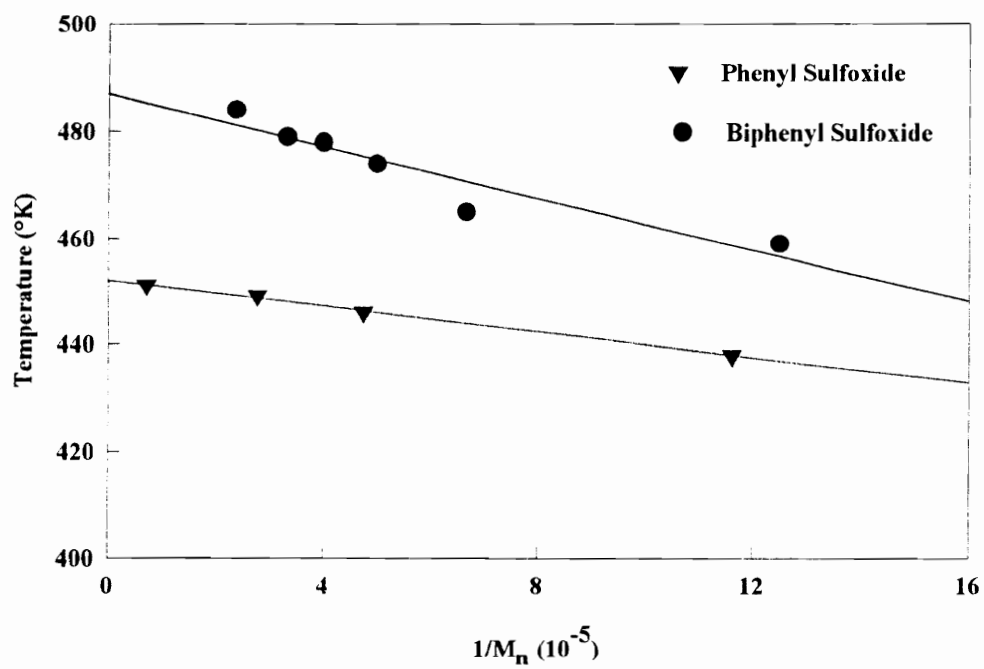


**Figure 1.1** Plot of  $T_g$  vs.  $1/M_n$  for poly(ether ether sulfoxide)s

patterns (Figure 1.2). Two broad peaks corresponding to the amorphous phase are evident in Figure 1.2, supporting the conclusion obtained from the DSC. The features of the diffraction pattern of the biphenyl sulfoxide (20K) polymer remained unchanged on annealing at 270 °C ( $T_g + 70$  °C) for 3 hours, thus reinforcing the belief that the sulfoxide system was indeed amorphous.

TGA studies on the sulfide materials indicated that the polymers had good thermal stability in air as well as in nitrogen. The sulfide materials showed a 5% weight loss occurring around 510 °C in air and in nitrogen. These degradation temperatures are substantially higher than the corresponding values for the sulfoxide precursors, indicating a significantly higher thermal stability for the sulfides as compared to the sulfoxides. Since the backbone chemical structure of the sulfoxides and sulfides are identical except for the presence of the S→O moiety on the chain, the lower thermal stability of the sulfoxides may well arise from an inherent thermal lability of the S→O group. Table 1.1 shows the 5% weight loss temperatures for the phenyl sulfide and biphenyl sulfide systems. It is obvious from the data that the degradation temperatures are essentially the same for both the phenyl and the biphenyl systems. The degradation temperatures also seemed to be independent of the choice of air or nitrogen as the purge gas. A critical point to be noted is that there appears to be no molecular weight dependence of degradation temperatures for either sulfide system. If the sulfoxide precursors had not been completely converted to the sulfide polymers, a weight loss would have been observed at a lower temperature

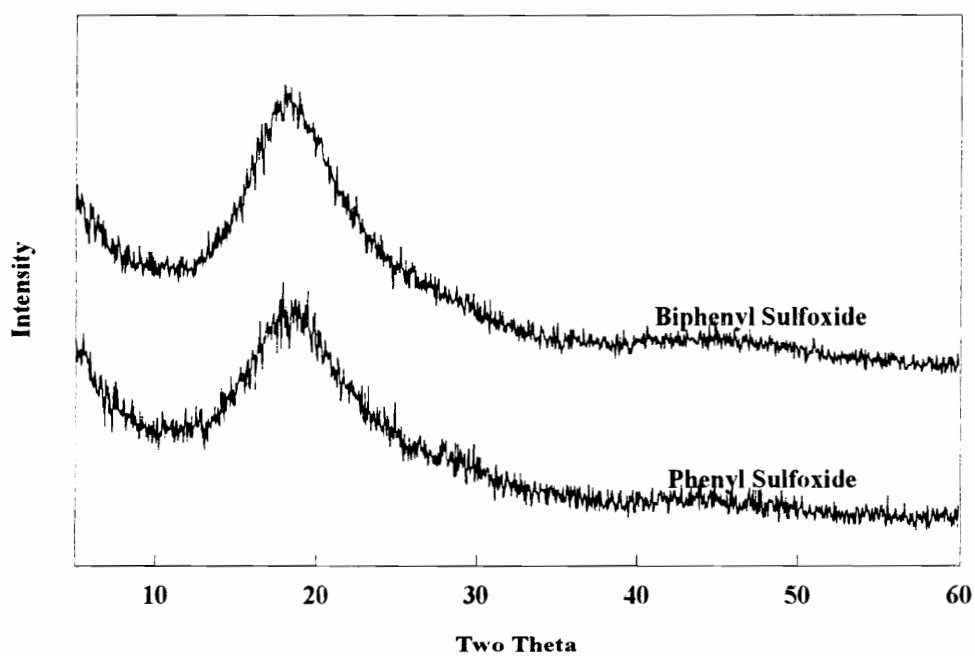


**Figure 1.2** Wide angle x-ray patterns for poly(ether ether sulfoxide)s.

corresponding to the degradation temperature of any remaining sulfoxide species. The absence of any such weight loss at lower temperatures strongly indicates complete quantitative conversion of the sulfoxides to the respective sulfides.

DSC traces of the first and second heats (Figures 1.3&1.4) of the phenyl sulfide polymers yielded melting temperatures ranging from 243 °C for the 34K polymer to 260 °C for the 8.1K polymer. Interestingly, the values of  $T_g = \text{ca. } 100 \text{ }^\circ\text{C}$  and  $T_m = \text{ca. } 245 \text{ }^\circ\text{C}$  are somewhat similar to the corresponding values for the well known commercial polymer poly (phenylene sulfide) (PPS) ( $T_g = \text{ca. } 85 \text{ }^\circ\text{C}$  and  $T_m = \text{ca. } 285 \text{ }^\circ\text{C}$ ), and poly para-phenylene oxide ( $T_g = \text{ca. } 105^\circ\text{C}$  and  $T_m = \text{ca. } 285 \text{ }^\circ\text{C}$ ), with PPS and PPO having slightly larger crystallization windows. The phenyl sulfide polymer can be considered a copolymer of PPS and PPO. The  $T_g$  value of 100 °C for the phenyl sulfide polymer is indeed consistent with copolymer theories of the glass transition<sup>17</sup>. The DSC traces of the phenyl sulfide system (Fig 1.3 & 1.4) show that the glass transition temperature was not prominent in the first heat for any molecular weight, and the  $T_g$  could be clearly observed in the second heat for the two higher molecular weight materials only. This is because the as-received polymers are recovered from solvent, which leads to a high degree of crystallinity and a low amorphous fraction, resulting in a small specific heat increase across the glass transition, and hence a very small transition in the DSC curve corresponding to  $T_g$ . At the end of the first heat, the polymers were quenched at 70 °C/min to room temperature. Due to greater mobility, the low molecular weight polymers crystallize relatively fast, resulting in crystallization during the quench process after the first heat.

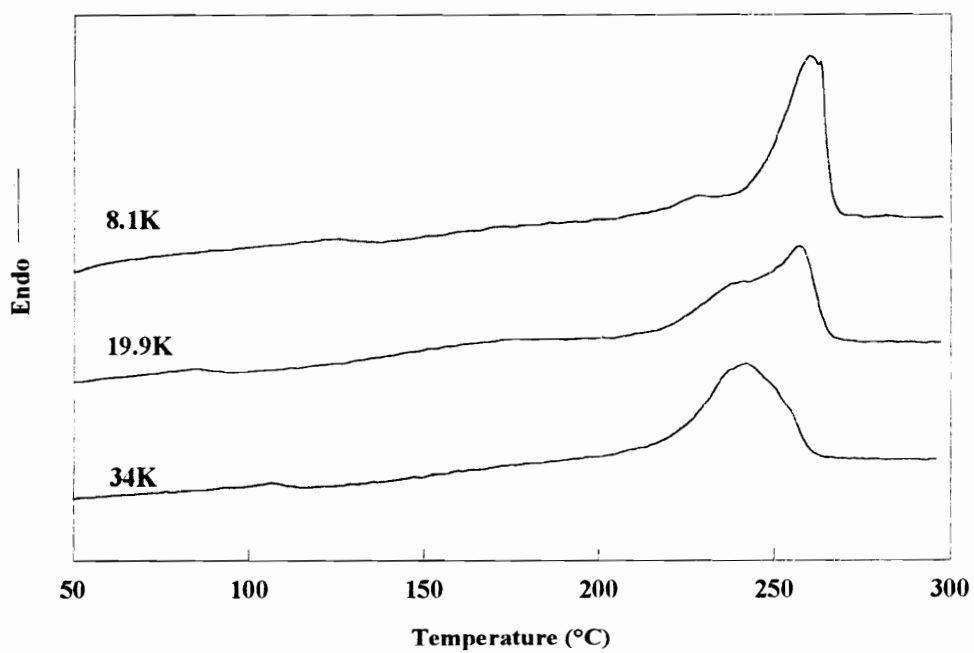


**Figure 1.3** First heat DSC scan for poly(phenyl ether ether sulfide)

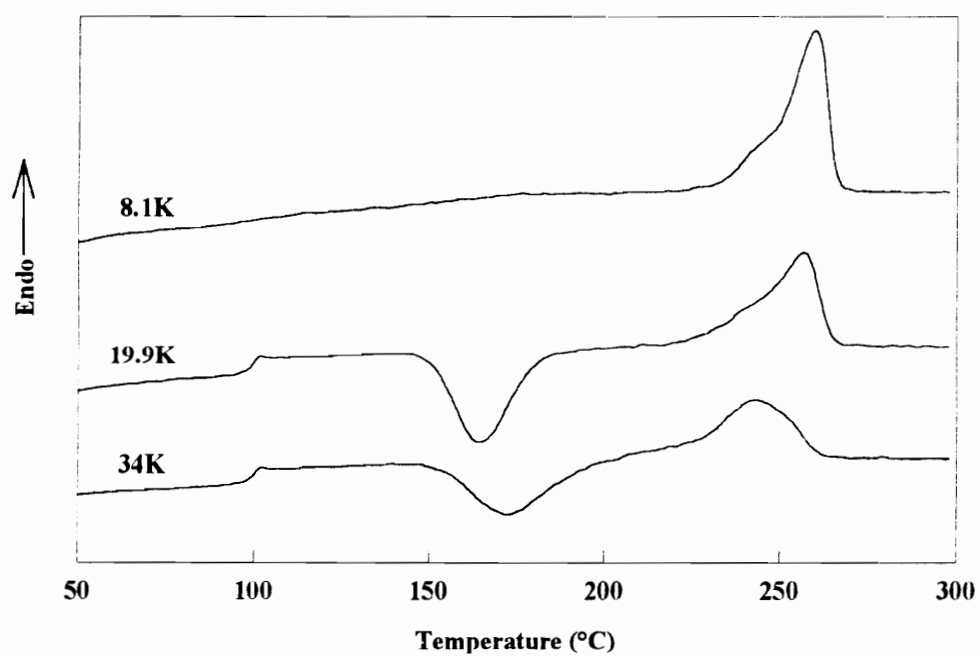


**Figure 1.4** Second heat DSC scan for poly(phenyl ether ether sulfide)

This again results in a low amorphous fraction and hence a very weak transition corresponding to the  $T_g$ , which could not be well resolved by the DSC during the second heat. This reasoning is supported by the fact that no crystallization exotherm is observed during the second heat for the low molecular weight polymer. On the other hand, due to lower mobility caused by higher viscosities, the higher molecular weight species could not crystallize during the quench, resulting in essentially amorphous polymers. During the reheat, the higher molecular weight polymers exhibit prominent  $T_g$ 's consistent with larger amorphous fractions. Due to the relatively slow heating rates involved, the polymers are able to crystallize during heating, and hence exhibit exotherms corresponding to crystallization. The melting point dependence on the molecular weight in the as-received samples can be best explained by the fact that low molecular weight polymers can form more perfect crystals than their higher molecular weight analogs, thus leading to higher melting temperatures. The molecular weight dependence of the melting point during the second heat can be explained as follows. The higher molecular weight polymers are initially amorphous, but crystallize during the heating scan, i.e. dynamic or non-isothermal crystallization. During such a process, the crystals formed are relatively unstable and hence undergo a continuous process of melting and recrystallization to form crystals of greater stability. Due to the high viscosity and hence lower mobility, the high molecular weight polymers need longer times to form stable crystals, which due to the continuous heating process, is not available. It would therefore be expected that higher molecular weight polymers would form less-stable crystals and hence melt at lower temperatures.

Figure 1.4 also shows that the position of the crystallization peak moves to higher temperatures as the molecular weight increases. This is certainly due to the higher mobility of the lower molecular weight polymers which results in faster crystallization and hence lower peak crystallization temperatures. This observation is consistent with reports in the literature of a similar molecular weight dependence for PEEK<sup>18</sup>. Comparison of the first and second heats showed the heats of fusion to be similar, indicating that the materials do not undergo significant degradation, and that the materials crystallize during the DSC scan.

DSC scans of the biphenyl sulfide materials (Figures 1.5 & 1.6) showed these materials had a  $T_g = \text{ca. } 142 \text{ }^\circ\text{C}$  and a  $T_m = \text{ca. } 347 \text{ }^\circ\text{C}$ . A comparison of these values with the corresponding values for the phenyl sulfide system shows that the biphenyl sulfide polymers have a substantially higher  $T_g$  and  $T_m$  than the phenyl sulfide polymers. This is undoubtedly due in part to the presence of the biphenyl linkage in the molecule (**Scheme I**), which causes stiffening of the backbone. Other factors being equal, a stiffer chain would exhibit a lower entropy of fusion, which would lead to a higher  $T_m^\circ$ . An interesting observation here is the very close similarity of the values of  $T_g$  and  $T_m$  for the biphenyl sulfide system to the corresponding values for commercial PEEK ( $T_g = \text{ca. } 144 \text{ }^\circ\text{C}$  and  $T_m = \text{ca. } 347 \text{ }^\circ\text{C}$ ).

As in the case of the phenyl sulfide materials, there were no prominent glass transitions during the first heats, and the 7.8K material did not show any  $T_g$  even in the second heat. Also, no crystallization exotherm was observed for the 7.8K material during

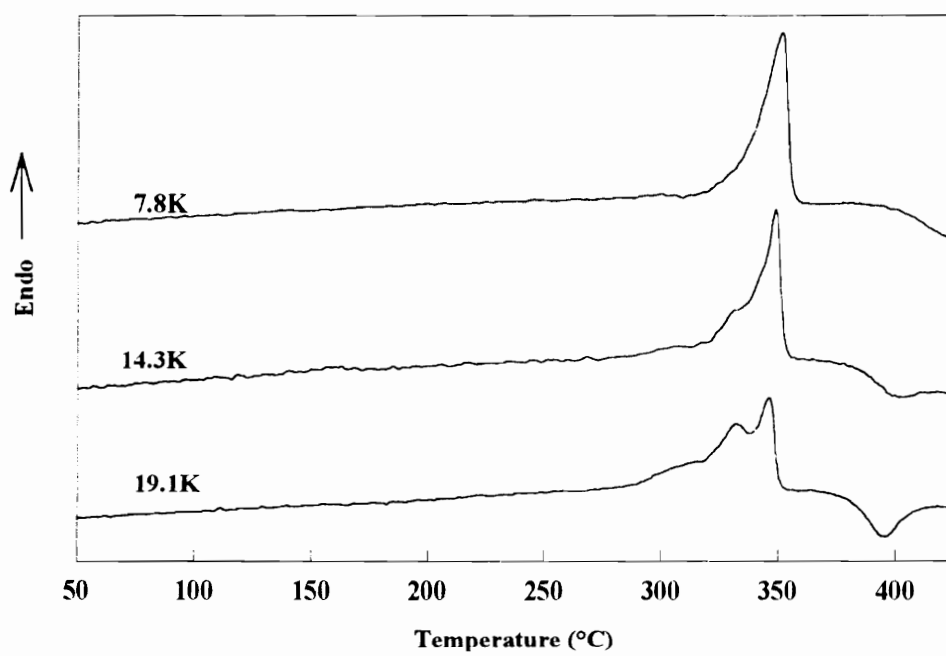


**Figure 1.5** First heat DSC scan for poly(biphenyl ether ether sulfide)

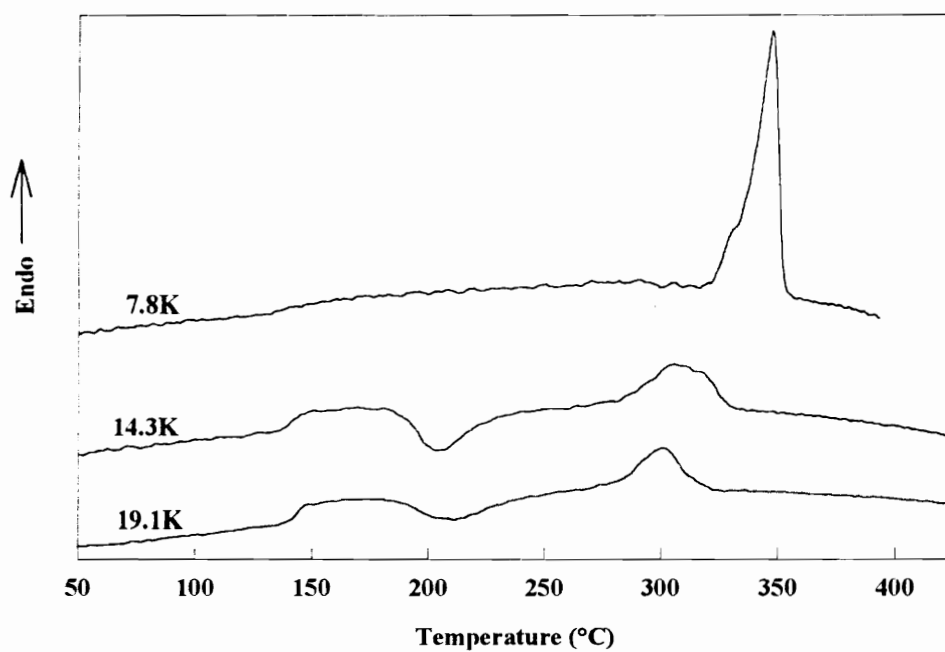


**Figure 1.6** Second heat DSC scan for poly(biphenyl ether ether sulfide)

the second heat, implying that the material rapidly crystallized during quenching.

Prominent glass transitions, crystallization exotherms and melting endotherms were observed for the two higher molecular weight polymers during the second heat. In contrast to the melting behavior of the phenyl sulfides, the melting temperatures of the as-received biphenyl sulfides (first heat) were essentially independent of molecular weight. As seen in the case of the phenyl sulfides, a molecular weight dependence can be seen for the melting temperatures and peak crystallization temperatures during the second heat.

An exotherm at 400 °C was prominent in the first heat DSC scans of the two higher molecular weight biphenyl sulfide polymers. This may correspond to some chemical process - possibly cross-linking. The absence of this exotherm in the second heat implies that the exotherm was due to some irreversible chemical change in the material. The exotherm could be a result of some melt state curing as has been reported for PPS<sup>19</sup>.

Comparison of the heats of fusion between the first and second heats showed no difference for the 7.8K polymer. However, for the higher molecular weight materials, the heats of fusion corresponding to the second heat were lower than that of the first heat. This could be either due to the slower crystallization rates of the higher molecular weight polymers or the result of some chemical changes that occurred in the polymer corresponding to the exotherm at 400 °C.

A comparison of the thermal stability of the phenyl and biphenyl sulfide systems with PPS and PEEK respectively, was carried out in air and nitrogen atmospheres. The data show that degradation temperatures for the phenyl sulfide polymers are about 30 °C

higher than for PPS. This may be due to the higher bond strength and hence thermal stability of the phenyl-oxygen linkage as compared to the phenyl-sulfur linkage<sup>20</sup>. There was no appreciable difference between the degradation temperatures of the biphenyl sulfide polymers and PEEK. The same trend was observed when air or nitrogen was used as the purge gas.

Wide angle diffraction studies on both types of sulfide polymers showed diffraction patterns characteristic of semicrystalline polymers. Figure 1.7 shows diffraction patterns for the phenyl sulfide (19.9K) and biphenyl sulfide (19.1K) polymers. The X-ray patterns are characteristic of a semicrystalline polymer with at least 3 prominent reflections and 6 other weak reflections evident in the patterns.

As mentioned earlier, holding the polymer at a melt temperature above its equilibrium melting temperature has been found to be effective in destroying all residual nuclei. Hence, the temperature just required to destroy all residual nuclei could give an indication of the equilibrium melting temperature of the polymer<sup>8</sup>. The equilibrium melting temperature ( $T_m^\circ$ ) is the temperature required to melt crystals of infinite thickness and is generally obtained using extrapolative procedures. Perhaps the most common method to determine  $T_m^\circ$  is through the Hoffman-Weeks plot<sup>21</sup>. This method requires one to obtain the melting temperatures ( $T_m$ ) of the polymer at various crystallization temperatures ( $T_c$ ). In a plot of  $T_m$  vs  $T_c$ , the line joining the points is extrapolated to the line  $T_m=T_c$ . The point of intersection is the equilibrium melting temperature ( $T_m^\circ$ ). An important point to be noted here is that small variations or errors in determining the

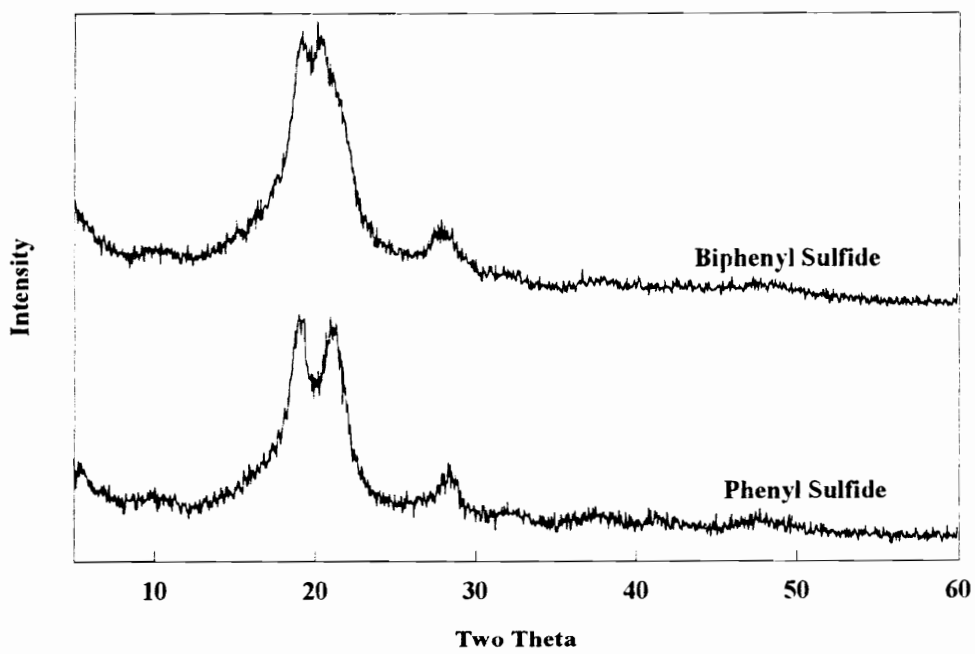


**Figure 1.7** Wide angle x-ray patterns for poly(ether ether sulfide)s.

crystallization temperature or melting temperature can lead to large variations in the equilibrium melting temperature due to the extrapolation procedure used. The value of  $T_m^\circ$  obtained from the Hoffman-Weeks plot should hence be used only as an indication of the true equilibrium melting temperature. Figure 1.8 shows the Hoffman-Weeks plots of the biphenyl sulfide (14.3K) and phenyl sulfide (19.9K) polymers, from which the equilibrium melting temperatures were determined to be 371 °C for the biphenyl sulfide and 278 °C for the phenyl sulfide respectively.

The effect of time and temperature in the melt on the subsequent crystallization behavior of the sulfide systems was investigated to optimize conditions for future isothermal crystallization experiments. As mentioned earlier, the melt history of the sample dictates the crystallization behavior due to the presence of residual nuclei. During the study of isothermal crystallization kinetics, it is desirable to destroy all residual nuclei in the melt, so as not to influence the nucleation mechanisms during isothermal crystallization. The absence of residual nuclei ensures that no self-nucleation occurs, i.e. crystal growth occurs only at those nuclei which were formed at the isothermal crystallization temperature, other heterogeneities, and the surfaces of the container. The DSC heating and cooling schedules used in these experiments were as follows. The samples were heated at 20 °C/min to various melt temperatures and held for different times. The samples were then cooled at 10 °C/min to room temperature. The temperature of exothermic deviation from the baseline is taken to be the onset of crystallization. The peak of the crystallization exotherm formed during the cooling is

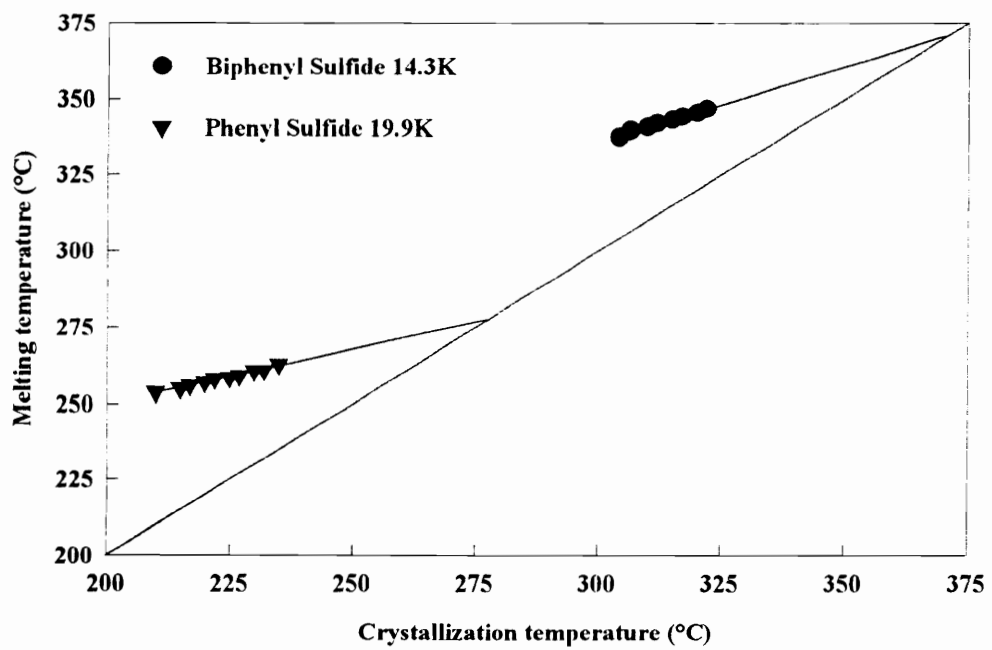


**Figure 1.8** Hoffman-Weeks plot for poly(ether ether sulfide)s.

denoted as the maximum crystallization temperature ( $T_{\text{cmax}}$ ). The area under the crystallization exotherm is denoted as the heat of crystallization.

Figures 1.9-1.11 show the effect of time and temperature in the melt on the maximum crystallization temperature ( $T_{\text{cmax}}$ ) and the heat of crystallization of the phenyl sulfide system. Figure 1.9 shows that higher temperatures in the melt result in lower values of  $T_{\text{cmax}}$ , this effect being most prominent for the higher molecular weight polymers. At temperatures above 282 °C, the changes in  $T_{\text{cmax}}$  are relatively small. The same trend was observed for the onset temperature as well. This can be explained by the fact that higher temperatures more effectively destroy any residual nuclei remaining in the material. The destruction of these nuclei causes crystallization to occur at larger supercoolings. Since the values of  $T_{\text{cmax}}$  are relatively constant above 282 °C, it can be concluded that the residual nuclei are effectively destroyed by residence temperatures of 282 °C and above. This is consistent with the earlier observation that the equilibrium melting temperature of the phenyl sulfide polymer has been determined to be 278 °C. Figure 1.10 shows that the heat of crystallization does not change for the low molecular weight polymer and that large changes occur only at higher temperatures for the higher molecular weight polymers. TGA studies of the 34K polymer held at 290 and 300 °C showed that the degradation temperatures were the same as that of the as-received sample, again implying no degradation during annealing of the melt. Figure 1.11 shows the effect of time in the melt at 265 °C on the maximum crystallization temperature. It can be seen that the maximum crystallization temperature is essentially independent of time in the melt. The onset

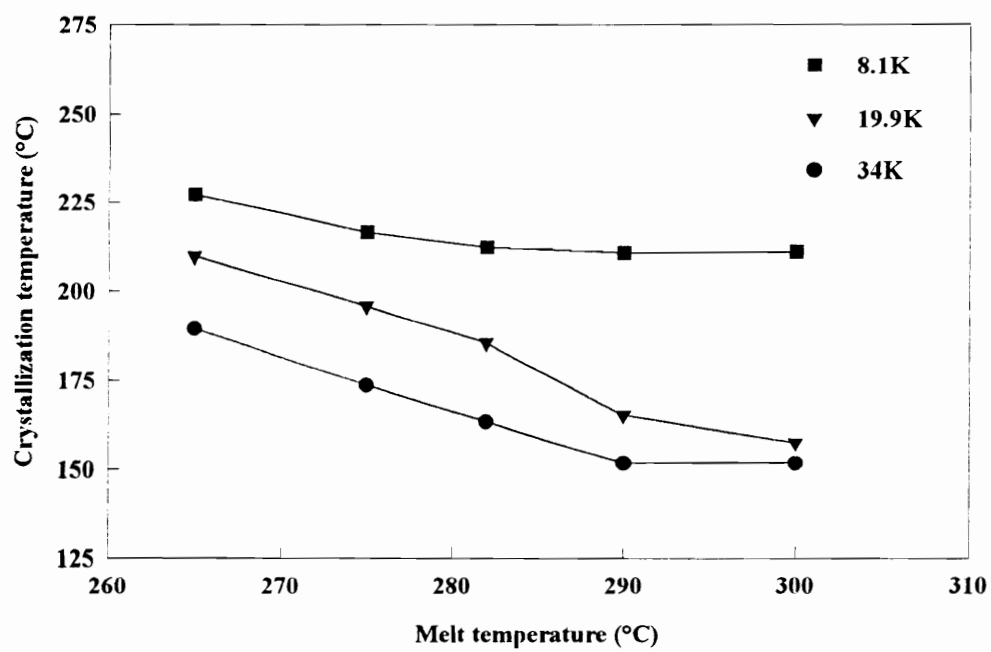


**Figure 1.9** Effect of melt temperature on the maximum crystallization temperature for poly(phenyl ether ether sulfide)s. Time in the melt is 5 min.

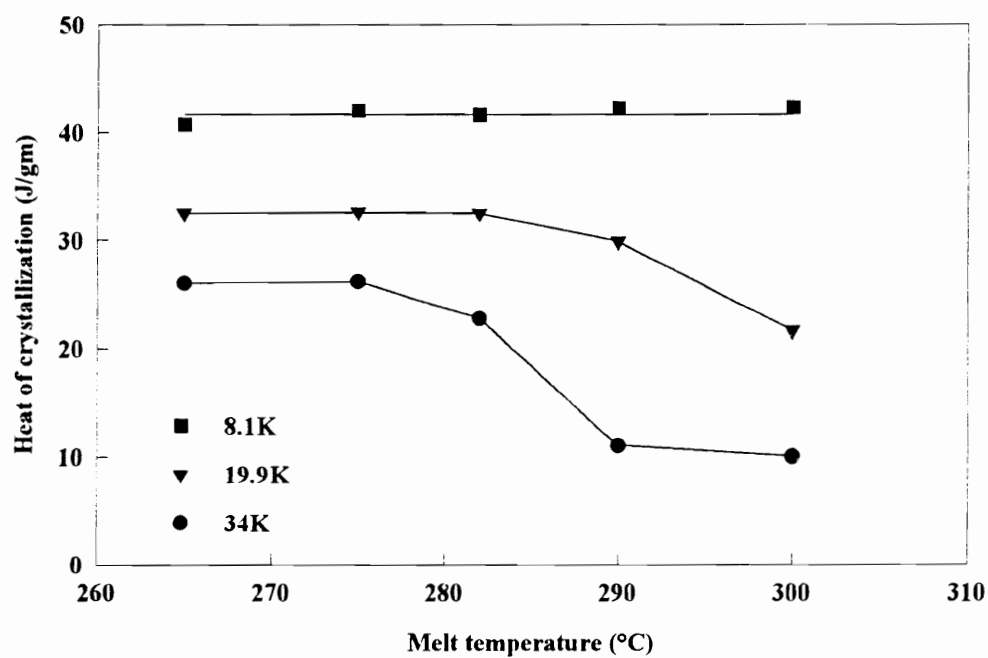


**Figure 1.10** Effect of melt temperature on the heat of crystallization for poly(phenyl ether ether sulfide)s. Time in the melt is 5 min.

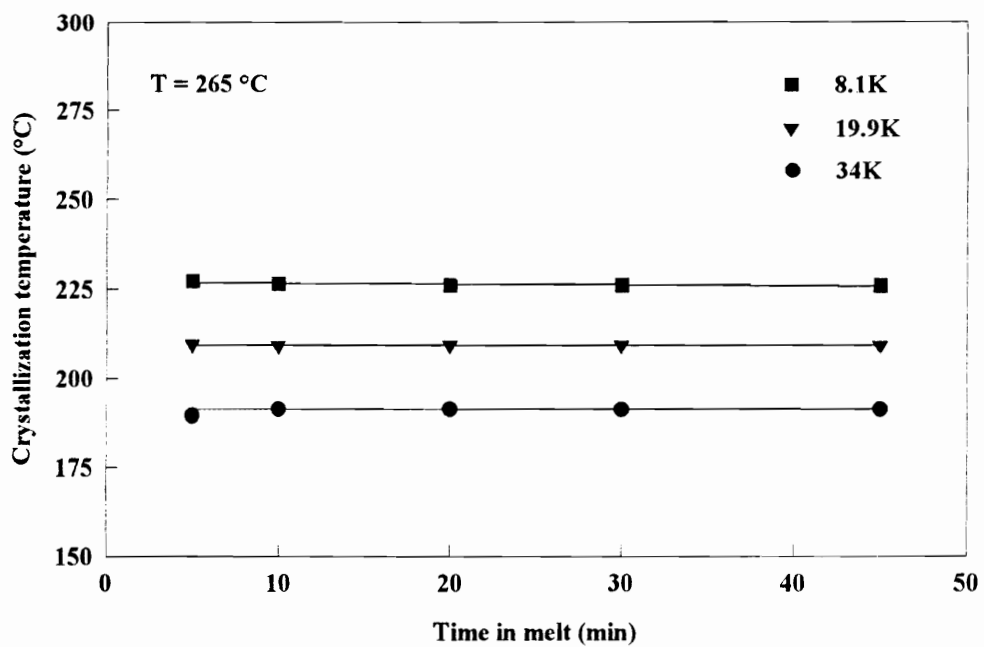


**Figure 1.11** Effect of time in the melt on the maximum crystallization temperature for poly(phenyl ether ether sulfide).

temperature and heat of fusion were also independent of time in the melt. The same behavior was observed for samples held at 282 °C for various times, implying that the crystallization behavior was insensitive to the residence time in the melt. This independence of the crystallization behavior on time in the melt is contrary to the behavior observed for PEEK and PPS. Such behavior is important from a processing point of view since a minimal residence time in the melt is sufficient to destroy residual nuclei in the material and allows for a reproducible crystallization response upon cooling.

This crystallization response to varying times in the melt can be explained as follows. Since 282 °C is above the equilibrium melting temperature of the phenyl sulfide system, at this temperature we would expect all of the residual crystalline regions to be completely destroyed. Varying time hence does not affect the crystallization behavior. However, the crystallization behavior has been shown to be independent of time in the melt even at 265 °C, which is below the equilibrium melting temperature. Lee et al.<sup>8</sup> observed that in the case of PEEK, at low enough melt temperatures, increasing time in the melt did not substantially influence the crystallization behavior; the time dependence of the crystallization behavior was observed only at temperatures well above the melting temperature. For the case of the phenyl sulfide polymers, since 265 °C is just 15 °C above the observed melting temperature of 250 °C, time in the melt does not play a significant role in affecting the crystallization behavior.

Figures 1.12-1.16 show results of the melt studies for the biphenyl sulfide system. It can be seen in Figure 1.12 that higher melt temperatures cause a decrease in the  $T_{\text{cmax}}$

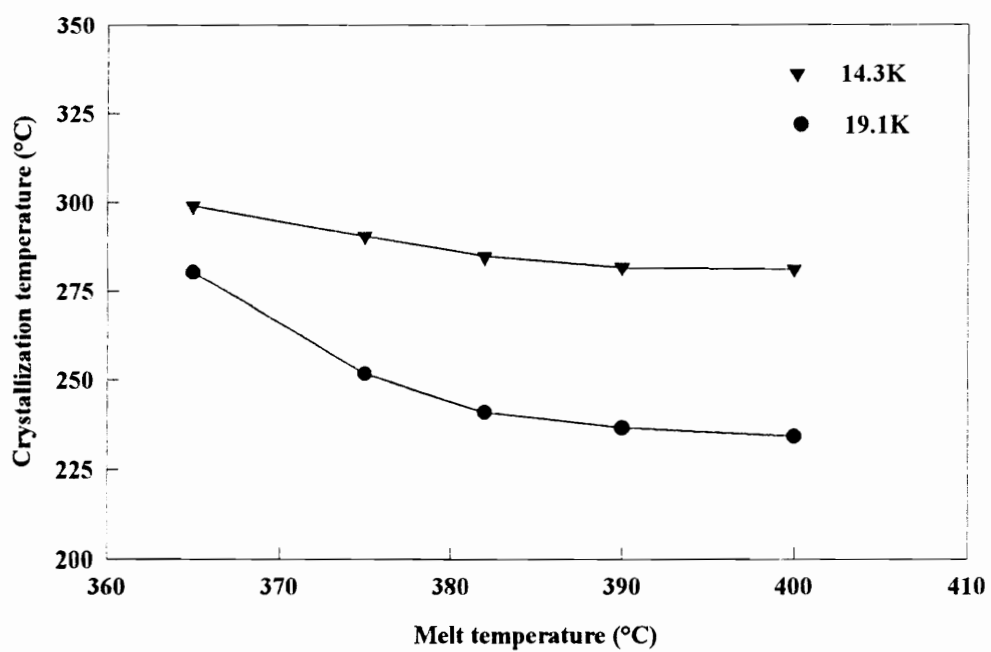


**Figure 1.12** Effect of melt temperature on the maximum crystallization temperature for poly(biphenyl ether ether sulfide). Time in the melt is 5 min.

values. This decrease is prominent up to a temperature of 382 °C, beyond which the value remains constant. The heat of crystallization variation with melt temperature is shown in Figure 1.13. For the 19.1K polymer, the heat of crystallization is a constant up to melt temperatures of 400 °C, at which point the value decreases. This may be due to the exotherm seen in the first heat DSC scan which occurs at ca. 400 °C. For the 14.3 K polymer, there is an initial decrease beyond which the value is a constant. The onset temperature dependence on the melt temperature is shown in Figure 1.14. The decrease in the onset temperature with melt temperature is obvious from the figure. The sudden drop in the onset temperature of the 19.1K polymer at 400 °C may also be due to the exothermic process occurring in the polymer. *In contrast to the phenyl sulfide system, the crystallization behavior of the biphenyl sulfide polymers showed a strong dependence on residence time in the melt.* Before discussing the effects of time in the melt on the crystallization behavior, a point worth mentioning is that the exotherm seen at 400 °C also occurred at lower temperatures on annealing for longer times. Keeping that fact in mind, the results of the time studies can be rationalized. Figure 1.15 shows the effect of melt time at 365 °C on the maximum crystallization temperature. It can be seen that the maximum crystallization temperature decreases with increasing time, after which it reaches a constant value. The behavior of the onset temperature is qualitatively the same. From Figure 1.16, one notes that the heat of crystallization remains a constant up to the first 10 min after which it decreases to a constant value. The effect of time in the melt at a melt temperature of 382 °C was qualitatively the same as that observed at 365 °C, except that

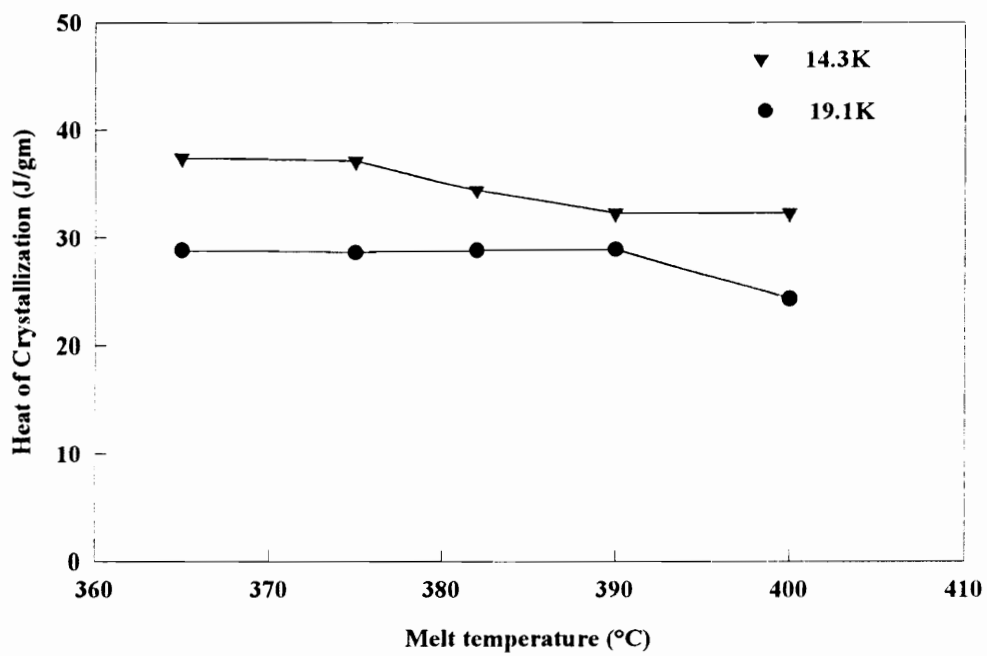


**Figure 1.13** Effect of melt temperature on the heat of crystallization for poly(biphenyl ether ether sulfide). Time in the melt is 5 min.

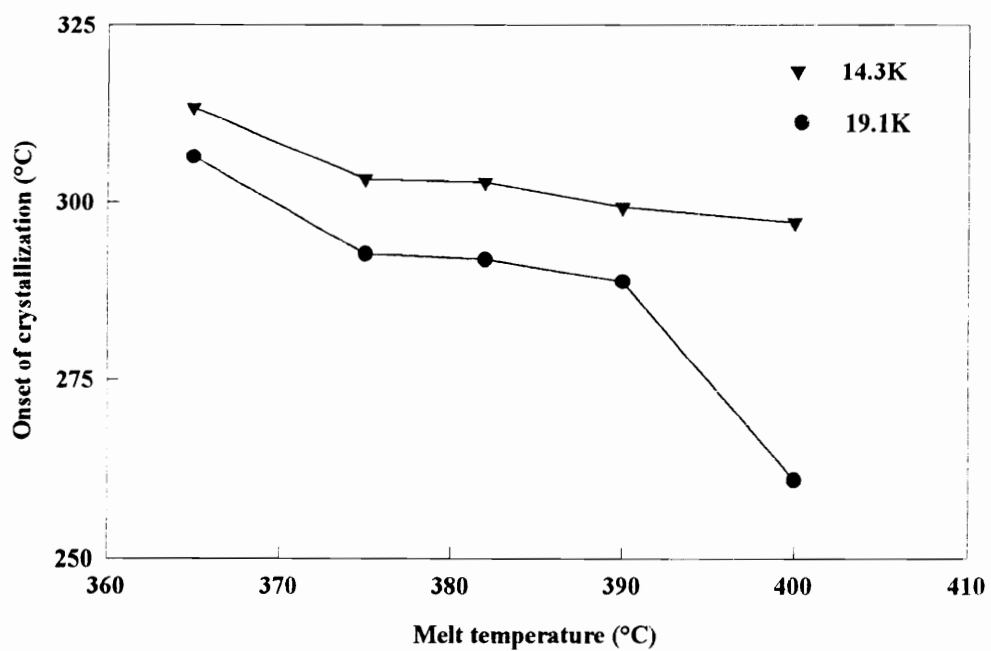


**Figure 1.14** Effect of melt temperature on the onset of crystallization for poly(biphenyl ether ether sulfide). Time in the melt is 5 min.

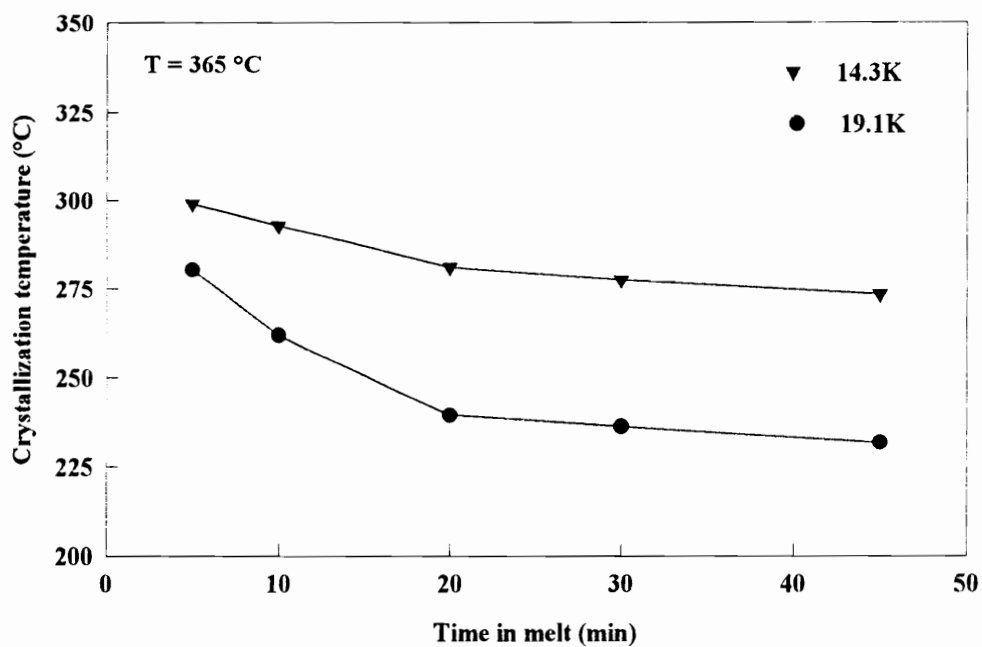


**Figure 1.15** Effect of time in the melt on the maximum crystallization temperature for poly(biphenyl ether ether sulfide).

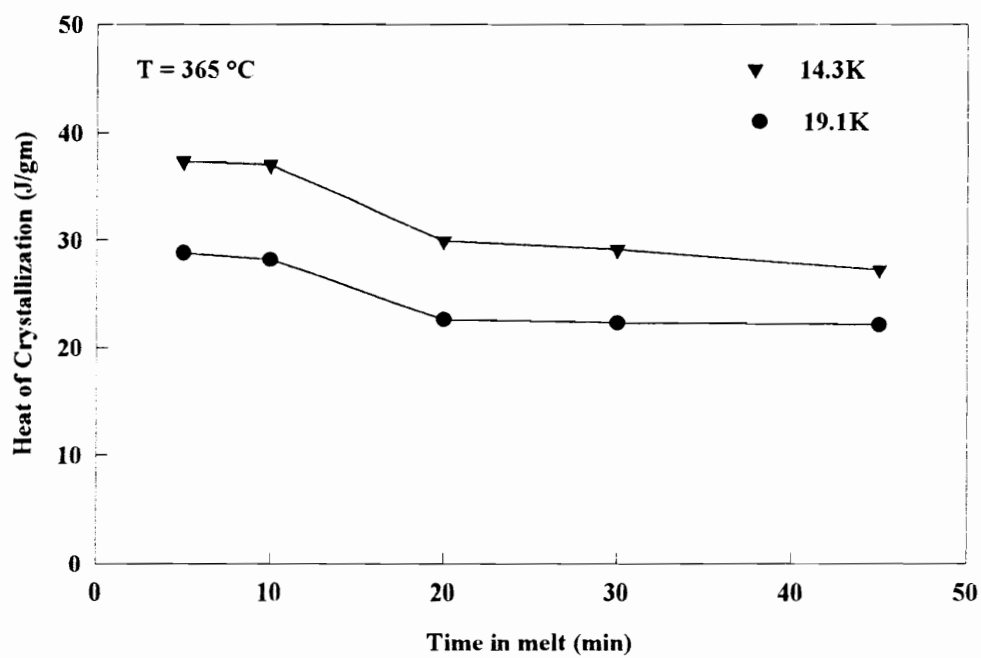


**Figure 1.16** Effect of time in the melt on the heat of crystallization of poly(biphenyl ether ether sulfide).

the initial decrease occurred at earlier times. This follows from the experimental observation that the exotherm was observed at shorter times at higher temperatures. To confirm the irreversible effect the exotherm had on the crystallization response, some samples were subjected to dual thermal treatments. Specifically, a sample of the biphenyl sulfide (19.1K) polymer was heated to 365 °C, held for 30 min, cooled to room temperature at 10 °C/min, then reheated to 365 °C, held for 5 min, then cooled to room temperature at 10 °C/min. The peak temperature and heat of crystallization of the exotherm developed during the second cooling step were compared to the crystallization exotherm of a sample subjected to a single thermal history at 365 °C for 5 min. The peak temperature as well as the heat of crystallization of the exotherm formed after the dual thermal treatment was lower than that formed after a single thermal treatment implying some irreversible change in the sample as a result of residence at 365 °C for 30 min. Data for the 7.8K biphenyl sulfide polymer are not reported here due to the observation of a dual exotherm on cooling from the melt.

It is obvious from the data presented above that the crystallization behavior of these polymers shows a strong molecular weight dependence, as might be expected in this range. The onset temperatures and peak temperatures of the crystallization exotherms are higher for the lower molecular weight polymers. This is certainly due to the higher mobility of the lower molecular weight polymers which allows for faster crystallization rates. The low molecular weight polymers also show higher heats of crystallization

implying a greater “ease” of crystallization. This also arises from the higher mobility and fewer number of entanglements for low molecular weight polymers.

## 1.5 Summary and Conclusions

This paper reports the initial characterization of a series of novel poly(arylene ether) systems. These poly(arylene ether ether sulfide)s could have potential applications as high performance polymers. In addition, due to the similarity of the phenyl sulfide polymer to PPS, this system could serve as a model system to study the effect of backbone structure on the crystallization behavior of aromatic polymers. X-ray diffraction studies showed the sulfoxide precursor materials to be amorphous and the sulfide materials to be semicrystalline. TGA studies indicated good thermal stability of the materials, particularly the sulfides, in air as well as in nitrogen.

DSC studies showed that higher melt temperatures or longer residence times in the melt decrease the maximum crystallization temperatures, consistent with more "severe" thermal treatments being more effective at destroying residual nuclei in the melt. A few common features noted in this study were that the low molecular weight polymers showed higher values of onset temperature,  $T_{cmax}$  and heat of crystallization as compared to the higher molecular weight polymers. Another significant fact is that the low molecular weight polymers were less affected by the melt conditions than the higher molecular weight polymers.

Based on the results of this study, isothermal and non-isothermal crystallization kinetic studies have been carried out and will be reported later.

## Acknowledgments

The authors would like to acknowledge the support of this study by NSF under contract # DMR 9120004.

## References

1. D. R. Senn, *J. Polym. Sci. Part A: Polym. Chem.*, **32**, 1175 (1994).
2. D. R. Senn, U.S. Pat. 5,268,449, to Phillips Petroleum Co. (1993).
3. D. R. Senn, U.S. Pat. 5,286,817, to Phillips Petroleum Co. (1994).
4. D. R. Senn, U.S. Pat. 5,298,573, to Phillips Petroleum Co. (1994).
5. D. R. Senn, U.S. Pat. 5,298,574, to Phillips Petroleum Co. (1994).
6. J. R. Babu, M. Konas, A. E. Brink, and J. S. Riffle, *ACS PMSE Preprints*, **68**, 99 (1993); J. R. Babu, M. Konas, A. E. Brink, and J. S. Riffle J. S., *Polymer*, **35**, 4949, (1994).
7. B. Wunderlich, *Macromolecular Physics Vol.2*, Academic, New York, (1977).
8. Y. Lee and R. S. Porter, *Macromolecules*, **21**, 2770 (1988).
9. Y. Deslandes, M. Day, N. F. Sabir, and T. Suprunchuk, *Polymer Composites*, **10**, 360 (1989).

10. S. Kumar, D. P. Anderson, and W. W. Adams, *Polymer*, **27**, 329 (1986).
11. N. Mehl and L. Rebenfeld *Polym. Eng. and Sci*, **32**, 1451 (1992).
12. Y. P. Khanna and A. C. Reimschuessel, *J. Appl. Polym. Sci.*, **35**, 2259 (1988).
13. Y. P. Khanna, A. C. Reimschuessel, A. Banerjee, and C. Altman, *Polym. Eng. and Sci.*, **28**, 1600 (1988).
14. Y. P. Khanna, R. Kumar, and A. C. Reimschuessel, *Polym. Eng. and Sci.*, **28**, 1607 (1988).
15. Y. P. Khanna, R. Kumar, and A. C. Reimschuessel, *Polym. Eng. and Sci.*, **28**, 1612 (1988).
16. T. G. Fox and P. J. Flory, *J. Appl. Polym. Sci.*, **21**, 581 (1950).
17. J. J. Aklonis and W. J. MacKnight, *Introduction to Polymer Viscoelasticity*, John Wiley, New York (1983).
18. M. Day and T. Suprunchuk, *Proceedings of 18<sup>th</sup> NATAS Conference*, **2**, 597 (1989).
19. H. W. Hill Jr. and D. G. Brady, *Encyclopedia of Chemical Technology*, **18**, 793 (1982).
20. *CRC Handbook of Chemistry and Physics*, 68<sup>th</sup> Ed., CRC Press (1988).
21. J. D. Hoffman and J. J. Weeks, *J. Res. Natl. Bur. Stand.*, **66(A)**, 13 (1962).

## Chapter - 2

### **Kinetics of Isothermal and Non-Isothermal Crystallization of Novel Poly(arylene ether ether sulfide)s**

#### **2.1 Abstract**

The kinetics of crystallization have been studied for a series of novel poly(ether ether sulfide)s based on a biphenyl moiety in the backbone, referred to as biphenyl sulfide, and phenyl moieties in the backbone, referred to as phenyl sulfide. Isothermal melt crystallization kinetic studies of these polymers were carried out and analyzed based on the well known Avrami equation. Avrami exponents close to 3 were obtained for the phenyl sulfides, independent of molecular weight or crystallization temperature, which could imply growth of 3-dimensional spherulitic superstructures following heterogeneous nucleation. For the biphenyl sulfides, values closer to 2 were obtained for the exponent, also independent of molecular weight or crystallization temperature, which could imply growth of 2-dimensional disc like superstructures or the incomplete development of 3-dimensional superstructures following heterogeneous nucleation. For both the sulfide systems studied, the lower molecular weight polymers showed lower half times, higher rate constants and higher heats of crystallization. As expected, in the nucleation-controlled regime, the rate constant increased with increasing undercooling, causing a decrease in crystallization half-times. The nucleation density was calculated from the rate

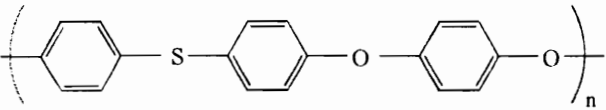
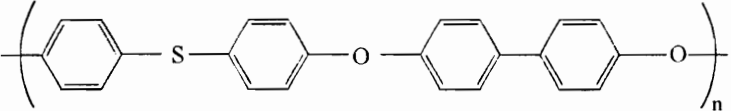
constant data in conjunction with growth rate data for the 19.9K phenyl sulfide polymer and found to be essentially independent of undercooling. The equilibrium melting temperature of the phenyl sulfide system was determined from a Hoffman-Weeks extrapolation to be 292 °C, independent of molecular weight. A detailed kinetic analysis of the bulk crystallization rate constants suggested that the lower molecular weight (8.1K, 19.9K) samples crystallized according to Regime II kinetics. The highest molecular weight sample (34K) showed a Regime II to III transition at ca. 205 °C. The regime transition was not affected by a slight variation in the values chosen for  $U^*$  and  $T_\infty$ . Non-isothermal crystallization kinetics from the melt were studied by utilizing cooling rates from 2°C/min to 70 °C/min. In all cases studied, the Ozawa analysis could not well describe the evolution of crystallinity, possibly due to the inapplicability of some of the inherent assumptions in this type of analysis. The non-isothermal data were hence analyzed using the conventional form of the Avrami equation, which yielded good fits to the data. This semi-quantitative method of analysis yields a reduced rate constant which was found to increase with increasing cooling rate, and decreasing molecular weight. The results of the isothermal and non-isothermal crystallization studies carried out on the poly(ether ether sulfide)s have been compared wherever possible to the results available for PPS and PEEK.

## 2.2 Introduction

Semicrystalline thermoplastic polymers are increasingly being considered as replacements for conventional thermosets in many engineering applications. This trend is due to the advantages of thermoplastics which includes a longer shelf life and the ability to be recycled; semicrystalline polymers offer the further advantages of excellent solvent and chemical resistance, thermal stability and improved radiation resistance. Among the widely studied semicrystalline thermoplastics include the poly(arylene ether) and poly(arylene thioether) based polymers, examples of which are poly(ether ether ketone) (PEEK)<sup>1-10</sup> and poly(phenylene sulfide) (PPS)<sup>11-23</sup> respectively. These polymers are being used in a variety of applications such as molding resins, composite matrix materials, and electrical and electronic applications. New additions to this class of polymers are the recently synthesized novel poly(arylene ether ether sulfide)s, the synthetic details of which have been reported earlier<sup>24</sup>. The structure of these poly(ether ether sulfide)s is shown in Table 2.1. For simplicity, the poly(ether ether sulfide)s based on the single phenyl group in the backbone will hereafter be referred to as phenyl sulfide and those based on the biphenyl groups in the backbone, as biphenyl sulfide.

The thermal characterization of these novel materials has already been carried out and reported elsewhere<sup>25</sup>, a few salient points of which are described here. Briefly, the phenyl sulfide showed a  $T_g$  of ca. 100 °C and  $T_m$  of ca. 243 °C, and the biphenyl sulfide exhibited a  $T_g$  of ca. 142 °C and  $T_m$  of ca. 347 °C. Interestingly, these values of  $T_g$  and  $T_m$

**Table 2.1** Chemical structures and transition temperatures of poly(ether ether sulfide)s.

Chemical Structure	$T_g$	$T_m$	$T_m^\circ$
<p>Phenyl Sulfide</p> 	100 °C	243 °C	292 °C
<p>Biphenyl Sulfide</p> 	142 °C	347 °C	371 °C

for the phenyl and biphenyl sulfide systems are quite similar to the corresponding values for PPS and PEEK respectively. The phenyl sulfide system is also quite similar to PPS in terms of its backbone structure, and indeed can be considered a copolymer of PPS and PPO (poly *p*-phenylene oxide).

The final properties of a semicrystalline polymer in an engineering application are critically dependent on the extent of crystallinity and the nature of crystalline morphology, which in turn depend on the processing conditions utilized. It is therefore necessary to understand the relationship between processing conditions and the development, nature and degree of crystallinity. Among the processing conditions that could influence the subsequent crystallization behavior are time and temperature of melt processing, i.e. the residence conditions in the melt that the polymer experiences prior to crystallization. The effect of melt history (time and temperature) on the subsequent crystallization behavior of the poly(ether ether sulfide)s has already been investigated<sup>25</sup>; based on the results of this earlier investigation, the melt conditions for this study were chosen. The crystallization process itself could occur either under isothermal conditions or under dynamic conditions, i.e. non-isothermal conditions. The development of crystallinity under these conditions must hence be investigated and understood prior to fabrication.

This chapter presents the results of investigations on both the isothermal and non-isothermal crystallization kinetic studies on these two poly(ether ether sulfide)s. The results of these studies will be compared wherever possible to the corresponding results

available for PPS and PEEK, in light of the similarity of the crystallization windows with the sulfide polymers studied here.

## **2.3 Experimental**

### *2.3.1 Materials*

The phenyl sulfide polymers were obtained in powder form and had number average molecular weights of 8.1K, 19.9K and 34K. Similarly, the biphenyl sulfide polymers had molecular weights of 14.3K and 19.1K. The details of the molecular weight characterization have been reported elsewhere<sup>24</sup>. The PEEK used in this study was also available in the powder form and had a number average molecular weight of 20K.

### *2.3.2 Characterization*

The crystallization kinetic studies were carried out on a Seiko DSC 220C on individual 12-14 mg samples under a nitrogen purge. Temperature and heat flow were calibrated using indium, tin, and zinc standards. The heating and cooling schedules involved in this study were as follows: the samples were heated to 282 °C (phenyl sulfide) or 382 °C (biphenyl sulfide) and held in the melt for 5 min. The melt times and temperatures used in this study were based on the results of the earlier study on the effect of melt time and temperature on the crystallization behavior<sup>25</sup>. For the case of isothermal crystallization, the samples were rapidly cooled (ca. 75 °C/min) to the required

temperature and held until there was no further noticeable exothermic deviation from the baseline. The heating rate during the melting scan was 10 °C/min. For the case of the non-isothermal crystallization studies, the samples were cooled from the melt at rates of 2, 5, 10, 20, 40 and 70 °C/min to room temperature. The crystallization exotherms in these studies were analyzed to extract further information on the kinetics.

### 2.3.3 Data Analysis

Isothermal crystallization kinetic data have been analyzed using the well known Avrami equation<sup>26-28</sup>

$$X_{cr}(t) = 1 - e^{-Kt^n} \quad (1)$$

where  $X_{cr}(t)$  is the relative crystallinity at time  $t$  and is defined by  $X_{cr}(t) = X_c(t)/X_c(\infty)$ ,  $K$  is the Avrami rate constant, and  $n$  is the Avrami exponent. The rate constant  $K$  contains information on the crystal growth rate  $G$ , and the nucleation density  $N$ . The Avrami exponent depends on the type of processes governing the nucleation and growth mechanisms<sup>29</sup>. For the case of growth of 3-dimensional crystallites (spherulites), and assuming a constant linear rate of growth of the spherulites, the rate constant can be related to the growth rate and nucleation density for the case of predetermined nucleation at a given crystallization temperature by

$$K = \frac{4}{3} \pi G^3 N \quad (2)$$

Rearranging Eqn.1 and taking a double log yields the following simplified form of the Avrami equation

$$\ln[-\ln(1-X_c)] = \ln K + n \ln t \quad (3)$$

Thus, a plot of  $\ln[-\ln(1-X_c)]$  vs.  $\ln t$  yields a straight line, the slope of which is the Avrami exponent  $n$  and the intercept yields the rate constant  $K$ . Depending on the mechanism of nucleation (homogeneous vs. heterogeneous) and type of crystal growth, i.e. one-dimensional (rods), two-dimensional (discs) or three-dimensional (spheres), different integer values of the Avrami exponent can be obtained. However, integer values of the Avrami exponent are seldom obtained from experimental data, making the precise interpretation of results obtained from this analysis somewhat difficult. This could occur due to the various simplifications assumed in the original derivation of the Avrami equation which do not necessarily apply to all polymer systems for all crystallization conditions.

1) The original Avrami equation was derived for a constant volume phase transformation, i.e. transformation of a volume of amorphous material to an equal volume of crystalline material. Since the density changes during crystallization, the Avrami analysis can strictly be applied only to the case of a weight of amorphous material transformed to an equal weight of crystalline material. The densities of the amorphous and crystalline material should hence be taken into account in this type of analysis<sup>30</sup>.

- 2) The original Avrami equation was developed to model the crystallization behavior in low molecular weight substances where secondary crystallization was not a factor, i.e. the entire crystallization was assumed to occur from a primary process. For the case of polymers, secondary crystallization can complicate the overall crystallization process. The Avrami equation should hence be applied *only* for low degrees of conversion where it can be reasonably assumed that secondary crystallization does not play a significant role.
- 3) The Avrami equation assumes a constant linear growth rate of the crystallizing macrostructure, and constancy in shape and density of the growing macrostructure. The early stages of growth of spherulites is typically not spherical, and various intermediate sheaf-like structures are formed prior to the formation of sphere-like structures. Also, as discussed above, secondary crystallization processes in the spherulites would violate the assumption of constant density of the growing spherulites.
- 4) A single nucleation mode is assumed in the derivation of the Avrami equation, i.e. either only heterogeneous nucleation or only homogeneous nucleation. This assumption may not be met for polymers under isothermal crystallization conditions, which usually show mixed nucleation modes during crystallization, i.e. a mixture of athermal and thermal nucleation.
- 5) The study of the crystallization of polymers using the Avrami analysis is most commonly carried out by following the crystallization exotherm on a DSC. The peak of the exotherm has generally been attributed to the impingement of the spherulites. As discussed above, the Avrami analysis must be restricted to data collected for times earlier

than the time corresponding to the crystallization peak. A major source of error in the Avrami analysis is introduced during assigning the zero point of the process, i.e. choosing a point on the DSC scan where the crystallization process is assumed to have begun<sup>31,32</sup>. The value of  $K$ , the Avrami rate constant can change by an order of magnitude by small changes in the start time of crystallization. Changes in the exponent  $n$  can also occur by changing the starting time of crystallization.

In spite of the above listed limitations, the Avrami analysis provides useful information regarding the mechanism and rates of crystallization, which could be used as a comparative tool for data obtained at different temperatures, or different molecular weights, or even different polymers.

The kinetics of bulk or overall crystallization can be modeled quite satisfactorily by an Avrami analysis as discussed above. This process involves a primary nucleation step, followed by crystal growth on the primary nuclei, usually by a process of secondary nucleation. The second step, i.e. the crystal growth process can often be described quite accurately by the description of Hoffman and Lauritzen<sup>33</sup>. According to the theory developed by Hoffman and Lauritzen, the crystal growth rate can exhibit specific regime transitions on changing the crystallization temperature, i.e. on increasing the undercooling. Several workers have shown that the bulk crystallization rate can also display these regime transitions<sup>9,34-36</sup>. Briefly, according to the regime theory of crystallization, one can plot  $\ln G + U^*/[R(T_c - T_\infty)]$  as a function of  $1/[T_c(\Delta T)f]$ , where  $G$  is the crystal growth rate,  $U^*$  is an activation energy generally taken to be 1500 cal/mol,  $T_c$  is the crystallization

temperature,  $T_{\infty}=T_g-30$  K,  $\Delta T=T_m^{\circ}-T_c$  (undercooling), and  $f=2T_c/(T_m^{\circ}+T_c)$  is a factor to account for the change in the heat of crystallization as a function of temperature. In order to analyze the overall kinetics of crystallization, the first term, i.e.  $\ln G$  can be replaced by  $\ln K$ , where  $K$  is the Avrami rate constant. Recall from the discussion of the Avrami equation that the rate constant is a function of both the growth rate as well as the nucleation density. Thus, extending the Lauritzen-Hoffman analysis to the bulk crystallization rate ignores the dependence of the bulk crystallization rate constant on the nucleation density.

In contrast to isothermal crystallization, non-isothermal crystallization kinetic data is most commonly analyzed using the Ozawa<sup>37</sup> approach to model the kinetics. The Ozawa approach is based on the Avrami equation, which as described earlier is used to describe isothermal crystallization kinetics. In the Ozawa approach, the time variable in the Avrami equation is replaced with a cooling (or heating) rate term. The equation is thus

$$\ln(1 - X_c) = \frac{K(T)}{\Phi^n} \quad (4)$$

where  $\Phi$  is the cooling (or heating) rate.  $K(T)$  is the cooling (or heating) function that is itself a complex function that contains the growth rate  $G$  as well as the nucleation density  $N$  terms.

Similar to the case of the Avrami equation, taking the log of both sides yields

$$\ln[-\ln(1 - X_c)] = \ln K(T) - n \ln \Phi \quad (5)$$

Thus, a plot of  $\ln[-\ln(1-X_c)]$  vs.  $\ln\Phi$  would yield  $n$  as the slope and  $K(T)$  as the intercept.

This method assumes that crystallization occurs under constant cooling (or heating) rates. In this method, rates of conversions at various temperatures are compared for the different cooling (or heating) rates. The rates of conversions are then plotted against the cooling rate resulting in a series of straight lines for each temperature. A drawback with this method is that, at a given temperature, the crystallization processes at different cooling rates are at different stages, i.e. the lower cooling rate process is towards the end of the crystallization process, whereas at the higher cooling rate, the crystallization process is at an early stage<sup>4</sup>. This can lead to substantial curvature in the Ozawa plot as is shown later. Any deviation from straight line behavior signifies the inability of this approach to model the non-isothermal crystallization. In spite of the above problem, this approach has been successfully used to describe the non-isothermal crystallization behavior of PET<sup>37</sup>, polypropylene<sup>38</sup>, PPS<sup>18</sup> and New TPI<sup>39</sup>. The limitations of this approach to analyzing data obtained for polyethylene<sup>38</sup> and PEEK<sup>4</sup> have been explained as being due to secondary crystallization and the comparisons of different stages of crystallization at different cooling rates.

Another approach that can potentially be used to analyze non-isothermal crystallization data is the traditional Avrami approach that is used for isothermal crystallization. Though the values of the Avrami rate parameter ( $K$ ) and the Avrami

exponent ( $n$ ) do not have the same significance as in the case of isothermal crystallization, nevertheless this approach has been found to be useful in describing non-isothermal crystallization<sup>4</sup>. As was done in the case of isothermal crystallization, data only at low conversions were analyzed by this approach, so as to minimize the influence of substantial secondary crystallization.

## 2.4 Results And Discussion

### 2.4.1 Isothermal Crystallization

Figure 2.1 shows the relative crystallinity plotted as a function of time for the phenyl sulfide 19.9K polymer at various temperatures. The development of relative crystallinity displays the familiar sigmoidal shape with time. It can be seen that as the crystallization temperature increases, the crystallization curve shifts to longer times, signifying slower bulk crystallization rates. The data shown in Figure 2.1 have been analyzed using the Avrami equation as described earlier. The classical Avrami plots obtained from these data are shown in Figure 2.2. It should be emphasized here that only the data at low conversions have been used to construct the plot. It is obvious from the straight line plots obtained that the Avrami equation is quite successful in describing the development of crystallinity with time. Similar Avrami plots were constructed for the other molecular weights of the phenyl sulfide system and the various molecular weight biphenyl sulfide polymers as well. The values of the slope and intercept of the straight line

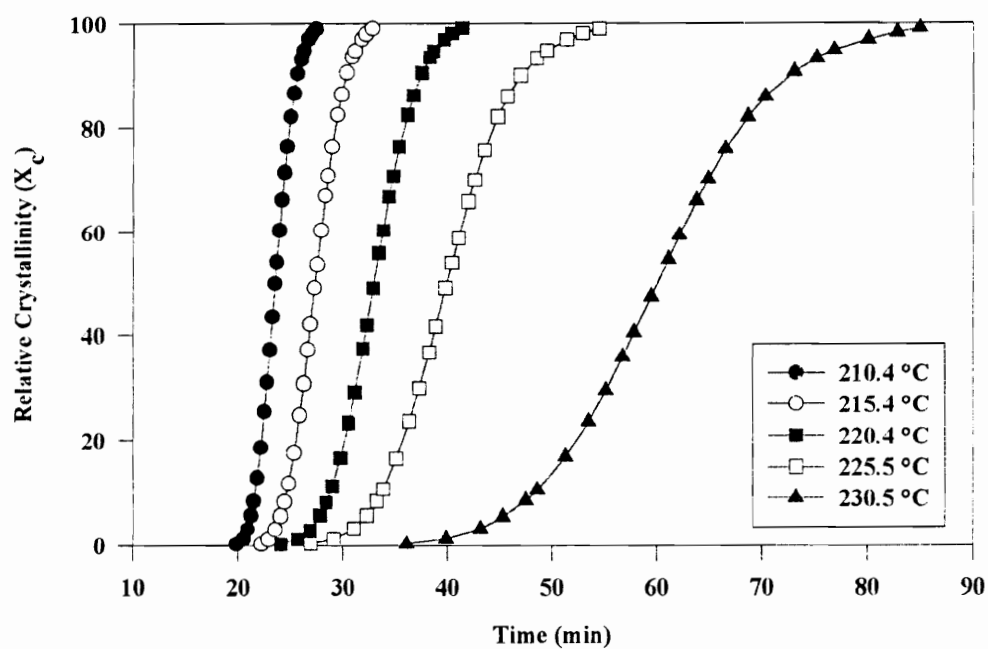


**Figure 2.1** Relative crystallinity as a function of time for isothermal crystallization from the melt for phenyl sulfide 19.9K.

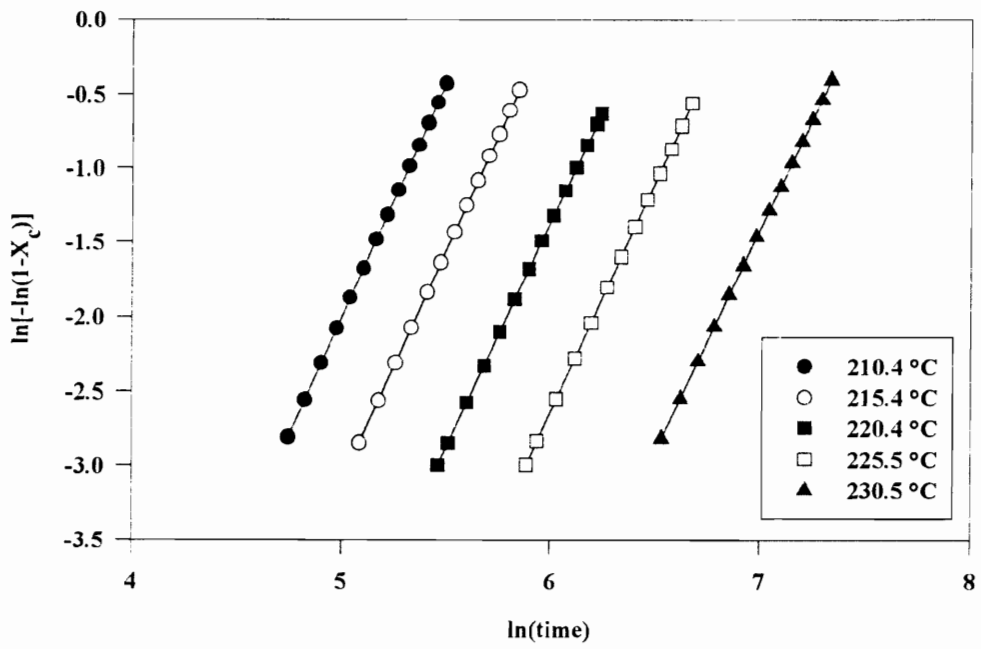


**Figure 2.2** Avrami plots for isothermal crystallization from the melt for phenyl sulfide 19.9K.

plots were used to obtain the Avrami exponent  $n$ , and the rate constant  $K$ . The values of the Avrami exponents and rate constants obtained for the phenyl sulfide and biphenyl sulfide polymers as a function of undercooling ( $T_m^\circ - T_c$ ) are shown in Figures 2.3 & 2.4 for the different molecular weights, where  $T_c$  is the crystallization temperature, and  $T_m^\circ$  is the equilibrium melting temperature, the value for the phenyl sulfide system being 292 °C, and the biphenyl sulfide system being 371 °C. The crystallization data have been presented as a function of undercooling so as to combine the results of all the polymers in a single graph, and also facilitates comparison between the various polymers.

From Figure 2.3 it can be seen that the phenyl sulfide systems yielded Avrami exponents of ca. 3, independent of molecular weight and crystallization temperature. Avrami exponents of 3 usually imply spherulitic growth preceded by heterogeneous nucleation. The biphenyl sulfide systems, however, yielded Avrami exponents closer to 2, also independent of molecular weight or crystallization temperature. A value of 2 for the Avrami exponent could imply growth of 2-dimensional crystallites (discs) after heterogeneous nucleation, i.e. non-spherulitic growth. Values close to 2 could also imply incomplete development of the crystallites, leading to the formation of some intermediate sheaf-like structure, that given the space and time could have developed into a spherulite. However, as discussed earlier, the various assumptions and limitations, both theoretical as well as experimental, of the Avrami formulation could yield values that do not accurately reflect the mode of growth of the crystalline superstructure.

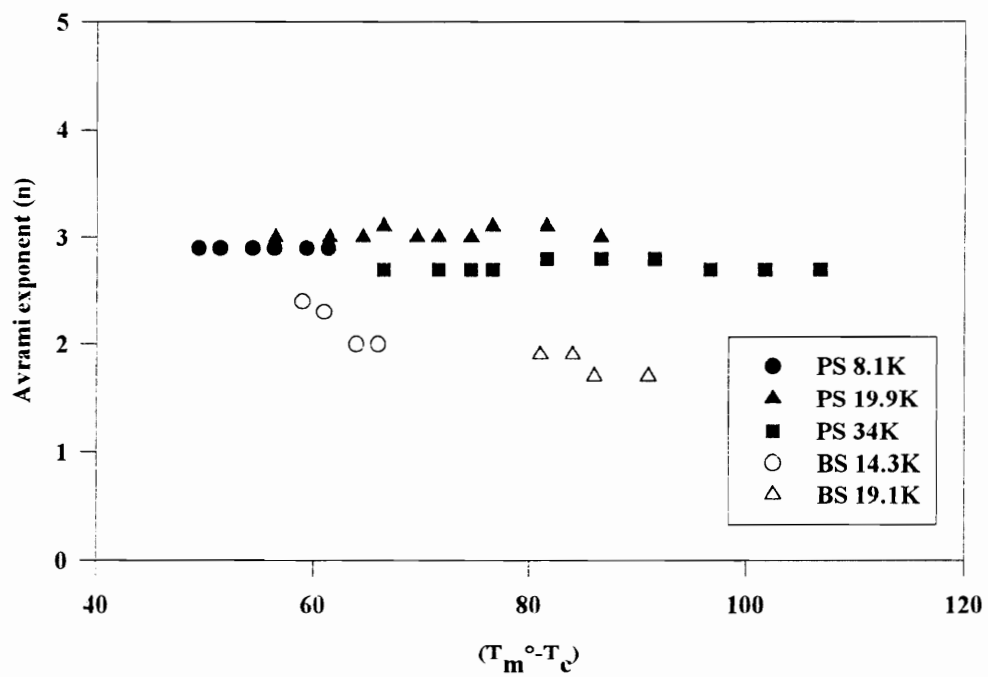


**Figure 2.3** Avrami exponents as a function of undercooling for phenyl sulfide and biphenyl sulfide systems.

The trends of the Avrami exponents observed in this study are similar to earlier reports in the literature on PEEK<sup>4,9</sup> where also the Avrami exponent was found to be independent of molecular weight and crystallization temperature. For the case of PPS, Lopez et al.<sup>16</sup> observed that while the Avrami exponents were essentially independent of crystallization temperature, the lower molecular weight polymer ( $M_n=17K$ ) displayed Avrami exponents lower than that of the higher molecular weight polymers ( $M_n= 35K, 42K$ ).

Figure 2.4 shows the rate constants obtained from the Avrami plots of the phenyl sulfide and biphenyl sulfide polymers shown as a function of undercooling; the curves constructed through the data points are polynomial best fits. It is obvious from the figure that as the undercooling increases, i.e. the crystallization temperature decreases, the rate constant increases, indicating an increase in the rate of bulk crystallization. This increase in the rate of bulk crystallization could occur due to an increase in both the crystal growth rate as well as nucleation density. From various theoretical considerations, it is well known that the crystal growth rate increases as a function of undercooling in the nucleation controlled regime, reaches a maximum value, then decreases with increasing undercooling in the diffusion controlled regime<sup>29</sup>. The nucleation density, however, typically increases continuously as a function of increasing undercooling<sup>40</sup>. Additional crystallization data could not be obtained for the lower molecular weight systems at higher undercoolings due to experimental difficulties associated with attaining thermal equilibration before crystallization was initiated. The rates of crystallization were too

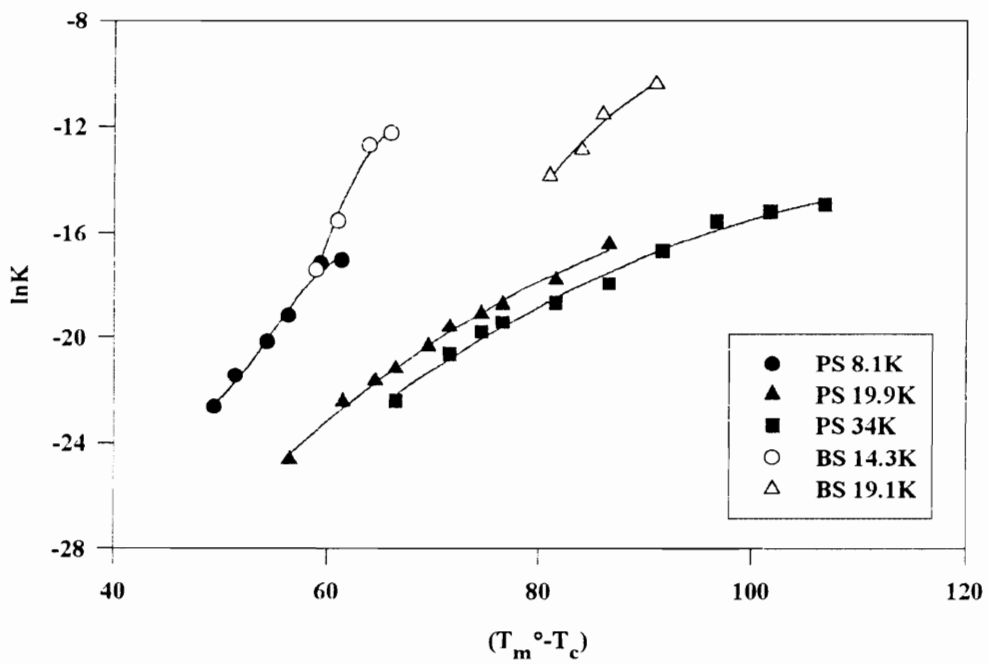


**Figure 2.4** Avrami rate constants as a function of undercooling for phenyl sulfide and biphenyl sulfide systems.

rapid to allow monitoring of the crystallization process in these cases. In contrast, for the case of the higher molecular weight polymers, data could not be obtained at low undercoolings due to the long times needed to complete the crystallization process, leading to a weak signal in the DSC. At higher temperatures, there is also the possibility of degradation occurring due to long residence times.

It is also obvious from Figure 2.4 that the crystallization rate constant decreases with increasing molecular weight. Indeed, at an undercooling of 70 °C, the rate constant decreased by a factor of 2.9 on increasing the molecular weight from 19.9K to 34 K for the phenyl sulfide system. At an undercooling of 40 °C, the rate constant decreased by a factor of 3.7 on increasing the molecular weight from 8.1K to 19.9K. It has been earlier reported for the case of PPS that the nucleation density at a given undercooling increases with increasing molecular weight<sup>16</sup>. Assuming a similar behavior for the case of the phenyl sulfide polymers under study here, this should cause an increase in the rate of bulk crystallization with increasing molecular weight, at a given undercooling. The fact that the reverse trend is observed indicates the prominent effect the spherulitic growth rate has on the bulk crystallization rate. The spherulitic growth rate for the lower molecular weight polymer has to be greater than that of the higher molecular weight polymers to cause the difference in bulk crystallization rates observed here. This is caused due to the higher melt mobility (lower melt viscosity) of the lower molecular weight species, resulting in easier transport of the chains to the crystal growth front. A corresponding comparison for the biphenyl sulfide system could not be made because crystallization data could not be

obtained for the two molecular weights at overlapping undercoolings due to experimental difficulties. The molecular weight dependence of the bulk crystallization rate constant of PPS was investigated by Lopez et al.<sup>16</sup>, who reported a decrease in the rate constant by a factor of 3.5 at undercoolings of 70 °C, on increasing the number average molecular weight from 17K to 42K. The decrease in the rate constant with increasing molecular weight of the phenyl sulfide system seems comparable to that reported for the case of PPS. This is not particularly surprising considering the similar chemical structures and crystallization windows of these two polymers.

It can be seen in Figure 2.4 that the rate constants of the biphenyl sulfide polymers appear to be higher than that of the phenyl sulfide polymers at similar undercoolings, this difference being larger at larger undercoolings. However, in order to make a valid comparison between the rate constants of the phenyl sulfide and biphenyl sulfide systems, the rate constants should be reduced to the same units, by normalizing it based on the Avrami exponents. As can be seen from Eqn. 2, the rate constant carries the same units as the growth rate term  $G$ . The growth rate is raised to the power  $n$ , which determines the time dependence of the crystallization rate. It is obvious that different values of  $n$  would yield different units of  $K$ . Reducing the rate constant to a factor  $K^{1/n}$  would cause all rate constants to yield the same units, and hence make any comparison valid. This analysis, however, ignores any geometrical effects of growth on the crystallization rate; the time dependence of the crystallization process is also ignored in such an analysis. Therefore, a

better method of comparison would be based on crystallization half-times as will now be addressed.

There are very few reports in literature dealing with the systematic study of the bulk crystallization kinetics of PPS and PEEK as a function of molecular weight. Lopez et al.<sup>16</sup> studied samples of PPS with number average molecular weights of 17K, 35K and 42K. Studies on the isothermal crystallization kinetics and spherulitic growth rate kinetics were carried out on these samples. Comparison of the rate constants from this study with those of Lopez et al. cannot be carried out in a quantitative manner because of the lack of data at equivalent molecular weights. However, a semi-quantitative comparison provides some interesting insights. At an undercooling of 80 °C, all the PPS polymers exhibited rate constants that were ca. 6 orders of magnitude greater than that of the 19.9K and 34K phenyl sulfide polymers. Indeed, at an undercooling of 60 °C, the highest molecular weight PPS polymer (42K) had a rate constant that was ca. 3 orders of magnitude greater than that of the lowest molecular weight phenyl sulfide polymer (8.1K). A comparison of crystallization half-times yielded a similar conclusion. This fact seems surprising in view of the similarities of the backbone structure between these two systems. As will be discussed shortly, the nucleation densities exhibited by these two polymeric systems are quite close under similar conditions of undercooling. The substantial difference between the rate constants must therefore arise due to differences in the growth rates of the two systems. This was indeed observed to be the case; at undercoolings of 80 °C, all the molecular weight samples of PPS exhibited growth rates that were at least one order of

magnitude greater than that of the 19.9K phenyl sulfide polymer. The kinetics of crystallization of PEEK samples as a systematic function of molecular weight was studied by Roovers et al.<sup>9</sup>. The results reported here can be compared with their kinetic results directly, since even they reported Avrami exponent values of 2 irrespective of molecular weight or crystallization temperature, similar to the behavior exhibited by the biphenyl sulfide polymers studied here. For the case of the biphenyl sulfide 14.3K polymer and a PEEK polymer of number average molecular weight of 14.5K, at undercoolings of 66 °C, the rate constant of PEEK was 2 orders of magnitude greater than the rate constant displayed by the biphenyl sulfide polymer. For the case of the 19.1K biphenyl sulfide polymer and a PEEK sample with an  $M_n$  of 21.5K, at an undercooling of 86 °C, the PEEK sample again displayed a rate constant that was 2 orders of magnitude greater than that of the biphenyl sulfide polymer. This indicates the relative “sluggishness” of the biphenyl polymer, reflecting perhaps an inherently slower crystallizability than that displayed by PEEK. In this case, it is difficult to speculate as to the causes of this behavior due to lack of growth rate data for the biphenyl sulfide polymer.

Figures 2.5 & 2.6 show the crystallization half-times and heats of crystallization of the various polymers as a function of undercooling. The crystallization half-time has been defined as the time to complete half the observed crystallization process, i.e. the time to attain a *relative* crystallinity of 50%. The half-time has been plotted as a function of undercooling for the various polymers as shown in Figure 2.5. This plot is similar to the

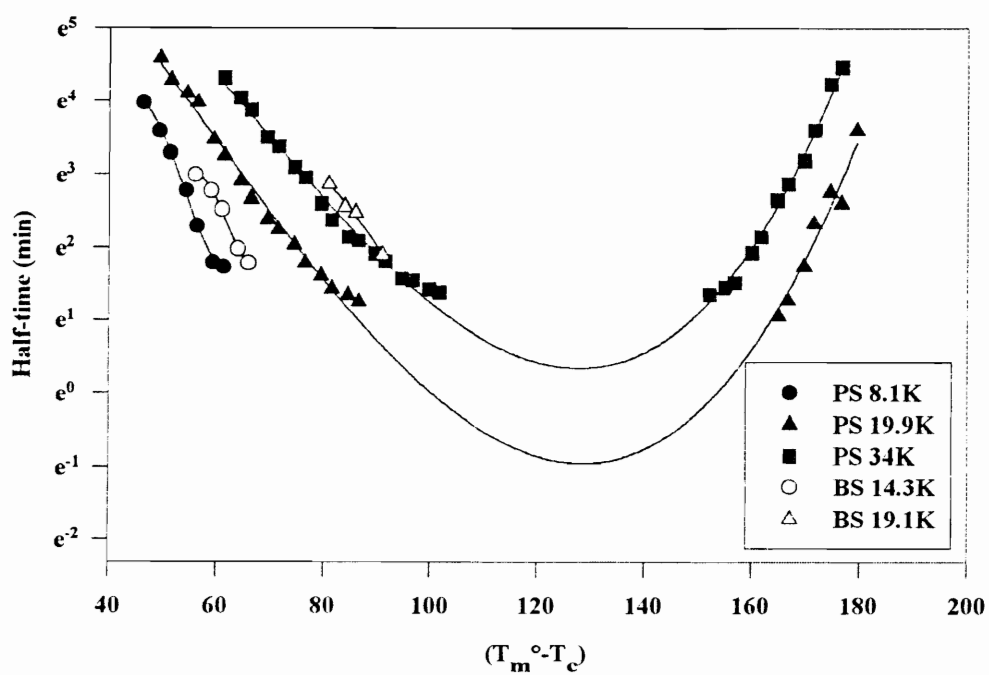


**Figure 2.5** Crystallization half-times as a function of undercooling for phenyl sulfide and biphenyl sulfide systems.

plot of rate constant as a function of undercooling. The lines drawn through the points have been constructed for convenience and are polynomial best fits of the data. Even from this plot, the dependence of the half-times on undercooling and molecular weight is quite obvious. It can also be seen that the biphenyl sulfide 19.1K polymer displays higher half-times than the phenyl sulfide polymers at all undercoolings, again implying slower inherent crystallizability. The biphenyl sulfide 14.3K polymer, however, displayed half-times that were lower than the phenyl sulfide 34K and 19.9K polymer, but higher than the 8.1K phenyl sulfide polymer. The estimated peak of the half-time curve from the polynomial regression for the phenyl sulfide 34K polymer occurs at an undercooling of ca. 115 °C, i.e. corresponding to a temperature of 165 °C. This temperature correlates well with the crystallization peak temperature observed during dynamic cooling of the same polymer at 10 °C/min from the melt. The characteristic “bell” shaped curves of the half-times are consistent with the well-known theories that the crystallization rates are limited by nucleation close to the melting temperature, and by diffusion at temperatures close to  $T_g$ <sup>29</sup>.

It can be seen from Figure 2.6 that the heats of crystallization were essentially independent of crystallization temperature for all the polymers studied here. However, there was a prominent molecular weight dependence of the heat of crystallization. This is consistent with the earlier studies on the crystallization behavior of these systems<sup>25</sup>, which also showed that the lower molecular weight samples exhibited higher heats of crystallization. This is certainly due to the higher mobility of the lower molecular weight samples. The behavior observed here is also consistent with earlier reports on PPS<sup>16</sup>;

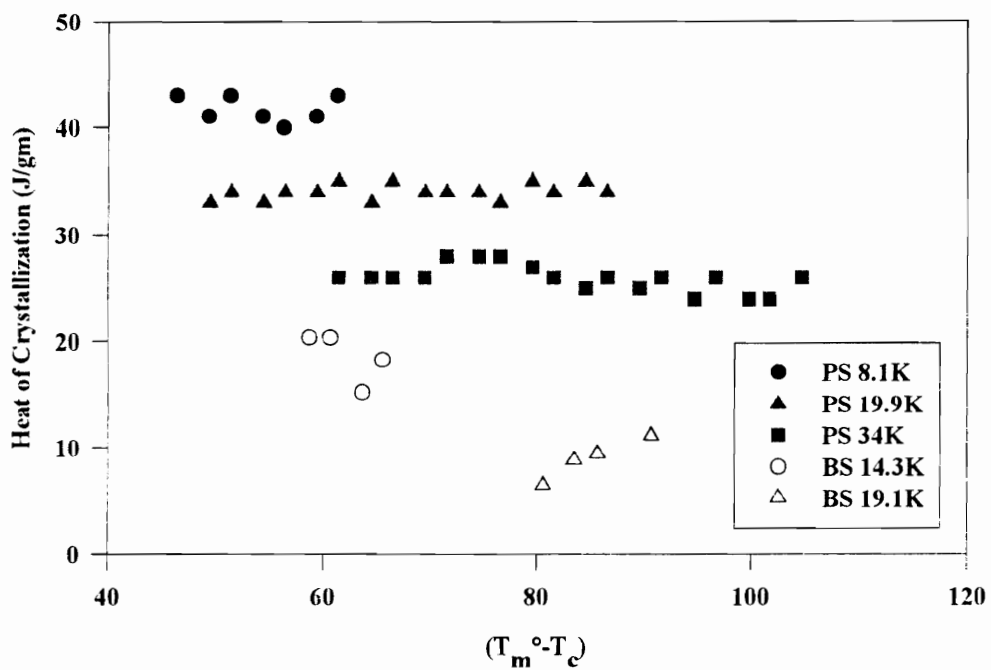


**Figure 2.6** Heat of crystallization as a function of undercooling for phenyl sulfide and biphenyl sulfide systems.

however, Lopez et al. observed an increase in the heat of crystallization of PPS with increasing crystallization temperature. Also, at higher crystallization temperatures, Lopez et al. observed that the heat of crystallization of PPS was independent of molecular weight. Roovers et al.<sup>9</sup> observed for the case of PEEK that the heat of crystallization was independent of crystallization temperature, and also observed the same molecular weight dependence as observed here.

As discussed earlier, the Avrami rate constant is a function of the growth rate and nucleation density. Therefore, given crystalline growth rate data, the nucleation density can be calculated from the rate constants determined from an Avrami analysis. Spherulitic growth rate experiments were carried out on the phenyl sulfide 19.9K polymer, the results of which are presented in the next chapter. Using this data, the nucleation densities for the 19.9K phenyl sulfide polymer have been calculated using Eqn. 2 and a constant Avrami exponent of 3. The calculated nucleation densities as a function of undercooling are shown in Figure 2.7. It can be seen from the figure that in the range of undercoolings investigated here, the nucleation density exhibits a very weak dependence on undercooling and is nearly constant. The values of the nucleation density are, however, very similar to the values obtained by Lopez et al.<sup>16</sup> for PPS samples ( $M_n=35K, 42K$ ) crystallized in the same range of undercoolings (at undercoolings of 80 °C, Lopez observed  $\ln N \approx 22$ ). In contrast to the findings of this study, Lopez et al.<sup>16</sup> observed the nucleation density to increase by ca. an order of magnitude with increasing undercooling of ca. 30 °C. This is a significant finding, in that any increase in the rate constant of the phenyl sulfide polymer

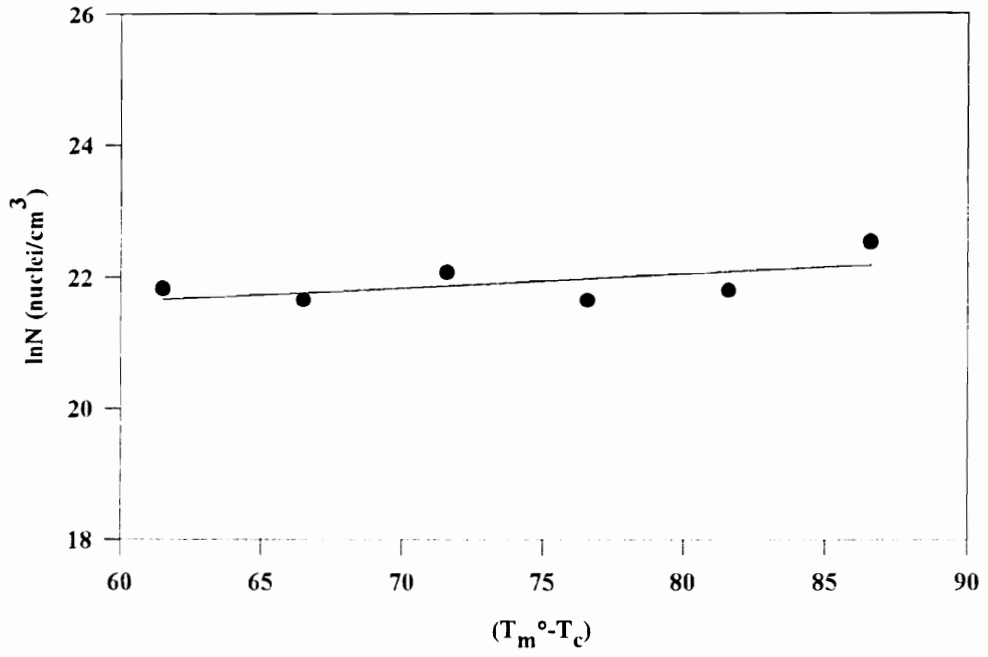


**Figure 2.7** Nucleation density as a function of undercooling for phenyl sulfide 19.9K.

with increasing undercooling occurs primarily due to an increase in the spherulitic growth rate.

In Chapter 1, the equilibrium melting temperatures of the phenyl sulfide (278 °C) and biphenyl sulfide (371 °C) systems were reported as determined from a Hoffman-Weeks extrapolation. In that work, data for only the 19.9K phenyl sulfide polymer and biphenyl sulfide 14.3K polymer, at relatively low crystallization temperatures were used in the extrapolation. Since then, data were obtained for the phenyl sulfide polymers at larger crystallization temperatures and the other molecular weights as well, which have been used in the extrapolation in order to estimate the equilibrium melting temperature ( $T_m^0$ ). Figure 2.8 shows the Hoffman-Weeks plot<sup>41</sup>, in which the melting temperatures of the phenyl sulfide samples crystallized at various temperatures are plotted against each other. The line joining these data points is extrapolated to the line  $T_m=T_c$ , the point of intersection yielding the equilibrium melting temperature. It can be seen from the figure, that the data points yield about the same value of 292 °C, irrespective of molecular weight. This value of the equilibrium melting temperature has been used in presenting all the data in this chapter. For the biphenyl sulfide system, the equilibrium melting temperature has been assumed to be 371 °C, since melting temperatures for samples crystallized at higher temperatures could not be obtained due to the earlier stated experimental problems concerning slow crystallization kinetics at higher temperatures, which could perhaps lead to some degradation as well at long residence times.

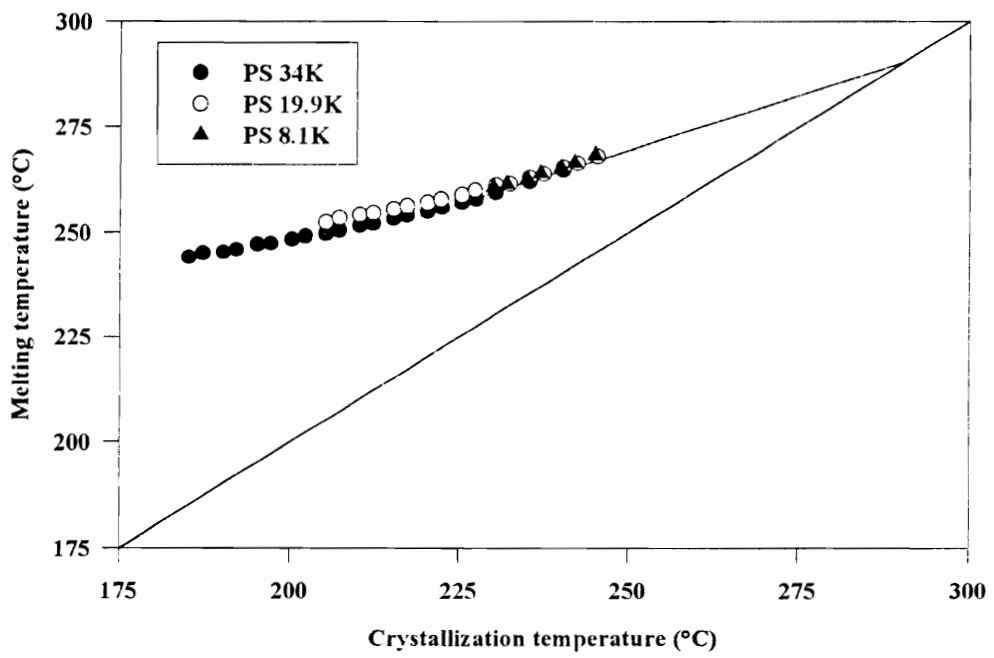


**Figure 2.8** Hoffman-Weeks plot for various molecular weights of phenyl sulfide polymer.

Figure 2.9 shows the rate constants obtained from the Avrami analysis plotted using the Lauritzen-Hoffman kinetic analysis of the rate constants described earlier, for the various molecular weights of the phenyl sulfide system. As can be seen in the plot, a regime transition is quite apparent for the 34K polymer, with the transition occurring at ca. 205 °C, an undercooling of ca. 85 °C; the ratios of the slopes of the lines was found to be 1.98, a value very close to the theoretically predicted value of 2. This regime transition signifies the transition from Regime II to Regime III kinetics as defined by Hoffman and Lauritzen<sup>33</sup>. Since data could not be obtained at low enough crystallization temperatures for the other molecular weight polymers, no distinct regime transition was observed for the lower molecular weight polymers. For the case of the 19.9K polymer, however, a regime transition can be observed in the same temperature range as that of the 34K polymer. It is also quite evident that the slopes of the lines below the regime transition (in Regime II) are equal for all three molecular weights. This type of analysis indicates that crystallization could occur by processes that have been described by Lauritzen and Hoffman. Regime II kinetics indicates that the growth of chain folded crystallites takes place by a secondary nucleation process on the already existing crystalline substrate, with the rate of secondary nucleation equivalent to the substrate completion rate. Regime III kinetics, however, takes place at higher undercoolings and is accompanied by a process in which the secondary nucleation rate is much higher than the substrate completion rate. It should be emphasized again at this point that such an analysis ignores the nucleation density changes with crystallization temperature, and its effect on the bulk crystallization

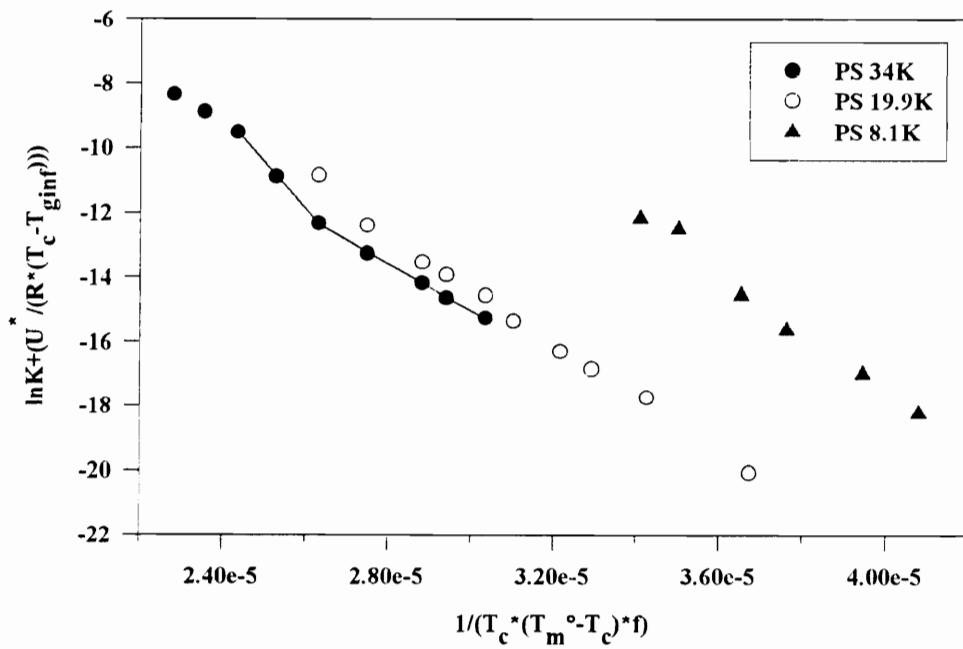


**Figure 2.9** Kinetic analysis of rate constants from melt isothermal crystallization for phenyl sulfide 34K.

rate. However, it should be noted that the earlier results indicated that the nucleation density was a weak function of undercooling, which could imply that the crystallization rate constant is primarily dependent on the crystal growth rate and its dependence on temperature.

It can be seen in the figure that the data at the two lowest crystallization temperatures for the 34K polymer were not used in the kinetic analysis since it is quite obvious that these data points did not fit the analysis performed here. This could well indicate the inaccuracy of the values of the rate constants at those temperatures, probably due to the very high undercooling at which crystallization took place. Under such conditions, there is a distinct possibility that the crystallization process was initiated before the DSC signal could equilibrate and record exothermic changes in heat flow. This could lead to an error in assigning the starting time of crystallization, which, as discussed earlier, could lead to large errors in the estimation of the Avrami rate constant. A point to be mentioned here is that the value of the activation energy  $U^*$  used here was 1500 cal/mol, as recommended by Hoffman et al.<sup>33</sup>, and the value of  $T_\infty$  was taken as  $T_g - 30K$ . The value of  $U^*$  was varied and  $T_\infty$  was alternately defined as  $T_g - 51.7$  (WLF value). Varying these two parameters, while changing the slopes of the lines, did not influence the transition temperature or the ratio of the slopes of the lines above and below the transition.

#### 2.4.2 *Non-isothermal crystallization*

The peak of the crystallization exotherm during the cooling scan was taken to be the maximum crystallization rate temperature, also referred to as the peak crystallization temperature  $T_{\text{cmax}}$ . Figure 2.10 shows the dependence of the peak crystallization temperature on the cooling rate for the phenyl sulfide, biphenyl sulfide polymers and PEEK. The data on the y-axis has been plotted as the undercooling required to attain the maximum crystallization temperature,  $(T_m^\circ - T_{\text{cmax}})$ , so as to allow comparison between the three different polymers. The equilibrium melting of PEEK was taken to be  $395\text{ }^\circ\text{C}^1$ , in order to calculate the undercooling.

It can be seen that, as expected, the peak crystallization temperature occurs at larger undercoolings, i.e. at lower temperatures, with increasing cooling rate for all the polymers studied here. This can be explained as being due to the lower time scale being afforded the polymer to crystallize as the cooling rate increases, therefore requiring a higher undercooling to initiate crystallization. The peak crystallization temperature showed a molecular weight dependence as well, with the lower molecular weights crystallizing at higher temperatures at a given cooling rate. Interestingly, the difference between the peak crystallization temperatures for the different molecular weights increased with increasing cooling rates, indicating the increased effect of chain mobility (viscosity) and cooling rate on the crystallization behavior. The higher mobility of the low molecular weight polymers allow for a faster rate of crystallization at a given temperature, which is consistent with the molecular weight dependence of the isothermal crystallization

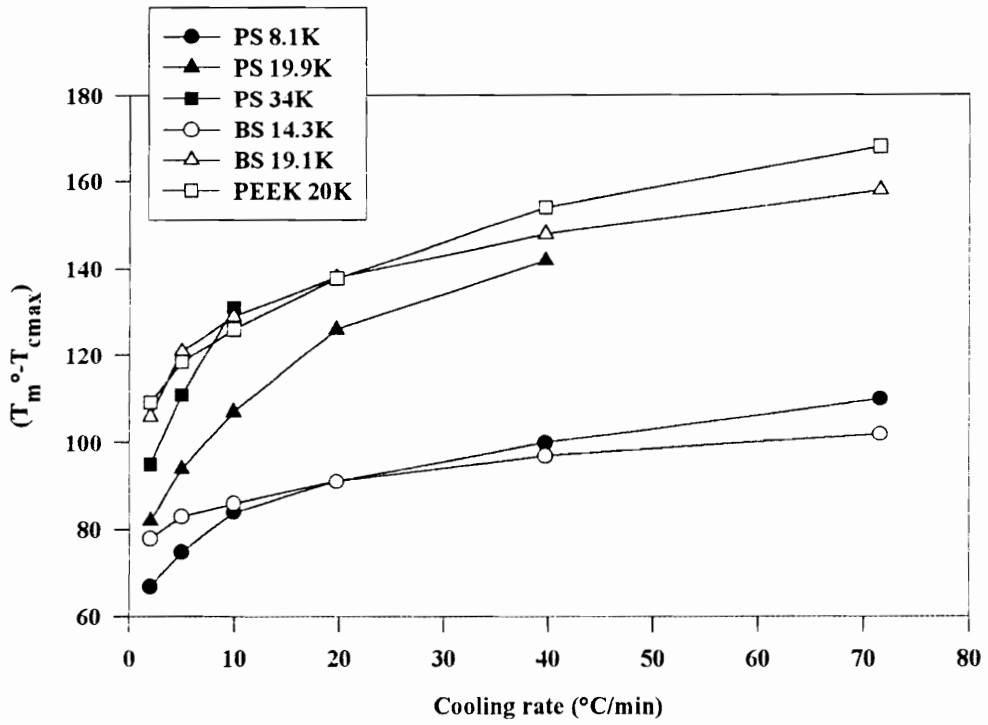


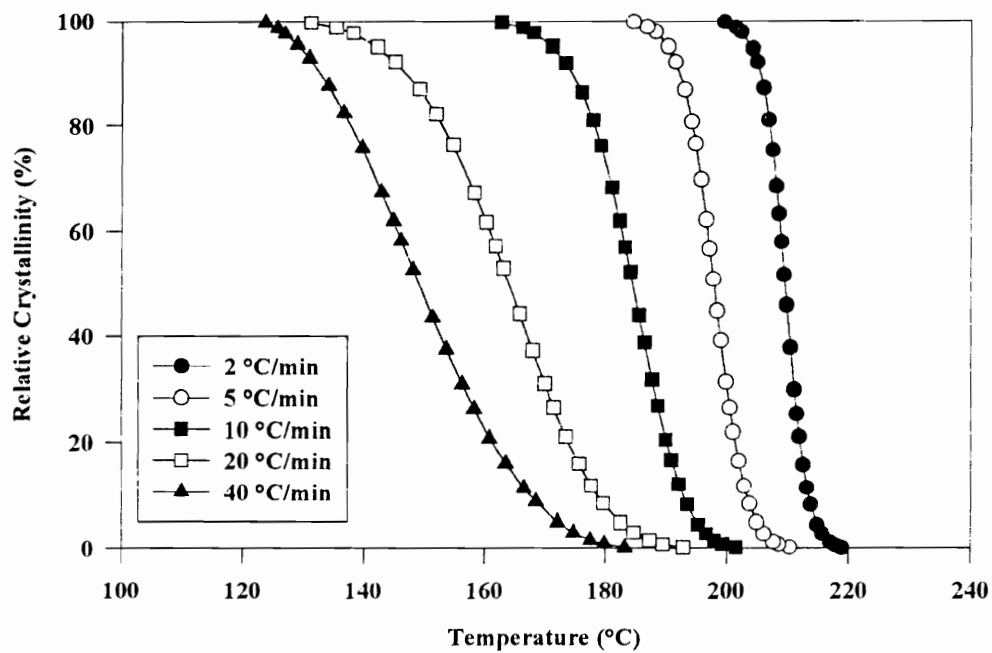
**Figure 2.10** Maximum crystallization temperature as a function of cooling rate for non-isothermal crystallization from the melt for various polymers.

kinetics. The dependence of the maximum crystallization temperature on the cooling rate for the biphenyl sulfide 14.3K polymer was less than that of all other polymers studied here, implying lower sensitivity to crystallization conditions. It is interesting to note that the biphenyl sulfide 19.1K polymer and the 20K PEEK required about the same undercooling at all cooling rates to attain the maximum crystallization temperature. For all samples investigated here, the dependence of the maximum crystallization temperature on cooling rate was most prominent at lower cooling rates; at the higher rates, the dependence was weaker.

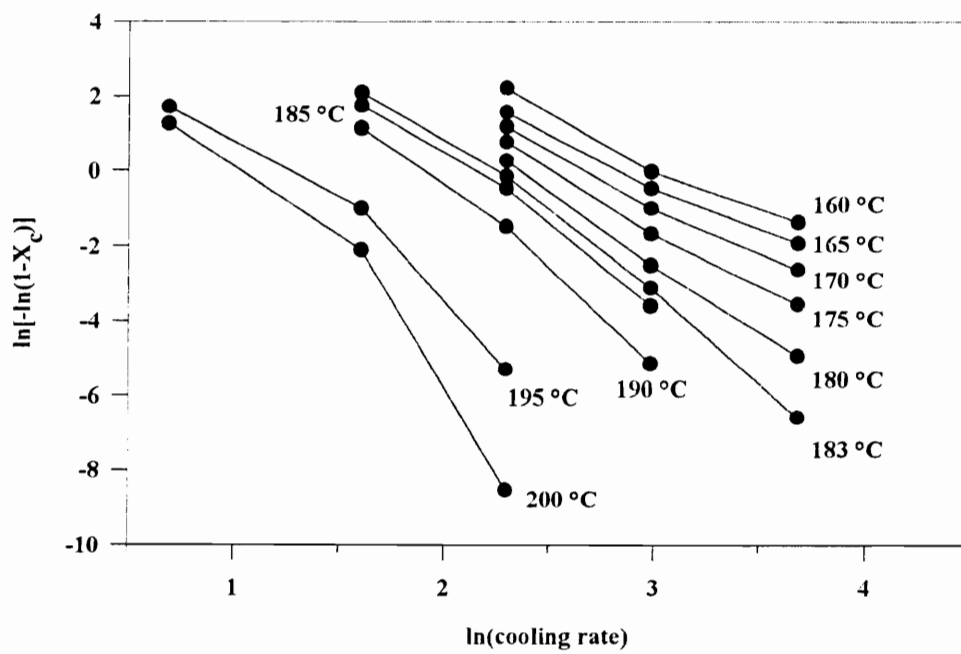
For the case of the phenyl sulfide polymers, it can be seen that the 19.9K polymer did not crystallize when the cooling rate was 70 °C/min, and the 34 K polymer crystallized only at the slowest cooling rates, 2, 5 and 10 °C/min. This indicates the strong molecular weight and cooling rate dependence of the crystallizability of the phenyl sulfide system. In contrast to the behavior exhibited by the higher molecular weight phenyl sulfide polymers (19.9K, 34K), both the biphenyl sulfide polymers were capable of crystallizing at all cooling rates investigated here. For the case of the biphenyl sulfide system, the 14.3K polymer crystallized at about the same undercoolings required to crystallize the lowest molecular weight phenyl sulfide polymer (8.1K). This agrees well with the isothermal crystallization studies, which showed the biphenyl sulfide 14.3K polymer to display half-times that were close to the phenyl sulfide 8.1K polymer and lower than the higher molecular weight phenyl sulfide polymers.

Figure 2.11 shows the development of crystallinity as a function of temperature for the phenyl sulfide 19.9K polymer at various cooling rates. As was observed in the case of isothermal crystallization, characteristic sigmoidal shaped curves are obtained. As discussed earlier, it can be seen that at a temperature of 185 °C, the curve corresponding to crystallization at a cooling rate of 40 °C/min is at very early stages of crystallization, the curve corresponding to crystallization at a cooling rate of 20 °C/min is also at early stages of crystallization, whereas the curve corresponding to crystallization at a cooling rate of 10 °C/min is at the end of the observed crystallization process. Therefore, as observed by Cebe et al.<sup>4</sup>, the cooling function parameter in the Ozawa approach may not be the same for the entire crystallization process, an assumption used in the derivation of the Ozawa equation. Since the Ozawa analysis compares the degree of conversion at a fixed temperature (e.g. 185 °C) for various cooling rates, this could lead to deviations from the predicted linear behavior. Indeed, this was observed in this study; the Ozawa plots at various temperatures are shown in Figure 2.12, corresponding to the crystallization data shown in Figure 2.11. The curvature in the plots at all temperatures prevents an accurate analysis of the non-isothermal crystallization data based on the Ozawa approach. The changing slope with temperature in the plot indicates that  $n$  is not constant with temperature during crystallization.

The alternative approach used here was based on the observation that the relative crystallinity displayed the characteristic sigmoidal shape as a function of temperature. Since the x-axis can be converted to a time axis instead of a temperature axis, the data can



**Figure 2.11** Relative crystallinity as a function of cooling rate for non-isothermal crystallization from the melt for phenyl sulfide 19.9K.



**Figure 2.12** Ozawa plot for non-isothermal crystallization from the melt for phenyl sulfide 19.9K.

be converted to relative crystallinity as a function of time. Furthermore, since the Avrami equation is quite successful in describing sigmoidal shaped curves, *the non-isothermal crystallization data has been analyzed using the conventional form of the Avrami equation*. The Avrami parameters, the rate constant  $K$  and the exponent  $n$  are in this case adjustable parameters that are varied to obtain the best numerical fits.

Figure 2.13 shows the Avrami plots calculated from the crystallization data shown in Fig 2.11. The straight line fits obtained suggest that the conventional form of the Avrami equation might be useful in modeling the non-isothermal crystallization kinetics of polymers, at least for comparative purposes. As was done in the case of the isothermal crystallization data, only data at low conversions were used in the analysis. Since the Ozawa analysis failed for all the samples investigated in this study, the data for all the samples were analyzed using the Avrami approach, which was found to be successful in all cases. From the slope and intercept of the plot, the values of  $K$  and  $n$  can be obtained. Even though the two Avrami parameters will be referred to as the rate constant and the Avrami exponent respectively, *it should be emphasized that the significance of these two parameters are not the same as in the case of isothermal crystallization*. Unlike in the case of isothermal crystallization, the exponent  $n$  displayed a wide range of values, and were higher and more scattered than those obtained from isothermal crystallization experiments. For the case of the phenyl sulfide polymers, the exponent varied from 2.6 to 4.4, for the biphenyl sulfide polymers the exponent values ranged from 2.8 to 4.3, and for the case of PEEK, values between 3.4 and 3.8 were obtained. Recall that from the

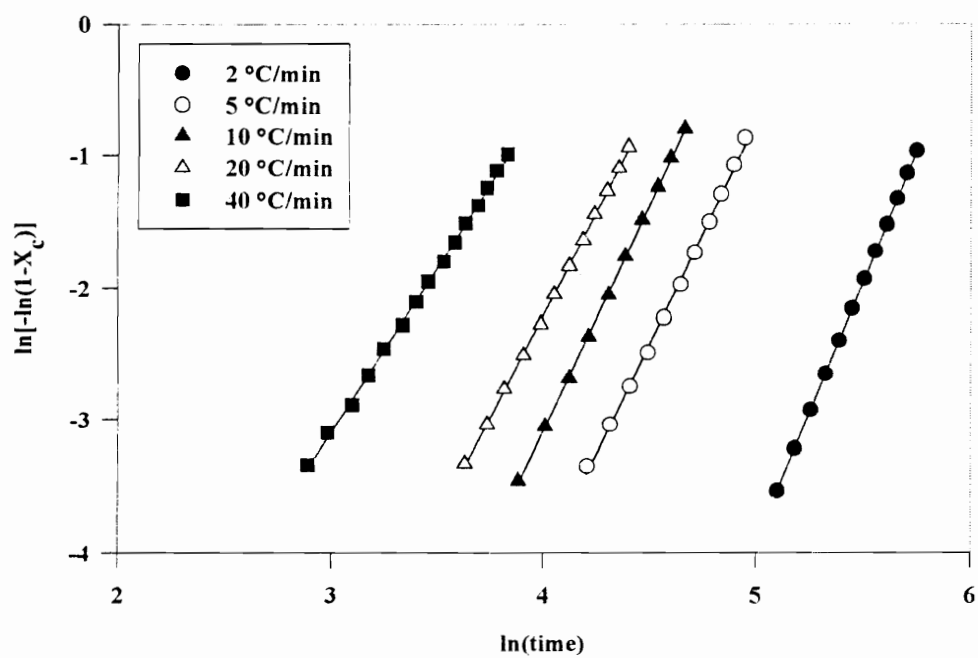


**Figure 2.13** Avrami plots for non-isothermal crystallization from the melt for phenyl sulfide 19.9K.

isothermal crystallization studies, the phenyl sulfide systems showed an Avrami exponent of 3 and the biphenyl sulfide showed an Avrami exponent of 2 over the entire temperature range. It was mentioned earlier that both the nucleation density as well as the crystal growth rate were functions of temperature. During a cooling scan, these two parameters vary continuously during the experiment; the time dependence of the crystallization therefore changes continuously as well. It is hence not possible to predict the nucleation and growth mechanisms occurring during crystallization from the Avrami exponent.

The rate constant  $K$  changes as a function of cooling as well, due to changes in the growth rate and nucleation density. Regardless, some comparative information on the overall kinetics can be obtained from the rate constant. Due to the large variations in the values of  $n$ , the rate parameters obtained for different cooling rates cannot be compared directly, as they are dimensionally different. To allow a fair comparison, the  $K$  values for the various cooling rates were normalized to a common basis as  $K^{1/n}$ . The dependence of the reduced rate parameter on the cooling rate for the various polymers is shown in Figure 2.14. It can be seen that as the cooling rate increases, the value of the modified rate parameter ( $K^{1/n}$ ) increases; this increase being more prominent for the lower molecular weight materials. At low cooling rates, the reduced rate parameters were very similar regardless of the nature of the polymer or molecular weight. This is consistent with the observed dependence of the maximum crystallization temperature with cooling rate. For the phenyl sulfide polymer (19.9K), as the cooling rate increased from 2 °C/min to 40 °C/min, the rate parameter increased by a factor of 7. At higher cooling rates, from

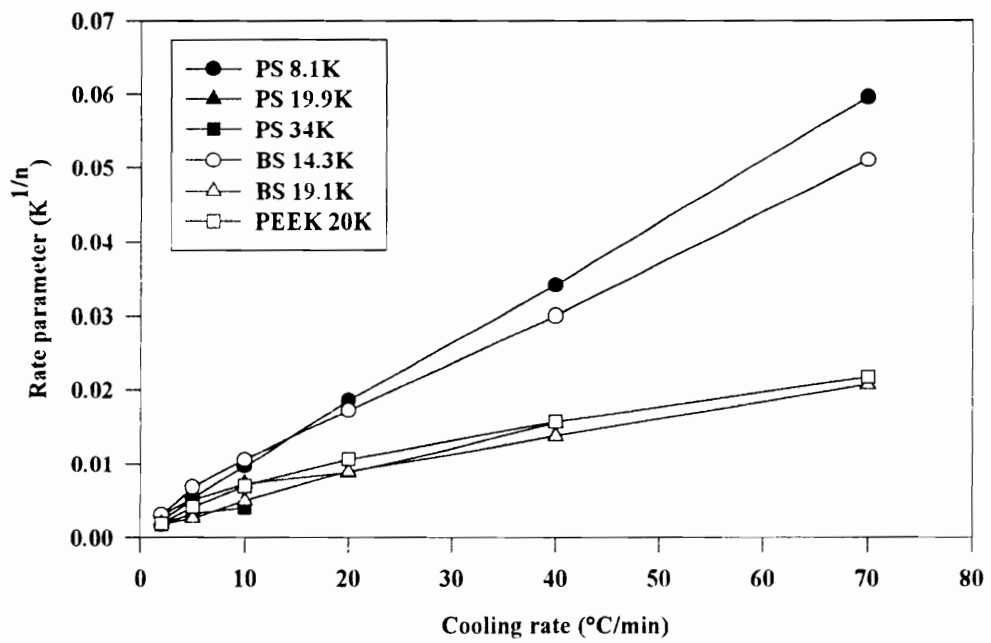


**Figure 2.14** Avrami reduced rate constants as a function of cooling rate for non-isothermal crystallization for various polymers.

Figure 2.10, it can be seen that crystallization occurs at higher undercoolings, i.e. lower temperatures. As discussed earlier, as the temperature decreases, the growth rate increases (in the nucleation controlled regime), and the nucleation density typically increases as well (though not prominently for the phenyl sulfide system). Hence, the overall crystallization rate would be expected to increase with increasing cooling rate. It can also be seen that as the molecular weight increases, the rate parameter decreases. For the phenyl sulfide polymers cooled at 10 °C/min, as the molecular weight increased from 8.1K to 34K, the rate parameter decreased by a factor of 2.5. This can be explained as being due to the slower crystallization rates of the higher molecular weight polymers due to lower mobility. For similar molecular weights of the phenyl (19.9K) and biphenyl sulfide (19.1K), and PEEK (20K), the rate parameters for the phenyl sulfide was higher; at a cooling rate of 10 °C/min, the phenyl sulfide had a rate parameter 1.5 times that of the biphenyl sulfide (19.1K) polymer, and was almost identical to that of PEEK.

The rate parameter can be considered an indication of the inherent crystallizability of the polymer and its dependence on crystallization conditions (cooling rate). This is hence a useful parameter to compare at different cooling rates, molecular weights, or even different polymers. Thus, it can be seen that the traditional Avrami approach allows a comparison of rate constants for various systems as a function of cooling rate, though it does not allow a mechanistic interpretation of the calculated parameters. This approach, however, could serve as a means of comparison of crystallization rates on changing various molecular and processing parameters.

## 2.5 Conclusions

Isothermal crystallization was carried out from the melt, and the data analyzed using the Avrami approach. For the phenyl sulfide systems, this analysis yielded Avrami exponents of ca. 3 for all molecular weight polymers and at all crystallization temperatures. This indicates that crystallization takes place by spherulitic growth following heterogeneous nucleation. For the case of the biphenyl sulfide polymers, however, Avrami exponents closer to 2 were observed, again for all molecular weights crystallized at all temperatures. This could indicate that crystallization occurs by the growth of 2-dimensional disc like superstructures, or could indicate the incomplete development of 3-dimensional spherulites leading to some sheaf-like intermediate morphology, following heterogeneous nucleation. All the crystallization parameters studied here exhibited a molecular weight dependence, with lower molecular weights yielding lower half times, and higher values of the rate constants. The heats of crystallization were independent of crystallization temperature, and were higher for the lower molecular weight systems. A comparison of the Avrami rate constants of the phenyl sulfide and biphenyl sulfide polymers with PPS and PEEK respectively indicated that the poly(ether ether sulfide) polymers crystallized slower than the commercial polymers at equivalent undercoolings, with the rate constants being at least 2 orders of magnitude lower than that of PPS and PEEK. For the case of the phenyl sulfide system and PPS, it has been suggested that the cause of this difference was the difference in spherulitic

growth rates. Nucleation densities calculated from the rate constant and growth rate data showed that, in the range of undercoolings studied here, the nucleation density was almost independent of undercooling for the phenyl sulfide 19.9K polymer.

The earlier estimate of the equilibrium melting temperature of the phenyl sulfide polymer has been improved by collecting data at higher crystallization temperatures and for all molecular weights. The equilibrium melting temperature determined from the Hoffman-Weeks extrapolation yielded a value of 292 °C, independent of molecular weight. This differs from the finding of Lopez et al.<sup>16</sup> who observed that the equilibrium melting temperature of PPS increased with an increase in molecular weight. The bulk crystallization rate constants determined from the Avrami analysis were analyzed by the method of Hoffman and Lauritzen. The results of such an analysis showed that while the lower molecular weight (8.1K, 19.9K) samples crystallized at higher temperatures according to Regime II kinetics, the highest molecular weight sample (34K) crystallized at intermediate temperatures and showed a Regime II to III transition at ca. 205 °C. The regime transition was not affected by the choice of values for  $U^*$  and  $T_\infty$ .

The results of studies on the non-isothermal crystallization kinetics from the melt are also reported here. Cooling rates from 2°C/min to 70 °C/min were utilized after a residence time in the melt. For the case of both the phenyl sulfide as well as the biphenyl sulfides, the Ozawa approach to analyze the data was not successful in describing the evolution of crystallinity. This could be attributed to secondary crystallization as well as the assumption of a constant cooling function at all cooling rates. The conventional form

of the Avrami equation has therefore been used in order to analyze the non-isothermal crystallization data. Even though good mathematical fits were obtained for the data in all cases studied here, direct interpretation of the fitting parameters is not simple. A reduced rate constant has been used as means for comparison to study the effects of cooling rate, molecular weight and polymer type on the crystallization kinetics. Such an analysis showed that the reduced rate constant increased with increasing cooling rate, and decreasing molecular weight, indicating an increase in the crystallization rate. Though this approach does not allow a mechanistic interpretation of the processes accompanying crystallization, it allows for a simple way to compare bulk crystallization rate constants for different cooling rates, different molecular weights, and indeed different polymers as well. This would be of particular importance in real processing situations where crystallization occurs under dynamic conditions.

## **Acknowledgments**

The authors would like to acknowledge the NSF Science and Technology Center for High Performance Polymeric Adhesives and Composites at Virginia Tech for full support of this study under contract # DMR 9120004.

## References

1. D. J. Blundell and B. N. Osborn, *Polymer*, **24**, 953 (1983).
2. A. J. Lovinger and D. D. Davis, *J. Appl. Phys.*, **58**, 2843 (1985).
3. S. Z. D. Cheng, M. Y. Cao, and B. Wunderlich, *Macromolecules*, **19**, 1868 (1986).
4. P. Cebe and S. D. Hong, *Polymer*, **27**, 1183 (1986).
5. C. N. Velisaris and J. C. Seferis, *Polym Eng. Sci.*, **26**, 1574 (1986).
6. S. Kumar, D. P. Anderson, and W. W. Adams, *Polymer*, **27**, 329 (1986).
7. Y. Deslandes, M. Day, N. F. Sabir, and T. Suprunchuk, *Polym. Composites*, **10**, 360 (1989).
8. J. N. Hay and D. J. Kemmish, *Plast. and Rub. Proces. and Appl.*, **11**, 29 (1989).
9. M. Day, Y. Deslandes, J. Roovers, and T. Suprunchuk, *Polymer*, **32**, 1258 (1991).
10. K. Könnecke, *J. Macromol. Sci.- Phys.*, **33**, 37 (1994).
11. A. J. Lovinger, D. D. Davis, and F. J. Padden, *Polymer*, **26**, 1595 (1985).
12. J. P. Jog and V. M. Nadkarni, *J. Appl. Polym. Sci.*, **30**, 997 (1985).
13. V. M. Nadkarni and J. P. Jog, *J. Appl. Polym. Sci.*, **32**, 5817 (1986).
14. L. C. Lopez and G. L. Wilkes, *J. Polym. Sci.: Polym. Lett. Ed.*, **24**, 573 (1986).
15. S. Z. D. Cheng, Z. Q. Wu, and B. Wunderlich, *Macromolecules*, **20**, 2802 (1987).
16. L. C. Lopez and G. L. Wilkes, *Polymer*, **29**, 106 (1988).
17. L. C. Lopez, G. L. Wilkes, and J. F. Geibel, *Polymer*, **30**, 147 (1989).

18. L. C. Lopez and G. L. Wilkes, *Polymer*, **30**, 882 (1989).
19. D. R. Budgell and M. Day, *Polym. Eng. Sci.*, **31**, 1271 (1991).
20. J. D. Menczel and G. L. Collins, *Polym. Eng. Sci.*, **32**, 1264 (1992).
21. J. D. Menczel and G. L. Collins, *Polym. Eng. Sci.*, **32**, 1270 (1992).
22. K. Ravindranath and J. P. Jog, *J. Appl. Polym. Sci.*, **49**, 1395 (1993).
23. B. G. Risch, S. Srinivas, G. L. Wilkes, J. F. Geibel, C. Ash, S. White, and M. Hicks, *Polymer* in print.
24. J. R. Babu, M. Konas, A. E. Brink, and J. S. Riffle, *Polymer*, **35**, 4949 (1994).
25. S. Srinivas, J. R. Babu, J. S. Riffle, and G. L. Wilkes, *Polymer*, **36**, 3317 (1995).
26. M. Avrami, *J. Chem. Phys.*, **7**, 1103 (1939).
27. M. Avrami, *J. Chem. Phys.*, **8**, 212 (1940).
28. M. Avrami, *J. Chem. Phys.*, **9**, 177 (1941).
29. B. Wunderlich, *Macromolecular Physics Vol.2*, Academic Press, New York, 1976.
30. F. P. Price, *J. Appl. Phys.*, **36**, 3014 (1965).
31. J. Tomka, *Eur. Polym. J.*, **4**, 237 (1968).
32. D. Grenier and R. E. Prud'homme, *J. Polym. Sci. Polym. Phys. Ed.*, **18**, 1655 (1980).
33. J. D. Hoffman, G. T. Davis, and J. I. Lauritzen, *Treatise on Solid State Chemistry Vol. 3*, Ed. N. B. Hannay, Plenum Press, New York, 1976.
34. R. C. Allen and L. Mandelkern, *Polym. Bull.*, **17**, 473 (1987).

35. P. J. Phillips and W. S. Lambert, *Macromolecules*, **23**, 2075 (1990).
36. D. P. Heberer, S. Z. D. Cheng, J. S. Barley, S. H. S. Lien, R. G. Bryant, and F. W. Harris, *Macromolecules*, **24**, 1890 (1991).
37. T. Ozawa, *Polymer*, **12**, 150 (1971).
38. M. Eder and A. Wlochowicz, *Polymer*, **24**, 1593 (1983).
39. J. B. Friler and P. Cebe, *Polym. Eng. Sci.*, **33**, 587 (1993).
40. D. W. van Krevelen, *Chimia*, **32**, 279 (1978).
41. J. D. Hoffman and J. J. Weeks, *J. Res. Natl. Bur. Stand.*, **66(A)**, 13 (1962).

## Chapter - 3

### **Crystallization and Morphology of Poly(Arylene Ether Ether Sulfide)s: Dual Spherulitic Morphology**

#### **3.1 Abstract**

Spherulitic growth rate studies carried out on novel poly(ether ether sulfide)s yielded dual spherulitic morphologies at all crystallization temperatures. Distinct populations of two kinds of spherulites were formed, with a population of coarse textured spherulites exhibiting a higher growth rate (Type II) than a population of fine textured spherulites (Type I), at all temperature studied. The growth rate dependence as a function of temperature for the Type I spherulites was consistent with the theoretically-predicted “bell shaped” curve, indicating nucleation-controlled growth at temperatures close to the melting temperature, and diffusion-controlled growth at temperatures closer to the glass transition temperature. The growth rate of the Type II spherulites, however, surprisingly did not exhibit any diffusion-controlled regime, with the growth rate increasing with decreasing temperature across the whole range of temperatures studied here. The above described phenomenon was found to be independent of the prior melt and crystallization history and nature of the substrate in all cases except one. The morphology of the different spherulites has been studied with a combination of optical microscopy, SEM, and AFM. The Type II spherulites exhibited a coarser and more “open” morphology, with

thicker bundles of fibrils with large inter-fibrillar gaps, radiating outward from the center of the spherulite. The Type I spherulites were found to exhibit a curvature indicative of spherical behavior, while the Type II spherulites appeared to have a flat disc-like shape; this finding is consistent with film thicknesses in samples exhibiting Type I (50-75  $\mu\text{m}$ ) and Type II (ca. 10  $\mu\text{m}$ ) spherulites, and also provides confirmation for the observed SALS  $V_v$  patterns. The differences in the growth rate and morphology between the Type I and Type II spherulites have been attributed to differences in film sample thickness, the causes behind such effects, however, still remain unclear.

## 3.2 Introduction

This chapter is the conclusion of the study of a series of novel poly (arylene ether ether sulfide)s, the structure of which is shown in Figure 3.1. The synthetic route and molecular weight characterization of these novel polymers have been reported earlier [1]. Briefly, soluble amorphous precursor poly(ether ether sulfoxide)s are prepared by nucleophilic aromatic substitution reactions between difluorodiphenyl sulfoxides and diphenols. The soluble precursors are then rapidly reduced to the insoluble crystallizable poly(arylene ether ether sulfide)s which precipitate out of solution in the form of fine particles. The poly(ether ether sulfide) used in this study is based on hydroquinone, and will be referred to simply as phenyl sulfide for the rest of this paper.

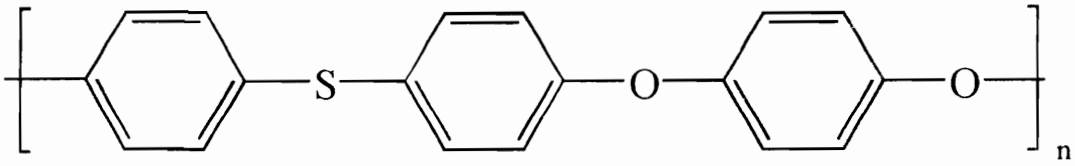


**Figure 3.1** Chemical structure of poly(ether ether sulfide).

As discussed in the previous chapters, this polymer exhibited a glass transition temperature of ca. 100 °C and an observed melting temperature of ca. 245 °C [2,3]. The equilibrium melting temperature as determined from a Hoffman-Weeks extrapolation yielded a value of 292 °C. It is obvious from Figure 3.1 and the transition temperatures, that this polymer is very similar to commercial poly(phenylene sulfide) (PPS) in terms of its chemical structure and transition temperatures ( $T_g = \text{ca. } 85 \text{ }^\circ\text{C}$ ,  $T_m = \text{ca. } 285 \text{ }^\circ\text{C}$ ), with PPS displaying a slightly higher crystallization window ( $T_m^\circ - T_g$ ).

The isothermal and non-isothermal crystallization kinetic studies were carried out from the melt and the data analyzed using the Avrami approach. For the case of melt isothermal crystallization, Avrami exponents of 3 were obtained independent of molecular weight or crystallization temperature, implying spherulitic growth. The rate constants and half-times exhibited molecular weight and crystallization temperature dependences as expected. A comparison of the Avrami crystallization parameters obtained for the phenyl sulfide polymer with corresponding values for PPS from literature showed that the phenyl sulfide system crystallized slower than PPS, with orders of magnitude difference noted in the bulk crystallization rate constants at equivalent undercoolings. The nucleation densities were, however, found to be comparable at equivalent undercoolings, implying that any differences in the rates of bulk crystallization were results of differences in the spherulitic growth rates.

It is now quite well accepted that polymers usually grow in the form of spherulites under quiescent conditions of melt crystallization [4]. These spherulites consist of bundles

of chain folded lamellae growing radially outward from the center, giving rise to a spherically symmetric superstructure. The growth of lamellae from the melt is usually studied by following the rate of growth of spherulites, and can be described by kinetic theories of polymer crystallization [5,6]. Hence, a study of the spherulitic growth rate yields information on the growth rates of the lamellae comprising the spherulite. Any fundamental investigation on the kinetics of polymer crystallization therefore, involves the study of the growth rate of spherulites as a function of undercooling. Such studies are also important from a morphological point of view, in that it is important to study the morphology and variations thereof as a function of undercooling and molecular weight.

There have been numerous reports in literature on studies of the spherulitic growth rate as a function of molecular weight and crystallization temperature for a variety of polymers like PPS [7], PEEK [8], isotactic polystyrene [9], and poly(oxymethylene) [10]. All such studies are typically carried out on thin film (ca. 200  $\mu\text{m}$ ) samples, which are subjected to the required thermal and crystallization histories, following which the rates of growth of spherulites are monitored, usually by polarized optical microscopy. None of these studies, however, deals with the film thickness effects on the subsequent growth rate. There are no indications in literature that the spherulitic growth rate is dependent on the film thickness in any systematic way. However, it is obvious that if the film thickness is substantially higher than the spherulitic diameter, the growth of 3-dimensional superstructures can take place unimpeded. However, if the film thickness is equal to or less than the spherulitic diameters, then the growth of 3-dimensional superstructures

would be impeded due to limitations in film thickness, and therefore limited in dimension by the surfaces in contact with the polymer. In this case, growth of 2-dimensional superstructures could be favored. At the same crystallization temperature it would be expected that the rate of growth of these disc-like structures would be equal to the spherulitic growth rate. Nevertheless, there seems to be no systematic study on the film thickness effects on the growth rate of the crystalline structures in the literature

In this study, the goal was to investigate the spherulitic growth kinetics and morphology upon crystallization from the melt for the poly(ether ether sulfide)s in order to gain a comprehensive understanding of the crystallization process in this system. During the course of this study, some interesting phenomena dealing with dual spherulitic morphology was observed. Most of the work reported here deals with this observation and details the studies carried out to investigate this phenomenon.

### **3.3 Experimental**

The poly(ether ether sulfide) polymer was available in powder form, and had a number average molecular weight ( $M_n$ ) of 19.9K. The details of the molecular weight characterization have been reported earlier [1].

The spherulitic growth rate experiments were carried out on thin films of sample sandwiched between microscope cover slips. The samples were prepared by melting the polymer on a glass cover slip placed on a hot-plate which was set to a temperature of ca.

280 °C, and placing another glass cover slip on top of the melt while pressing the top cover slip in order to obtain a thin film, as shown in Figure 3.2. In some cases, the top cover slip was used to impart a shear to the melt, after which the top cover slip was removed as also shown schematically in Figure 3.2. These samples will therefore be referred to as quiescent samples and sheared samples respectively. The terminology adopted in describing these samples merely reflects the sample preparation technique and is not intended to imply that crystallization takes place under either quiescent conditions or under shear. It should be emphasized that all samples in this study were crystallized under quiescent conditions. In some cases, a sheet of Kapton was used to prepare quiescent samples instead of a top cover slip. At the end of sample preparation, the Kapton was removed. All samples were heated at 90 °C/min to 290 °C, and held there for 5 min, after which they were quenched rapidly to the required crystallization temperature. For some experiments different melt temperatures were used prior to crystallization, which are discussed along with the results.

The growth rates were monitored in a Linkam THM 600 hot stage and a Zeiss polarizing light microscope equipped with a video camera. The hot stage was calibrated using melting point standards, and run under a nitrogen purge. The growth of spherulites was measured as a function of time using a Boeckeler Video measurement system. The radial growth rates were determined by measuring the radii of the spherulites as a function of time. In order to calculate the growth rate at a given temperature, measurements were made on 3-5 spherulites depending on the nucleation density. At each time, the radius of

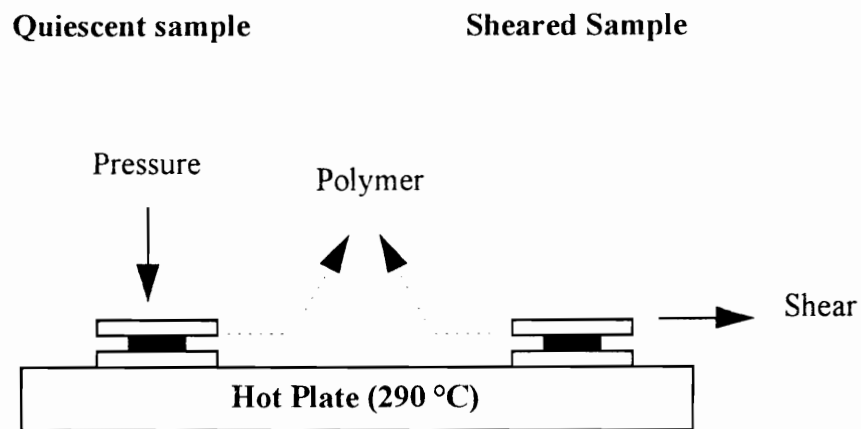


**Figure 3.2** Schematic of sample preparation for hot stage optical microscopy.

each spherulite was determined by averaging over 5 measurements made at different points on the circumference. The growth rates of all the spherulites measured were averaged and the mean value taken to be the growth rate at that temperature.

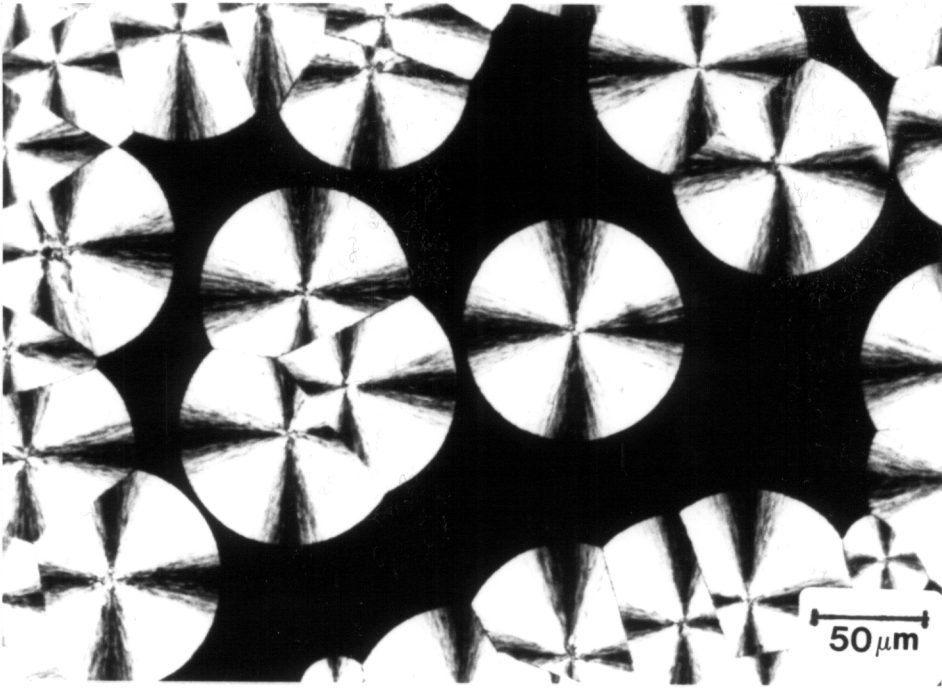
Small angle light scattering (SALS) experiments were carried out on film samples obtained from the optical microscopy studies. A He-Ne laser ( $\lambda=6328 \text{ \AA}$ ) was used in conjunction with a camera to record the  $H_v$  and  $V_v$  scattering patterns.

Scanning electron microscopy was performed on a Cambridge Stereoscan 200 SEM. Samples crystallized on glass cover slips without top cover slips were prepared in the hot stage for use in this study, and used after sputtering with gold.

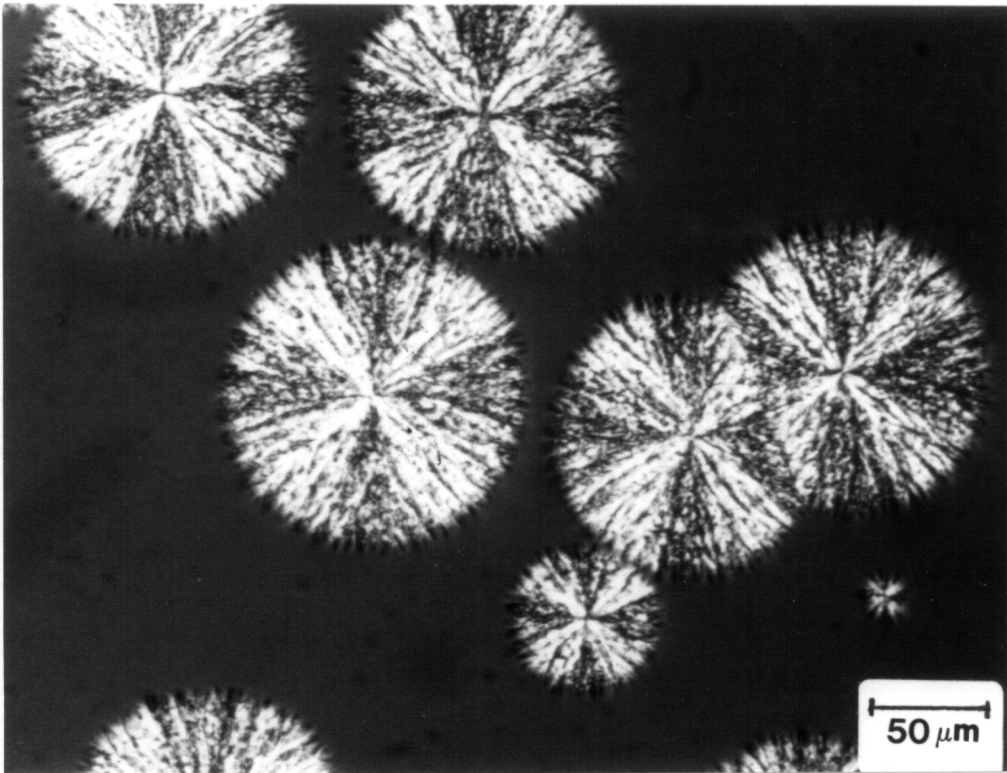
Atomic Force Microscopy (AFM), also called Scanning Probe Microscopy (SPM) experiments were carried out in the tapping mode on a NanoScope III<sup>®</sup> (Dimension 3000) scanning probe microscope from Digital Instruments.

### 3.4 Results And Discussion

Growth rate studies were performed on the phenyl sulfide 19.9K polymer at various temperatures. An interesting feature of this study was the observation of distinct populations of two kinds of spherulites, denoted Type I and Type II, *exhibiting distinctly different growth rates at the same temperature*. The polarized optical micrographs of the two types of spherulites are shown in Figure 3.3. It is quite obvious from the micrographs that the Type I and Type II spherulites exhibit distinctly different morphological textures,



A



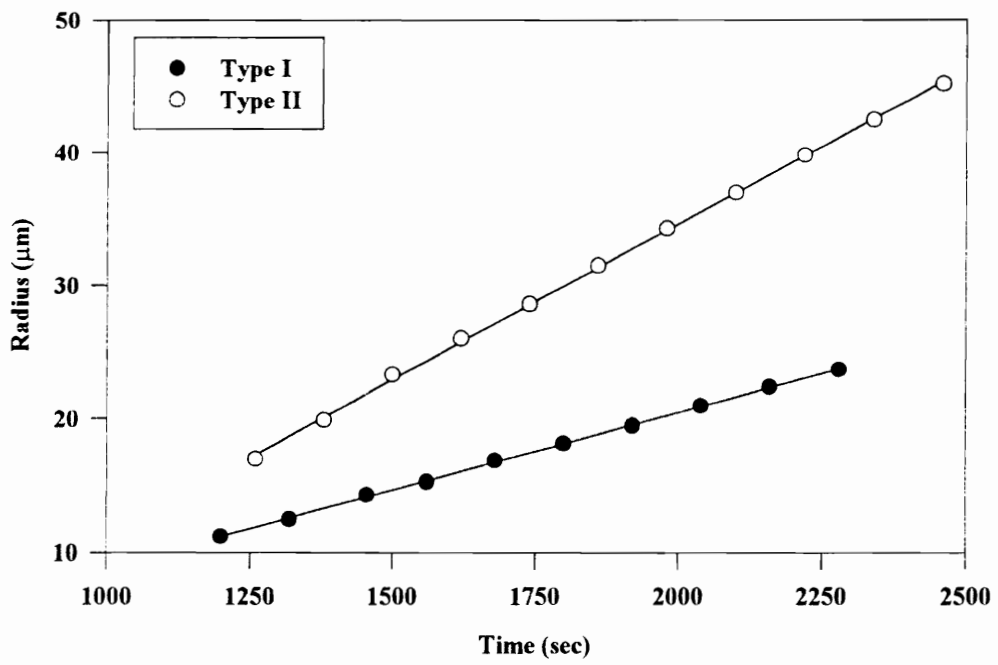
B

**Figure 3.3** Polarized optical micrographs of (A) Type I and (B) Type II spherulites.

with the Type I showing a “smooth” texture and the Type II showing a “rough” texture. This point will be discussed in more detail later in the paper. An important point to note here is that the Type I and Type II spherulites always occurred in different regions, i.e. there were no Type I spherulites observed in the middle of a region of Type II spherulites and vice-versa.

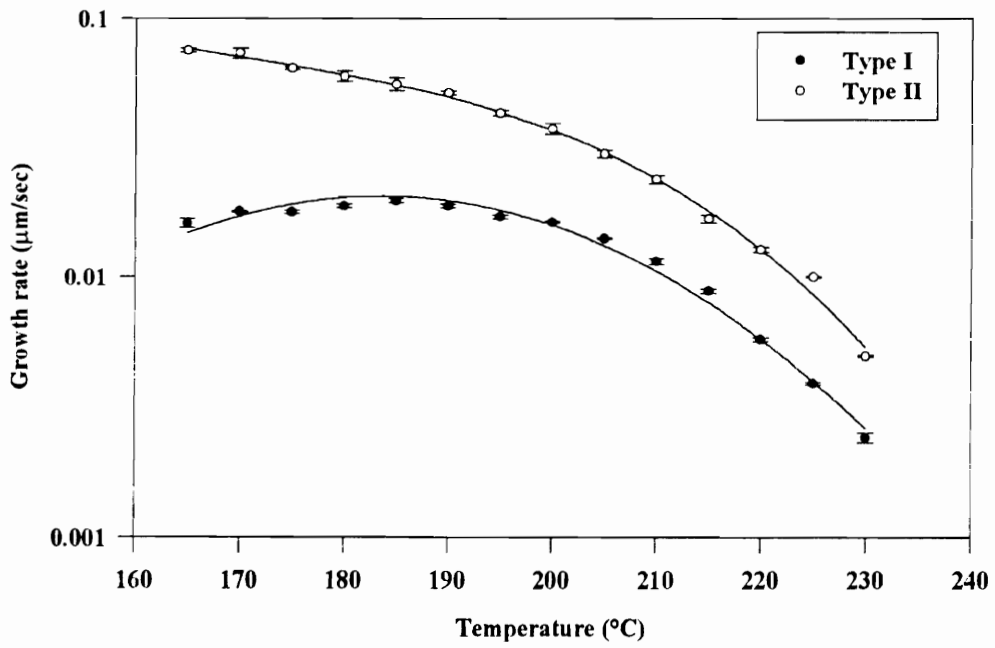
A possible explanation is that the dual spherulitic morphology arises as an artifact of the sample preparation technique shown in Figure 3.2. To better illustrate this point, studies were carried out on samples which were sheared as described in the experimental section. Under these conditions, *only Type II spherulites were observed*. The growth rates of the spherulites observed in sheared samples were identical to the Type II spherulites observed in quiescent samples, at the same temperature. This seems to suggest that the sample preparation technique might play a role in determining both the morphology as well as the rate of spherulitic growth. The observations described until now imply that growth of Type I spherulites are favored in quiescent samples, and that Type II spherulites are preferred in sheared samples.

Figure 3.4 shows the growth rates of Type I and Type II spherulites crystallized isothermally at 210 °C. The Type I spherulites were grown with a top cover slip, whereas the Type II spherulites were grown on sheared samples, i.e. without a top cover slip. *It can be seen that the Type II spherulites showed a significantly higher growth rate than the Type I spherulites*. This in fact was observed at all temperatures at which experiments were carried out. The variation of growth rate of both Type I and Type II spherulites as a



**Figure 3.4** Growth rate plots for Type I and Type II spherulites at 210 °C.

function of crystallization temperature is shown in Figure 3.5. *The Type II spherulites exhibited higher growth rates at all temperatures studied, with the difference increasing with decreasing temperature.* It is interesting to note that the growth rate of the Type I spherulites as a function of temperature displays the expected “bell” shape which follows from theoretical considerations [5,6]. At temperatures close to the melting temperature, the growth is limited by nucleation, and hence the growth rate increases with decreasing temperature. At temperatures close to the glass transition temperature, the growth is limited by mobility, and hence the growth rate decreases with decreasing temperature. At some intermediate temperature, where both these effects balance, a maximum in the growth rate can be seen. It can be seen that at the higher temperatures, the growth rate of both Type I as well as Type II spherulites increases with decreasing temperature, implying nucleation-controlled growth. As the temperature is decreased, the growth rate of Type I spherulites exhibits a maximum at ca. 185 °C, then decreases with decreasing temperature, indicating mobility-controlled growth. The growth rate curve of the Type II spherulites, however, does not exhibit a maximum in the range of temperatures studied here. Growth rate studies could not be carried out at lower temperatures due to problems associated with high nucleation densities. The lack of a clearly defined maximum in the growth rate versus temperature curve of the Type II spherulites could either imply that the maximum takes place at lower temperatures compared to that observed for the Type I spherulites, or could imply that growth is controlled only by nucleation, and that there is no mobility controlled region. Such an explanation is possible only if there are no barriers to the



**Figure 3.5** Growth rates as a function of temperature for Type I and Type II spherulites.

transport of crystallizable polymer molecules to the lamellar growth front of a spherulite. This observation is quite unexpected based on the fact that numerous experimental and theoretical investigations on the crystallization processes in polymers have shown the existence of a diffusion controlled regime of crystallization at temperatures close to the glass transition temperature.

Based on the observations presented, a variety of possible reasons can be offered to explain the observed behavior. The various possible causes shall be discussed along with the validity of the explanations. One possible explanation could be based on thermal degradation. Since the Type II spherulites are grown in samples without top cover slips, thermal degradation of the polymer that is exposed to the atmosphere could occur, and the resulting chain scission could cause a higher growth rate and coarser morphology. To test this hypothesis, Type I spherulites were grown without a top cover slip, by sample preparation using a Kapton sheet as discussed earlier. The growth rate of the Type I spherulites was in this case, identical to the Type I spherulites grown with the top cover slip, thereby implying that thermal degradation did not play a critical role in influencing the growth rates. Also, as mentioned earlier, the growth rates of Type II spherulites grown in the sheared samples were identical to those observed in quiescent samples with the top cover slip, again implying that thermal degradation did not play a role in influencing the growth rate and morphology.

Another possible explanation is that, in preparing the sheared samples, the top cover slip imparts a shear to the polymer melt as shown in the schematic in Figure 3.2. It

is possible that the sample “remembers” the shear history, which could influence the subsequent crystallization behavior. Indeed, there have been several studies in literature which have shown the effect of shear/strain on the crystallization behavior of polymers. Wilkes et al. [11] showed that imposing a strain on an amorphous sample of a polyester film below its  $T_g$  caused an increase in the subsequent nucleation density on heating the sample above  $T_g$ , even though the amorphous sample showed no sign of any orientation. Khanna et al. [12-15] showed that shearing a polar polymer like nylon 6,6 in the melt caused an increase in the nucleation density on subsequent cooling. These studies show conclusively that preshearing a polymer prior to crystallization can potentially influence the subsequent nucleation behavior. However, there seem to be no reports in the literature on the preshearing influencing the subsequent *growth rate of spherulites*. Several experiments were therefore carried out to investigate if the preshear on the melt indeed influences the subsequent spherulitic growth rate and morphology.

First, the effect of melt temperature prior to crystallization on the subsequent growth rate was investigated. Since all samples in this study were melted at 290 °C for 5 min prior to crystallization, it would be expected that the molecules would relax to an isotropic state, and would no longer be affected by the prior shear history. If the shear imparted to the samples during sample preparation does indeed affect the crystallization growth rate, it can be hypothesized that the melt treatment of 290 °C for 5 min is not sufficient to erase the prior shear history. In such a case, it would be expected that higher melt residence temperatures prior to crystallization would be more effective in erasing the

shear history. This would cause a reduction in the growth rate of the Type II spherulites, such that the growth rates approach the values displayed by the Type I spherulites at the same temperature. Melt temperatures of 300 °C and 310 °C were therefore employed for quiescent and sheared samples in order to investigate the effect of melt temperature on the growth rates. Figures 3.6 & 3.7 display the results of these studies, which show that the growth rates of Type I as well as Type II spherulites were independent of prior melt history. This indicates that shear history is not a probable cause of the observed behavior, since the high melt temperatures utilized would be expected to erase the history of the sample preparation. This experiment also confirms the earlier statement that thermal degradation does not likely cause the observed behavior, since higher melt temperature would increase degradation effects, and hence cause a further increase in the growth rates.

Further experiments were carried out to confirm the hypothesis that the shear history does not cause the dual morphology and differences in growth rates. Type I spherulites were grown in quiescent samples and Type II samples were grown in sheared samples, at 210 °C and allowed to crystallize for 2 hr, after which the entire volume was filled with spherulites. As was mentioned earlier, spherulites are formed by radiating bundles of fibrils, which consist of folded chain lamellar stacks, to form a spherically symmetric superstructure. A spherulite can thus be viewed as a globally isotropic semicrystalline structure. Assuming that all chains in the sheared sample formed Type II spherulites, melting of the Type II spherulites followed by recrystallization should yield only Type I spherulites, since melting of a spherulite would yield an isotropic melt, which

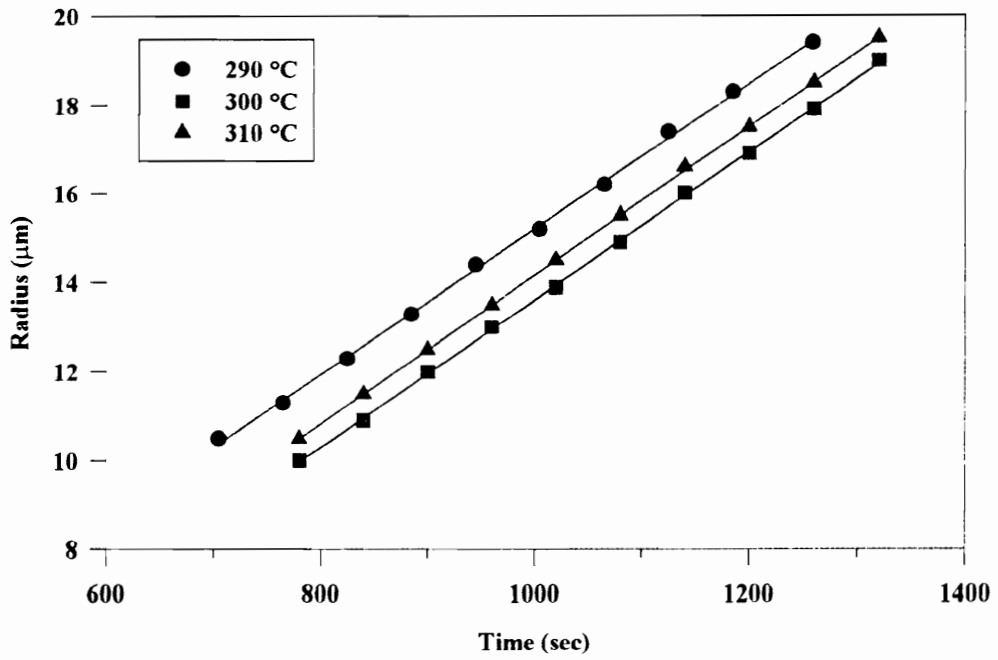


**Figure 3.6** Growth rate of Type I spherulites at 200 °C as a function of melt temperature.

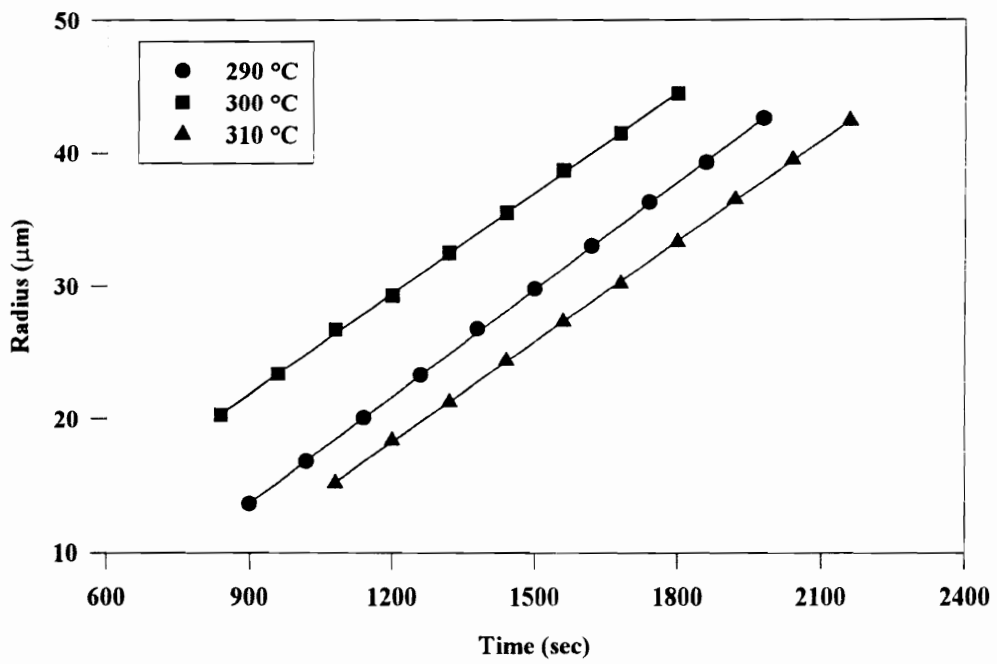


**Figure 3.7** Growth rate of Type II spherulites at 210 °C as a function of melt temperature.

would not be influenced by the shear imparted to the polymer during sample preparation. *It was observed that melting and recrystallizing a sample of Type II spherulites yielded Type II spherulites again, which had the same growth rate as observed during the first run.* This finding also rules against the hypothesis that shear history influences the spherulitic growth rate and morphology. Not surprisingly, only Type I spherulites were observed to grow in the case when Type I spherulites were grown, melted, and recrystallized. The results of these studies are shown in Figures 3.8 & 3.9, where the growth rates of Type I and Type II spherulites are shown during the first run, and the second run which denotes crystallization after melting the existing spherulites.

It is possible that surface effects of the glass cover slip probably play a role in either influencing the growth rate and morphology, or in maintaining the “shear” condition even after the melt treatment prior to crystallization. There are reports [16-18] in the literature dealing with the surface effects on nucleation, in which the authors showed that the surface of the substrate used in crystallizing thin films influenced the nucleation density. There are no reports in the literature dealing with surface effects influencing the growth of crystals after the primary nucleation process, though the substrate would not a priori be expected to affect the crystal growth process or the spherulitic morphology (not taking into account phenomena like transcrystallinity). This fact was investigated by crystallizing the polymer on three different substrates. The glass cover slips used in all experiments were coated with a thin layer of gold by sputter coating. This was done to provide a crystalline substrate for the polymer to grow on. In order to provide an

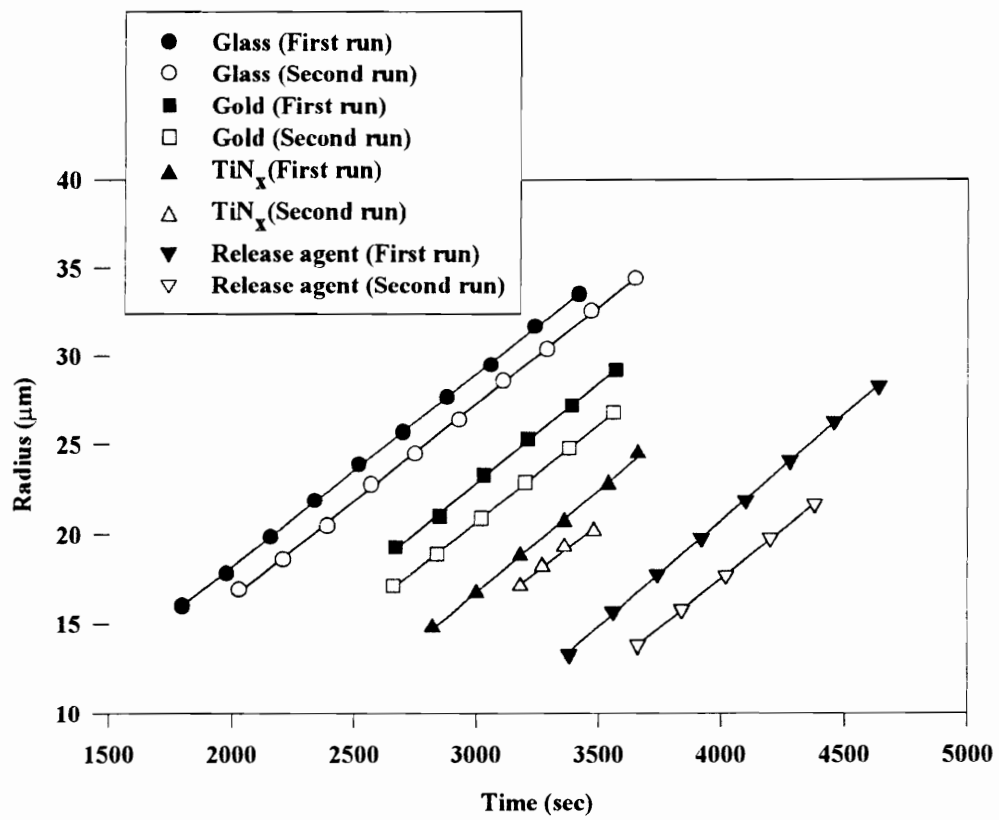


**Figure 3.8** Growth rates of Type I spherulites at 210 °C on different substrates.

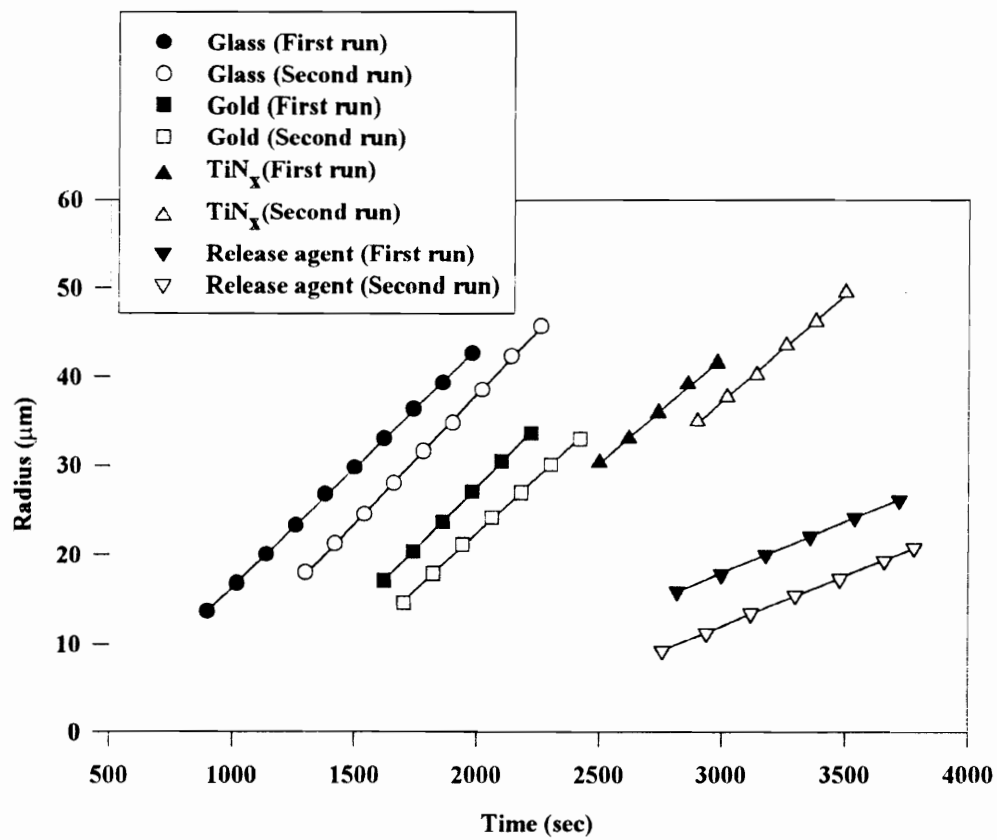


**Figure 3.9** Growth rates of Type II spherulites at 210 °C on different substrates.

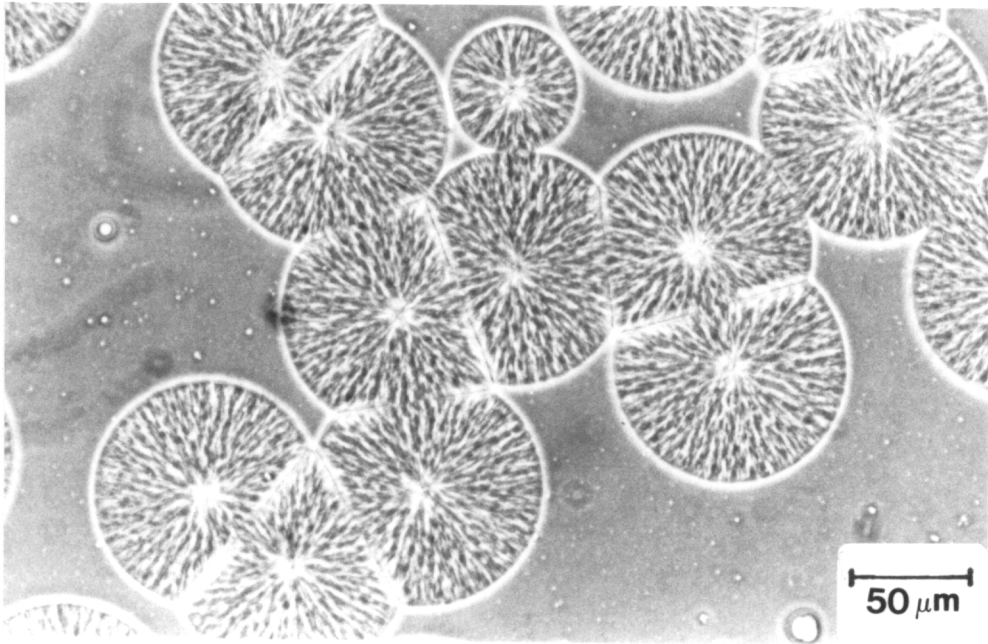
alternative amorphous substrate for the polymer to grow on, the glass cover slips were sputter coated with titanium nitride ( $\text{TiN}_x$ ). Some samples were grown on the cover slips after coating with a mold release agent prior to sample preparation. Both quiescent as well as sheared samples were prepared on all substrates in order to grow Type I as well as Type II spherulites. As was done in the case of the glass substrates, all samples were allowed to grow at 210 °C for 2 hr in order to obtain samples where the spherulites had filled the sample volume, melting these samples, and recrystallizing them at 210 °C. These experiments will therefore be identified by the nature of the substrate, and labeled as the first or second run.

The results of these studies are shown in Figures 3.8 & 3.9 for the various substrates, and compared to the results obtained by crystallization on the glass substrate. The curves for the various cases have been moved on the x-axis for clarity. It was observed that the sheared samples always yielded Type II spherulites for the cases of glass substrate, gold substrate, and the  $\text{TiN}_x$  substrate. For the case of the quiescent samples, Type I spherulites were grown for the case of the glass substrate, gold and  $\text{TiN}_x$  substrates. For the case of the substrates prepared with the mold release agent, both the sheared as well as the quiescently prepared samples yielded Type I spherulites. From the figure, it can also be seen that the growth rates of the first and second runs are identical and independent of the nature of the substrate for both Type I and Type II spherulites, with the exception of the substrate with the mold release agent. A possible reason for this behavior is discussed later in the paper. It can thus be concluded that the nature of the

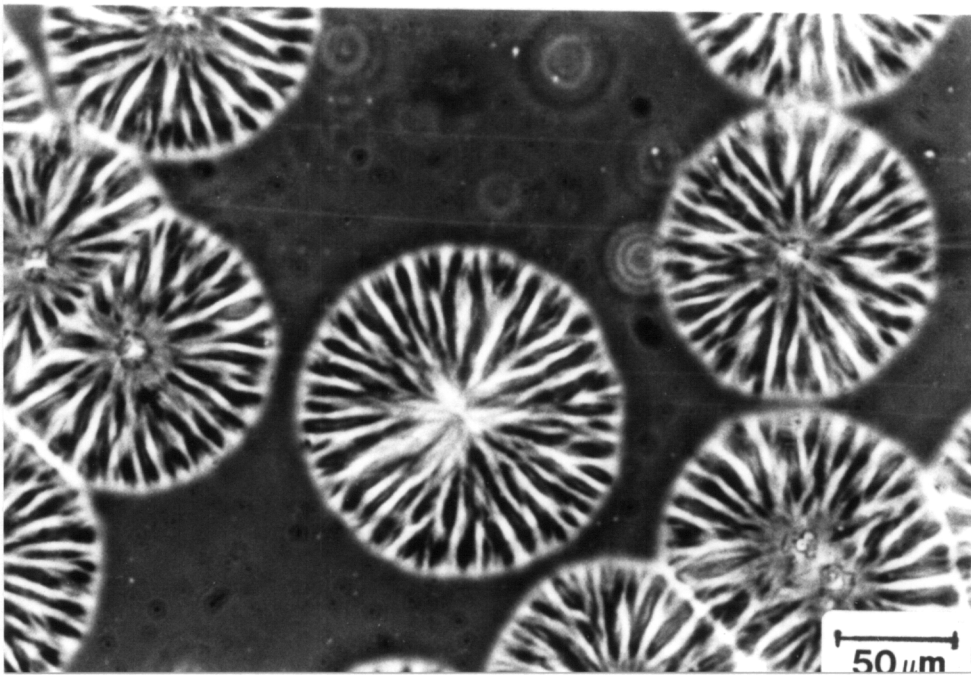
substrate does not play a critical role in determining the growth and morphology of the spherulites.

It was mentioned earlier that the morphology of the Type I and Type II spherulites were quite different in terms of the texture, with the Type II spherulite exhibiting a coarser texture, as shown in Figure 3.3. Before a more detailed discussion of the morphology of the different types of spherulites, it is worth mentioning that both the Type I and Type II spherulites exhibited negatively birefringent spherulites with prominent Maltese cross extinction patterns, thereby implying that the chain packing in the spherulites is likely the same in the two cases. The optical melting point of the spherulites were determined in 2 cases - Type I and Type II spherulites grown with and without top cover slips on a glass substrate at 210 °C. The melting point was noted to be the temperature when all the birefringence disappeared (as observed visually) from the sample on slow heating at increments of 1 °C. The melting points were observed to be 262 °C, irrespective of the type of spherulite or presence of a top cover slip. This indicates that there is likely no degradation caused in the samples without the top cover slip, and that the crystal lamellar thickness is identical in both the Type I and Type II spherulites. This is to be expected on thermodynamic grounds, since the lamellar thicknesses would be expected to be equal at similar undercoolings.

Figure 3.10 shows the phase contrast micrographs of the Type I and Type II spherulites. It is obvious from the micrographs that the Type II spherulite displays a coarser morphology than the Type I spherulites, as is evidenced by the coarser fibrils



A



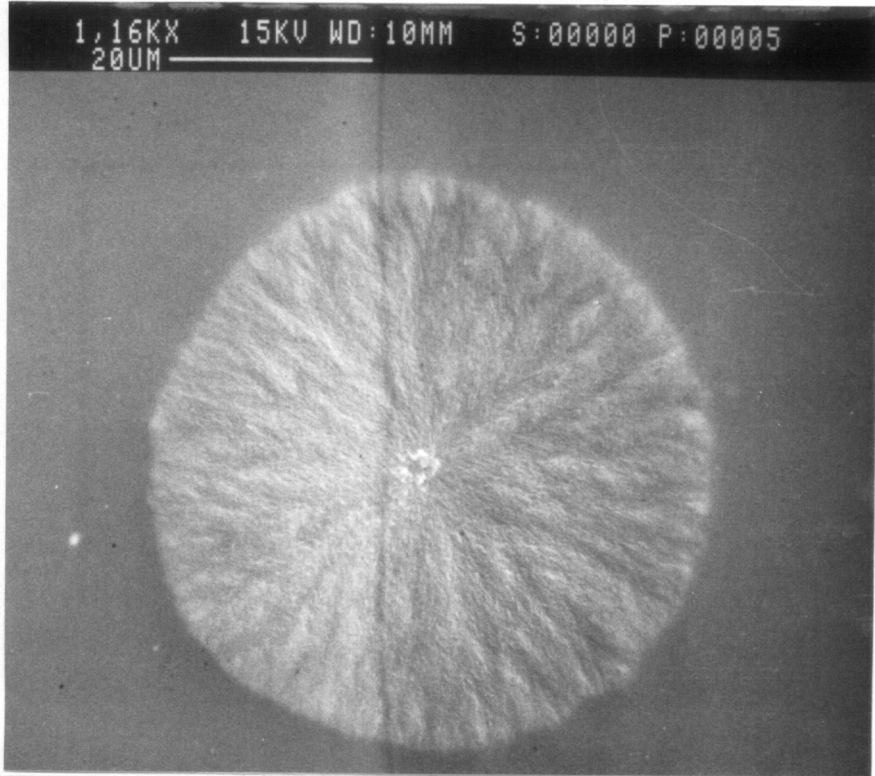
B

**Figure 3.10** Phase contrast optical micrographs for (A) Type I and (B) Type II spherulites.

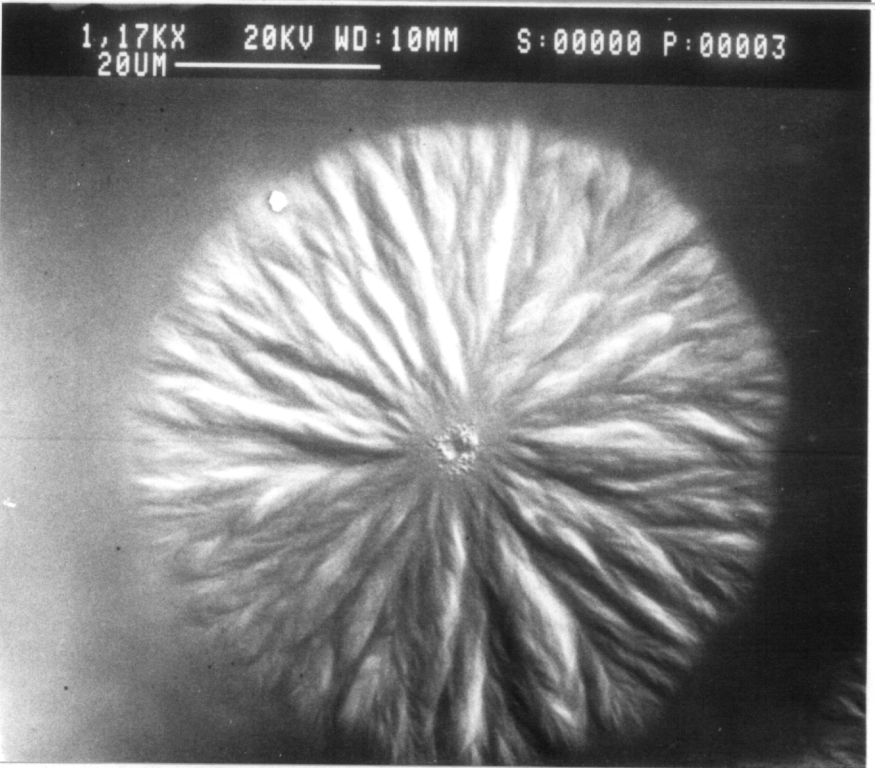
radiating from the center. The same conclusion can be drawn from Figures 3.11 & 3.12, in which the SEM micrographs of the two kinds of spherulites are shown, and Figures 3.13 & 3.14, in which are shown the AFM images of the two kinds of spherulites. The Type II spherulites seemed to consist of thicker fibrils with larger inter-fibrillar “gaps” than the Type I spherulites, which are characterized by closely packed thinner fibrils. It should be mentioned that each of these fibrils consists of bundles of lamellae separated by inter-lamellar amorphous layers.

Figure 3.13 shows the height image from the AFM. In this image, the light areas are indicative of the largest “heights” in the topographical image, and the dark areas are the “lowest” areas. The gray scale in the image indicates intermediate heights. It can be seen in the figure that the Type I spherulite displays some curvature on going from the center outwards, which is characteristic of a spherical object. The Type II spherulite is shown in Figure 3.13B, in which the center of the spherulite is towards the top left of the image, whereas the outer boundary of the spherulite can be seen near the lower right of the image. It is quite clear from this image that there is no curvature in the Type II spherulite, rather indications of a disc-like object are quite prominent.

Film thickness measurements were carried out with a micrometer, on quiescent samples that displayed Type I spherulites and sheared samples that displayed Type II spherulites, for all the substrates investigated here. A total of ca. 15 samples were measured in each case. Quiescent samples that displayed Type I spherulites displayed film thicknesses between 50-70  $\mu\text{m}$  for all the substrates investigated here. Sheared samples

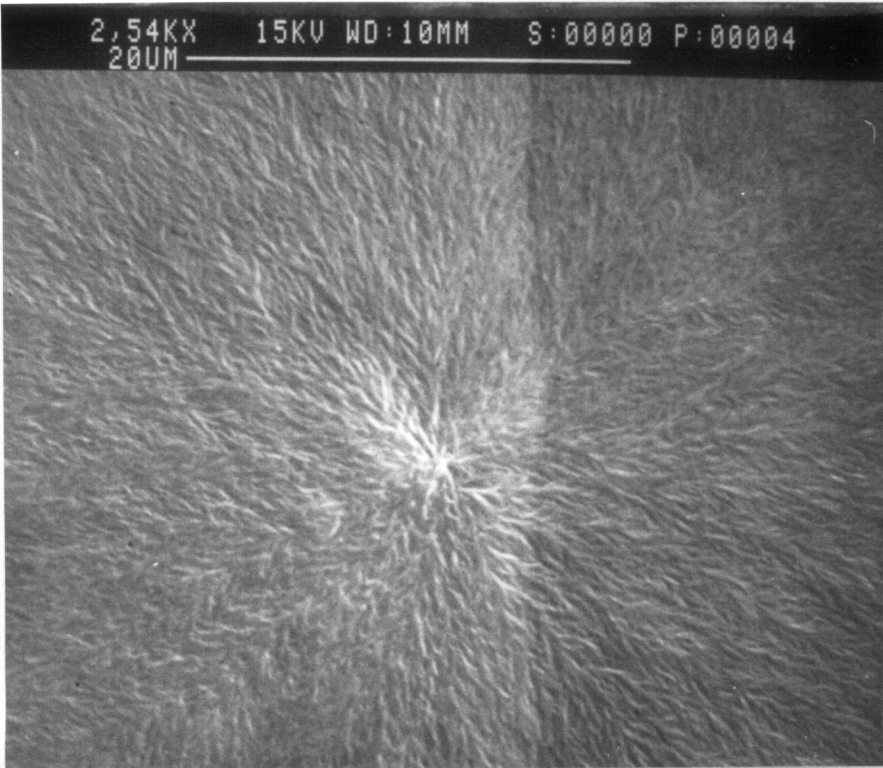


**A**

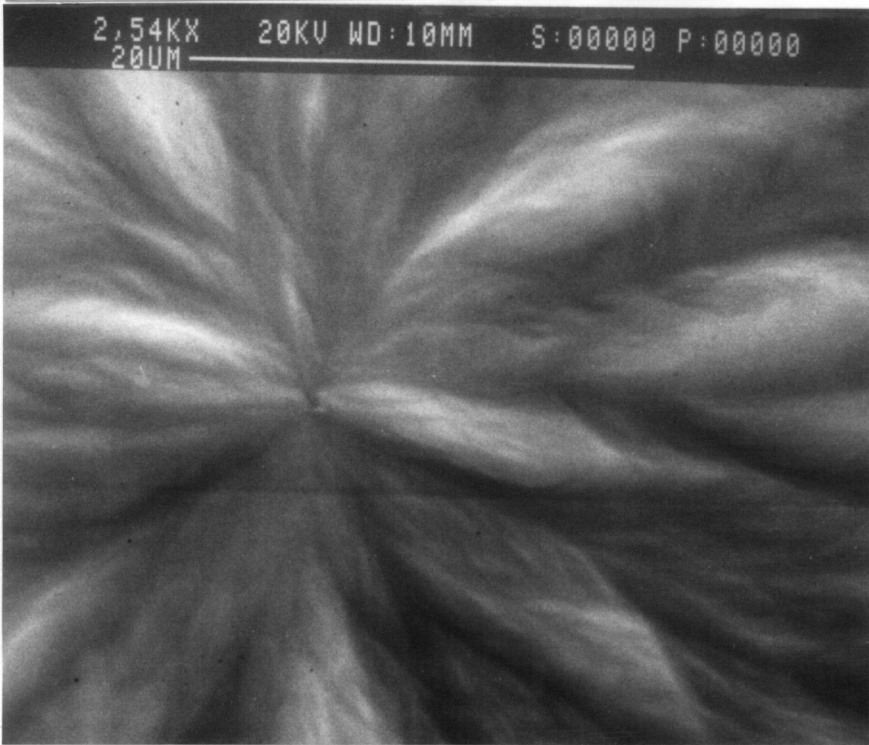


**B**

**Figure 3.11** SEM micrographs for (A) Type I and (B) Type II spherulites.



**A**



**B**

**Figure 3.12** SEM micrographs for (A) Type I and (B) Type II spherulites.

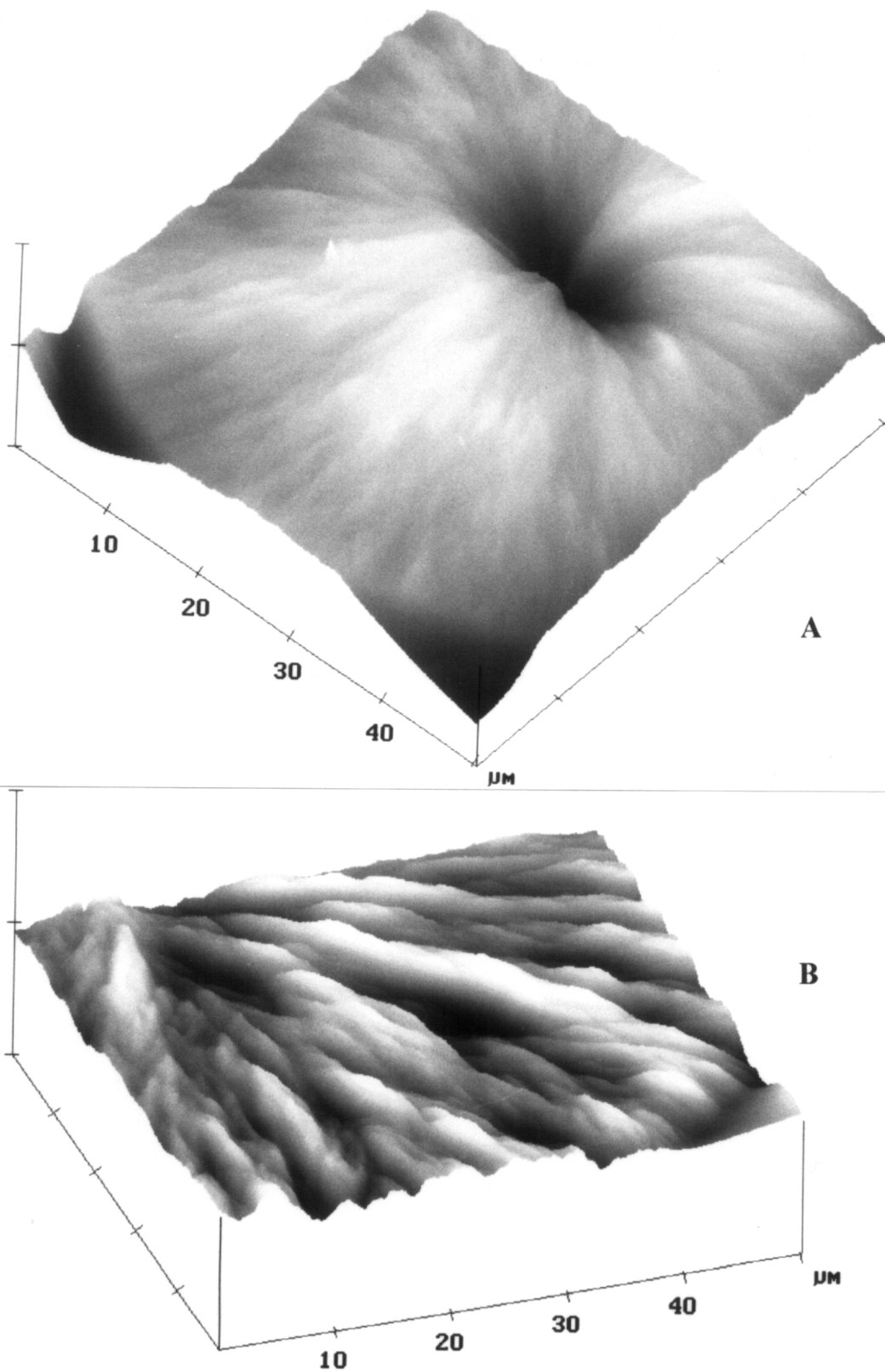


**Figure 3.13** AFM height images for (A) Type I and (B) Type II spherulites.

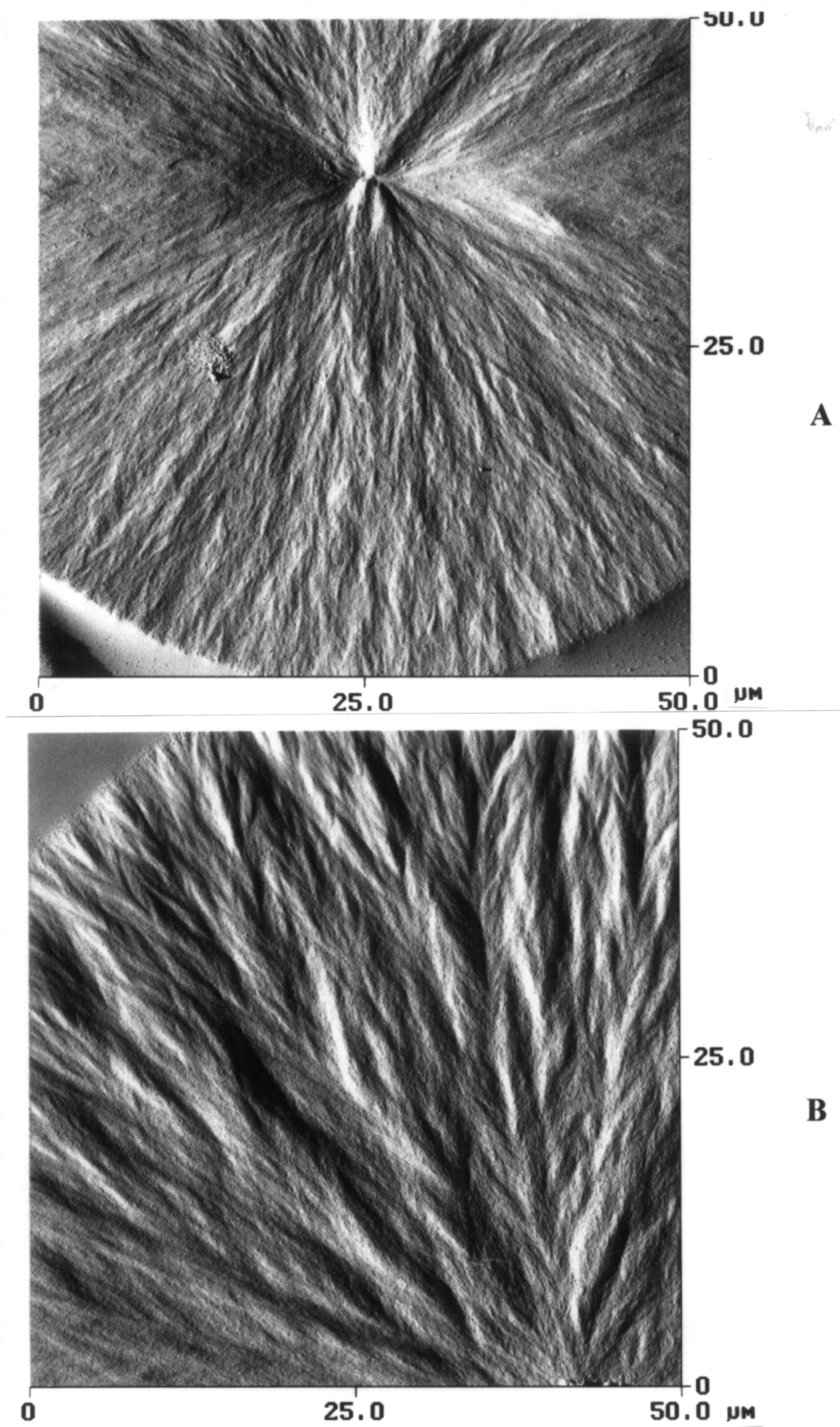
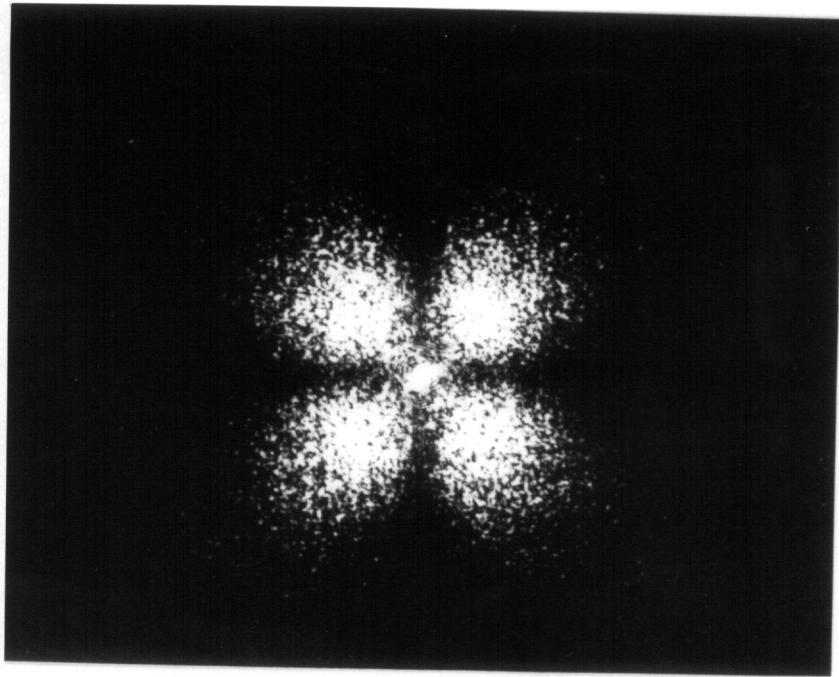


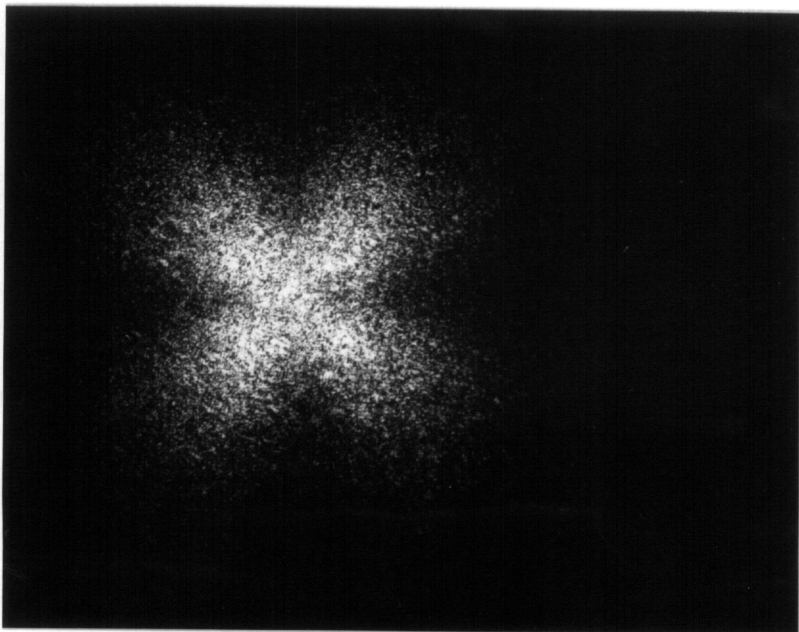
**Figure 3.14** AFM amplitude images for (A) Type I and (B) Type II spherulites.

that displayed Type II spherulites, however, were 10-13  $\mu\text{m}$  thick on all the substrates, except the substrate with the mold release agent. The sheared sample with the mold release agent displayed a film thickness of ca. 50  $\mu\text{m}$ . From all the micrographs shown here, it is obvious that the spherulites are of the order of 50  $\mu\text{m}$  in diameter. This strongly suggests that the Type II spherulites are disc-like structures grown in thin samples, which is consistent with the AFM height image shown in Figure 3.13B. The observed phenomena can thus be attributed to film thickness effects, with thinner films causing 2-dimensional coarser textured disc-like superstructures, and thicker films permitting the growth of 3-dimensional finer textured spherulites.

One possible method to determine the shape of growing crystalline superstructures is by small angle light scattering [19]. The  $H_v$  scattering pattern is dependent only on the size and shape of the scattering particle. Furthermore, theoretically predicted patterns from spheres and disks are very similar under identical optical conditions. The forms of the intensity equations for disks and spheres are very similar, which causes the intensity maxima of  $H_v$  patterns from spheres to appear at almost identical angles as for disks of the same radii [19]. The  $H_v$  patterns from spheres and disks would therefore be expected to be essentially identical. Figure 3.15 show the  $H_v$  SALS patterns for the Type I and Type II spherulites respectively. Indeed, it is quite difficult to differentiate between the SALS patterns shown in this figure, and to assign any one of them conclusively to either a sphere or a disk. Under  $V_v$  conditions, the scattering is more complicated as it depends not only



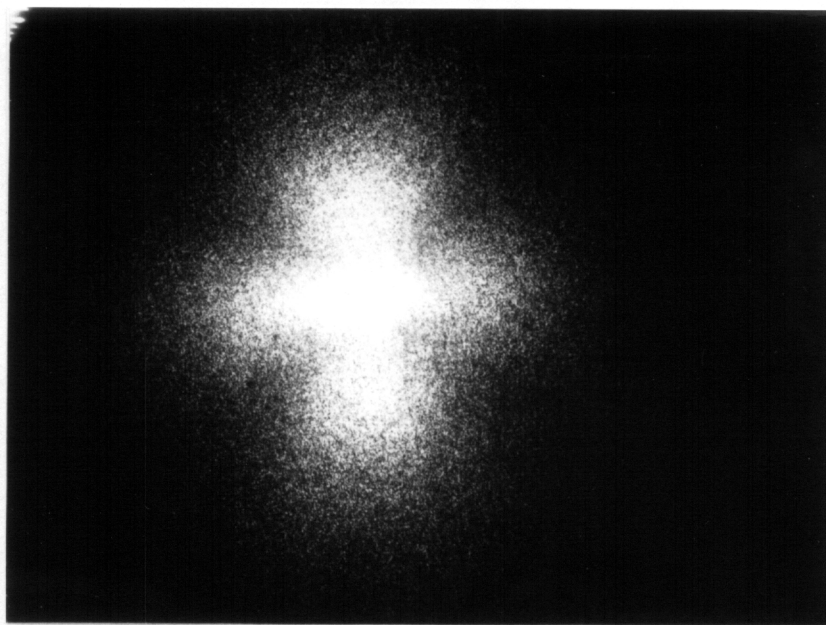
**A**



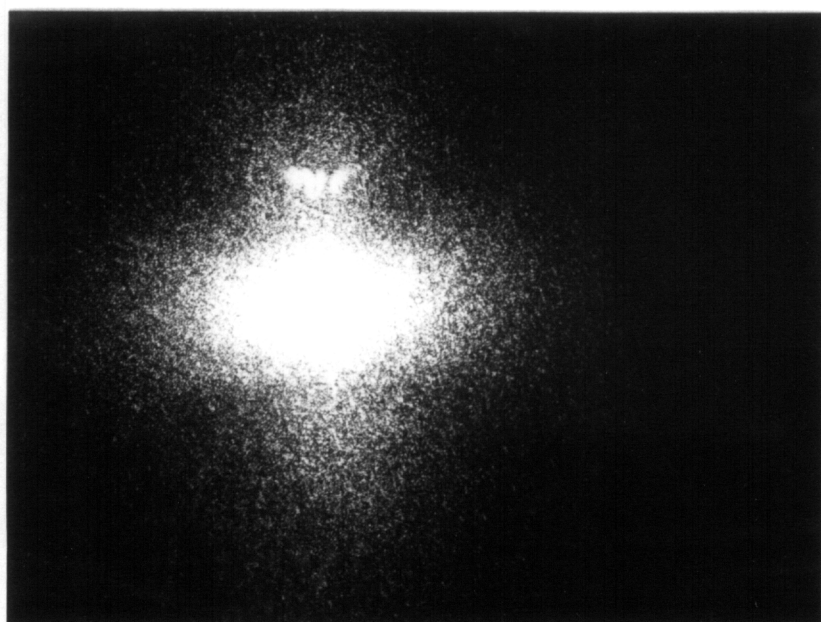
**B**

**Figure 3.15**  $H_v$  SALS patterns for (A) Type I and (B) Type II spherulites.

on the size and shape of the scattering particle, but also on both the optical anisotropy of the scattering particle and the polarizability of the surroundings. As in the case of the  $H_v$  scattering, the  $V_v$  scattering patterns from spheres and disks are functionally quite similar, and therefore yield similar patterns. The differences between the patterns are often quite subtle, and occur in the relative intensity of the scattering lobes. Under certain conditions (when the background polarizability is close to either the radial or tangential polarizability of a spherulite), both disks and spheres can cause almost identical scattering patterns. However, under other conditions (when the surrounding polarizability is intermediate between the radial and tangential polarizabilities of a spherulite), there are enough differences between the two in order to successfully differentiate between them. Figure 3.16 shows the  $V_v$  scattering patterns of the Type I and Type II spherulites. It can be seen that for the case of the Type I spherulites, the meridional lobes exhibit higher intensity than the equatorial lobes. However, in the case of the Type II spherulite, the equatorial elliptical pattern displays a higher intensity than the lobes present in the meridional region. Samuels has catalogued a series of  $V_v$  SALS patterns in an earlier report [19], by generating theoretical scattering patterns for spheres and disks for negatively birefringent spherulites, for changing background anisotropy. A comparison of the  $V_v$  patterns shown here with his theoretically generated patterns for spheres and discs were made for the case of the background polarizability being greater than the radial polarizability, but less than the tangential polarizability of the spherulite. This comparison revealed some similarities between the patterns, suggesting that the Type I spherulites were spherical, and that the



**A**



**B**

**Figure 3.16**  $V_v$  SALS patterns for (A) Type I and (B) Type II spherulites.

Type II spherulites were disc-like, a finding that is consistent with the AFM and film thickness measurements. It should be mentioned that the samples used in this study had the complete volume filled with spherulites, which would cause the background polarizability to be on the average, greater than the radial and less than the tangential polarizability of an individual spherulite.

### **3.5 Conclusions**

Isothermal crystallization of spherulites in thin films of a poly(ether ether sulfide) were carried out in this study. A dual population of spherulites was observed with different morphologies and growth rates; these have been designated Type I and Type II spherulites. The coarse-textured spherulites (Type II) were shown to grow faster than the finer-textured spherulites (Type I) at the same crystallization temperature. This phenomenon was observed at all temperatures studied here. Though there are no mentions of similar phenomena in literature, it should be emphasized that the phenomena reported here are not limited to the system studied here, but may well be quite general. Some preliminary investigations on PPS revealed similar effects. Crystallization growth rate studies on narrow molecular weight fractions of isotactic polystyrene have also yielded similar behavior [20]. One point to note here is that the possibility of the Type I and Type II spherulites exhibiting different unit cell structures, thus causing the observed differences in growth rates and morphology has not been considered here. This point

could not be experimentally verified due to the fact that Type II spherulites could be grown only in thin films, which prevented a good signal during a diffraction experiment. Growth rate studies on various substrates (glass, gold, titanium nitride, glass with mold release agent) yielded similar phenomena, indicating that the nature of the substrate was not responsible for the observations. The study of the effect of prior melt and crystallization history revealed again that these parameters did not affect the observed phenomena. An interesting finding was that the growth rate of the Type I spherulites showed a nucleation-controlled regime as well as a diffusion-controlled regime separated by a maximum. The Type II spherulites, however, did not display this expected behavior, but increased continuously with decreasing temperature, indicating that in the temperature range investigated, there seemed to be no diffusion-controlled regime. The texture of the Type II spherulites was found to be coarser by a variety of techniques. Though it is difficult to speculate as to the exact cause of this observed behavior, certain causes based on thermal degradation and shear history have been ruled out as causing this phenomenon. It is speculated that the sample preparation technique used in this study caused variations in film thicknesses. For sample thicknesses of ca. 10  $\mu\text{m}$ , the growth of 3-dimensional spherulitic superstructures is prevented by the limited thickness of the film, thus causing the formation of disc-like superstructures, with increased coarseness and displaying higher growth rates, referred to as the Type II spherulites. For sample thicknesses of ca. 50  $\mu\text{m}$ , growth of 3-dimensional spherulitic superstructures is not impeded, and results in spherulites displaying a finer texture and slower growth rates, which have been termed

Type I spherulites. These conclusions were drawn based on film thickness measurements, AFM and SALS studies. The causes as to why the disc-like structures display coarser morphologies and increased growth rates is, however, still not clear. The kinetic theories of polymer crystallization mathematically describe the growth of chain folded lamellae from a quiescent melt. In practice, the growth rate of the lamellae are studied by following the spherulitic growth rate. The growth rate is dependent on the undercooling from the melt, all other factors remaining constant. Therefore, at similar undercoolings, similar growth rates would be expected regardless of the geometry of the growing superstructure. Since the observed phenomenon is not in agreement with this hypothesis, it is clear that the film thickness either modifies some of the parameters in the growth rate expressions, or is not considered at all during the derivation of the theories. Indeed, in one experiment the spherulites were observed to grow at a rate intermediate to those displayed by Type I and Type II spherulites. This suggests that the growth rate could vary systematically as a function of film thickness up to a point where the film thickness exceeded the spherulitic diameter. For film thicknesses greater than the spherulitic diameter, however, the spherulitic growth rate would be expected to be independent of film thickness. It is evident, however, that any theory of crystal growth and kinetics should not only explain the phenomena reported here, but must also consider the geometry of growth, as they influence the growth of the observed superstructure.

## Acknowledgments

The authors would like to acknowledge the NSF Science and Technology Center for full support of this study under contract # DMR 9120004. The assistance of Steve McCartney in obtaining the AFM micrographs is acknowledged. Useful discussions with Dr. Hervé Marand and Dr. Darrell Iler are also acknowledged.

## References

1. J. R. Babu, M. Konas, A. E. Brink, and J. S. Riffle, *Polymer*, **35**, 4949 (1994).
2. S. Srinivas, J. R. Babu, J. S. Riffle, and G. L. Wilkes, *Polymer*, **36**, 3317 (1995).
3. S. Srinivas, J. R. Babu, J. S. Riffle, and G. L. Wilkes, submitted for publication.
4. F. Khoury and E. Passaglia, *Treatise on Solid State Chemistry Vol.3*, Ed. N. B. Hannay, Plenum Press, New York, 1976.
5. J. D. Hoffman, G. T. Davis, and J. I. Lauritzen, *Treatise on Solid State Chemistry Vol.3*, Ed. N. B. Hannay, Plenum Press, New York, 1976.
6. J. D. Hoffman and R. L. Miller, submitted for publication.
7. A. J. Lovinger, D. D. Davis, and F. J. Padden, *Polymer*, **26**, 1595 (1985).
8. Y. Deslandes, F. N. Sabir, and J. Roovers, *Polymer*, **32**, 1267 (1991).
9. J. Boon, G. Challa, and D. W. van Krevelen, *J. Polym. Sci. A-2*, **6**, 1791 (1968).
10. Z. Pelzbauer and A. Galeski, *J. Polym. Sci. C*, **38**, 23 (1972).
11. Y. Mohajer, G. L. Wilkes, and B. Orler, *Polym. Eng. Sci.*, **24**, 319 (1984).

12. Y. P. Khanna and A. C. Reimschuessel, *J. Appl. Polym. Sci.*, 35, 2259 (1988).
13. Y. P. Khanna, A. C. Reimschuessel, A. Banerjee, and C. Altman, *Polym. Eng. and Sci.*, 28, 1600 (1988).
14. Y. P. Khanna, R. Kumar, and A. C. Reimschuessel, *Polym. Eng. and Sci.*, 28, 1607 (1988).
15. Y. P. Khanna, R. Kumar, and A. C. Reimschuessel, *Polym. Eng. and Sci.*, 28, 1612 (1988).
16. A. M. Chatterjee, F. P. Price, and S. Newman, *J. Polym. Sci. Polym. Phys. Ed.*, 13, 2369 (1975).
17. A. M. Chatterjee, F. P. Price, and S. Newman, *J. Polym. Sci. Polym. Phys. Ed.*, 13, 2385 (1975).
18. A. M. Chatterjee, F. P. Price, and S. Newman, *J. Polym. Sci. Polym. Phys. Ed.*, 13, 2391 (1975).
19. R. J. Samuels, *J. Polym. Sci. A-2*, 9, 2165 (1971).
20. H. Marand and D. Iler, personal communication.

## Chapter - 4

### **Influence of Melt Stability on the Crystallization Behavior of Bis(4-aminophenoxy)benzene-Oxydiphthalic Anhydride Based Polyimides**

#### **4.1 Abstract**

Novel high performance semicrystalline polyimides based on controlled molecular weight phthalic anhydride (PA) endcapped 1,4-bis(4-aminophenoxy)benzene (TPEQ diamine) and oxydiphthalic dianhydride (ODPA) were synthesized which exhibited excellent thermal stability in nitrogen and air atmospheres as determined by thermogravimetric analysis (TGA). The glass transition temperatures ( $T_g$ ) for these polymers ranged from 225 °C for the 10,000  $M_n$  polymer, to 238 °C for the 30,000  $M_n$  material, and the observed melting temperatures for all the polymers was ca. 420 °C. The crystallization behavior of these polymers showed a strong molecular weight dependence, as illustrated by the observation that the 10K and 12.5K polymers crystallized with relative ease, whereas the 15K, 20K and 30K showed little or no ability to undergo thermal recrystallization. The thermal stability of these polymers above  $T_m$  was investigated by studying the effect of time and temperature in the melt on the cold-crystallization and melting behavior of these polymers. Increased time and temperature in the melt resulted in lower crystallinity, due to some melt state degradation, such as crosslinking and branching,

as evidenced by an increase in melt viscosity, which was more prominent for the higher molecular weight polymers.

## 4.2 Introduction

Polyimides are an important class of high performance polymers that are finding increasing use in high temperature applications as adhesives, films, composite matrix materials, and other electrical and electronic applications. The aromatic rings in the backbone of these polymers impart high stiffness, often resulting in high glass transition and melting temperatures. The excellent thermal stability, chemical and radiation resistance of these polymers is generally coupled with good mechanical, electrical and adhesive properties. These properties have made polyimides excellent candidates for study in various laboratories<sup>1-9</sup>. Many of the polyimide polymers in use are amorphous in nature, with high glass transition temperatures in the range of 200 °C - 400 °C or higher, but suffer from the disadvantage of displaying relatively poor solvent resistance. Semicrystalline polyimides, however, display increased solvent resistance, enhanced modulus above  $T_g$ , and improved thermal and radiation stability<sup>10</sup>.

Polyimides for structural applications often require high temperatures for melt processing. The semicrystalline polyimides are normally insoluble in most common organic solvents, and typically display melting temperatures greater than ca. 400 °C. At these very high temperatures, organic based systems may rapidly degrade during processing. Approaches to solve these problems have focused on reducing the stiffness of

the backbone by introducing flexible linkages such as ether and ketone groups, and introducing meta linkages. However, increasing the flexibility, often reduces the transition temperatures thereby decreasing the upper use temperature. Other factors being constant, increasing the flexibility may also increase the rate of crystallization from the melt upon cooling.

Since thermal stability is of prime concern during processing, it is important to study the thermal stability in the melt and its subsequent effect on the crystallization behavior of these high temperature polyimides. Thermogravimetric analysis (TGA) is the most widely used technique to determine the thermal stability of polymers. This technique can provide the weight loss in a sample as a function of temperature, which is an indicator of the degradation occurring in the sample at those temperatures. However, only the weight loss, leading to volatiles is detected, and the method neglects other degradative mechanisms such as cross-linking or branching, which could occur at high temperatures with little accompanying weight loss<sup>11</sup>. Any form of degradation - chain scission or cross-linking critically affects the crystallizability of the polymer. Often the crystallizability itself, i.e. the crystallization and melting behavior can be used as an indirect monitor of the thermal stability of the material.

Thermal history can also influence the crystallization behavior by influencing the nucleation density during subsequent crystallization<sup>12-15</sup>. Thus, holding a semicrystalline polymer at temperatures just above its experimentally measured melting temperature does not necessarily result in complete melting and can result in regions of localized order.

These regions may then act as nuclei for crystallization when the polymer is subsequently cooled. Higher temperatures and longer times in the melt can result in the true “melting” or disordering of these regions of localized order. This, in turn can result in a reduction in the nucleation density and hence a decrease in the rate of crystallization.

Though the approach of studying the thermal stability of a polymer by monitoring the crystallization behavior is not new in itself<sup>16,17</sup>, a systematic study of the crystallization behavior as a function of melt conditions presents a more realistic picture of the thermal stability as compared to a simple TGA study, and has rarely been applied to polyimides.

The synthesis and crystallization studies of a novel high melting semicrystalline polyimide based on 1,4-bis(4-aminophenoxy) benzene (TPEQ) and oxydiphthalic anhydride (ODPA) are reported here. The thermal stability, and the crystallization and melting behavior have been investigated as a function of molecular weight. In particular, the effect of time and temperature in the melt on the thermal stability as illustrated by the crystallization behavior has been systematically studied.

## **4.3 Experimental**

### *4.3.1 Materials*

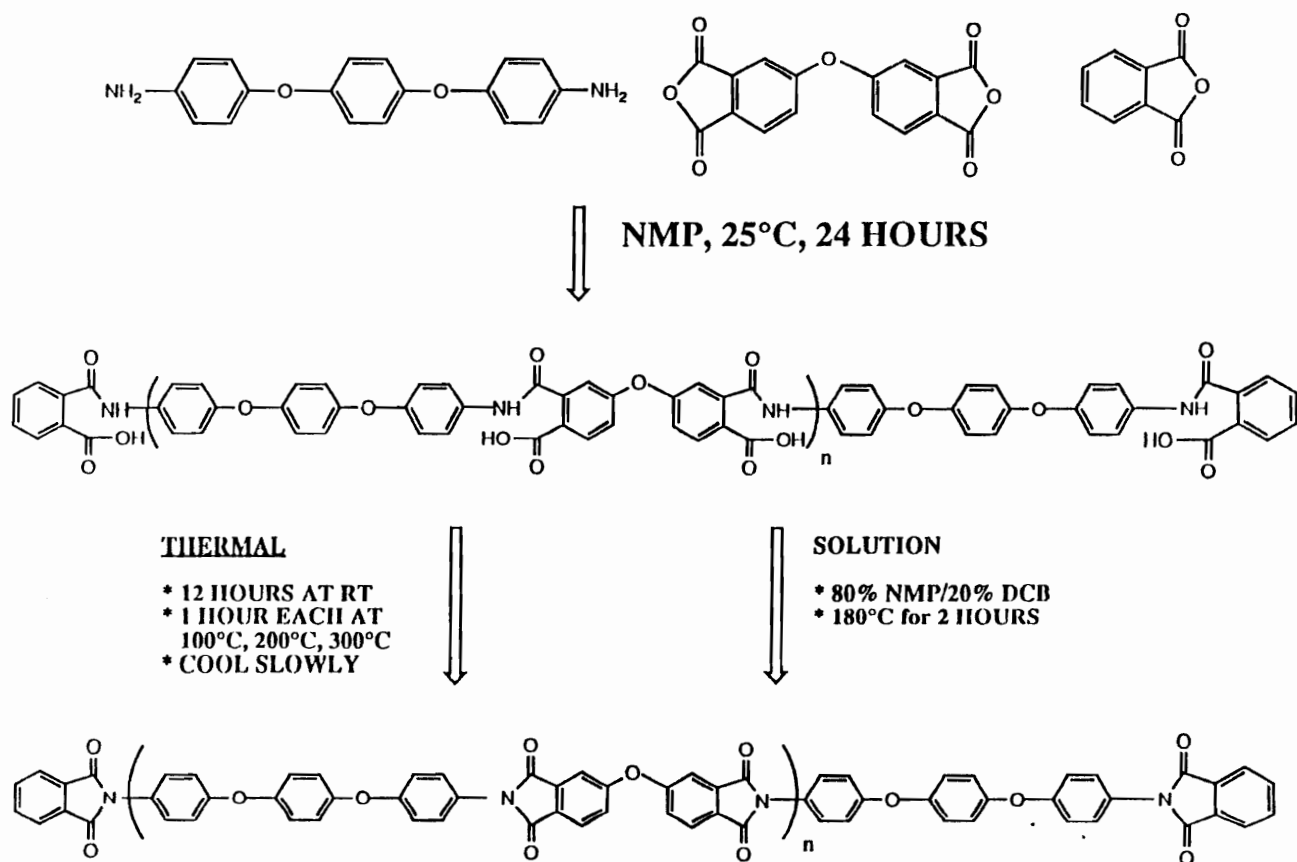
1,4-bis(4-aminophenoxy) benzene (or triphenylether hydroquinone diamine, referred to as TPEQ) was graciously supplied by Ken-Seika and was recrystallized from toluene before use. Oxydiphthalic anhydride (ODPA) was supplied by the Occidental Chemical Corporation and was dried at 120 °C prior to use. Phthalic anhydride (PA) was

obtained from Aldrich and sublimed prior to use. N-methylpyrrolidinone (NMP) and 1,2-dichlorobenzene (DCB) were obtained from Fisher and vacuum distilled after drying over  $P_2O_5$  before use.

#### 4.3.2 Polymer Synthesis

A series of polyimides with nonreactive phthalimide end-groups were synthesized consisting of number average molecular weights ranging from 10,000 to 30,000 gm/mol. As an example, the general procedure for making the 30,000 gm/mol polyimide is given below. The monomer concentrations were calculated utilizing the Carothers equation. A three-neck round bottom flask equipped with a mechanical stirrer, nitrogen inlet, and drying tube was utilized as the reaction vessel. To this apparatus, 2.9234 gm (100 mmol) TPEQ was added and a few ml of NMP were added to dissolve the diamine. To this solution, 0.0560 gm (3.8 mmol) of the endcapping agent phthalic anhydride (PA) was added and followed by a few ml of NMP. Following this, 3.0442 gm (98.1 mmol) of ODPA was added to the solution. Sufficient NMP was added to achieve a 10% solids concentration (ca. 53 ml total). This solution was allowed to stir under a nitrogen atmosphere for 24 hours, to afford a homogeneous poly(amic acid) solution as shown in **Scheme I**<sup>18</sup>.

The poly(amic acid) was converted to the polyimide, also shown in **Scheme I**, using two different methods. A stepwise thermal imidization procedure was utilized<sup>19</sup>, which has also been used by others<sup>20,21</sup>. Thermal imidization of the amic acid precursor



Scheme I

was achieved by first casting the poly(amic acid) solution onto pyrex glass plates. These plates were then placed in a dry box under dry air flow until smooth non-tacky films were obtained. The plates were then placed in a vacuum oven and the temperature slowly raised to 100 °C, and held for 1 hour. The temperature was then quickly raised to 200 °C, and held for 1 hour. Finally the temperature was raised to 300 °C and held for 1 hour to minimize or eliminate residual poly (amic acid). The plates were allowed to cool down to about 200 °C before being removed from the oven.

Solution imidization techniques were also utilized in order to cyclodehydrate the poly(amic acid) precursor. In this case, the drying tube used in the apparatus described above was replaced with a reverse Dean Stark trap. An azeotroping liquid, *o*-dichlorobenzene (DCB) was added to solution so as to achieve an 80/20 ratio of NMP to DCB, and stirred at about 175 °C. After about 90 minutes, a tannish off-white powder first precipitated from the solution. After 2 hours the resulting slurry was added to a beaker of water with stirring. Next, the powder was filtered, washed with water and dried in a vacuum oven at ca. 235 °C overnight, and subsequently at 300 °C for an hour to ensure complete imidization.

A series of samples were synthesized with number average molecular weights 10,000 (10K), 12,500 (12.5K), 15,000 (15K), 20,000 (20K), and 30,000 (30K) gm/mol by controlling monomer and endcapper concentration. The 10K samples were prepared with different degrees of imidization in order to investigate the influence of imidization on the thermal behavior. Specifically, one sample was heated to 100 °C for 1 hour and then

cooled, and is designated in this paper as 10K (100 °C). The second sample was heated to 100 °C and held for 1 hour, then heated to 200 °C, held for 1 hour then cooled, and is designated 10K (200 °C). The third sample was taken through the complete imidization cycle as described above and is designated 10K (300 °C).

#### 4.3.3 *Characterization*

Thermogravimetric (TGA) studies utilized a Seiko TG/DTA on the film samples. All experiments were carried out in either a nitrogen or air atmosphere at heating rates of 10 °C/min. The temperature calibration was based on the melting temperatures of indium and zinc. The values reported in this paper are temperatures for 5% weight loss.

The DSC measurements were conducted with a Seiko DSC 220C, on 8-9 mg of sample under a nitrogen purge, at heating rates of 10 °C/min unless otherwise specified. Temperature and heat flow were calibrated using indium, tin and zinc standards. The DSC curves shown in this paper have been normalized to 1 mg sample mass. The first heat data referred to in this paper are the DSC traces of the as-received samples, which were heated to 450 °C. At the end of the first heat, the samples were quenched to room temperature at cooling rates of ca. 75 °C/min. The subsequent reheat has been designated as the second heat. The specific details of the second heat will be discussed later.

The melt time/temperature studies were carried out on a Perkin Elmer DSC-7 using 6-7 mg of sample under a nitrogen purge. The temperature and heat flow were calibrated using indium and zinc standards. The heating and cooling schedules used in this

study were as follows. The samples were heated at 20 °C/min to the various melt temperatures and held for different times. The samples were then quenched to 100 °C at a rate of about 200 °C/min, following which they were reheated at a rate of 10 °C/min. As is well known, the crystallization and melting behavior of a semicrystalline polymer can be influenced by changes in nucleation density in the material, and/or the thermal stability of the material. Five parameters were chosen which were representative of the crystallization and melting behavior, and their dependence on the melt time and temperature were followed. The temperature of exothermic deviation from the baseline was taken to be the onset crystallization temperature, and the peak of the crystallization exotherm was taken to be the maximum crystallization temperature. The area under the crystallization exotherm was denoted as the heat of crystallization. The peak of the melting endotherm was taken as the melting temperature, and the area under the endotherm was denoted as the heat of melting.

Wide angle x-ray scattering was carried out on a Nicolet diffractometer equipped with a STOE Bragg-Brentano type goniometer.  $\text{CuK}\alpha$  radiation of wavelength 1.54 Å was used after monochromatization through a graphite monochromator. Data were collected at 0.05° increments at angles between 5-40°.

Rheological experiments were carried out on a Bohlin VOR Rheometer with a 12 mm diameter parallel plate fixture. Temperature control was accomplished with a Bohlin HTC using nitrogen as the heating gas. A sample of the 12.5K polyimide approximately 1

mm thick was prepared at room temperature by pressing together several imidized films which were made using the procedure described earlier. The HTC oven was preheated to 450 °C. The sample was then placed between the plates and the oven door was quickly closed. Approximately two minutes elapsed from the time the sample was placed in the rheometer to when the oven temperature again was 450 °C. The viscosity measurements began at this point. The temperature was controlled at 450±1 °C. The Fluids torque measuring head was used with a 96 g-cm torque bar. Testing was done using the oscillation mode with a frequency of 0.1 Hz and a strain of 2%.

#### 4.4 Results And Discussion

TGA studies were conducted in air and nitrogen environments. Figure 4.1 shows the TGA scans in a nitrogen environment for the 10K polymers with different imidization histories. The full thermal cycle described in the experimental section is usually required to maximize the imidization of the poly(amic acid), as shown among others by Brandom and Wilkes<sup>21</sup>. The 10K sample which was imidized at 100 °C showed a weight loss of ca. 10% in the temperature range 150 °C - 325 °C. This can be explained as being due to loss of solvent and water during completion of the imidization process. The onset of the mass loss is shifted to higher temperatures for the 10K sample imidized at 200 °C, with a 5 % weight loss observed in the temperature range 200 °C - 325 °C. This can also be explained by loss of solvent, accompanied perhaps by some additional imidization, leading to loss of water. The 10K sample which was imidized at 300 °C did not show any weight

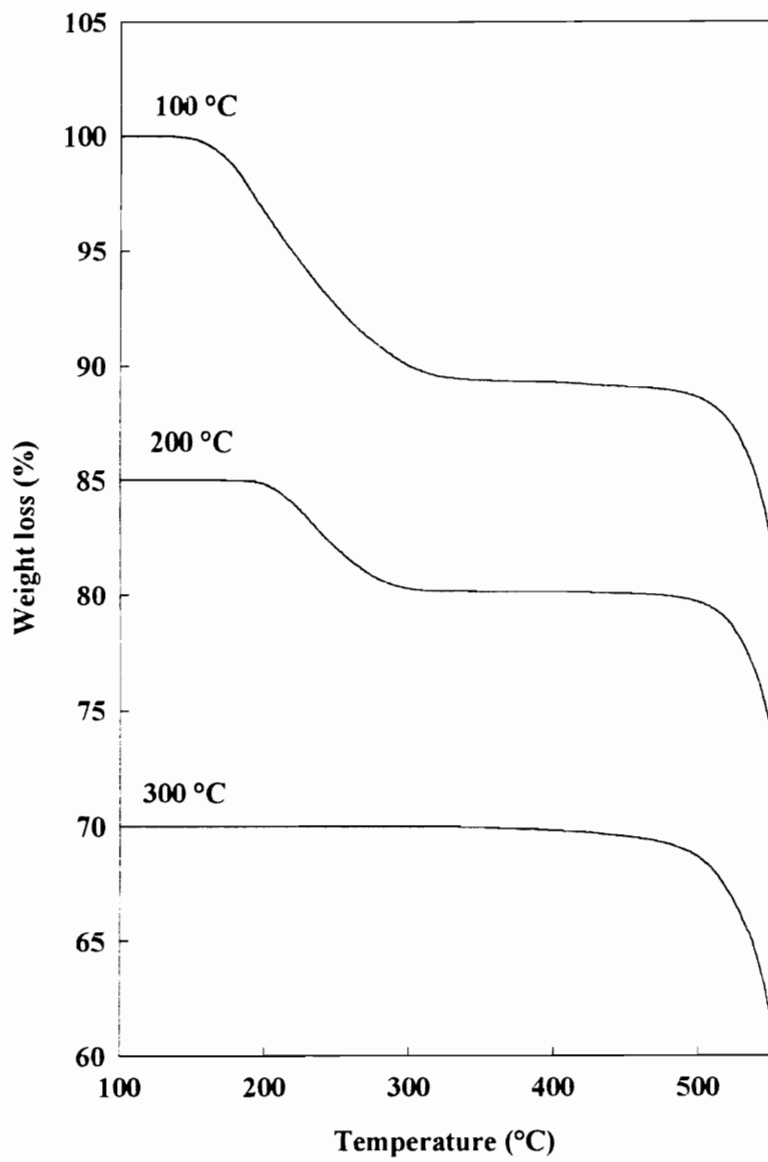


**Figure 4.1** TGA scans for 10K samples imidized at different conditions.

loss at lower temperatures, implying that the imidization cycle consisting of the full temperature treatment resulted in very high if not complete conversion of the poly(amic acid) to the corresponding polyimide. There was no noticeable difference in the results when air was used as the purge gas as compared to nitrogen, implying that the imidization process is not significantly affected by the nature of the environment. This is of particular importance in the case where the polymer is processed first in the poly(amic acid) form, and then thermally converted to the polyimide.

Figure 4.2 shows the 5% weight loss temperatures of the various samples in air and nitrogen environments. The temperatures for 5% weight loss reported here for the 10K (100 °C) and 10K (200 °C) samples are the 5% weight loss observed after the initial weight loss due to solvent loss and imidization. The results indicate that all samples had excellent thermal stability in air as well as nitrogen with all 5 % weight loss temperatures above 500 °C. The temperatures for 5% weight loss were moderately higher in nitrogen environments as compared to air (ca. 25°C), which is consistent with earlier reports on the thermal stability of polyimides<sup>11</sup>.

The TGA results indicated no molecular weight dependence for the 5% weight loss temperatures of these materials. The lack of any molecular weight dependence of the thermal stability indirectly indicates that the endcapping was efficient and that any primary degradation mechanism does not likely involve the end-group. It has been shown that amine end-groups are detrimental to polymer stability, and that anhydride end-groups are also susceptible to degradation at high temperatures<sup>11</sup>. If there were no endcapping on

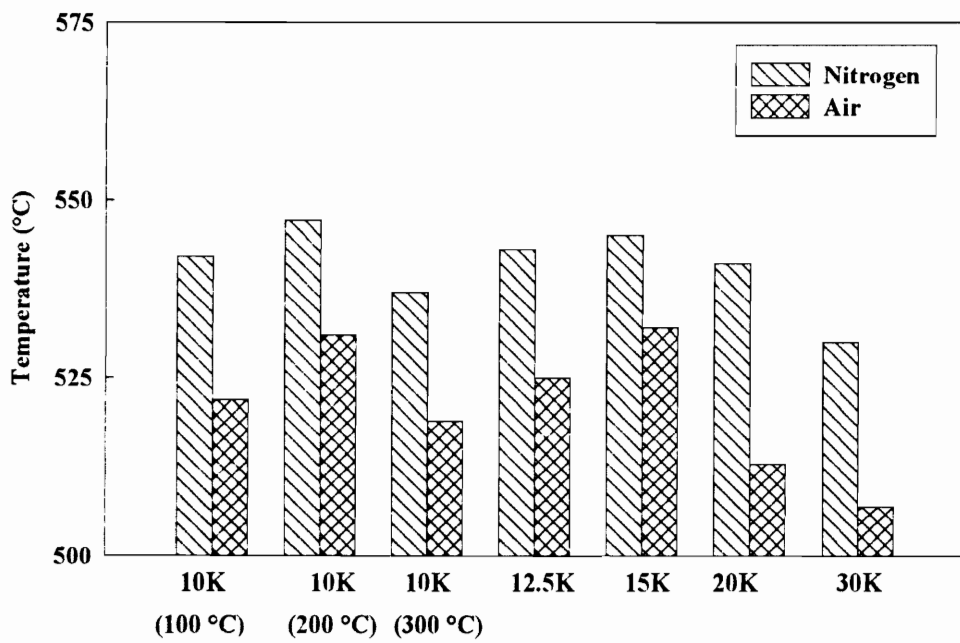


**Figure 4.2** Temperatures for 5% weight loss by TGA.

these polymers, one would expect the low molecular weight polymers to display lower degradation temperatures than the higher molecular weight polymers, because of a greater number of reactive chain ends. The fact that no such dependence is observed indicates effective endcapping, and high thermal stability of the phthalimide end groups at elevated temperatures.

Figure 4.3 shows the DSC traces of the various as-received samples, designated here as the first heat. It can be seen in the figure that the partially imidized 10K (100 °C) sample shows some complex endothermic/exothermic transitions in the temperature range where weight loss was observed by TGA. The complex transitions in the DSC scan can be attributed to solvent loss, completion of imidization accompanied by water loss and crystallization of the polyimide<sup>21</sup>. The endothermic/exothermic transitions are followed by a weak exotherm at ca. 275 °C which can be attributed to crystallization, and is followed by a melting endotherm at 428 °C. The 10K (200 °C) sample shows a broad endotherm in the temperature range where weight loss was observed in the TGA, which could result from solvent loss and completion of imidization, and is followed by an exotherm. This exotherm could result from the crystallization of the polyimide molecules following the completion of the imidization process. A melting endotherm is finally observed at 428 °C. The 10K (300 °C) sample shows a small endotherm at ca. 280 °C, which could be the result of some premelting of crystals, and is followed by the melting endotherm. It is interesting to note that the melting temperatures and heat of melting of all the 10K samples is essentially the same *regardless of the prior imidization history*. If one

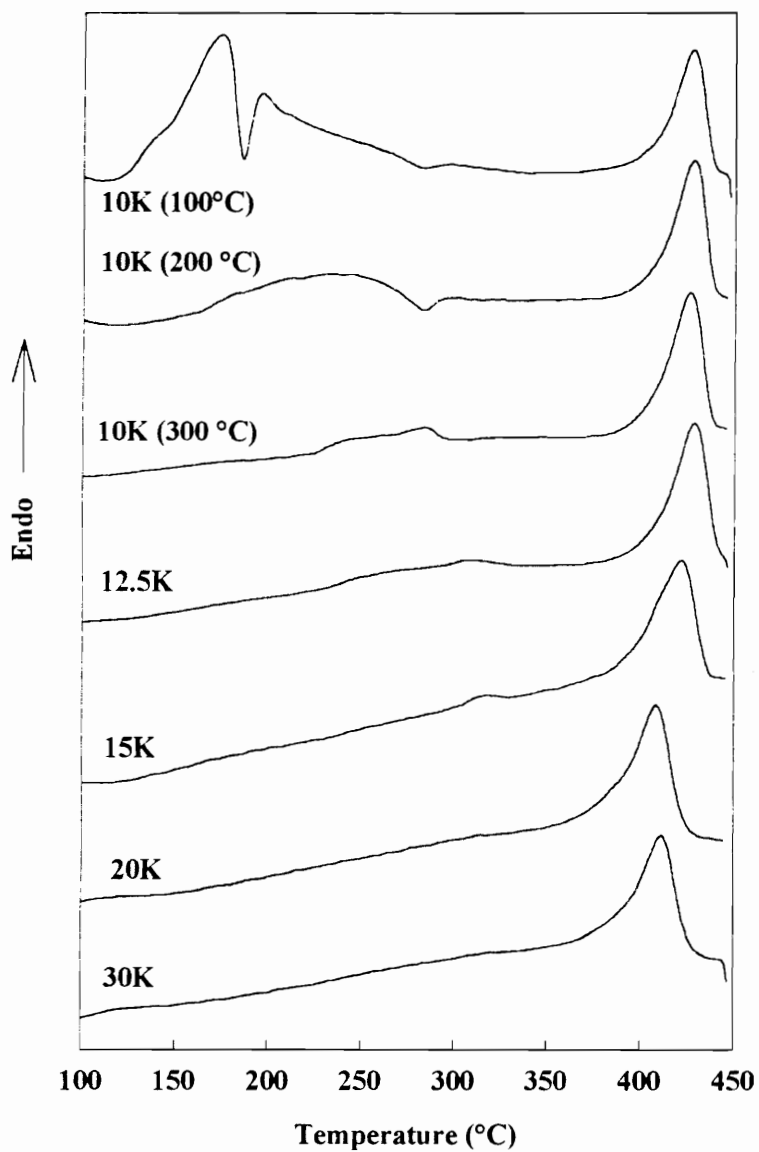


**Figure 4.3** First heat DSC scans for various molecular weights.

reasonably assumes that the 10K(100 °C) and 10K(200 °C) samples were incompletely imidized before the first heat DSC scan, then the degree of crystallinity would be lower for the 10K(100 °C) and 10K(200 °C), as compared to the completely imidized 10K(300 °C). During the DSC scan, imidization takes place, which increases the number of crystallizable chains. These chains crystallize quite rapidly during the DSC scan, likely due in part to the presence of residual solvent, and hence exhibit melting temperatures and heats of melting comparable to the fully thermally treated sample.

The 12.5K and 15K samples exhibit weak endotherms at ca. 315 °C which can be attributed to the melting of crystals formed at the last step of the imidization process carried out at 300 °C. This endotherm is similar to the “crystallization” or “annealing”, ( $T_c+15$ ) endotherm commonly reported for polymers which have been isothermally crystallized or annealed<sup>22</sup>. Somewhat surprisingly, the 20K and 30K polymers exhibit no distinct transitions, either endothermic or exothermic below the main melting endotherm.

From Figure 4.3 it is evident that the melting temperature and the heat of melting in the first thermal scan exhibit no molecular weight dependence. All the as-received polymers, irrespective of molecular weight had nearly comparable melting temperatures (ca. 420 °C) as well as heats of melting (ca. 30 J/gm) implying that the crystallization following imidization is equally effective for all the molecular weights. This behavior contrasts sharply with the extreme molecular weight dependence of these polymers observed during the second heat. Finally, the DSC traces in Figure 4.3 show that the glass transition cannot be resolved for any of the samples. This is because the as-received

samples probably possess a relatively high rigid content above the glass transition temperature (crystalline and rigid amorphous fraction), and therefore have relatively low mobile amorphous fractions, which results in only a small specific heat jump at the glass transition, that additionally may be broadened by the presence of the crystal phase, thereby not allowing adequate resolution by the DSC. At the end of the first heat, all the samples were quenched rapidly (ca. 75 °C/min) to room temperature, and reheated.

The second heat DSC scans of the above samples are shown in Figure 4.4. The 10K samples, exhibit glass transition temperatures at 225 °C, crystallization exotherms at 312 °C, followed by melting endotherms at 420 °C. The 12.5K sample exhibits a  $T_g$  at 226 °C, a crystallization exotherm at 313 °C, and a melting endotherm at 422 °C. The 15K sample exhibits a  $T_g$  at 231 °C, a very broad and indistinct crystallization exotherm, followed by a weak melting endotherm at 415 °C. The 20K sample exhibits a  $T_g$  at 236 °C, no crystallization exotherm and no melting endotherm, and the 30K sample exhibits a  $T_g$  at 238 °C, with no crystallization or melting transitions. *The strong molecular weight dependence of the various transition temperatures is very evident from Figure 4.4.* It should be noted that the  $T_g$  of this system increases from 225 °C for the 10K polymer, to 238 °C for the 30K system. This increase in the glass transition temperature with molecular weight is entirely consistent with theories of the glass transition. The strong molecular weight dependence of the crystallization and melting behavior during the second heat is quite evident in the DSC traces. The 10K and 12.5K polymers seem quite capable of crystallizing from the melt, however on going from the 12.5K to the 15K system, the

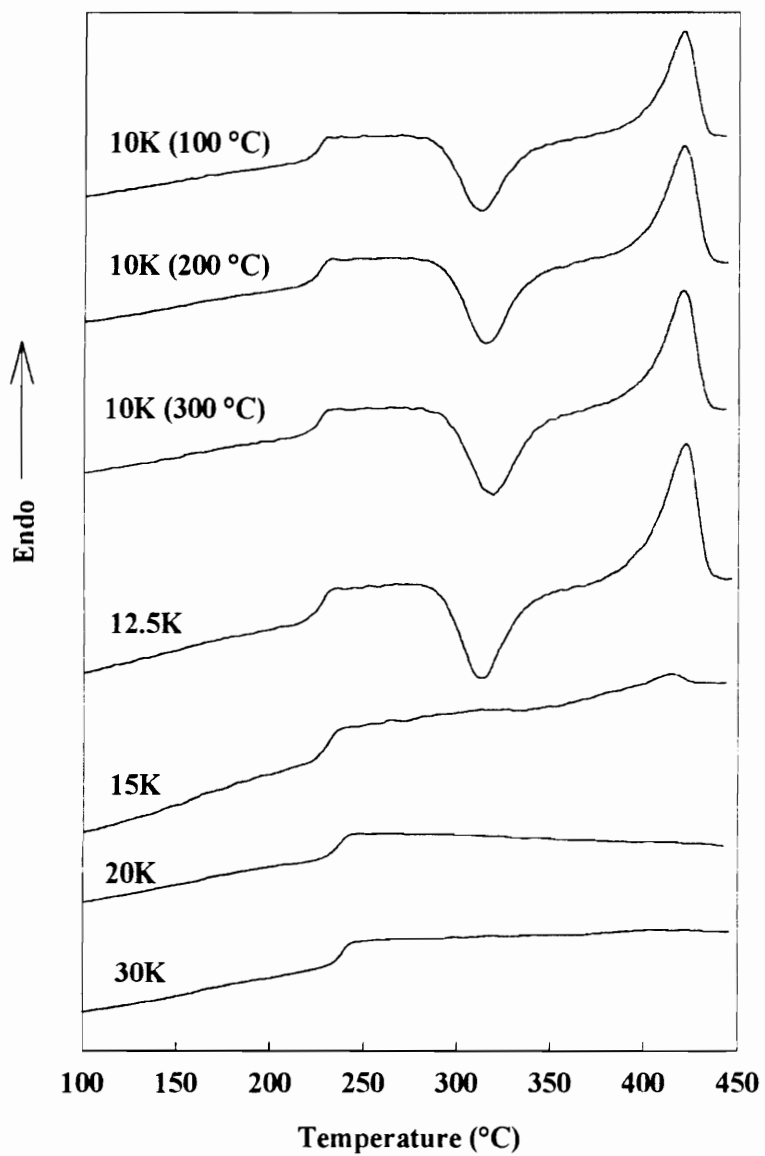


**Figure 4.4** Second heat DSC scans for various molecular weights.

ability to crystallize seems to be depressed considerably. The 20K and 30K show absolutely no tendency to crystallize during the DSC scan.

The results within Figure 4.4 can be rationalized as follows. The polyimides under study are relatively stiff chain high  $T_g$  polymers and thus have low mobility. At the end of the first heat, the low melt mobility does not permit the molecules to crystallize during the rapid quench. Hence all the samples are amorphous after the quench, and therefore, during the reheat exhibit prominent specific heat increases at the glass transition consistent with large amorphous fractions. The low molecular weight polymers, 10K and 12.5K have sufficient mobility above the glass transition temperature, allowing them to crystallize, which results in the crystallization exotherms observed for these polymers. The higher molecular weight polymers, i.e. 15K and higher, are more highly viscous, and do not have sufficient mobility to crystallize in the time frame allowed in the experiment, i.e. a heating rate of 10 °C/min. Therefore, no prominent crystallization exotherms and therefore no resulting melting endotherms are observed for these systems. A probable result of slow crystallization kinetics from the melt is that, even for the low molecular weight polymers, (10K and 12.5K), the heat of melting during the second heat is ca. 30% lower than that observed in the first heat. A point to be emphasized here is that the first heat was probably successful in destroying residual nuclei in all the samples. This is because the higher molecular weight samples have lower melt mobility, and tend to have a greater fraction of residual nuclei after a melt treatment than the lower molecular weight samples. These residual nuclei could then initiate crystallization during the second heat.

Such behavior is in fact not observed in this case implying that the first heat was effective in destroying the residual nuclei.

There are strong indications that the absence of crystallization exotherms and accompanying melting endotherms in the higher molecular weight systems is solely due to mobility reasons. This same behavior, however, could also result from some irreversible chemical change in these polymers, like cross-linking or branching, that subsequently prevent these materials from crystallizing. In order to investigate this point, further experiments were performed to try to regenerate crystallinity in the higher molecular weight samples.

Figure 4.5 shows the DSC traces for the as-received 15K polymer and the quenched samples with different heating schedules and thermal treatments. It was mentioned earlier that the low mobility of the polymers could cause slow crystallization kinetics, which resulted in insufficient time being allowed for the sample to crystallize in the time frame of the experiment. This implies that slower heating rates might result in higher crystallinity, since more time would be available in the crystallization window ( $T_m - T_g$ ). Indeed, this is shown in the DSC scans in Figure 4.5, where it is evident that slower heating rates do lead to larger crystallization exotherms and resulting melting endotherms. Isothermal crystallization of the sample at 320 °C, which is in the midrange of the crystallization window, results in a crystallization/annealing endotherm at ( $T_c + 15$  °C), followed by a prominent melting endotherm. The heat of melting after isothermal crystallization is substantially higher than those obtained after slow heating rates. This

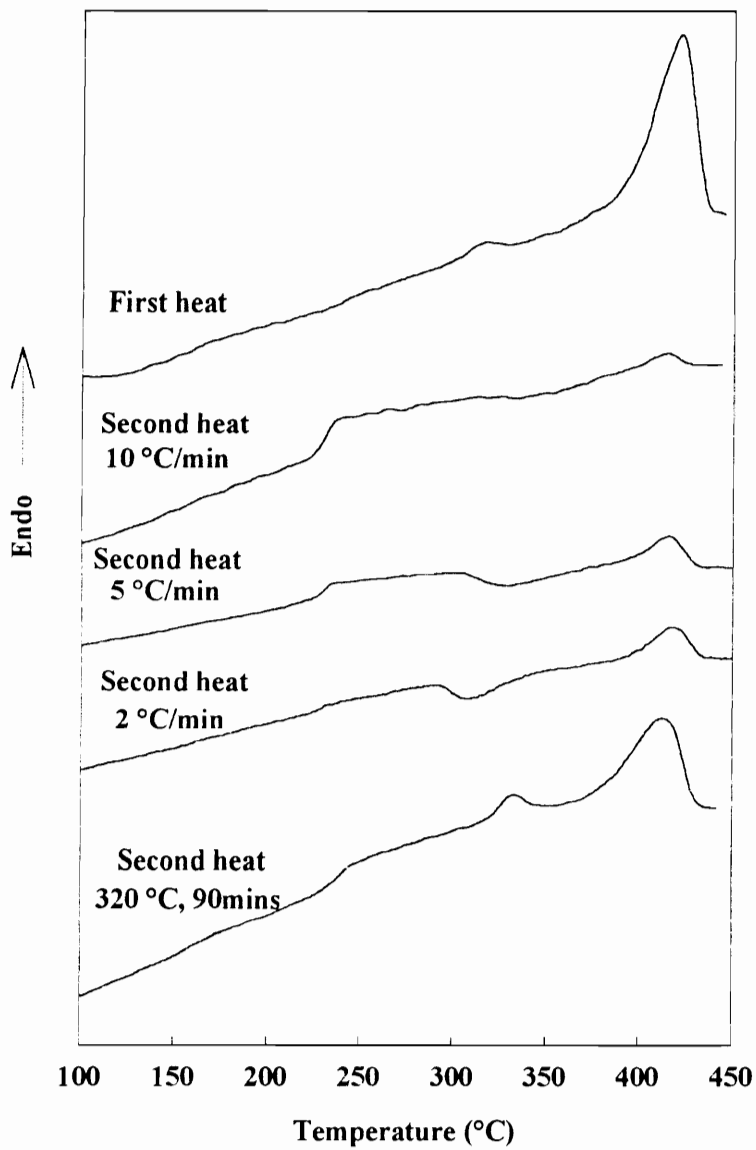


**Figure 4.5** DSC scans for 15K polyimide.

clearly shows that it is the low mobility of the polymer chains which causes sluggish crystallization, as opposed to any chemical changes in the melt. However, it is clearly evident from the figure, that both the melting temperature (412 °C) as well as the heat of crystallization (24 J/gm) of the isothermally crystallized sample is still lower than the corresponding values (422 °C, 39 J/gm) for the as-received sample.

For the 20K polymer, it was observed that slower heating rates and isothermal crystallization were not successful in regenerating crystallinity, which again could result from slow crystallization kinetics. Figure 4.6 shows the DSC thermograms for the 30K polymer, where it is obvious that slower heating rates were not successful in developing crystallinity. Since isothermal annealing also could not generate crystallinity in the 20K sample, such a treatment was not attempted for the higher molecular weight 30K sample. Since the experiments above indicate that the 20K and 30K polymers could not be thermally crystallized, solvent induced crystallization was attempted in order to try and regenerate crystallinity using the method of DiBenedetto et al.<sup>23</sup>. A sample of the 30K polymer which was subjected to a first heat as described earlier, and quenched, was placed in an NMP bath at 205 °C for 3 hours under a nitrogen atmosphere. As has been reported earlier for LaRC-CPI and NEW-TPI<sup>17,24</sup>, NMP does not dissolve these materials, but can plasticize it sufficiently to increase polymer mobility and hence facilitate crystallization. The samples were washed in water for 6 hours and dried overnight at room temperature in a vacuum oven, prior to the DSC scan. The sample weight increased as a result of the solvent treatment, as a result of residual NMP absorbed by the material. As can be seen

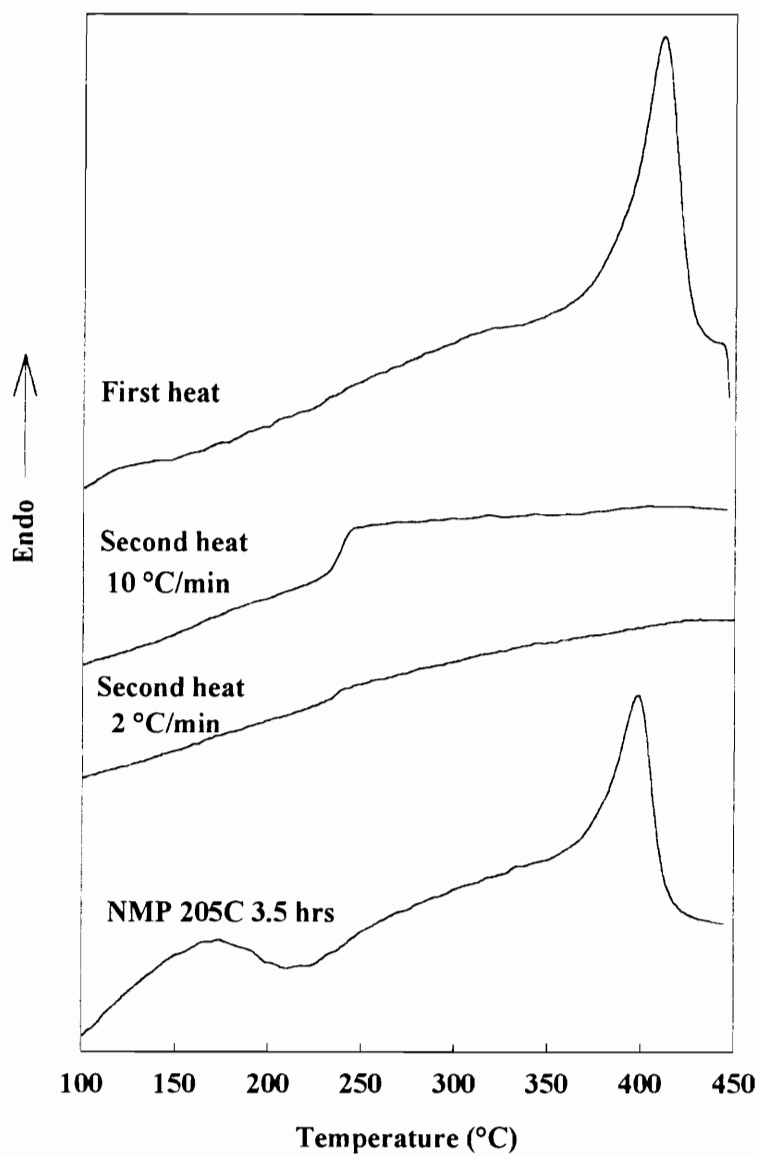


**Figure 4.6** DSC scans for 30K polyimide.

in Figure 4.6, the DSC scan of the sample shows a broad endotherm at lower temperatures corresponding possibly to the loss of NMP, followed by an exotherm that may correspond to crystallization, and then a prominent melting peak. This clearly demonstrates that the loss of crystallinity after the first heat is not completely irreversible, but only the result of slow crystallization kinetics.

Wide angle x-ray scattering patterns of the as-received and quenched samples of the 15K polyimide are provided in Figure 4.7. The amorphous sample was obtained by quenching an as-received sample after a first heat, as described earlier. It can be seen that the as-received sample exhibits a scattering pattern characteristic of a semicrystalline polymer, whereas the quenched sample displays a broad halo characteristic of an amorphous system. From the scattering patterns, a rough estimate of the degree of crystallinity can be made by scaling down the amorphous pattern to “fit” under the pattern of the semicrystalline system. An estimate made this way yielded a number of ca. 40% degree of crystallinity.

As mentioned earlier, the crystallization and melting behavior of polymers can give an indication of the thermal stability of the material. Based on the results discussed above, only the 10K and 12.5K samples were chosen for a detailed study of thermal stability. It should be emphasized here that in spite of the low molecular weight, the 10K and 12.5K polymers were available in the form of creasable films, hence suggesting suitability for high performance applications. A comparison of the DSC traces of the 10K and 12.5K polymers cooled from the melt and heated from the amorphous glassy phase shows that

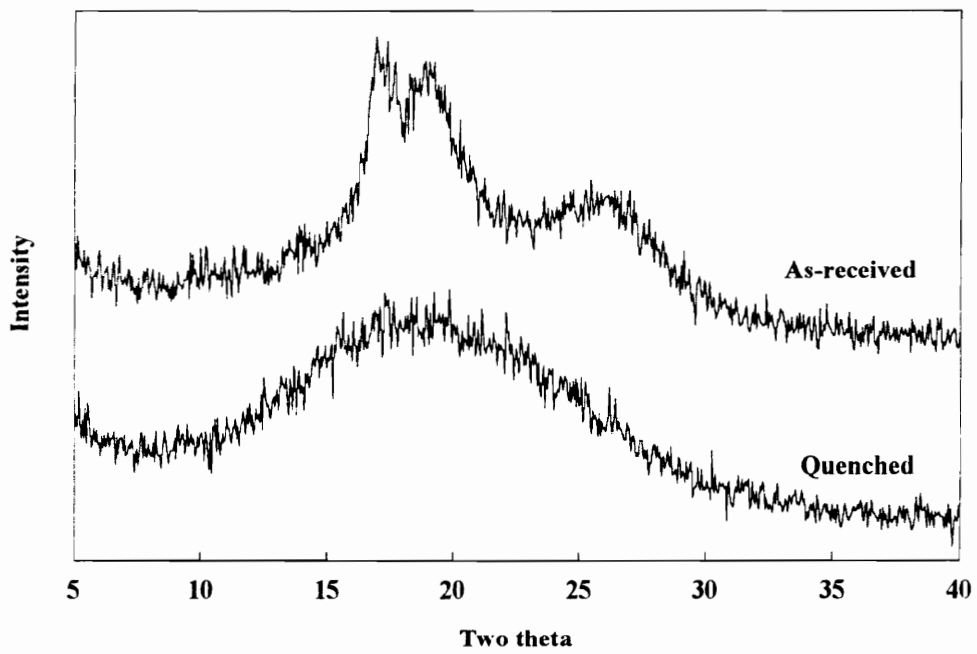


**Figure 4.7** Wide angle x-ray scattering patterns for as-received and quenched samples for 15K polyimide.

the polymers do not exhibit prominent crystallization exotherms on cooling from the melt, but show large crystallization exotherms on being heated from the glass. The rate of bulk crystallization depends on the combination of nucleation density and crystal growth rate. The crystal growth rate is a function only of undercooling, whereas at a specific crystallization temperature, the nucleation density of a sample crystallized from the glass is typically substantially higher than when crystallized from the melt<sup>25</sup>. The crystallization exotherms of the polyimide samples are thus more prominent when crystallized from the glass. It is for this reason, that for the melt time/temperature experiments, the samples were first quenched, and the crystallization and melting parameters on reheat were investigated. The samples of the 10K and 12.5K polymers were subjected to various thermal histories as discussed in the experimental section. The various parameters studied have been plotted as a function of melt time and melt temperature in order to gain information on the melt thermal stability of these polyimides.

Figure 4.8 shows the maximum crystallization temperature of the 10K polymer as a function of melt temperature for various melt times. It can be seen that as the melt temperature increases, the maximum crystallization temperature shifts to higher temperatures and it may be noted that this effect is more prominent for longer times in the melt. The shift of the maximum crystallization temperature indicates a slower rate of bulk crystallization. It can also be seen from the figure that as the time in the melt increases, the maximum crystallization temperature increases, this effect being greater for higher melt temperatures. The shift of the maximum crystallization temperature could arise due to a

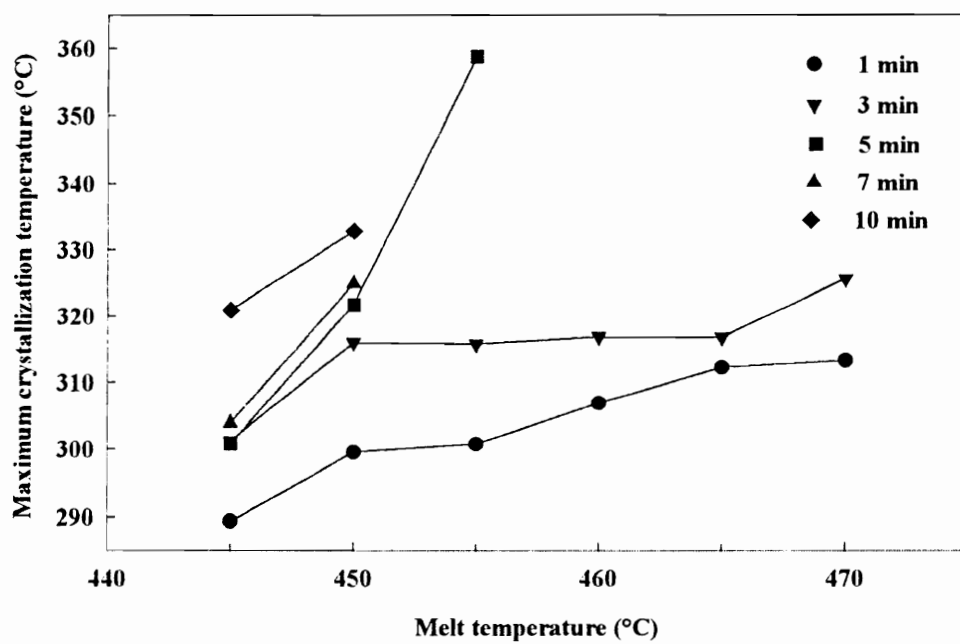


**Figure 4.8** Effect of temperature and time in the melt on the maximum crystallization temperature of 10K polymer.

reduction in the bulk nucleation density and/or as a result of chemical changes in the material, like cross-linking or branching, which retards the crystallization process.

It is obvious from Figure 4.8 that for low melt times, i.e. 1 and 3 min, crystallization occurs regardless of the previous melt temperature. However, when the time in the melt increases, e.g. 7 and 10 min, crystallization does not occur during the second reheat when the previous melt temperature is greater than 450 °C. In effect, a melt temperature of 450 °C and higher combined with 7 or more minutes in the melt prevents crystallization altogether during the subsequent reheat. This indicates that the cause of this suppression in crystallization may well be due to some irreversible chemical change occurring in the material, rather than a reduction in the nucleation effect.

The variation of the second heat melting temperature with varying melt temperatures and times is shown in Figure 4.9. The melting temperature clearly decreases with increasing temperatures in the melt, particularly at higher melt times. This is certainly due to the fact that the chemical changes occurring in the material cause the formation of imperfect crystals, thus resulting in lower melting temperatures. This strongly suggests that any changes in nucleation density are not solely responsible for altering the crystallization behavior of the material, since a decrease in the nucleation density would not cause such a significant decrease in the melting temperature. The figure also shows that the melting temperature is a strong function of the time in the melt and large decreases in the melting temperature are observed with increasing time in the melt. Also apparent from the figure is the fact that for longer melt times, no melting can be observed

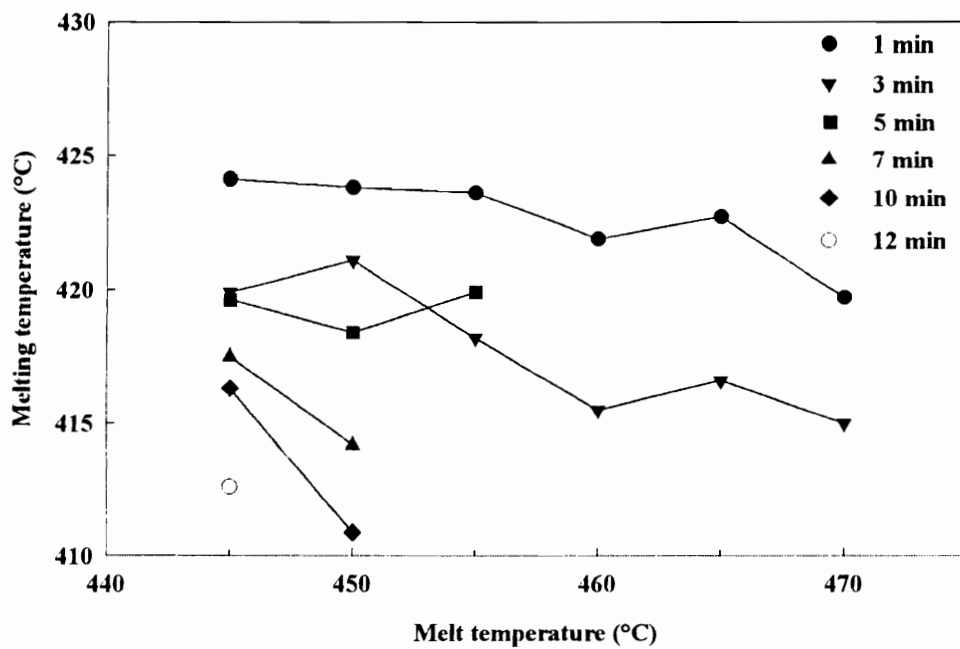


**Figure 4.9** Effect of temperature and time in the melt on the melting temperature of 10K polymer.

when larger melt temperatures were used, due to the fact that no crystallization occurred in the material.

The temperature for the onset of crystallization was also studied as a function of melt time and temperature. The results show that the behavior of the onset crystallization temperature is qualitatively the same as that of the maximum crystallization temperature discussed above.

The area under the crystallization exotherm (heat of crystallization) for the 10K polymer is shown in Figure 4.10 as a function of time and temperature in the melt. Each grid point on the 3-D plot represents an experimental data point. This 3-D plot helps in visualizing the combined effect of melt time and temperature on the heat of crystallization, and also helps in optimizing the melt conditions for potential processing of this material. From the plot, it can be seen that as time in the melt or melt temperature increase, the heat of crystallization decreases, with the drop-off being more sudden under more harsh melt conditions. For example, when time in the melt is 1 minute, the heat of crystallization shows a small decrease as the melt temperature increases. However, when the time in the melt is 5 minutes, the decrease in the heat of crystallization with increasing melt temperature is more pronounced.

The variation of the heat of melting of the 10K polymer as a function of melt time and melt temperature indicates the same general behavior as shown in the previous figure. Specifically, the higher melt times and melt temperatures hinder the ability of the material to recrystallize. All the above results indicate that the decrease in nucleation density is not

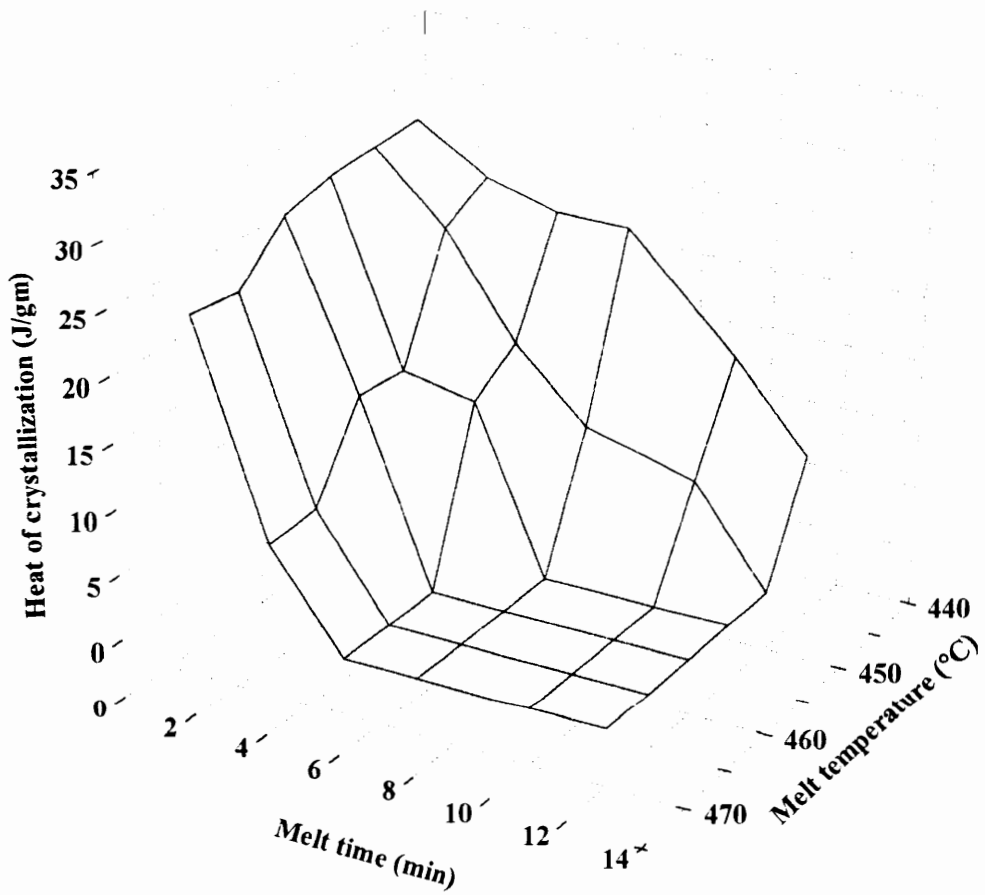


**Figure 4.10** Effect of temperature and time in the melt on the heat of crystallization of 10K polymer.

a likely cause for the reduction in the heats of crystallization and melting and the slower crystallization kinetics. Rather, chemical changes like cross-linking or branching is the cause of this effect.

Figures 4.11 & 4.12 show the results of similar studies carried out on the 12.5K polymer. The results for this higher molecular weight are qualitatively similar to the 10K polymer, although it is to be noted that that the various parameters now show even a much greater dependency on the melt conditions. For example, Figure 4.11 shows the maximum crystallization temperature of the 12.5K polymer plotted as a function of melt time and temperature. It can be seen that for the case when time in the melt is 1 min, on increasing the melt temperature from 445 °C to 465 °C, the maximum crystallization temperature increases by ca. 50 °C. However, for the case of the 10K polymer, (Figure 4.8), under similar conditions, the maximum crystallization temperature changes only by ca. 20 °C. From a comparison of Figures 4.8 and 4.11, one can also see that when the temperature of the melt is 450 °C, crystallization does not occur when time in the melt is greater than 5 min for the 12.5K polymer, whereas for the 10K polymer, crystallization occurs even for times in the melt as high as 10 min. This implies that the ability to crystallize is lost under less harsh conditions for the 12.5K polymer, as compared to the 10K polymer. The same conclusion can be drawn on comparing Figures 4.10 and 4.12. This indicates that the melt stability has a molecular weight dependence. An important point to be noted here is that a simple TGA study revealed only that the 5% weight loss temperatures were independent of molecular weight.

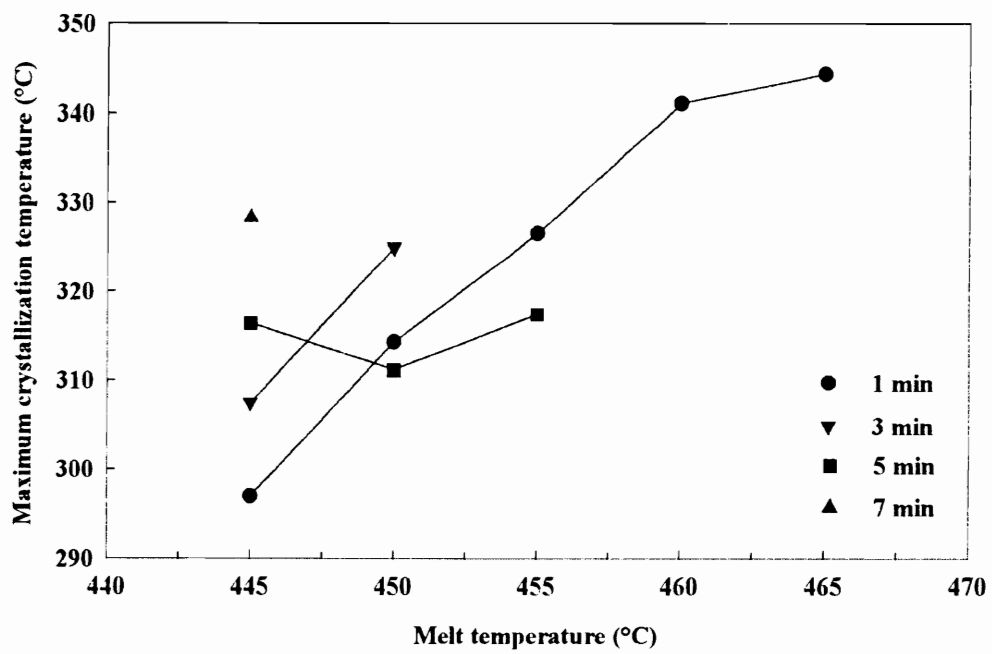


**Figure 4.11** Effect of temperature and time in the melt on the maximum crystallization temperature of 12.5K polymer.

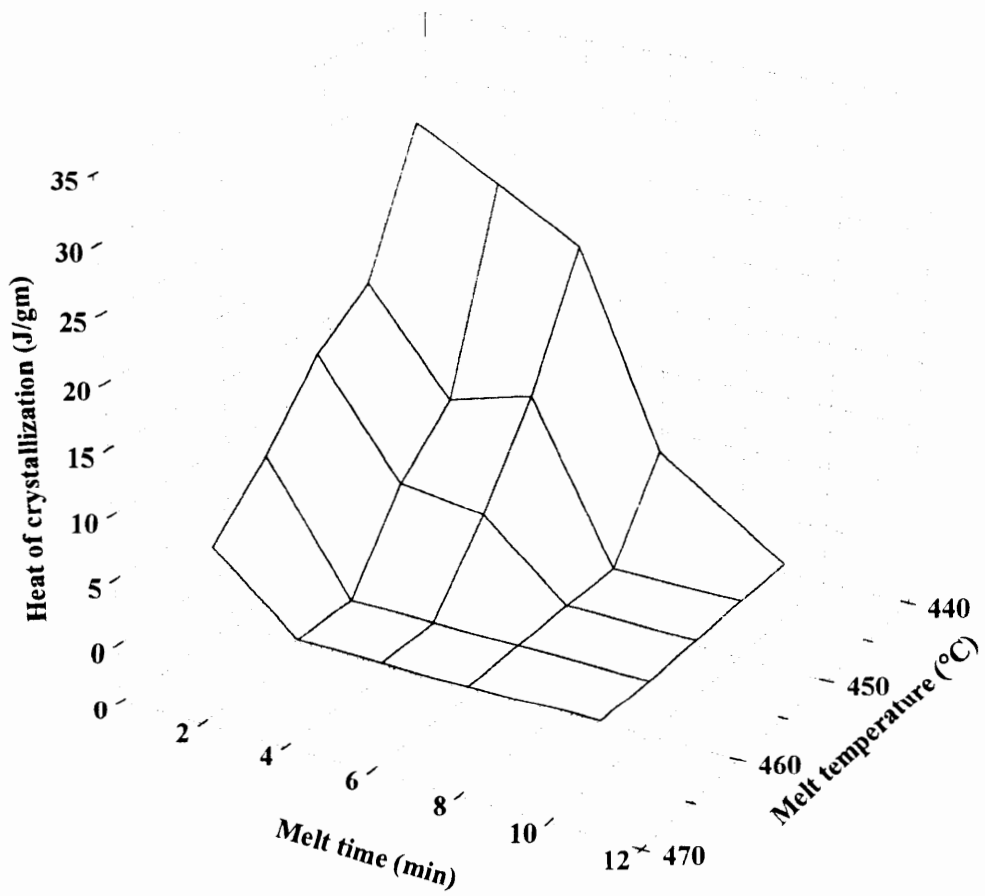


**Figure 4.12** Effect of temperature and time in the melt on the heat of crystallization of 12.5K polymer.

The molecular weight dependence observed here as well as the suppression of crystallizability implies some form of melt chemical changes like cross-linking or branching. If more severe melt conditions only caused some chain scission, an increase in crystallizability would have been expected corresponding to any decrease in molecular weight. The dependence of the crystallization and melting parameters on melt conditions can successfully be explained if the concept of chain branching or cross-linking were to be invoked.

To address the above issues, it is obvious that chain scission would lead to smaller chains, and hence a lower melt viscosity, whereas cross-linking or branching would lead to an increase in the melt viscosity. Figure 4.13 shows the complex viscosity of the 12.5K polymer as a function of time at 450 °C. From the figure it can be seen that the viscosity increased from ca. 30 KPas to ca. 300 KPas, i.e. by an order of magnitude over 35 minutes. This increase in viscosity provides an indirect measure of inter-chain branching and/or cross-linking. Indeed, if only chain scission were to occur, one would notice a decrease in viscosity with time. An important point to be noted is that, for times greater than 5 minutes at 450 °C, the viscosity starts to increase appreciably. This parallels exactly the results of the DSC experiments which show that for a melt temperature of 450 °C, the crystallizability is suppressed for times greater than 5 minutes.

Further evidence to support chemical changes was obtained by comparing the DSC scans of the 12.5K polymer, subjected to two extreme melt conditions, as shown in Figure 4.14. A comparison of the glass transition temperatures show that the  $T_g$  of the sample

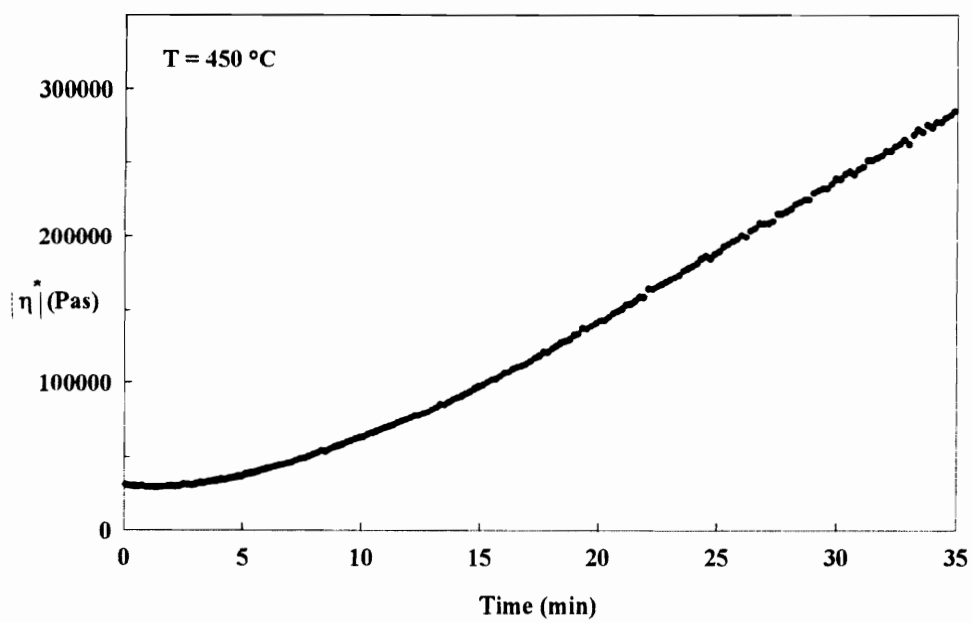


**Figure 4.13** Complex viscosity as a function of time for 12.5K polymer.

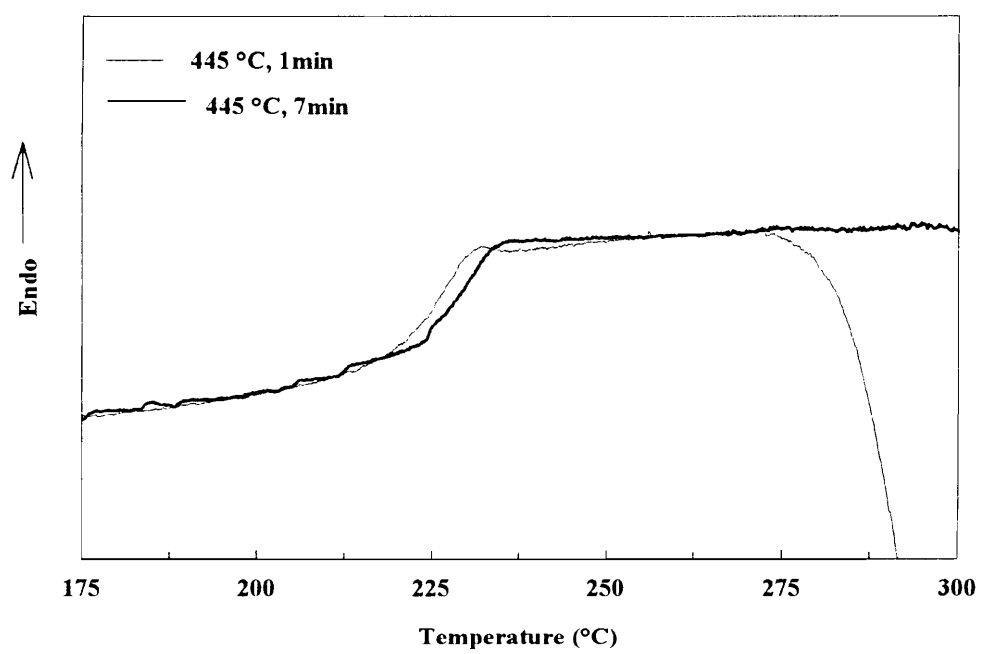


**Figure 4.14** DSC scans for 12.5K polyimide subjected to different melt treatments.

which was exposed to milder melt conditions (445 °C, 1 min), was lower than the  $T_g$  of the sample which was subjected to more harsh melt conditions (445 °C, 7 min). There appears to be no apparent decrease or broadening of the specific heat jump at the glass transition, ruling out extensive cross-linking in the system. The increase in the  $T_g$ , however, suggests an increase in the molecular weight of the sample.

It was shown earlier that NMP could induce crystallinity in the higher molecular weight samples, which did not have the ability to undergo thermal crystallization after initial melting. In order to determine if the loss of crystallinity was irreversible in the lower molecular weight samples, the 12.5K polymer was subjected to a melt condition of 465 °C for 5 minutes. The data shown in Figures 4.11 & 4.12 indicates that under these conditions, crystallization does not occur. This sample was then subjected to NMP at 205 °C for 3 hr, as described earlier. The DSC trace of the solvent treated sample showed a melting endotherm, the area under which was comparable to the area under the melting endotherm during the second heat (Figure 4.4), thereby indicating that the loss of crystallinity was not completely irreversible. This implies that the loss of molecular mobility through chain branching and/or cross-linking is still the principal reason for the loss of crystallizability. An experimental observation to be emphasized here is that for the case of the 12.5K sample which had undergone a harsh melt treatment, and subsequently exposed to NMP, there was a considerable loss of weight (ca. 25%) of the sample after the solvent treatment. It was mentioned earlier that the polyimide is not soluble in NMP, but is plasticized by it. The loss of weight implies some degradation products are formed

during the melt history, which were now soluble in NMP. Recall that the 30K polymer which had not been subject to harsh melt conditions did not show any weight loss after solvent treatment. Based on this observation it should be emphasized that the presence of low molecular weight species in the polymer would tend to decrease the glass transition temperature, which is contrary to the experimental finding. One may speculate that the low molecular soluble products are formed during the chain branching/extension and cross-linking reactions at the very high temperatures.

The loss of crystallinity after harsh melt conditions could imply loss of nucleation as discussed earlier. Destruction of residual nuclei would cause slower bulk crystallization kinetics, which could result in no crystallization being observed in the time scale of the experiment, as is observed in the studies here. The destruction of residual nuclei cannot, however, cause a reduction in the melting temperature. The reduction in melting temperature with increasingly harsh melt histories implies some chemical changes occurring in the material, which could arise from chain scission or chain branching/crosslinking, the latter two processes being accompanied by an increase in molecular weight. The occurrence of only chain degradation leading to a decrease in molecular weight, however, can be ruled out, as this would cause a decrease in both the glass transition temperature as well as the viscosity, which is contrary to the observations. Chain branching with an increase in molecular weight, chain extension, and cross-linking, would all lead to an increase in both the glass transition temperature as well as the melt viscosity. However, the fact that solvent treatment regenerates crystallinity, again rules

out extensive cross-linking in the system. Rather, a low level of chain branching and/or cross-linking, leading to an increase in molecular weight, could explain the inability of the material to crystallize thermally, an increase in the glass transition temperature, and increase in melt viscosity, and also the ability to crystallize in the presence of solvent.

## 4.5 Conclusions

A series of molecular weights of a novel semicrystalline polyimides based on TPEQ and ODPA were successfully synthesized. All the polymers exhibited very good stability in air as well as nitrogen, as evidenced by high weight loss temperatures by TGA. It should be emphasized that the 5% weight loss temperatures obtained by TGA were independent of molecular weight. The polymers exhibited glass transition temperatures of ca. 230 °C and melting temperatures of ca. 420 °C. The high thermal stability, as well as the high glass transition and melting temperatures could make this polymer a potential candidate for a variety of high temperature applications. A series of molecular weights were synthesized in order to study the molecular weight dependence of the thermal stability as well as the crystallization and melting behavior.

The DSC scans of the as-received samples showed no molecular weight dependence, however, the second heat DSC scans showed dramatic dependences on molecular weight. The low molecular weight 10K and 12.5K polymers could be thermally recrystallized whereas the higher molecular weight polymers showed little or no ability to thermally crystallize under the conditions utilized here. The utility of high performance,

high melting polyimides is dependent upon the processability of the polymer. Indeed, as mentioned earlier, the polymer should be able to withstand the high process temperatures that it would be subjected to during processing. The studies carried out in this paper not only help to optimize the processing conditions for this system, but also provide an indication of the thermal stability of this polymer under harsh melt conditions. The thermal stability of the polymers was investigated by studying the crystallization response of the material under different melt time and temperature conditions. The decrease in crystallizability of the polymer with increasing time and temperature in the melt was paralleled by an increase in the melt viscosity of the polymer, and an increase in the glass transition temperature, believed to be due to melt state branching and/or cross-linking. The studies carried out showed that crystallinity could be thermally regenerated for melt temperatures and times below 450 °C and 10 min for the 10K polymer, and below 450 °C and 5 min for the 12.5K polymer. Solvent studies showed however, that crystallinity could be regenerated in samples which had undergone harsh melt treatments by solvent treatment.

## **Acknowledgments**

The authors would like to thank the NSF Center for High Performance Polymeric Adhesives and Composites for full support of this study under contract number DMR 9120004.

## References

1. P. M. Hergenrother, Heat Resistant Polymers in *Encycl. Polym. Sci. Eng. (2nd ed)* **7**, 639 (1987).
2. A. K. St. Clair and T. L. St. Clair, *Polymers for High Technology, Electronics and Photonics, ACS Symposium Series*, **346**, 437, M. J. Bowden and S. R. Turner, eds., (1987).
3. K. L. Mittal ed. *Polyimides, Synthesis, Characterization and Applications, Vols. 1&2*, Plenum Press, New York (1984).
4. C. J. Feger, M. M. Khojasteh, and J. E. McGrath, Eds. *Polyimides: Materials, Chemistry and Characterization*, Elsevier Science Publishers B. V. Amsterdam (1989).
5. D. Wilson, H. D. Stenzenberger, P. M. Hergenrother Eds. *Polyimides*, Blackie and Son Ltd. London (1990).
6. M. E. Rogers, M. H. Brink, A. Brennan, and J. E. McGrath, *Polymer*, **34**, 849 (1993).
7. P. M. Hergenrother and S. J. Havens, *J. Polym. Sci.*, **27**, 1161 (1989).
8. Y. J. Kim, T. E. Glass, G. D. Lyle, and J. E. McGrath, *Macromolecules*, **26**, 1344 (1993).
9. M. H. Brink, D. K. Bandom, G. L. Wilkes, and J. E. McGrath, *Polymer*, **35**, 5018 (1994).

10. D. C. McHerron and G. L. Wilkes, *J. Appl. Polym. Sci.*, **46**, 1313 (1992).
11. J. A. Cella, *Polym. Degrad. Stab.*, **36**, 99 (1992).
12. Y. P. Khanna and A. C. Reimschuessel, *J. Appl. Polym. Sci.*, **35**, 2259 (1988).
13. Y. P. Khanna, A. C. Reimschuessel, A. Banerjee, and C. Altman, *Polym. Eng. and Sci.*, **28**, 1600 (1988).
14. Y. P. Khanna, R. Kumar, and A. C. Reimschuessel, *Polym. Eng. and Sci.*, **28**, 1607 (1988).
15. Y. P. Khanna, R. Kumar, and A. C. Reimschuessel, *Polym. Eng. and Sci.*, **28**, 1612 (1988).
16. T. H. Hou and R. M. Reddy, *SAMPE Q*, 38, Jan (1991).
17. J. B. Friler and P. Cebe, *Polym. Eng. and Sci.*, **33**, 587 (1993).
18. M. H. Brink, *Ph.D. Dissertation*, Virginia Tech, (1994)
19. V. L. Bell, B. L. Stump, and H. Gager, *J. Polym. Sci.*, **14**, 2275 (1976).
20. D. K. Bandom and G. L. Wilkes, *Polymer*, **35**, 5672 (1994).
21. D. K. Bandom and G. L. Wilkes, accepted for publication in *Polymer* 1995
22. P. P. Huo, J. B. Friler, and P. Cebe, *Polymer*, **34**, 4387 (1993).
23. J. Wang, A. T. DiBenedetto, J. F. Johnson, S. J. Huang, and Jane L. Cercena, *Polymer*, **30**, 718 (1989).
24. M. V. Brillhart and P. Cebe, *J. Polym. Sci.: Part B, Polym. Phys.*, **33**, 927 (1995).
25. D. W. van Krevelen, *Chimia*, **32**, 279 (1978).

## **Chapter - 5**

### **Semicrystalline Polyimides Based on Controlled Molecular Weight Phthalimide Endcapped 1,3-bis(4-aminophenoxy)benzene and 3,3', 4,4'-biphenyltetracarboxylic dianhydride: Synthesis, Crystallization, Melting and Thermal Stability**

#### **5.1 Abstract**

The successful synthesis of controlled molecular weight semicrystalline polyimides based on 1,3-bis(4-aminophenoxy)benzene (TPER diamine) and 3,3', 4,4'-biphenyltetracarboxylic dianhydride (BPDA), endcapped with phthalic anhydride is reported herein. The above polyimide henceforth referred to as TPER polyimide ( $M_n=20K,30K$ ) displayed excellent thermal stability as evidenced by dynamic thermogravimetric analysis in both air and nitrogen atmospheres. This polyimide displayed a glass transition temperature of ca. 210 °C based on DSC measurements, and a melting temperature of 395 °C. A unique feature of this polyimide was the fact that quenching the polymer from the melt, even at very high cooling rates (ca. 200 °C/min), did not result in an amorphous polymer implying very high crystallization rates from the melt. The subsequent melting endotherm was also shown to be extremely narrow as evidenced by a sharp endotherm in the DSC trace, which was attributed to a narrow distribution of crystal

thicknesses, also confirmed by SAXS results. Based on the results of the melting behavior of non-isothermally and isothermally crystallized samples, a process of melting/recrystallization has been shown to occur in the system during the DSC heating scan. This melting/recrystallization phenomenon has been shown to give rise to the observed multiple melting endotherms in the DSC scans of isothermally crystallized samples. The equilibrium melting temperature of this polymer estimated using a Hoffman-Weeks plot was shown to be 408 °C. Dynamic mechanical relaxation studies showed three relaxation  $\tan \delta$  peaks, the upper two of which were found to depend on the crystal morphology. Based on the results of the dynamic mechanical studies and DSC results, this behavior has been attributed to a dual population of amorphous material in the system (interlamellar amorphous and amorphous regions between different lamellar stacks). The thermal stability of the TPER based system has been investigated by monitoring the crystallization and melting response after residence in the melt at various times and temperatures. Based on the melt time and temperature studies, the exceptional thermal stability of the TPER polyimide has been demonstrated and compared to the corresponding results for the commercial polyimide "New TPI" and for a polyimide based on bis(4-aminophenoxy) benzene and oxydiphthalic anhydride (TPEQ polyimide). Increased times and temperatures in the melt were shown to retard the crystallization behavior which was accompanied by an increase in the melt viscosity. Polyimide samples deliberately quantitatively fitted with amine endgroups, as well as samples partially endcapped with phthalic anhydride were shown to display distinctly lower thermal stability compared to

well designed phthalimide endgrouped samples. The improved behavior was demonstrated by melt rheological and crystallization experiments.

## 5.2 Introduction

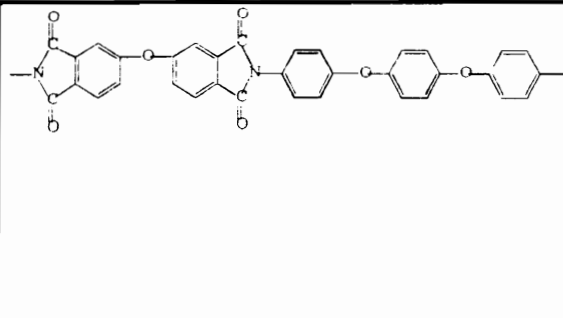
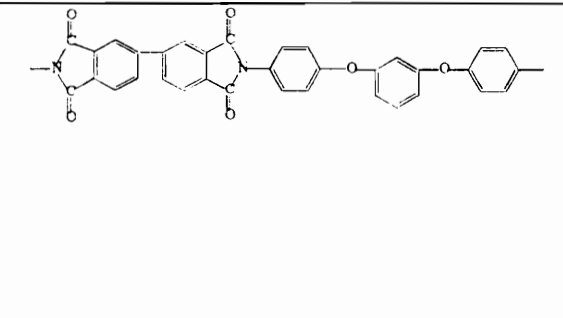
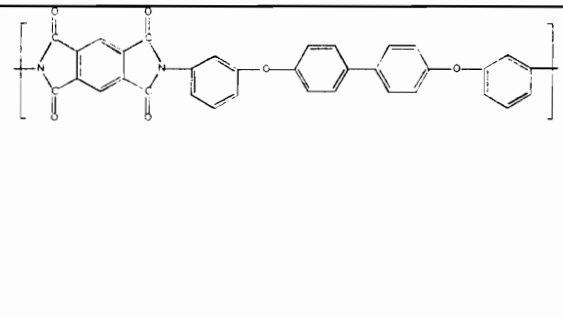
Aromatic polyimides are high performance polymeric materials possessing an exceptional array of properties. Thermal stability, radiation and chemical resistance, and excellent mechanical properties have enabled this class of polymer to be utilized in a variety of applications such as electronic packaging, aerospace applications, adhesives, and as matrix materials for composites<sup>1-3</sup>. Semicrystalline polyimides offer the advantages of increased solvent resistance and retention of mechanical properties above the glass transition temperature. The solvent resistance provided by the rigid crystalline phase is especially valuable, as it is lacking in amorphous polymers and is essential when the material is used in the presence of interactive organic solvents. These features have made semicrystalline polyimides the focus of considerable research over the recent years<sup>4-14</sup>.

The high temperature rigidity of aromatic polyimides arises from the relatively stiff backbone structure, leading to glass transition temperatures and melting temperatures that range from 200 to above 400°C. The higher transition temperatures have traditionally led to difficulties in melt processing of polyimides, since 400°C is nearing the upper bound of stability for most organic systems. Hence, these polymers typically undergo degradation before melt processing can be undertaken and completed. Traditional processing therefore

has often involved the solution casting of the poly(amic acid) precursor into the desired shape, followed by thermal imidization into the polyimide. However, since melt processing is more desirable from both a cost and environmental safety point of view, the synthesis of melt processable, thermally stable, semicrystalline resins is desirable and of prime interest. The rigid nature of the chain could also result in the “sluggish” crystallization kinetics of reasonably high molecular weight polyimides. Indeed, it was shown in an earlier study<sup>6</sup>, that whereas moderate molecular weight samples (10K, 12.5K) of a TPEQ/ODPA based polyimide (see Table 5.1) could be crystallized from the glass, the 15K, 20K and 30K molecular weight polymers showed little or no tendency to crystallize. Since the development of crystallinity is important from both a solvent resistance and high temperature applicability point of view, processing of stiff chain crystallizable polyimides often entail a post-processing annealing step to induce crystallinity.

Attempts to solve the problem of poor processability due to high transition temperatures have led to the modification of the backbone structure of the polyimide to increase the flexibility of the chain thereby lowering the transition temperatures. Effective modifications have included the addition of flexible ether and carbonyl linkages<sup>10,11</sup>, ethylene glycol sequences<sup>13,14</sup>, as well as the incorporation of meta-substituted diamines. Increasing the chain flexibility can also result in an increase in the rate of crystallization, other factors remaining the same. However, lower transition temperatures could reduce the effective upper use temperatures of these materials. The goal of this research has

**Table 5.1** Chemical structures and transition temperatures of TPER/BPDA, TPEQ/ODPA and New TPI polyimides.

		$T_g$	$T_m$
	TPEQ-ODPA	238 °C	420 °C
	TPER-BPDA	210 °C	395 °C
	Aurum™ New TPI	250 °C	388 °C

therefore focused on the development of high melting polyimides possessing good thermal stability and the ability to crystallize in a reasonable time frame allowed for processing.

Any melt processing or consolidation operation would be expected to involve holding the polymer at temperatures ca. 20 °C above their melting temperature for up to 10 minutes. For melting points in the range of 400 °C, this thermal history in the melt could easily result in some chemical degradation and/or vary the residual nuclei in the melt. Either of these two events could potentially influence the crystallization behavior of the polymer during subsequent cooling. Thus, thermal history in the melt i.e. residence time and temperature in the melt are important parameters to consider and study in terms of influencing the subsequent crystallization behavior of the material. Traditional analysis of thermal stability of polymers has involved the use of thermogravimetric analysis (TGA) to evaluate the degree of degradation occurring in the material as a function of temperature and/or time. TGA detects degradation through loss of sample weight by the emission of volatiles from degradation reactions. However, degradation reactions such as cross-linking or chain extension could occur in the melt with little accompanying weight loss<sup>6,15</sup>. Therefore, the TGA technique by itself may well prove inadequate for reflecting the effect of temperature/time in the melt upon the thermal stability of the material.

Both chain scission as well as cross-linking affect the crystallizability of the polymer during subsequent cooling. Therefore, a more appropriate, but indirect, measure of thermal stability could be the actual crystallization/melting behavior of the material. Evaluation of the crystallization and melting response of a sample after being treated at

representative conditions in the melt can reveal a more precise description of the stability than that provided by a simple TGA study. Interpretation of results obtained by this method is not as straightforward since crystallization is affected by changes in nucleation density as well as degradation; however, after accounting for residual nuclei surviving the melt period, a more accurate picture of the degradation behavior of the material is achieved. This approach of studying the thermal stability of a polymer by a systematic study of the crystallization and melting behavior as a function of melt conditions has been applied to polyimides<sup>4,6</sup>.

This study reports the synthesis and characterization of a high temperature polyimide based on 1,3-bis(4-aminophenoxy)benzene (TPER diamine) and biphenyl dianhydride (BPDA), endcapped with phthalic anhydride. Since the completion of this study, recent studies have appeared in the literature that included nominally the same polyimide studied here<sup>16,17</sup>. The first part of this paper reports details of the synthesis of the precursor poly(amic acid) and its conversion to the semicrystalline polyimide. The crystallization and melting behavior of this system indicated some unique features, and these have been investigated utilizing DSC, dynamic mechanical analysis (DMS), and x-ray scattering. The thermal stability of this polymer has been investigated as a function of melt conditions, utilizing thermal analysis, by monitoring the crystallization and melting parameters as an indicator of the stability. The thermal stability of this system is compared with that of a commercial polyimide, Mitsui Toatsu's Aurum™ New TPI<sup>18-23</sup>, and also a phthalimide endcapped bis(4-aminophenoxy)benzene (TPEQ diamine) and oxydiphthalic

anhydride (ODPA) based polyimide<sup>6</sup>, the structures of which are shown in Table 5.1. The important effect of endgroup chemistry on the thermal stability as judged not only by TGA, but also via crystallizability and rheological behavior has also been investigated.

## 5.3 Experimental

### 5.3.1 Materials

1,3-bis(4-aminophenoxy)benzene (trivially termed triphenyl ether resorcinol diamine, referred to as TPER) was supplied by Ken-Seika Corporation. The biphenyl dianhydride (BPDA) was obtained from Chriskev Corporation and dried at 120 °C prior to use. Phthalic anhydride (PA) was obtained from Aldrich and sublimed prior to use. N-methylpyrrolidinone (NMP) and 1,2-dichlorobenzene (DCB) were obtained from Fisher and vacuum distilled after drying over P<sub>2</sub>O<sub>5</sub> before use.

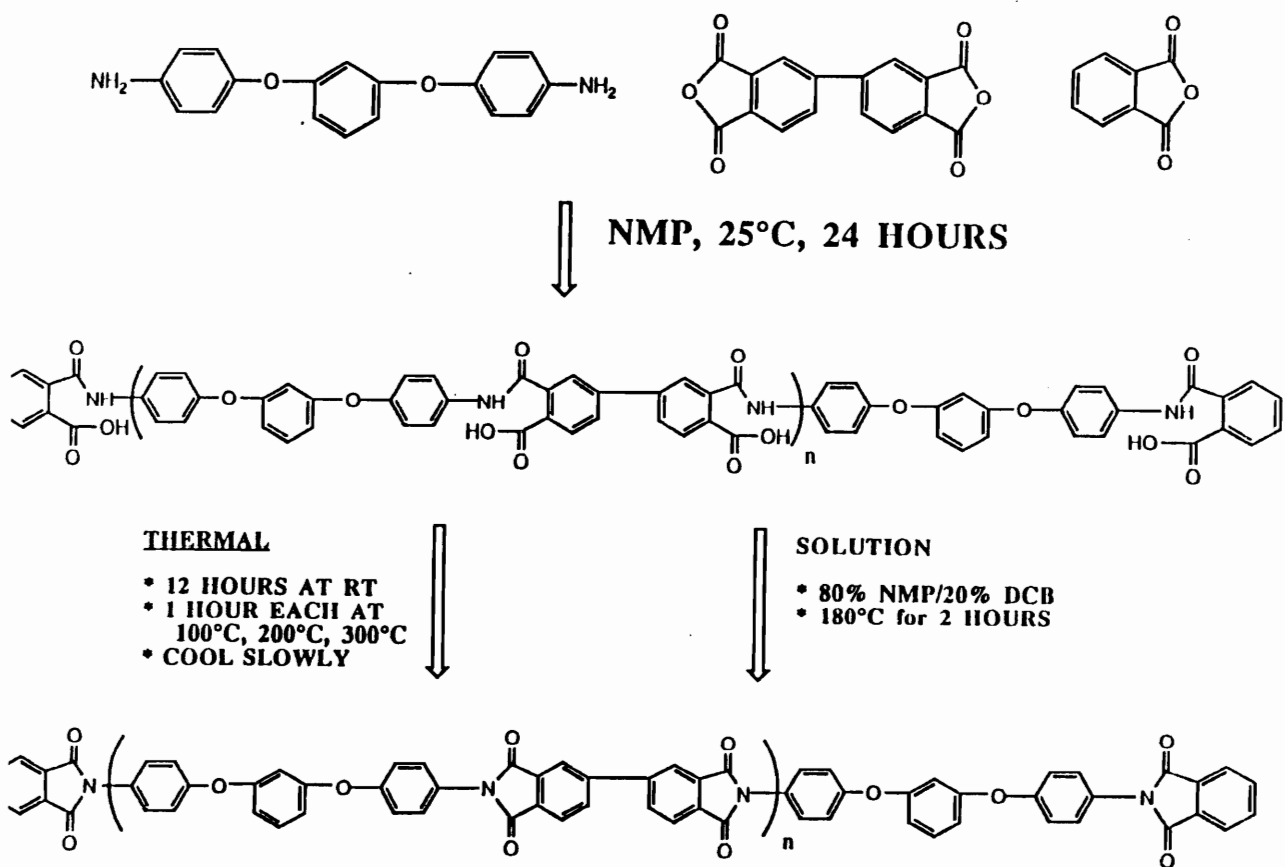
The commercial polyimide used in this study for purposes of comparison was Mitsui Toatsu's Aurum™ New TPI, which was kindly donated in the form of amorphous extruded film by Dr. Kent Blizard.

The phthalimide endcapped TPEQ/ODPA polyimide used in this study was available in film form, the synthesis and properties of which are described in the previous chapter.

### 5.3.2 Polymer Synthesis

Polyimides capped with nonreactive phthalimide endgroups were synthesized with calculated number average molecular weights of 20,000 and 30,000. A three-neck round bottom flask equipped with a mechanical stirrer, nitrogen inlet and a drying tube, was utilized as the reaction vessel. The appropriate monomer concentrations for the synthesis were calculated using the well known Carothers equation. Thus, to the reaction vessel was added a calculated amount of TPER diamine, and subsequently dissolved in dry NMP. To this solution was added a calculated amount of phthalic anhydride (PA). Upon dissolution of the PA, a calculated amount of the dianhydride, BPDA was added to the solution. Enough NMP was added to achieve a 10% solids concentration. This solution was stirred and allowed to react under nitrogen atmosphere for 24 hours, to afford the phthalimide acid endcapped poly(amic acid) as shown in **Scheme I**.

The above process was repeated utilizing differing degrees of endcapping. A 30,000 g/mol amine terminated poly(amic acid) was synthesized by eliminating all PA from the above described procedure. In addition, a 30,000 g/mol “half” phthalimide-endcapped poly(amic acid) was synthesized in which only half of the calculated amount of PA needed for full endcapping was added to the reaction vessel. For all the polymers described above, the poly(amic acid) solutions were drawn and precipitated into cold water to yield the solid poly(amic acid). The samples were vacuum dried at 50 °C prior to imidization. Titration procedures described by Kim et al.<sup>8</sup> were utilized to verify that the amine terminated polymers were within the target range of molecular weight. SEC,



Scheme I

utilizing a viscosity detector also confirmed molecular weights, utilizing the procedure of Konas et al.<sup>24,25</sup>.

The poly(amic acid) was converted to the respective polyimides utilizing two different methods as shown in **Scheme I**. In the case of thermal imidization, the poly(amic acid) was first solvent cast into films from solution onto glass plates. These plates were placed in a dry box in the presence of a nitrogen flow until smooth, non-tacky films were obtained. The plates were then placed in a vacuum oven, and the temperature was slowly raised to 100 °C, and held at this temperature for 1 hour. The temperature was then raised to 200 °C, held for 1 hour, and finally raised to 300 °C and held for 1 hour. The oven was turned off and allowed to cool to below 200 °C before taking out the films. This above described imidization procedure developed by researchers at NASA<sup>26</sup> has been applied by others as well<sup>5,6,10-12</sup>.

Solution imidization techniques were also used in order to obtain polyimide powder from the precursor poly(amic acid). In this case, the drying tube used in the apparatus described above was replaced with a reverse Dean Stark trap. Dichlorobenzene (DCB) was added as an azeotroping liquid, to the solution so as to achieve a 80/20 ratio of NMP to DCB. The solution was heated to about 175 °C and allowed to stir. After about 2 hours, partially imidized yellow particulates precipitated from the solution, after which the resulting slurry was poured into water with stirring. The resulting powder was filtered, washed with water, dried in a vacuum oven overnight at 250 °C, and subsequently dried at 300 °C for an hour to ensure complete imidization. For the remainder of this

paper, the phthalimide endcapped polyimide will be referred to as PA endcapped, the half phthalimide endcapped polymer will be referred to as half-endcapped, and the polymer synthesized with no phthalic anhydride will be referred to as amine terminated polyimide.

### 5.3.3 *Characterization*

Thermogravimetric (TGA) studies were carried out on a Seiko TG/DTA on the film samples. Heating rates of 10 °C/min were utilized for all experiments which were carried out in either a nitrogen or air atmosphere. The temperature calibration of the TG/DTA was based on the melting temperatures of indium and zinc. The values reported in this paper are temperatures for 2% weight loss.

The DSC measurements were conducted with a Perkin Elmer DSC-7, on 6-7 mg of sample under a nitrogen purge, at heating rates of 10 °C/min unless otherwise specified. Temperature and heat flow were calibrated using indium and zinc standards. The DSC curves shown in this paper have been normalized to 1 mg sample mass.

The melt time/temperature studies were carried out on a Seiko DSC 220C using 6-7 mg of sample under a nitrogen purge. The temperature and heat flow were calibrated using indium, tin and zinc standards. The heating and cooling schedules used in this study were as follows. The samples were heated at 20 °C/min to the various melt temperatures and held for different times. The samples were cooled at 10 °C/min to room temperature, following which they were reheated at a rate of 10 °C/min. Four parameters were chosen which were representative of the crystallization and melting behavior, and their

dependence on the melt time and temperature were followed. The peak of the crystallization exotherm during the cooling scan was taken to be the maximum crystallization temperature, and the area under the crystallization exotherm was denoted as the heat of crystallization. The peak of the melting endotherm during the second heat was taken as the melting temperature, and the area under the endotherm was denoted as the heat of melting. The heating and cooling schedules utilized for the melt time/temperature experiments for the New TPI system and the TPEQ/ODPA polyimide are described later.

Dynamic mechanical experiments were carried out on a Seiko DMS 210 using a heating rate of 1 °C/min under a nitrogen flow. Sample lengths of 10 mm and cross-section areas of ca. 0.9 mm<sup>2</sup> were tested in the tensile mode. Frequencies of measurements varied from 0.01 Hz to 20 Hz, over a temperature range from -155 °C to 350 °C.

Wide angle x-ray scattering was carried out on a Nicolet diffractometer equipped with a STOE Bragg-Brentano type goniometer. CuK $\alpha$  radiation of wavelength 1.54 Å was used after monochromatization through a graphite monochromator. Data were collected at 0.05° increments at angles between 5-50°.

Small angle x-ray scattering (SAXS) experiments were carried out using Ni filtered Cu K $\alpha$  radiation ( $\lambda=1.54$  Å) in conjunction with pinhole collimation and a helium purged flight path. The detector used was a Siemens High Star Area detector (resolution 200  $\mu\text{m}$ , grid 512x512).

A portion of the rheological experiments utilized a Bohlin VOR Rheometer with a 25 mm diameter parallel plate fixture. A Bohlin HTC using nitrogen as the heating gas was used for temperature control. Both powder as well as film samples of the polyimides ca. 1 mm thick were used in the experiments. Samples were pressed at room temperature in a matched steel cylindrical mold of 25 mm diameter. The samples were placed between the plates in the HTC oven which was preheated to the required temperature.

Approximately two minutes elapsed from the time the sample was placed in the rheometer to when the oven temperature equilibrated to the required temperature, after which the measurements were started. Dynamic oscillatory viscosity data were collected at a frequency of 0.1 Hz and a strain of 2%. The fluids head was used for all measurements along with a 12.54 gcm resistance torque bar.

The frequency dependence of the viscosity was investigated using a Rheometrics Mechanical Spectrometer (Model 800) using a parallel plate fixture of 25mm diameter. Samples similar to those in the above study were utilized in these experiments. The oven was preheated to the required temperature, and the samples placed between the plates. After an equilibration time of ca. 4 min, the tests were started.

## **5.4 Results and Discussion**

Thermogravimetric analysis (TGA) experiments were carried out on all the samples in air as well as nitrogen atmospheres at heating rates of 10 °C/min. Table 5.2

**Table 5.2** Temperatures for 2% weight loss by TGA for various polyimides.

<b>Polymer</b>	<b>Molecular weight</b>	<b>Air</b>	<b>Nitrogen</b>
TPER-PA	20K	502 °C	539 °C
TPER-PA	30K	526 °C	545 °C
TPER-Amine terminated	30K	527 °C	549 °C
TPER-Half endcapped	30K	527 °C	549 °C
Aurum™ New-TPI	-	545 °C	545 °C

shows the 2 % weight loss temperatures of all the polymers synthesized as well as the corresponding values for the commercial polyimide, Mitsui Toatsu's Aurum™ New TPI. It can be seen from the table that by this test, all the samples investigated exhibited excellent thermal stability in air as well as nitrogen as evidenced by the very high temperatures for 2% weight loss. As expected, the weight loss temperatures were slightly lower in air as compared to nitrogen (ca. 25 °C), except for the case of New TPI. The TGA data suggests that New TPI exhibits superior thermal stability compared to the TPER system. However, this point will be discussed further with respect to critical crystallization/melting studies as a function of time and temperature in the melt. An interesting point to note is that the amine terminated and half-encapped polyimide samples showed about the same values for 2% weight loss as the PA encapped polyimide, thus implying that the nature of the endgroup does not influence the thermal stability of the polymer when analyzed by this procedure. As will be discussed later, the PA encapped TPER polyimide exhibits superior thermal crystallization stability compared to its partially encapped and amine terminated analogues, thus emphasizing a major inadequacy of the TGA technique to provide an accurate indication of critical structural changes that do not involve weight loss.

#### 5.4.1 DSC studies

Figure 5.1 shows the DSC scans for the as-received polymer films and the New TPI film, designated here as the first heat DSC scan. All the TPER polymers exhibited

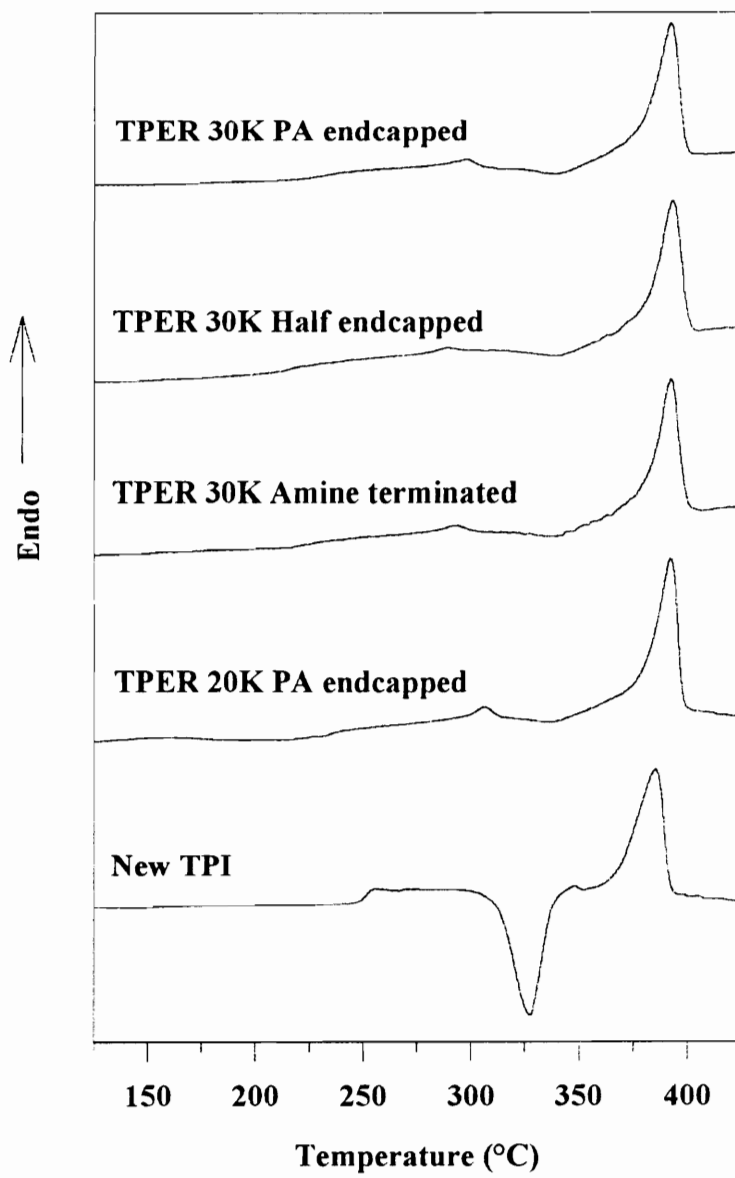


**Figure 5.1** First heat DSC scan for TPER polyimide and New TPI.

weak specific heat jumps corresponding to the glass transition temperature at ca. 230 °C. The weak transition is probably due to the relatively high degree of crystallinity in the as-received samples, and/or the possibility of a significant fraction of a rigid amorphous fraction. All the samples exhibited weak endotherms at ca. 295 °C (30K) or 300 °C (20K), possibly caused by the melting of imperfect crystals. Recall that the final step in the thermal imidization cycle involved residence at 300 °C for 1 hour. The weak endotherm can therefore be attributed to the melting of less perfect crystals formed at the final imidization temperature. This is followed by broad, weak exotherms corresponding probably to recrystallization/perfection following the melting of the less perfect crystals. Regardless of the nature of the endgroup or molecular weight, prominent melting endotherms were observed at ca. 390 °C. The New TPI sample on the other hand exhibited a prominent glass transition temperature at 250 °C, followed by a cold crystallization exotherm at 327 °C, and finally a melting endotherm at 385 °C. Based on a calculation of the areas under the crystallization exotherm and the melting endotherm, it was concluded that the as-received film samples of New TPI were essentially amorphous. At the end of the first heat (425 °C), the samples were held for 1 min at that temperature, following which they were rapidly quenched (ca. 200 °C/min), and then reheated.

Figure 5.2 shows the second heat DSC scans of all the samples. *It is interesting to note that none of the TPER samples could be quenched into a pure amorphous state after the first heat, implying very fast crystallization kinetics of this system.* It is also worth emphasizing that relatively high molecular weight samples were utilized in this study (20K

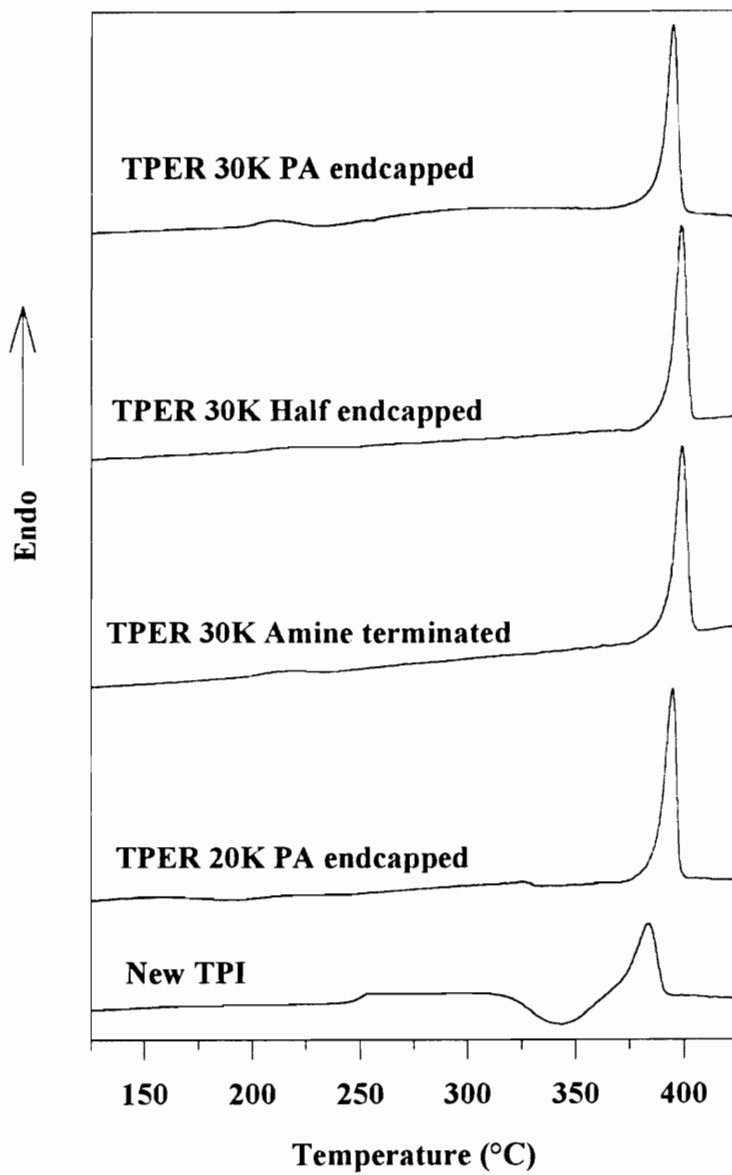


**Figure 5.2** Second heat DSC scans for TPER polyimide and New TPI.

and 30K). As mentioned in the previous chapter, it was possible to quench even a 10K TPEQ/ODPA based polymer into a purely amorphous state with relative ease. All the TPER samples exhibited weak specific heat transitions corresponding to the glass transition temperature at ca. 210 °C, followed immediately by very weak crystallization exotherms, and finally by a sharp melting endotherm at ca. 395 °C. The unique features of this system include both the extremely fast crystallization kinetics as well as the sharp melting behavior implying a narrow distribution of crystal thicknesses and perfection. A point to note here is that the melting temperatures of the quenched samples of the TPER systems were ca. 5 °C greater than that of the as-received samples. Possible causes of this interesting behavior are discussed in the next section. In contrast, the New TPI sample displayed a glass transition temperature at 250 °C, a somewhat broad crystallization exotherm at 343 °C, followed by a similar broad melting endotherm at 385 °C. It is worth noting that both the glass transition and melting temperatures for New TPI on second heat were the same as that during the first heat, however, the maximum crystallization temperature during the second heat was shifted by as much as 16 °C to higher temperatures during the second heat, implying that a single melt treatment likely destroyed some residual nuclei present as a result of the film extrusion process. This same behavior could also occur due to some degradation as a result of residence in the melt, but as will be shown later, this is not believed to be the cause of this behavior.

The effect of repeated melting on the subsequent melting behavior of the PA endcapped TPER 30K polymer was studied by cyclic heating/quenching cycles. The

samples in this study were heated at 10 °C/min to 425 °C, held for 1 min, quenched to 100 °C, then reheated at 10 °C/min. This procedure was repeated 4 times, the results of which are shown in Figure 5.3. The first heat and second heat are similar to the traces shown in Figures 5.1 and 5.2. It is clear that the second, third and fourth heats are identical in every respect in that weak glass transitions, indistinct crystallization exotherms, and sharp melting endotherms are quite evident. Both the position as well as the area under the endotherms were quite unaffected by repeated melting and quenching. This indicates the high thermal stability of this system, which complements the findings by TGA, as well as reemphasizes the fast crystallization kinetics of this system.

#### 5.4.2 *Melting studies*

The second heat DSC scans of the TPER systems indicated the fast crystallization kinetics of this system. Hence, the effect of cooling rates on the subsequent melting behavior of the PA endcapped TPER 30K polyimide was investigated by utilizing different rates after the system was subjected to 425 °C for 1 min. Figure 5.4 shows the subsequent DSC heating scans at 10 °C/min after the various cooling rates utilized. It is quite clear that up to a cooling rate of 100 °C/min, the polymer could not be prevented from crystallizing as is evident from the lack of a clear glass transition and absence of a crystallization exotherm. At a cooling rate of 200 °C/min, a larger fraction of the polymer could be quenched into the amorphous state as evidenced by a weak glass transition and crystallization exotherm during the heating scan. Quite surprisingly, the melting

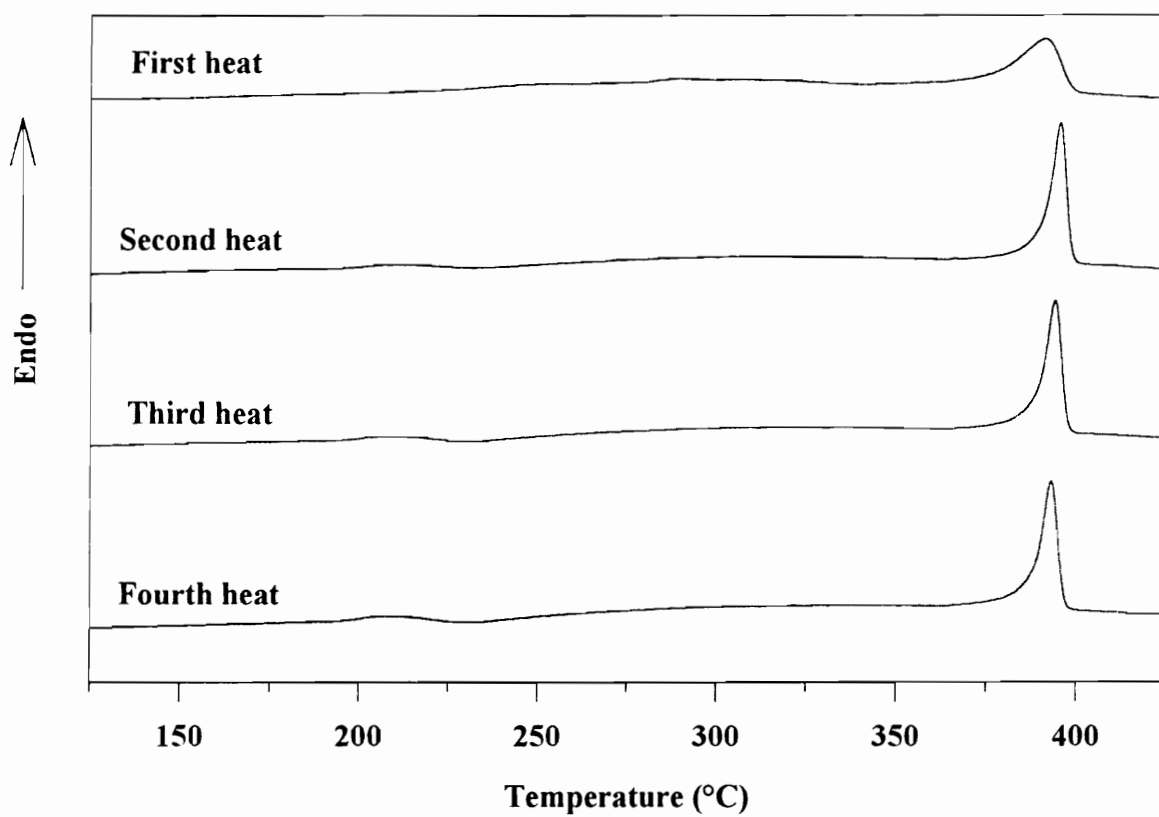


**Figure 5.3** Repeated heating DSC scans for PA endcapped TPER 30K.

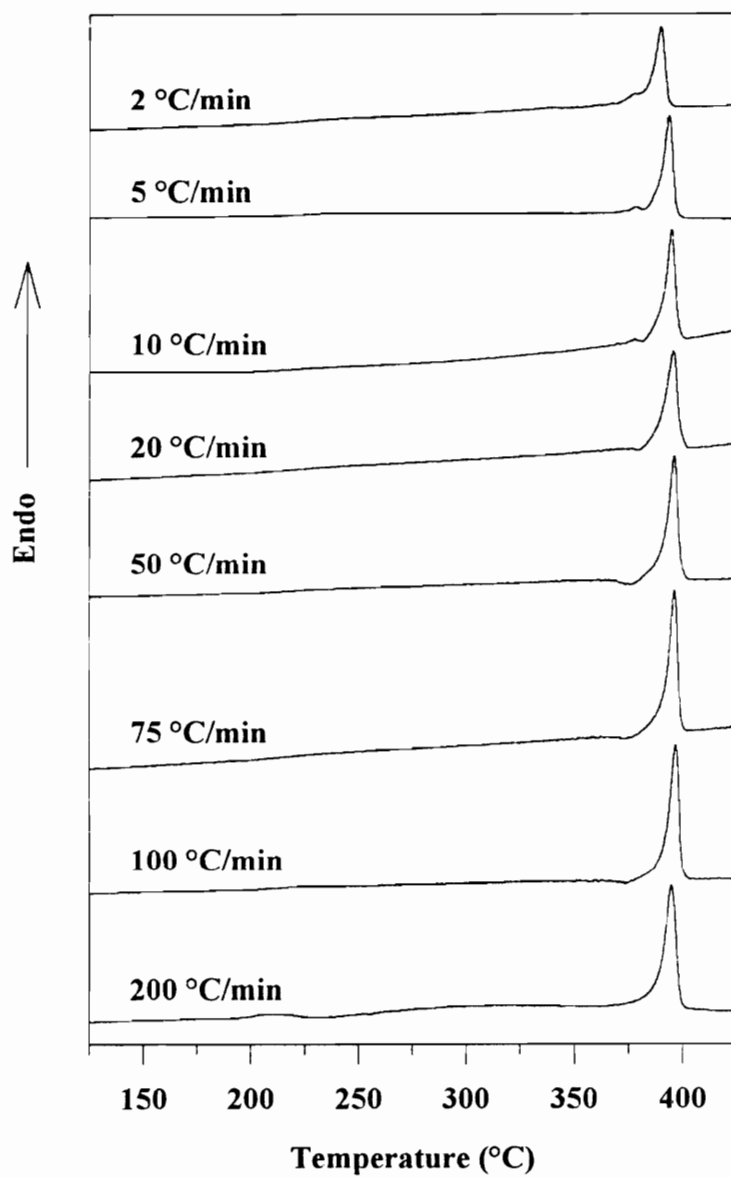


**Figure 5.4** DSC scans for PA endcapped TPER 30K subjected to various cooling rates from the melt.

temperatures as well as the heats of melting were found to increase with increasing cooling rates (except for the case of the sample cooled at 200 °C/min, which displayed a melting temperature slightly lower than that of the sample cooled at 100 °C/min). On increasing the cooling rate, the melting temperatures increased by 7 °C, whereas the heats of melting increased by ca. 25%! The peak of the crystallization exotherm (maximum crystallization temperature) during the cooling scan was depressed from 338 °C at 2 °C/min to 300 °C at 100 °C/min, i.e. a change of almost 40 °C in undercooling. The differences in crystallization temperature would be expected to yield different melting temperatures, with the slower cooling rates displaying slightly higher melting temperatures. At slower cooling rates, the system would be expected to have a greater residence time in the crystallization window and hence yield higher heats of melting as well.

Due to the fast crystallization kinetics, it can be reasonably assumed that under slow cooling rates, crystallization occurs at low undercooling under quasi-isothermal conditions and therefore would yield a narrower distribution of more “perfect” and thicker crystals. Since the crystals are formed mainly at low undercoolings, the fraction of “imperfect” crystals and thinner crystals that melt at lower temperatures is reduced. On the other hand, for the case of higher cooling rates, one would expect a much wider distribution of crystal thicknesses and perfection, leading to a wide distribution of melting temperatures. The fraction of crystals that could melt at lower temperatures would therefore be larger compared to the case of the slow-cooled sample. It is hypothesized

that these thinner and “imperfect” crystals undergo a process of almost continuous melting and recrystallization/perfection during the DSC heating scan to yield the observed melting endotherm. If the process of melting and recrystallization/perfection is almost simultaneous, one would not necessarily expect any exothermic or endothermic deviations from the baseline. For the case of the slow-cooled samples, however, since the crystals formed are thicker and more “perfect”, the phenomenon of melting and recrystallization/perfection would be reduced. The evidence presented here implies that lower melting “imperfect” crystals are more prone to a process of melting and recrystallization/perfection than thicker and more “perfect” crystals. The dependence of the melting temperature and heat of melting on cooling rate can therefore be attributed to melting accompanied by recrystallization/perfection during the DSC heating scan. Further treatment of the reorganization phenomenon is discussed next. It can also be seen that slower cooling rates result in a dual endothermic behavior as evidenced by a shoulder on the main melting endotherm, implying that crystallization at lower undercoolings might result in dual melting behavior. This is supported by the following isothermal crystallization studies.

Figure 5.5 shows the melting endotherms of the PA endcapped TPER 30K samples isothermally crystallized at various temperatures. The heating schedules used were as follows: the samples were heated at 20 °C/min to 420 °C, held for 5 min in order to destroy residual nuclei, quenched to the different crystallization temperatures, held for a specified period of time, following which they were quenched to room temperature.

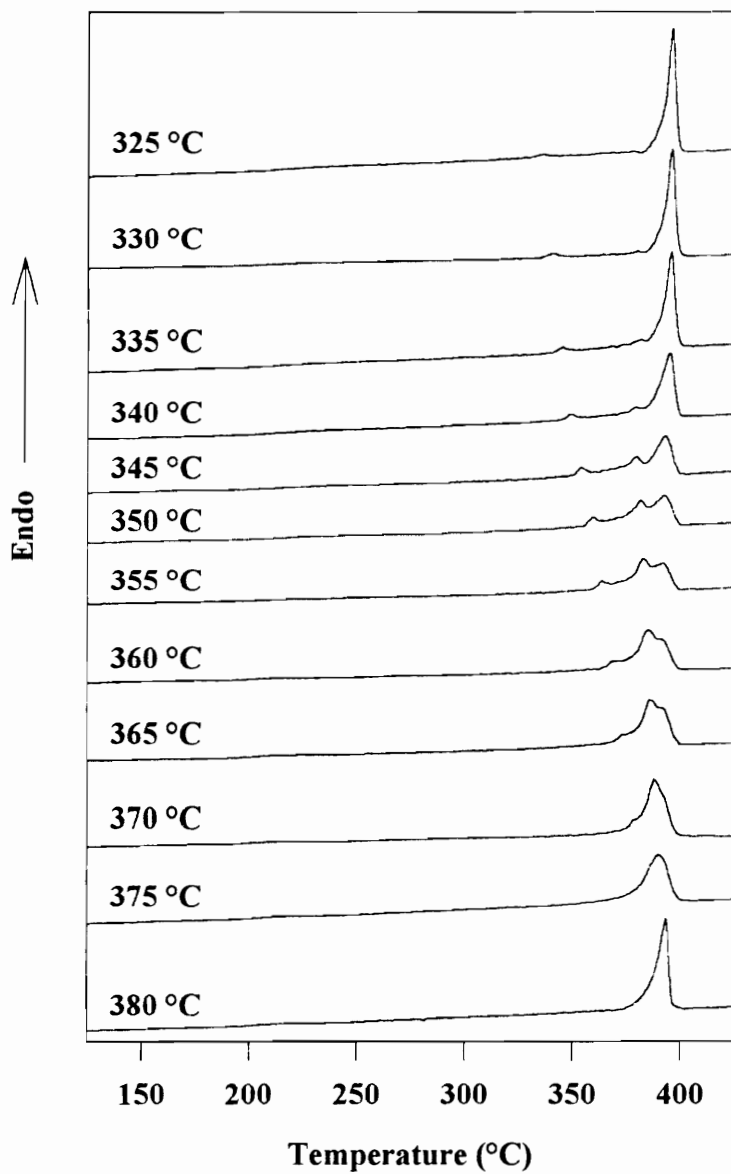


**Figure 5.5** DSC scans for PA endcapped TPER 30K samples isothermally crystallized at various temperatures.

Unless otherwise specified, all samples were then reheated at 10 °C/min. It is quite evident from the figure that multiple endotherms are observed in the melting behavior when the samples are crystallized in the range 325 °C to 370 °C. For crystallization temperatures ( $T_c$ ) between 325 °C and 370 °C, the lowest endotherm (Peak I) is observed at temperatures of ca.  $T_c + 10$  °C. An intermediate endotherm (Peak II) is observed at crystallization temperatures from 330 °C to 370 °C, which first appears as a low temperature shoulder on the main melting endotherm (Peak III) and gradually increases in size and temperature with increasing crystallization temperature. The high temperature endotherm (Peak III) is initially independent of crystallization temperature (until a  $T_c$  of 340 °C) after which it shows a slight decrease, then remains essentially independent of crystallization temperature. The size of Peak III decreases in size relative to the size of Peak II with increasing crystallization temperature, until it appears as a shoulder on the high temperature side of Peak II. At crystallization temperatures of 375 °C and higher, only a single endotherm is observed.

Multiple endothermic behavior for isothermally crystallized or annealed samples have been observed for nearly all semicrystalline polymers. Among the high temperature polymers, multiple melting behavior has been reported for PPS<sup>27,28</sup>, PEEK<sup>29</sup>, and other polyimides<sup>20,30</sup>. Before the data regarding the multiple endothermic behavior is discussed, it would be useful to review the various possible causes for this behavior. In general, multiple melting endotherms for the case of quiescently crystallized polymers could arise due to:

- 1) Different populations of crystals having different unit cell crystal structures.
- 2) Distinct populations of crystallites with different thicknesses, e.g. thick crystals grown during primary crystallization and thinner crystals grown during a) secondary crystallization, or during cooling after primary crystallization step, or during the heating scan in the DSC.
- 3) Melting and reorganization during the heating scan giving rise to melting of crystals, their subsequent crystallization to a higher melting species, and subsequent melting, all during the dynamic heating scan in the DSC.
- 4) Partial melting and reorganization/perfection of the existing crystals to a higher melting form during the DSC heating scan.

As stated earlier, the samples were cooled to room temperature at the end of the crystallization step before subsequent heating. In order to investigate if the cooling run at the end of the crystallization gave rise to any of the endotherms, a sample was heated at the end of the crystallization step without first cooling to room temperature. Figure 5.6 shows the DSC scans of a sample crystallized at 345 °C for 5 min, and scanned from 345 °C, and compared to a sample that had been first cooled to room temperature. As can be seen from the figure, the positions and sizes of the melting endotherms were essentially identical, implying that cooling to room temperature prior to the heating scan did not give rise to any of the endotherms. The multiple endotherms are therefore characteristic of the isothermal crystallization, and/or the subsequent heating scan.

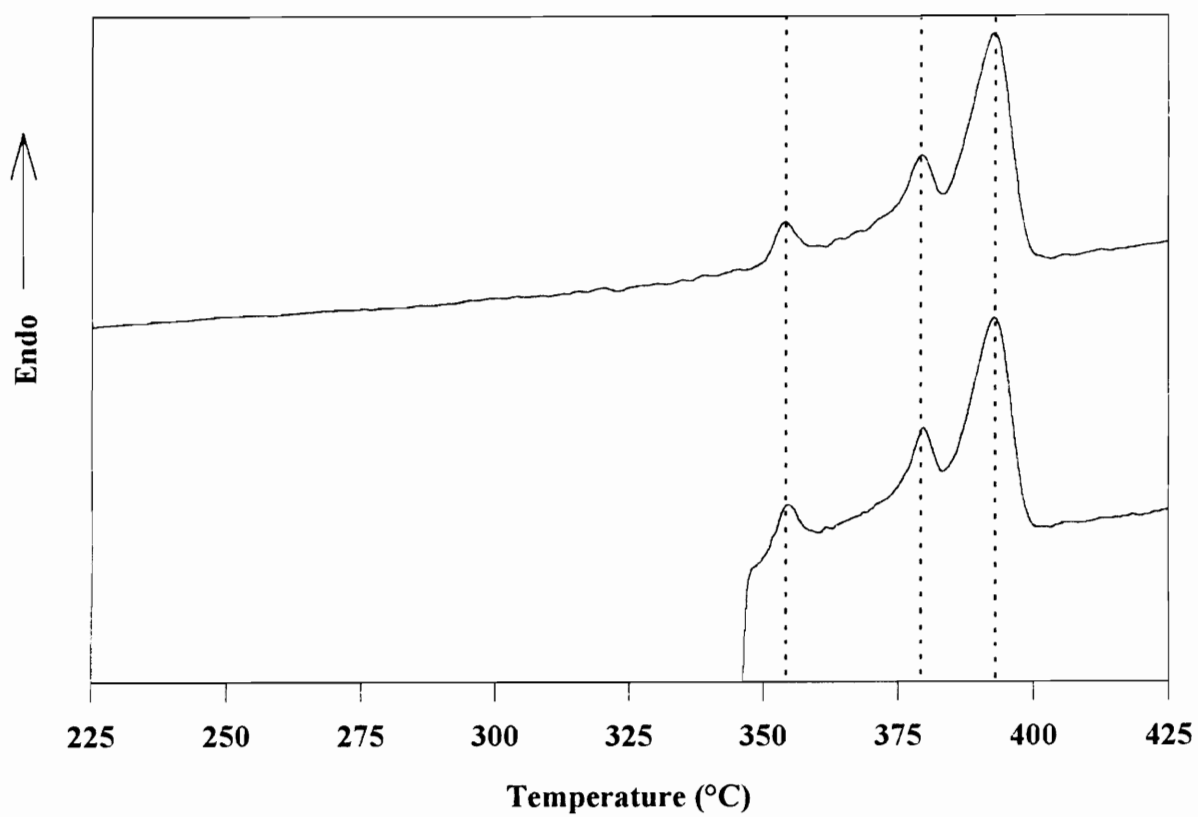


**Figure 5.6** DSC scans for PA endcapped TPER 30K samples crystallized at 345 °C for 5 min.

The effect of the crystallization time on the melting endotherms was investigated by crystallizing samples for different times at 345 °C. Isothermal crystallization experiments showed that at this temperature, the primary crystallization process was complete within 5 min. As can be seen in Figure 5.7, the position and relative sizes of the upper two endotherms were independent of the crystallization time. However, both the position as well as the size of the lowest endotherm increased with the log of annealing time. The dependence of the lowest endotherm ( $T_c+10$  °C) on crystallization temperature and time is consistent with the trends reported for the  $T_c+10$  endotherm for other polymers including PEEK<sup>29</sup>. Though there has been considerable debate in literature<sup>31-39</sup> on the origin and nature of the  $T_c+10$  °C endotherm, evidence favors the explanation that this endotherm arises as a result of the melting of thinner lamellae that are formed as a result of secondary crystallization at the crystallization/annealing temperature. These thinner lamellae are probably formed as separate stacks in the amorphous regions between primary lamellar stacks, as shown in the schematic later in the paper. Thus, at this stage the lowest endotherm (Peak I) can be attributed to the melting of thin “in-filling” lamellae that are formed as a result of secondary crystallization at the crystallization temperature.

In order to further investigate the cause of the other two endotherms, samples crystallized at 345 °C for 30 min were scanned at different heating rates. Figure 5.8 shows the DSC thermograms of the samples scanned from 2 °C/min to 75 °C/min. The heat flow scale (y-axis) shown in the figure is an arbitrary scale, and so the heats of melting of the different scans cannot be directly compared to one another. However,

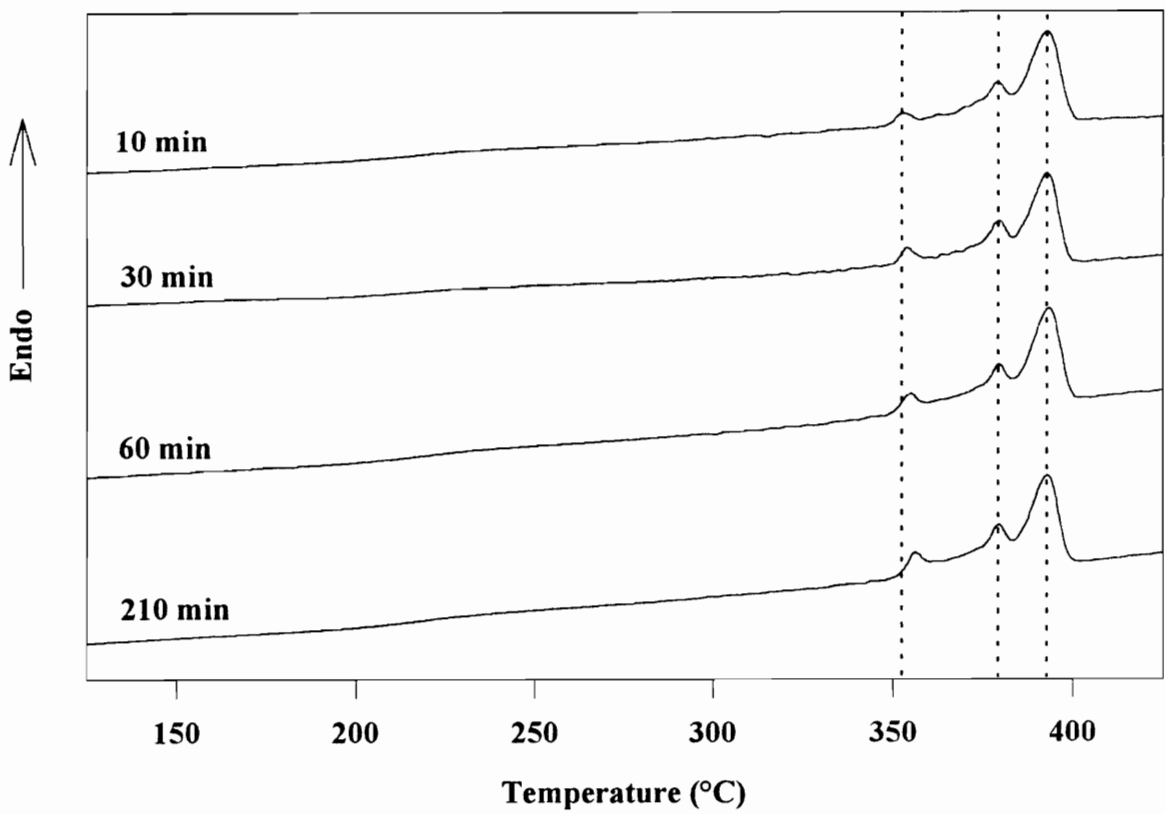


**Figure 5.7** DSC scans for PA endcapped TPER 30K isothermally crystallized at 345 °C for various times.

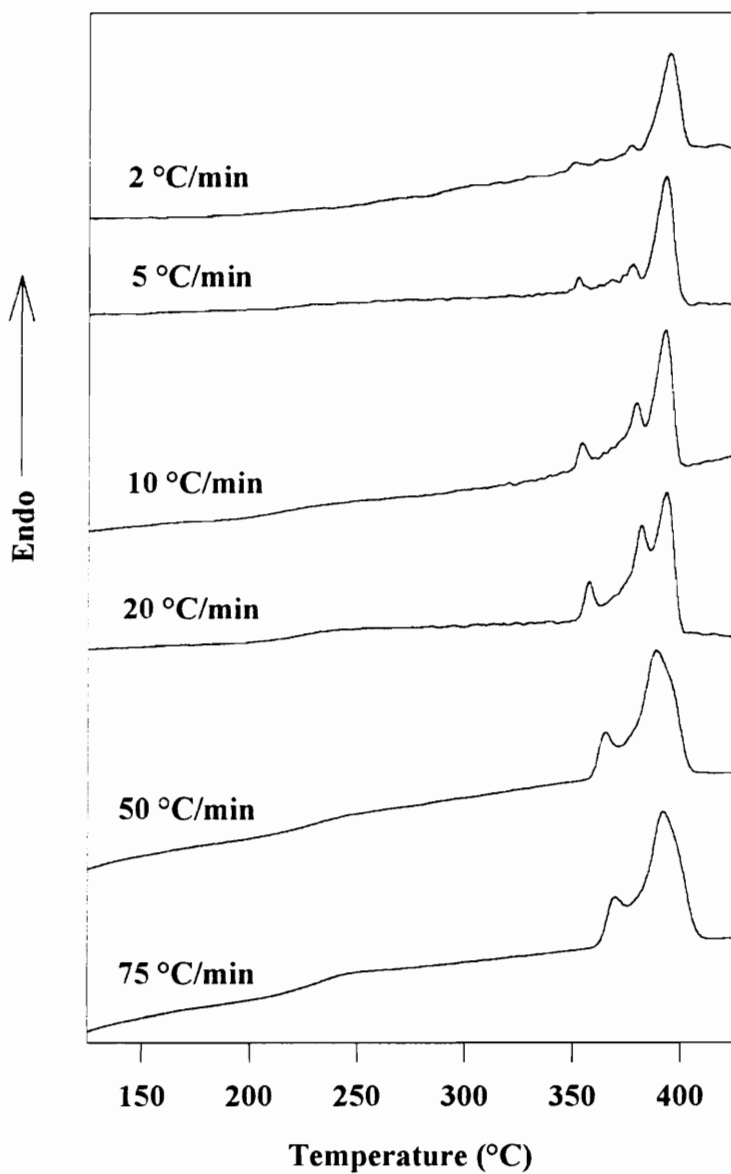


**Figure 5.8** DSC scans at different heating rates for PA endcapped TPER 30K isothermally crystallized at 345 °C for 30 min.

trends in the relative sizes of Peaks II and III can be compared. As can be seen from the figure, the relative size of Peak II increases at the expense of Peak III with increasing heating rate. Indeed, at a heating rate of 50 °C/min Peak III appears as a shoulder on the high temperature side of Peak II, and at a heating rate of 75 °C/min, Peak III is hardly visible at all. This is consistent with a melting/recrystallization phenomenon. So, at the isothermal crystallization temperature, crystals are formed that melt at a temperature that gives rise to the endotherm corresponding to Peak II. The melting process is accompanied simultaneously by a recrystallization process, which gives rise to thicker and more perfect crystals that eventually melt at a temperature corresponding to the endotherm denoted as Peak III. Since melt recrystallization is a kinetic phenomenon, at slower DSC scanning rates, more time is available for the melting/recrystallization process, which leads to a small Peak II and a prominent Peak III. At faster heating rates, however, the time scale allowed the recrystallization process is reduced, leading to a prominent Peak II and a smaller Peak III.

Since the upper endotherm (Peak III) is formed as a result of the reorganization process, its position would be expected to be independent of the crystallization temperature, which in fact is observed in this study. However, since Peak II is representative of the melting of pre-existing crystals, its temperature would be expected to increase with crystallization temperature since the crystal thickness would increase with increasing crystallization temperature, which in fact is again observed here.

Figure 5.9 shows the wide angle x-ray scattering profiles (WAXS) of two samples, one that gives rise to only a single prominent endotherm (not taking into account the  $T_c+10$  °C endotherm), and another sample that gives rise to multiple melting endotherms. From Fig 5.5, it is clear that the crystallization conditions required to yield the following samples correspond to crystallization at 325 °C for 15 min and that corresponding to crystallization at 345 °C for 30 min. From the scattering profiles, it can be seen that there is no obvious difference between the scattering peaks of the two samples, implying that there is no noticeable difference in the unit cell crystal structure between the two samples.

Following the earlier discussion outlining the various reasons that could give rise to multiple endothermic behavior, one can rule out different crystal structures causing the multiple endotherms; one can also rule out thinner lamellae formed during the cooling scan after crystallization at a given temperature, in the DSC, causing the multiple endotherms observed in this study. Peak I has already been attributed to the thinner lamellae formed during the secondary crystallization process at the crystallization temperature. It has been shown that Peak II and Peak III occur due to the melting of crystals that were formed at the isothermal crystallization temperature and due to a melting/reorganization process of those crystals respectively.

Based on the assignment of Peak II to the crystals formed at the isothermal crystallization process, an attempt has been made to construct a Hoffman-Weeks plot to determine the equilibrium melting temperature of this polymer. By definition, the equilibrium melting temperature is the temperature required to melt crystals of infinite

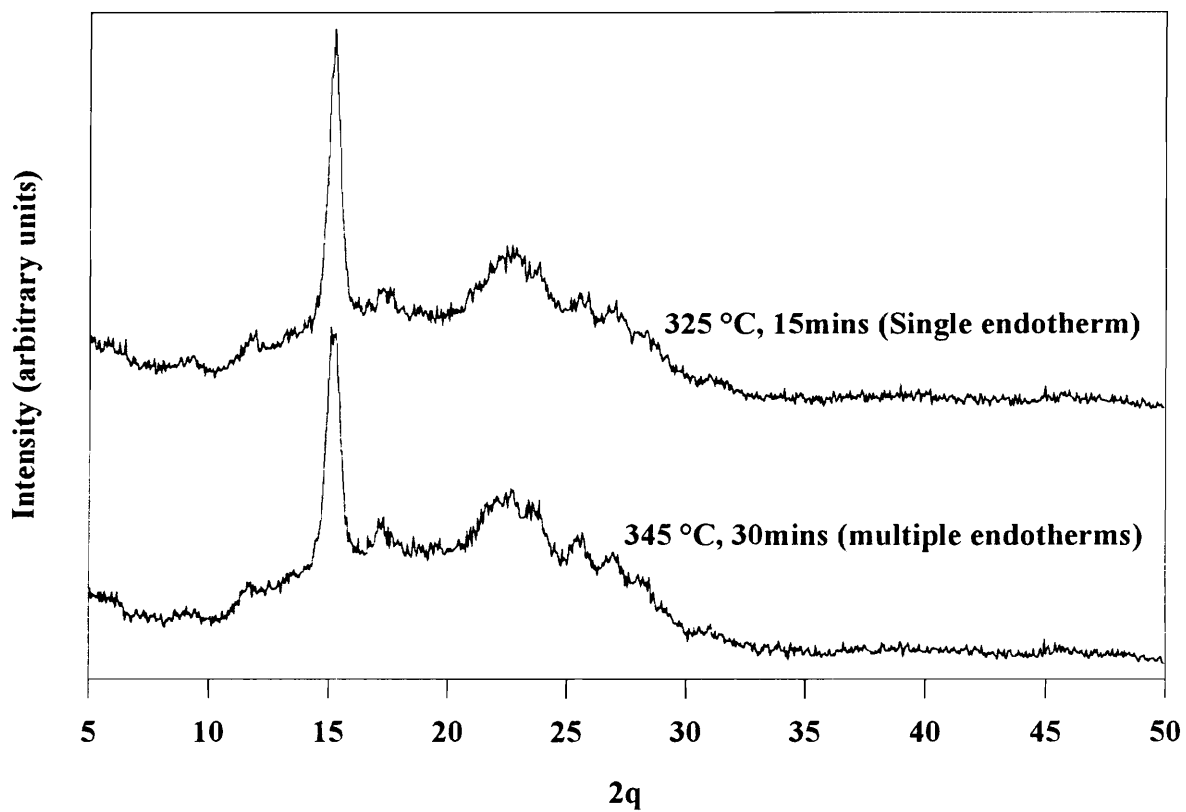


**Figure 5.9** Wide angle x-ray scattering patterns for PA endcapped TPER 30K samples exhibiting single melting endotherm and multiple melting endotherms.

thickness. Since such crystals cannot be grown experimentally, this value can be estimated by some extrapolative techniques such as the Gibbs-Thomson method<sup>40</sup> or the Hoffman-Weeks method<sup>40</sup>. The more common method is the Hoffman-Weeks method which requires the melting temperatures ( $T_m$ ) of samples crystallized at different temperatures ( $T_c$ ) to be plotted against each other, and the line joining them to be extrapolated to the  $T_m=T_c$  line, the point of intersection being the equilibrium melting temperature  $T_m^\circ$ . As can be seen in Figure 5.10, the peak temperatures of the three endotherms have been plotted as a function of crystallization temperature. The points corresponding to Peak I are parallel to the  $T_m=T_c$  line, and further emphasizes the earlier statements ruling out Peak I as arising from primary crystals formed at the isothermal crystallization temperature (though it should be noted that the position of Peak I is also a function of crystallization time). It can be seen that the Peak III values are almost independent of crystallization temperature, and in fact shows a small decrease at  $T_c = 345$  °C, after which it is again independent of crystallization temperature. This again reinforces the earlier statement that the endotherm corresponding to Peak III does not represent the melting of crystals formed at the isothermal crystallization temperature. The values corresponding to Peak II temperatures were therefore utilized in order to make the extrapolation. The value of the equilibrium melting temperature determined this way was found to be 408 °C. Two points regarding this method should be emphasized: first that the values of the melting temperatures were determined by using the peak of the second endotherm from the DSC scan. Due to the overlapping melting/recrystallization events, the observed DSC

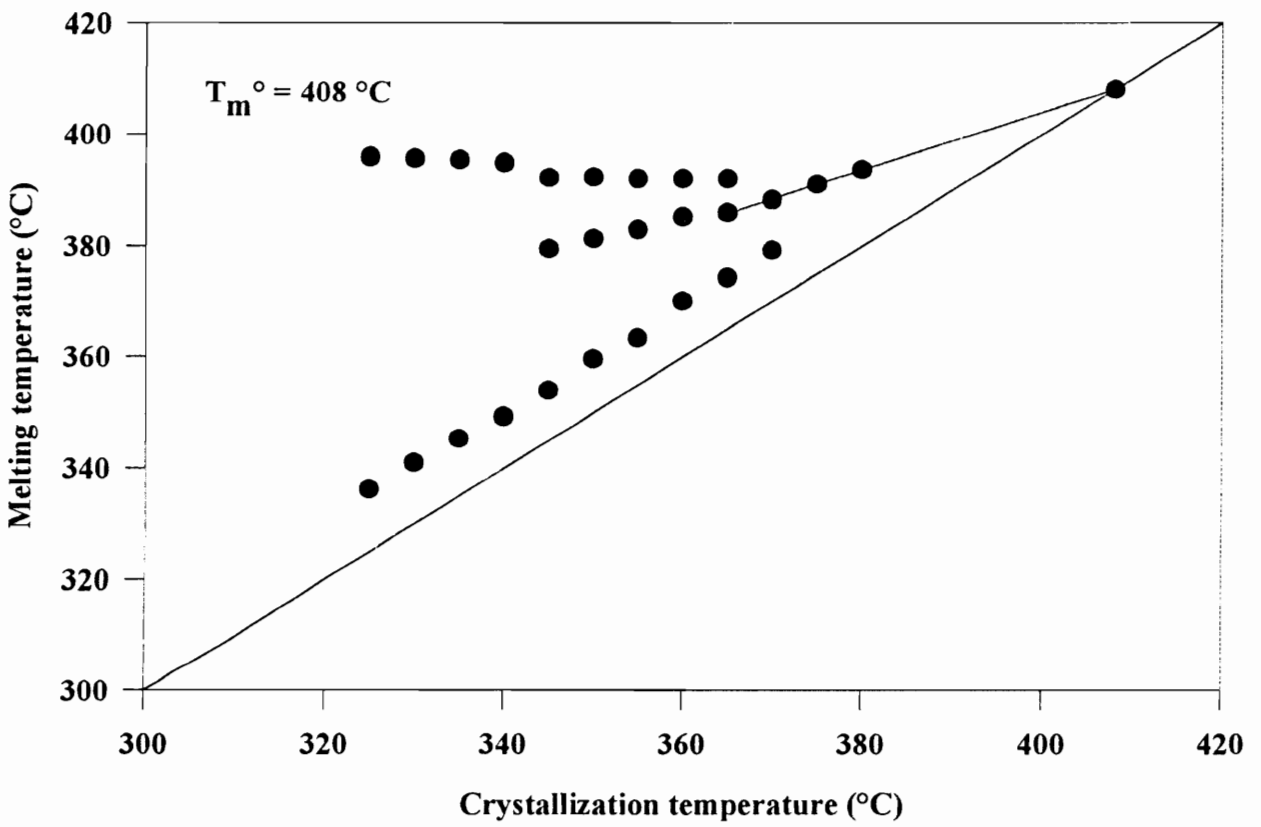


Figure 5.10 Hoffman-Weeks plot for PA endcapped TPER 30K polyimide.

thermogram is a convolution of simultaneously occurring melting endotherms and a recrystallization exotherm. The real value of the peak of the melting endotherm is therefore probably somewhat different from that observed in the DSC. The peak value can be estimated by some curve fitting procedure, which again could introduce some uncertainties in the values. This uncertainty in the values of the melting temperatures introduces some uncertainties in the value of  $T_m^\circ$  determined from the plot. The second point to be emphasized here is that the Hoffman-Weeks procedure is an extrapolative procedure, hence any errors/uncertainties in evaluating either  $T_c$  or  $T_m$  could lead to large variations in the value of  $T_m^\circ$  determined from the plot. Hence the value of the equilibrium melting temperature determined from this plot should be treated at best as a semi-quantitative estimate of the real value.

The melting/recrystallization process has been shown to occur for all cases of melt crystallized samples. A point worth noting here is that the as-received sample exhibited a broad melting endotherm, implying a broad distribution of crystal thicknesses and perfection. This sample did not seem to undergo a process of melting/recrystallization during the DSC heating scan. Recall also that the as-received sample had undergone a complex crystallization history consisting of a step-wise thermal imidization cycle, during which the poly(amic acid) was chemically converted to the crystallizable polyimide, which was accompanied by loss of solvent and water. Since the crystallization history of the as-received sample is quite complex, it is difficult to speculate as to why this sample did not seem to undergo a process of melting/recrystallization during the initial DSC scan.

### 5.4.3 *Dynamic Mechanical studies*

Figure 5.11 shows the dynamic mechanical spectra (1Hz) of two samples of the PA endcapped TPER 30K polyimide. The first sample is the as-received film sample, and the second sample is one that had been heated in an oven at 425 °C for 1 min, and subsequently slow cooled to room temperature. Three transitions are evident in the spectra, a prominent glass to rubber  $\alpha$  relaxation at ca. 240 °C, a sub-glass  $\beta$  relaxation at ca. 100 °C, and a low temperature  $\gamma$  relaxation at ca. -90 °C.

It is obvious from the figure that neither the position nor the magnitude of the  $\gamma$  relaxation changes from the as-received sample to the slow cooled sample. This is probably due to the extremely localized range (short range) of molecular motions responsible for the  $\gamma$  relaxation. The  $\gamma$  relaxation would thus not be expected to depend on the crystal morphology and its resulting influence on the amorphous phase. The activation energies for the various relaxations were calculated by plotting the log of frequency versus the reciprocal temperature corresponding to the peak of the  $\tan\delta$  curve. In all cases, this Arrhenius relation was found to yield satisfactory results, with the slope of the linear regression yielding the activation energy  $E_a$ . The activation energies of the  $\gamma$  relaxation of the two samples were calculated and found to be essentially identical (ca. 50 kJ/mol) as shown in Figure 5.12.

There is a noticeable difference, however, between the  $\beta$  relaxations of the two samples. The relaxation temperature of the as-received sample is lower compared to the

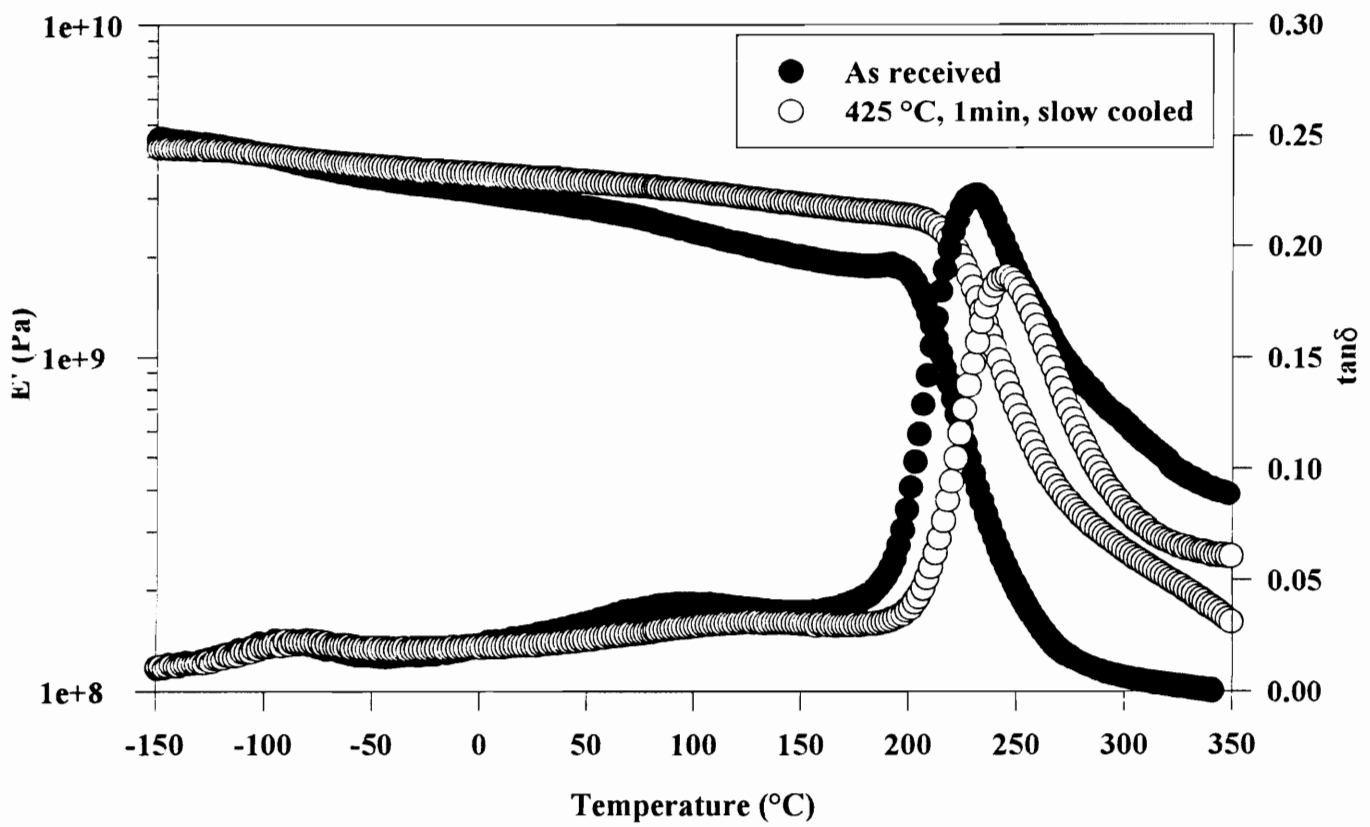


**Figure 5.11** Dynamic mechanical spectra of as-received and slow cooled samples of TPER 30K.

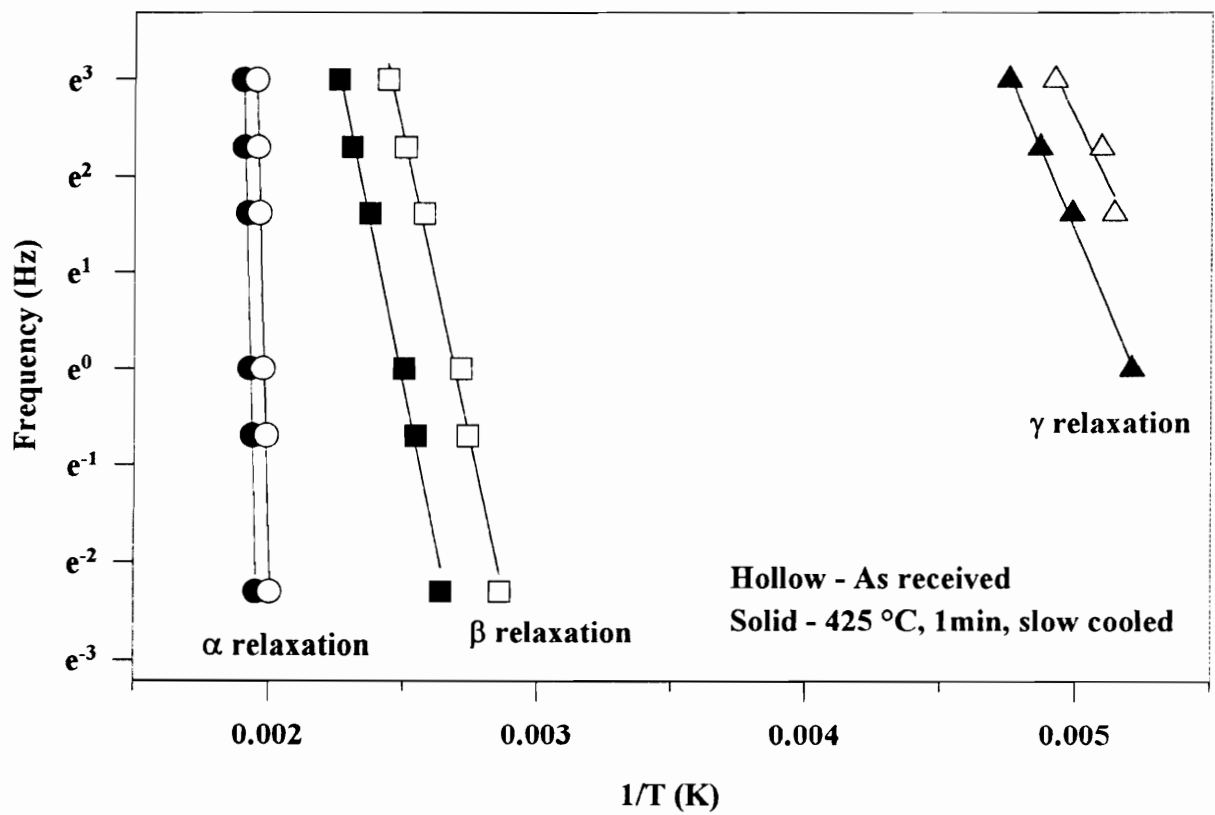


**Figure 5.12** Arrhenius plots of frequency vs.  $1/T$  based on dynamic mechanical relaxation experiments for as-received and slow cooled samples of PA endcapped TPER 30K.

slow cooled sample, while the relaxation intensity is larger. Assuming that the  $\beta$  relaxation occurs due to motions *only in the amorphous phase*, the observed differences reflect the effect the crystalline phase has on the amorphous phase motions that give rise to the  $\beta$  relaxation. For the case of the as-received sample, it is recalled from the DSC scan shown in Figure 5.3, that the melting endotherm is very broad, indicating a broad distribution of crystal thicknesses. For the case of the slow cooled sample, recall from Figure 5.4, that the melting endotherm is very sharp and narrow, indicating a narrow distribution of crystal thicknesses. It is worth emphasizing at this juncture that the relative degree of crystallinity (as determined by the heat of melting by DSC) of the two samples were essentially identical, the only difference between the two samples being the distribution of crystal thicknesses. The dynamic mechanical spectra indicate the constraining effect of the crystalline phase on the amorphous phase. For the case of the as-received sample, the amorphous phase appears to be less constrained and therefore more mobile compared to the slow cooled sample, thereby resulting in a lower relaxation temperature. The higher relaxation intensity for the case of the as-received sample also indicates that a larger fraction of the amorphous phase is capable of the motions that give rise to the  $\beta$  relaxation, as compared to the slow cooled sample. The drop in the storage modulus ( $E'$ ) values of the as-received sample across a large temperature range indicates the broad spectrum of relaxation mechanisms that occur in the sample, indicating a broad range of amorphous chain motions. The storage modulus for the slow cooled sample on

the other hand does not display as prominent a decrease across the same temperature range, indicating the narrower range of molecular motions in the amorphous phase, and that a lower fraction of the amorphous phase is capable of undergoing motions which characterize the  $\beta$  relaxation. The higher value of the  $\beta$  relaxation temperature as well as the decreased magnitude of the relaxation of the slow cooled sample indicate the greater constraining effect the crystalline phase has on the amorphous phase motions. It is worth mentioning that the activation energies for the  $\beta$  relaxations were essentially identical for the two samples (ca. 110 kJ/mol) as seen in Figure 5.12, suggesting that the nature of molecular motions were similar for the two samples, the only difference being the fraction of amorphous chains capable of this relaxation mechanism at these temperatures.

The relaxation corresponding to the glass transition temperature or glass to rubber relaxation, the  $\alpha$  relaxation, shows a strong dependence on the sample history. As can be seen from Figure 5.11, for the case of the as-received sample, the  $\alpha$  relaxation occurs at a lower temperature and displays a greater relaxation intensity, than for the case of the slow cooled sample. This again indicates a greater fraction of the amorphous phase is mobile and relaxes across the glass transition in the as-received sample, and also indicates the lesser constraining effect of the crystallites on the amorphous phase, which is also consistent with the behavior of the  $\beta$  relaxation. The same fact is also evident from the greater drop in the value of the storage modulus across the glass transition for the as-received sample. The breadth of the relaxation peak is also greater for the case of the as-

received sample indicating that the amorphous phase motions show a broader distribution, possibly arising due to the broader distribution of crystal thicknesses. As was evident from a closer inspection of the  $\beta$  relaxation, the behavior of the  $\alpha$  relaxation of the slow cooled sample also suggests that the crystallites cause a greater constraining effect on the amorphous phase, and also cause a smaller fraction of the amorphous phase to undergo relaxation across the glass to rubber transition. A narrower relaxation peak also suggests a narrower distribution of motions are involved in the transition from the glassy to the rubbery state. It should be mentioned here that even in the case of the  $\alpha$  relaxation, the activation energies were essentially identical for the two samples (ca. 830 kJ/mol) as shown in Figure 5.12. This high value of the activation energy is typical of the values reported for other polymers<sup>41</sup>, and indicates the multi-segmental cooperative motion involved in the glass transition.

The glass transition temperature occurs due to the cooperative nature of large scale molecular motions. As such, it would be expected to depend upon the crystal morphology and the subsequent constraining effect on the amorphous chains. The data above indicates that the behavior of the  $\alpha$  relaxation depends on the crystalline morphology of the system, as is to be expected. The dependence of the  $\beta$  relaxation on the crystal morphology is not so simple however. The  $\beta$  relaxation has been shown to be sensitive to the crystal morphology for stiff chain polymers like PEEK<sup>42,43</sup>, and essentially independent of morphology for a more flexible chain polymer like PET<sup>44</sup>. The dependence

of the  $\beta$  relaxation on the morphology implies some cooperativity involved in the motions giving rise to the  $\beta$  relaxation. The  $\gamma$  relaxation is, however, independent of the morphology, implying that this relaxation involves extremely short range motions. Before these findings are dealt with any further, it would be instructive to visualize the morphology of a semicrystalline polymer.

Polymers crystallize in the form of chain folded lamellae, each lamella being separated from the other by an amorphous interlayer. Though there is still considerable debate on the nature of chain folding, one can assume that even stiff chain polymers like polyimides crystallize in the form of chain folded lamellae, separated from each other by amorphous interlayers. The maximum degree of crystallinity that can be attained is also expected to be lower for stiff chain polymers. This raises the issue of the nature of the considerable fraction comprising the amorphous phase. In general, the amorphous interlayer between chain folded lamellae (inter-lamellar amorphous) can then be visualized as loose folds, long cilia, short cilia, tie molecules, and all those molecules which were not allowed to join a lamella due to a variety of reasons. The question to be asked is, where is the rest of the amorphous phase? This question must be addressed because the degree of crystallinity in lamellar stacks has been shown to be considerably higher than the bulk degree of crystallinity<sup>31,45</sup> as estimated by DSC, WAXS, density etc., for the case of stiff-chain polymers. There are amorphous regions in spherulites that occur between different lamellar stacks which are quite substantial, as shown in the schematic in Figure 5.13. The

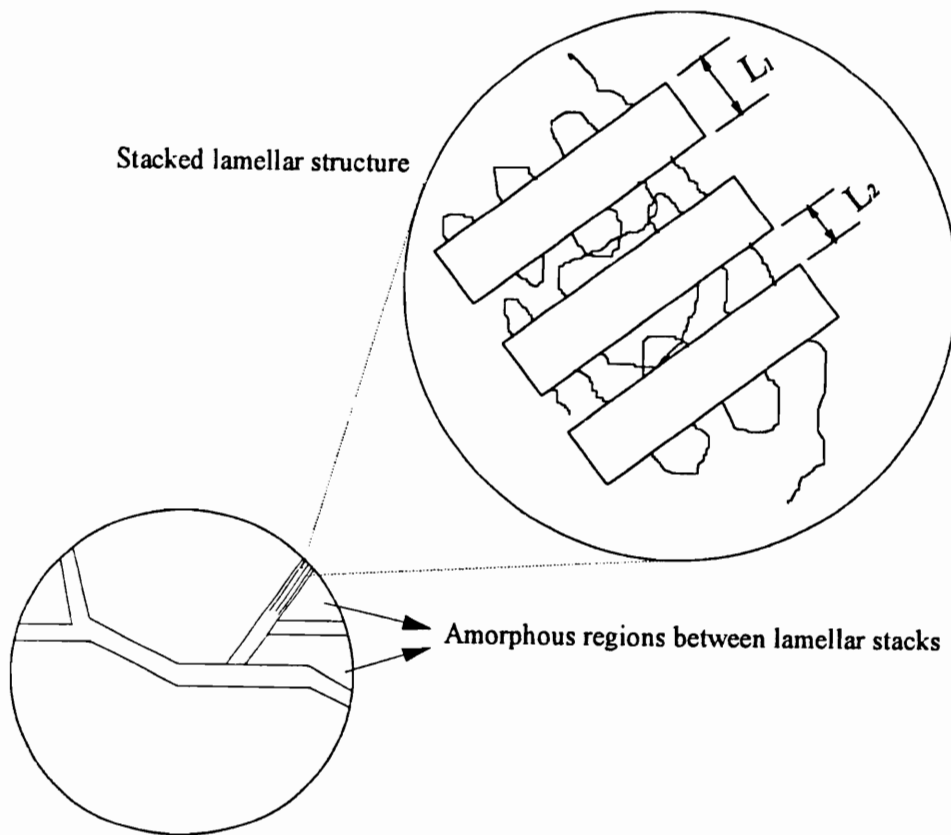


**Figure 5.13** Schematic representation of spherulitic and lamellar morphology.

schematic shows bundles of outwardly radiating lamellae from the center of the spherulite. Between different bundles are the amorphous regions; each bundle consists of stacks of folded chain lamellae with amorphous interlayers between the lamellae, and have been represented as  $L_1$  and  $L_2$  in the schematic respectively. At this stage one can accept the presence of two different amorphous populations, one existing between lamellae and the other in the regions between different lamellar stacks, as also shown by the experimental results of Lovinger et al.<sup>46</sup>, Santa Cruz et al.<sup>47</sup>, and Verma et al.<sup>48</sup>. It can be assumed for now that every polymer molecule is involved in a lamella (except those that are prevented from crystallizing). Since every chain is “stuck” to a certain degree in a crystallite, all chains in a semicrystalline polymer will behave as constrained chains relative to the fully amorphous case. Indeed, experiments with the DSC and other dynamic methods have shown that the  $T_g$  increases in stiff chain semicrystalline polymers by as much as 10 °C or more<sup>29,41-43</sup> compared to the fully amorphous system.

It can be argued that molecules in the amorphous regions between different lamellar stacks more closely resemble the molecules in the fully amorphous state, compared to the inter-lamellar amorphous regions which are more constrained. An extension of this idea of two kinds of amorphous regions finds support from the studies of Wunderlich et al. who showed that a certain fraction of the amorphous phase does not relax at the glass transition temperature. This fraction of the amorphous phase that remains rigid above the observed glass transition temperature has been termed the rigid amorphous phase (RAP)<sup>29,49,50</sup>. Though it is not possible to assign the rigid amorphous

phase to only the inter-lamellar amorphous regions, it can be hypothesized that the rigid amorphous fraction arises due to the high degree of constraints on the amorphous chains, and hence could be a part of the inter-lamellar regions. Any molecular motion requiring cooperative molecular motions would be influenced by the nature and number of constraints imposed on the amorphous phase by the presence of crystallites, particularly at the interface. If the constraints on the amorphous chains in the interlamellar regions differ from the constraints on the amorphous chains in the amorphous regions between lamellar stacks, then the cooperative motions giving rise to the  $\alpha$  relaxation (and in this case the  $\beta$  relaxation as well) would be expected to depend on the fraction of the amorphous phase that resides in the interlamellar regions, and in the amorphous regions between different lamellar stacks.

The above dynamic mechanical relaxation data in conjunction with the DSC data suggests that the slow cooled sample has a narrow distribution of crystal thicknesses (and probably interlamellar amorphous layer thicknesses as well) which imposes large constraints on the amorphous phase and also reduces the fraction of the amorphous phase capable of undergoing the necessary motions leading to the  $\alpha$  and  $\beta$  relaxations. From the above discussion on the morphology of semicrystalline polymers, one can speculate that a larger fraction of the amorphous phase resides in the lamellar stacks for the slow cooled sample, and acts as a “rigid amorphous phase” across the  $\alpha$  and  $\beta$  relaxations. For the case of the as-received sample, the DSC and dynamic mechanical results indicate that

this sample has a broad distribution of crystal thicknesses (and probably interlamellar amorphous layer thicknesses) which imposes lesser constraints on the amorphous phase as compared to the slow-cooled sample. Since a larger fraction of the amorphous phase is also available for motions across the  $\alpha$  and  $\beta$  relaxations, it is speculated that a larger fraction of the amorphous phase resides in the amorphous regions between different lamellar stacks. The  $\gamma$  relaxation believed to arise from very short range motions, however, is unaffected by the crystalline morphology.

#### 5.4.4 SAXS studies

Figure 5.14 shows the Lorentz corrected plot for the as-received sample and the slow-cooled sample, as described in the previous section. The low angle “bump” in the scattering pattern of the as-received sample is a result of the extrapolation procedure to  $q=0$ , where  $q$  is the scattering vector defined as  $q = 4\pi\sin\theta/\lambda$  (where the radial scattering angle is  $2\theta$ ). From the scattering pattern it is obvious that the as-received sample shows a much broader scattering peak with a Bragg spacing of 105 Å. The slow-cooled sample shows a sharper scattering peak with a higher Bragg spacing (163 Å). These results imply that the slow-cooled sample has a narrow distribution of crystal thicknesses, and the as-received sample has a broad distribution of crystal thicknesses, which is consistent with the DSC data presented earlier.

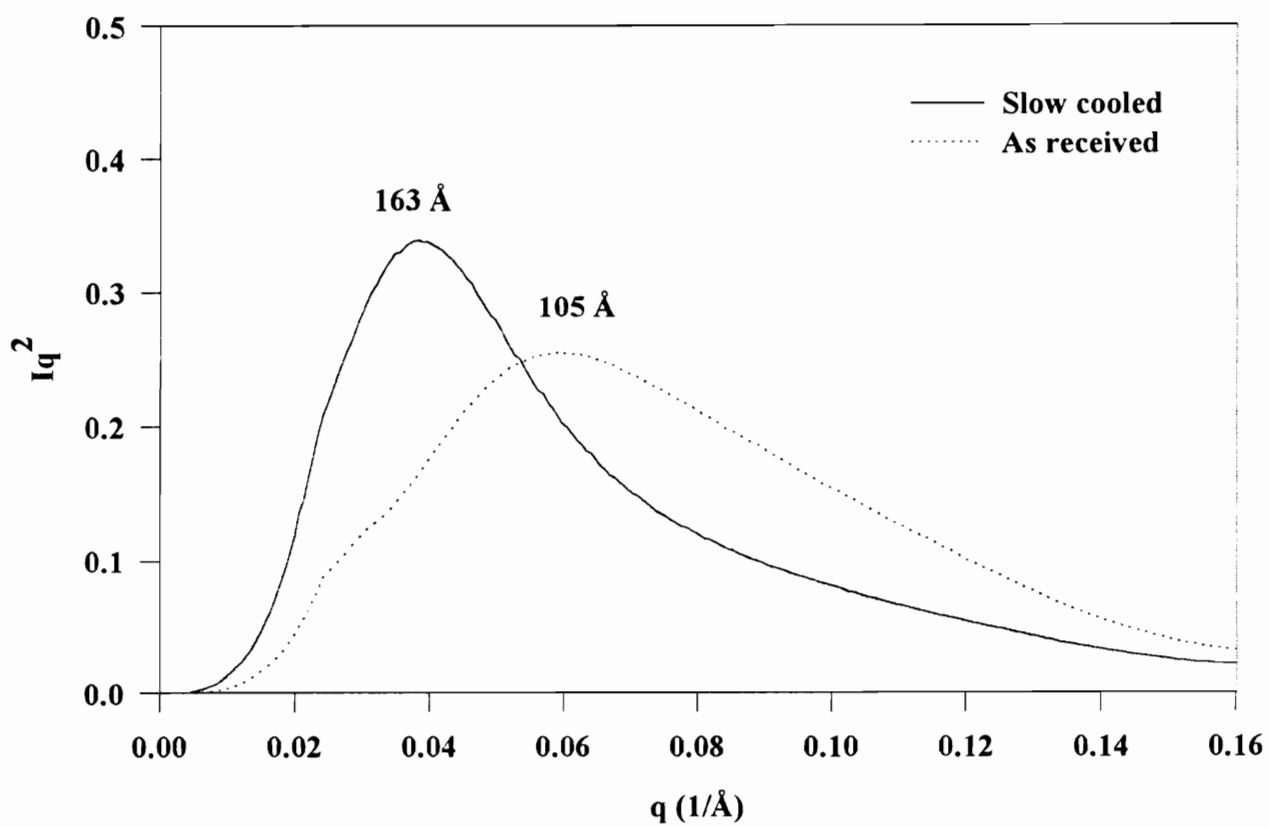


**Figure 5.14** Lorentz corrected SAXS plots for PA endcapped TPER 30K.

#### 5.4.5 Thermal Stability

As discussed earlier, the thermal stability of the polyimides were studied by a systematic variation of melt times and temperatures. The stability of the PA endcapped TPER 30K polymer was compared to the stability of New TPI and the earlier studied PA endcapped TPEQ/ODPA system<sup>6</sup>. The effect of the nature of the endgroup on thermal stability was also investigated by comparing the thermal stability of the PA endcapped TPER 30K system with that of the amine terminated and half-endcapped TPER 30K polymers. The samples were subjected to various thermal treatments as discussed earlier. The various parameters characterizing the crystallization and melting processes were plotted as a function of melt time and melt temperature in order to gain information on the melt thermal stability of these polyimides.

The area under the melting endotherm (heat of melting) for the PA endcapped TPER 30K polymer is shown in Figure 5.15 as a function of time and temperature in the melt. *Each grid point on the 3-D plot represents a specific thermal history.* This 3-D plot not only helps in optimizing the melt conditions for potential processing of this material but also assists in the qualitative understanding of the effect of thermal history on the melting behavior, as it relates to changes in nucleation density and/or chemical changes in the polymer. The exceptional thermal stability of this polymer is evident from the figure. It is obvious that melt times up to 45 min at temperatures as high as 420 °C, did not depress the heat of melting. A melt temperature of 420 °C is not only ca. 25 °C above the observed melting temperature, but is probably above the equilibrium melting

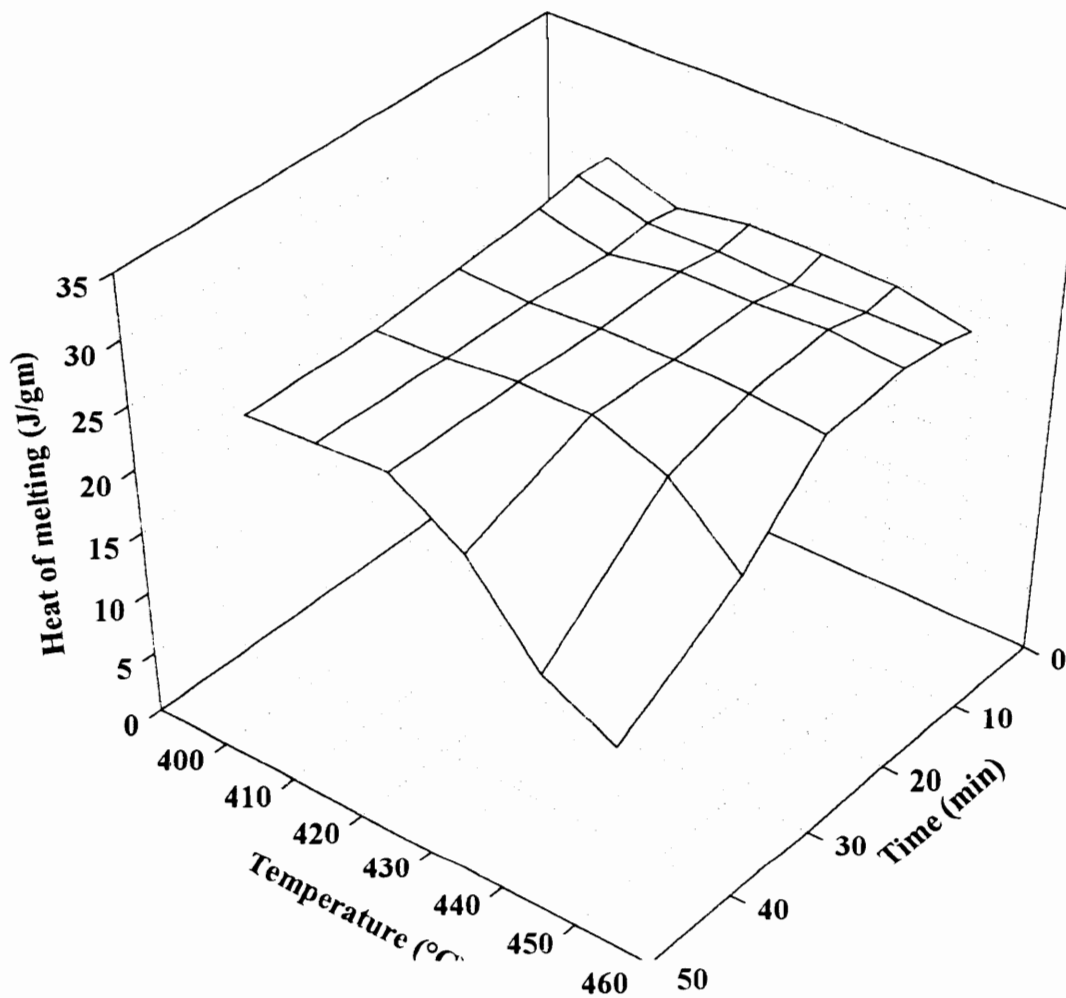


**Figure 5.15** Effect of time and temperature in the melt on the heat of melting of PA endcapped TPER 30K.

temperature as well, as suggested from the Hoffman-Weeks analysis discussed earlier. At a melt temperature of 430 °C, there was no change in the heat of melting up to a time in the melt of 30 min. Even at temperatures as high as 450 °C, the heat of melting remained unchanged for times as high as 20 min! *Thus, this study shows that any processing operation of this material can involve temperatures of 420-430 °C, for times up to 30 min, and still maintain the original heat of melting characteristics.* At a time of 45 min, for temperatures above 420 °C, or at a temperature of 450 °C for times above 20 min, there was, however, a drop in the heat of melting, implying a reduction in the degree of crystallinity. This is caused by chemical changes in the material induced by chain branching/crosslinking, as evidenced by an increase in the melt state viscosity, the results of which are discussed later.

The heat of crystallization (area under crystallization exotherm) dependence on the time and temperature in the melt is shown in Figure 5.16. As can be seen in the figure, the dependence of the heat of crystallization is qualitatively the same as the heat of melting shown in Figure 5.15, except that the drop in the heat of crystallization occurred under less harsh melt conditions than did the heat of melting. For example, under melt conditions of 420 °C and 45 min, the heat of melting did not show any drop, however, the heat of crystallization decreased by about 5% as compared to the value at a melt condition of 410 °C, 45mins. Under the most harsh condition studied here, i.e. 450 °C, 45 min, there was no crystallization exotherm on cooling, however the heat of melting showed a value that was about 50% of that observed under less harsh conditions. This is

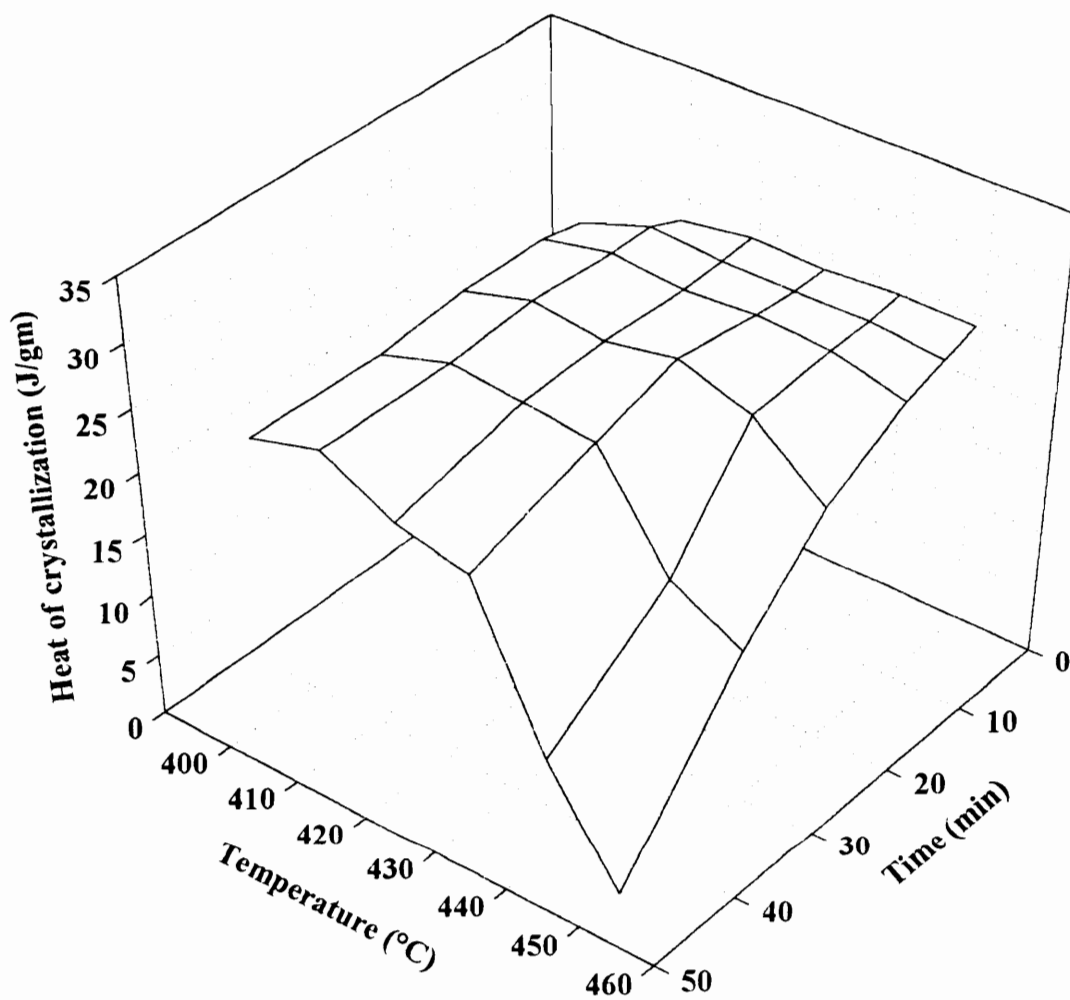


**Figure 5.16** Effect of time and temperature in the melt on the heat of crystallization of PA endcapped TPER 30K.

because some crystallization occurred on heating the sample from below the glass transition at 10 °C/min.

It is a well known fact that the rate of bulk crystallization depends on the both the crystal growth rate as well as nucleation density. The crystal growth rate is a function only of undercooling, however, at a given crystallization temperature, it is typically well known that the nucleation density of a sample crystallized by heating from below  $T_g$  is substantially higher than when cooled from the melt<sup>51</sup>. Under harsh melt conditions, there is an increase in the polymer molecular weight due to chain branching/crosslinking reactions accompanied by an increase in the melt viscosity, which would be expected to lead to a decrease in the crystal growth rate. This decrease in growth rate coupled with a reasonably low nucleation density could prevent the polymer from crystallizing during the cooling scan. However, on heating this amorphous polymer from below its  $T_g$ , the polymer crystallized during the heating scan due to a much larger nucleation density. This was evidenced by an exotherm observed immediately above the glass transition, which gave rise to a melting endotherm during the subsequent heating scan. A point to be emphasized here is that except for the case of harsh melt conditions, the heat of melting was essentially the same as the heat of crystallization. *This has important implications for the processing of this material, since the above data indicates that a substantial fraction of crystallinity is developed during the cooling scan, and no post-processing annealing step is required in order to generate crystallinity, as may be required for the case of slow crystallizing polymers.*

The variation of the melting temperature with varying melt temperatures and times is shown in Figure 5.17. An interesting point to note here is the fact that there is actually an increase in the melting temperature when the melt residence temperature increases from 400 °C to 410 °C. Recall that 400 °C is just at the tail end of the melting endotherm and below the equilibrium melting temperature. Thus, residence at this temperature even for very long times would probably not result in complete melting and would result in a melt having residual nuclei. The observed maximum crystallization temperatures after a melt residence temperature of 400 °C were ca. 10 °C above the maximum crystallization temperatures observed after melt temperatures of 410 °C, for all melt times, implying a large number of residual nuclei persisted after a melt treatment at 400 °C. For melt residence temperatures above 410 °C, there was a weak dependence of the maximum crystallization temperature on the prior melt residence temperature, implying that melt temperatures above 410 °C probably succeeded in effectively destroying a large fraction of residual nuclei in the melt. This is consistent with the Hoffman-Weeks prediction of the equilibrium melting temperature of 408 °C.

The melting temperature decreased with increasing temperatures in the melt for the case of the higher melt times, i.e. 20, 30 and 45 min, this decrease being prominent only at the highest melt time of 45 min. The maximum decrease in the melting temperature was observed to be ca. 14 °C on changing the melt time from 1 min to 45 min at a melt temperature of 450 °C. Under possible processing conditions (420 °C, 30 min) the melting temperature did not exhibit any decrease, implying that under these conditions

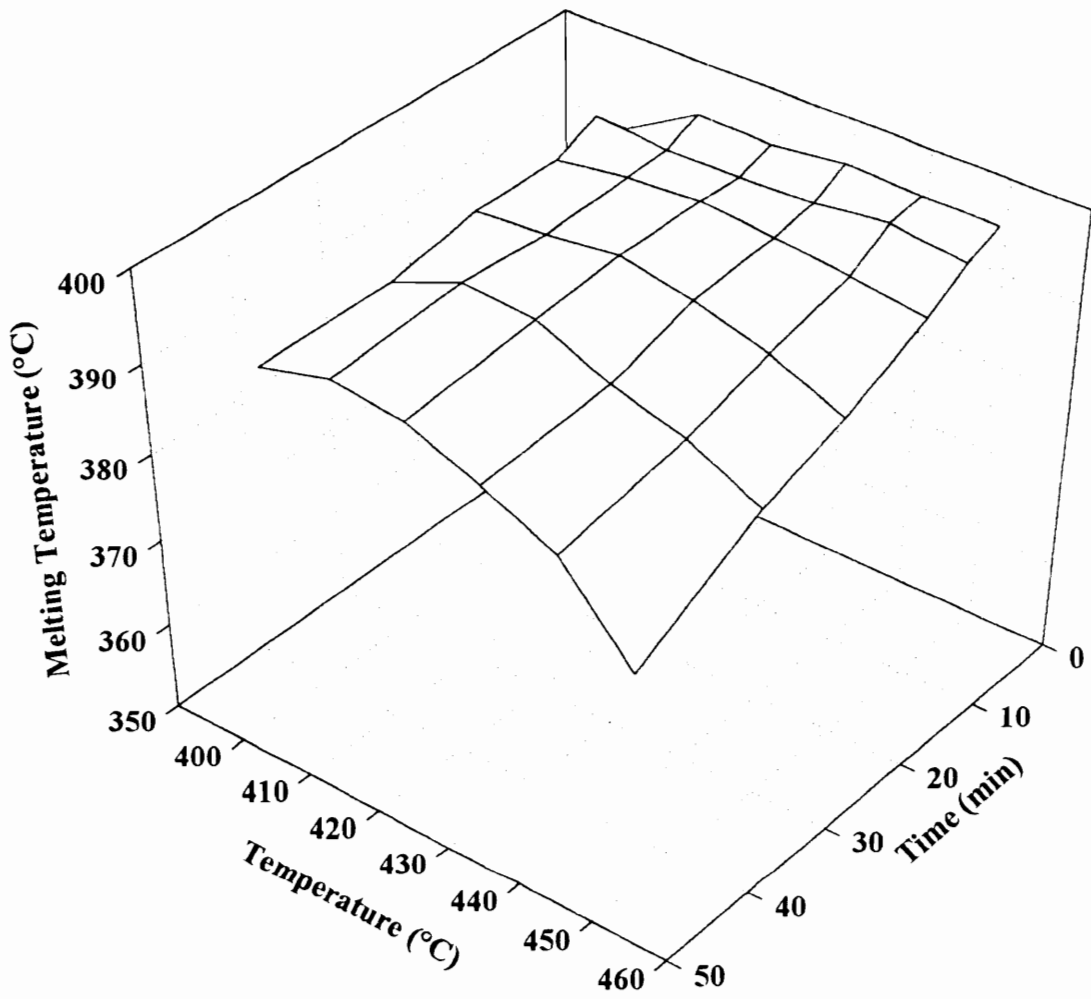


**Figure 5.17** Effect of time and temperature in the melt on the melting temperature of PA endcapped TPER 30K.

there was no substantial change in the chemical structure of the polymer. This, combined with the earlier findings regarding the heat of crystallization and heat of melting, present strong evidence in favor of the exceptional thermal stability of this polymer. The fact that the melting temperature and the heat of melting did not change under the same conditions that the heat of crystallization decreased (Fig. 5.16) indicates that this decrease was probably due to changes in nucleation density. The decrease in melt temperature with harsher melt conditions is certainly due to the fact that chemical changes like chain branching/crosslinking occur, leading to the formation of imperfect crystals, thus resulting in lower melting temperatures.

The variation of the heat of melting of Aurum™ New TPI as a function of melt time and temperature is shown in Figure 5.18. Since the crystallization kinetics of New TPI were very slow on cooling from the melt, samples of New TPI were quenched from the melt, and reheated at 10 °C/min. This caused crystallization to occur from the glass during the DSC heating scan. In contrast to the behavior exhibited by the TPER 30K polymer, the heat of melting of New TPI showed a strong dependence on the prior thermal history, in that higher temperatures and longer times in the melt caused the heat of melting to exhibit sharp decreases. The decrease in the heat of melting was more prominent at higher melt temperatures and longer melt times. For example, at a melt temperature of 420 °C, the heat of melting decreased to one-eighth of its original value when the melt time was increased from 1 min to 30mins. The decrease in the heat of melting was accompanied by a decrease in the melting temperature as well; on increasing

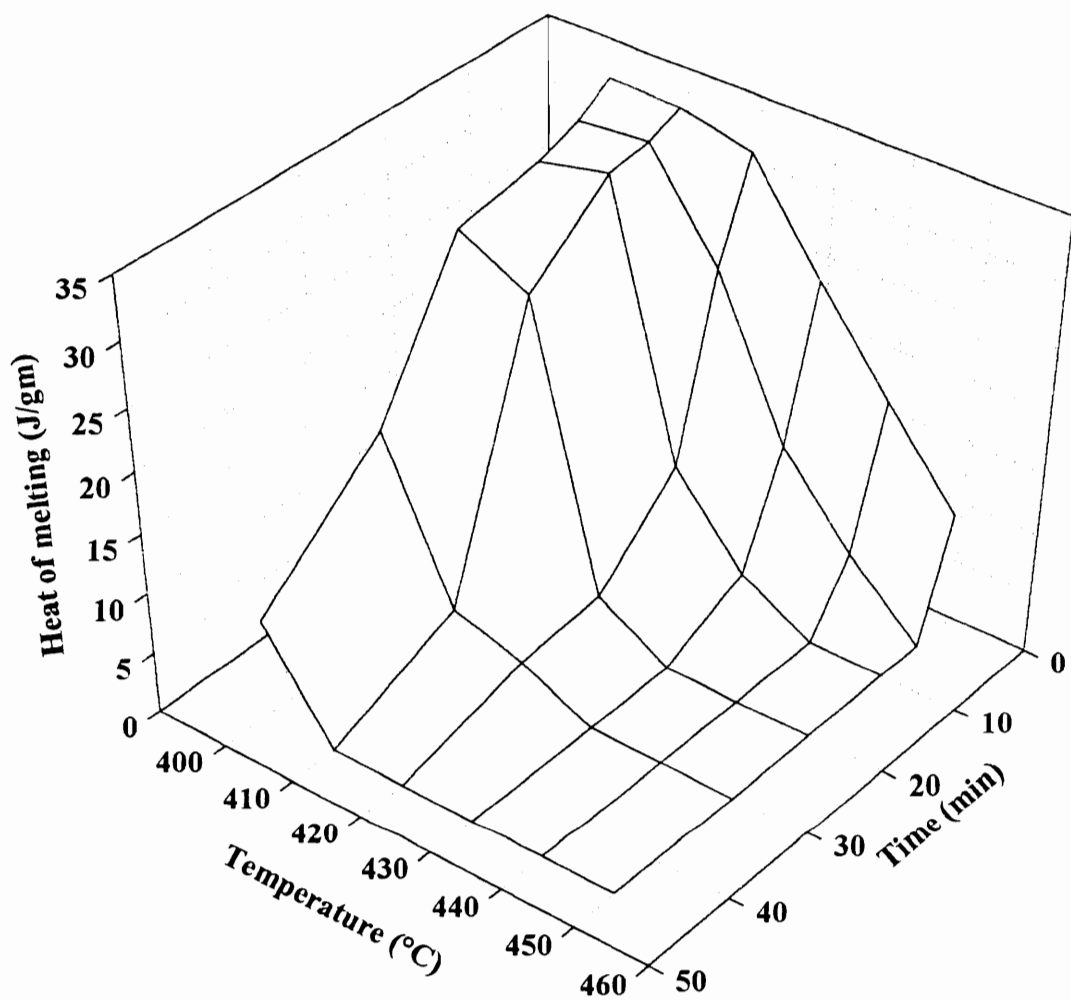


**Figure 5.18** Effect of time and temperature in the melt on the heat of melting of New TPI.

the melt time from 1 min to 30 min at 420 °C, the melting temperature decreased by ca. 4 °C. This decrease in the heat of melting of the New TPI polyimide with increasing time/temperature in the melt arises as a result of changes in both nucleation density as well as chemical changes like chain branching/crosslinking occurring in the melt.

The thermal stability of the TPER polyimide has also been compared to the stability of a similar stiff-chain polyimide, which was the focus of the previous chapter. Figure 5.19 shows the variation of the heat of melting of a PA endcapped TPEQ/ODPA polyimide as a function of time and temperature in the melt. Due to the slow crystallization kinetics of this system, samples of this polymer were also quenched from the melt, and reheated in order to study the crystallization and melting behavior. Just as was observed for the New TPI system, this polyimide also showed a strong dependence on the melt conditions, in that higher melt temperatures and longer melt times hindered the ability of the material to recrystallize in the time frame allowed in the experiment. The decrease in the heat of melting was in this case also accompanied by a decrease in the melting temperature, again implying that melt state chemical changes leading to an increase in molecular weight caused lower heats of melting<sup>6</sup>.

The above figures clearly emphasize the fact that the PA endcapped TPER 30K material shows superior thermal stability with respect to the crystallizability, as well as the ability to maintain high values of heats of melting. An important point to be noted here is that a simple TGA study revealed only that the 2% weight loss temperatures indicated

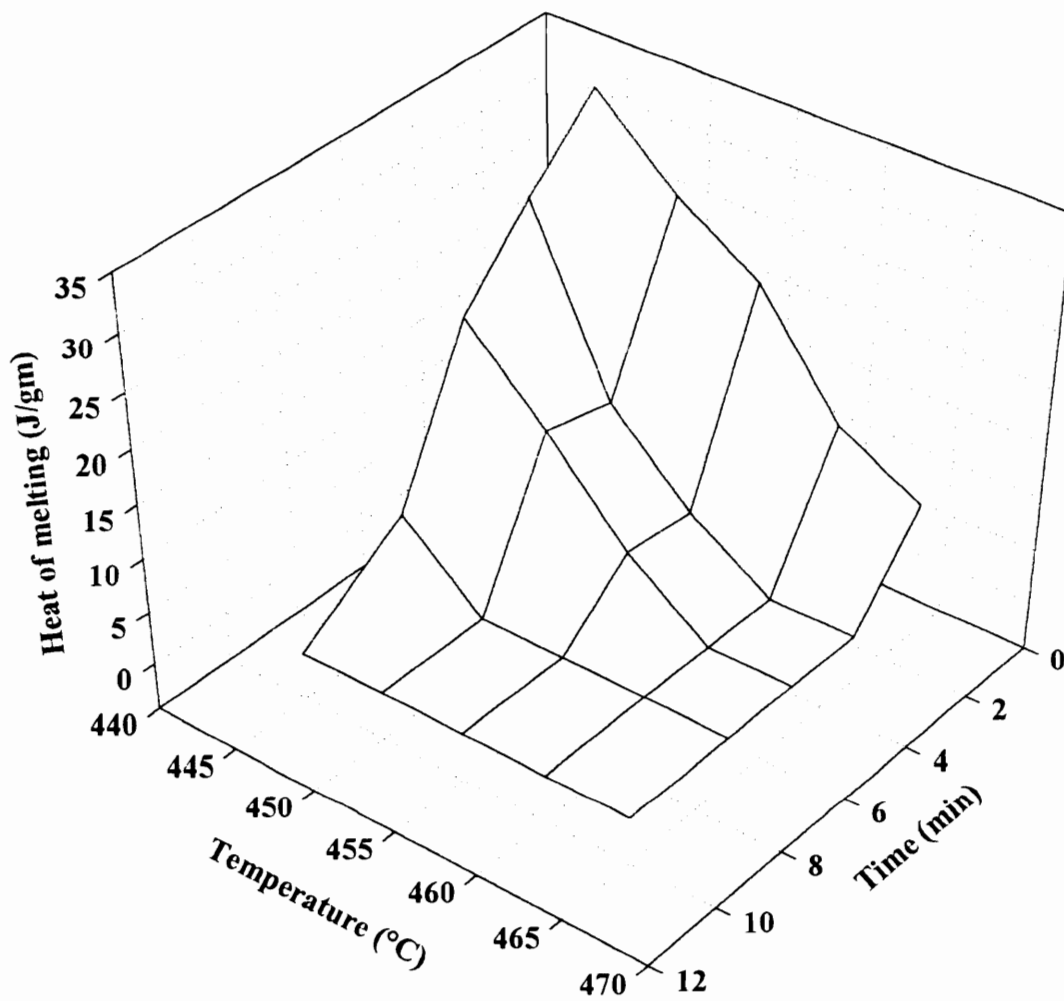


**Figure 5.19** Effect of time and temperature in the melt on the heat of melting of PA endcapped TPEQ/ODPA polyimide.

excellent thermal stability. Recall also that according to the TGA results, New TPI displayed superior thermal stability as compared to the TPER system.

The effect of varying endgroup chemistry on the thermal stability of the material was also investigated. Recall that the TGA studies indicated only that the 2% weight loss temperatures were independent of the nature of the endgroup, thus implying that endgroup chemistry does not influence the thermal stability of the polyimide. The DSC heating and cooling schedules used in this study were as follows: the samples were heated at 20 °C/min to 430 °C and held at this temperature for 30 min, following which they were cooled at a rate of 10 °C/min to room temperature. The samples were then heated at 10 °C/min up to 425 °C. Figure 5.20 shows the DSC cooling scans of the 3 samples- PA endcapped, half-endcapped and amine terminated TPER 30K samples. As can be seen from the DSC scans, the PA endcapped sample exhibited a prominent crystallization exotherm, consistent with the data presented earlier regarding the excellent thermal stability of this material. The half-endcapped sample exhibited only a small crystallization exotherm, indicating the reduced ability of this material to crystallize during the time frame allowed the material. The amine terminated sample did not exhibit any exotherm during the cooling cycle, implying that the melt treatment had suppressed the ability of this material to crystallize under the melt conditions utilized here. Figure 5.21 shows the subsequent DSC heating scans. Note that the PA endcapped sample displayed a weak glass transition, no exothermic activity beyond the glass transition region, and displayed a melting endotherm. The half-endcapped sample displayed a glass transition, followed by a

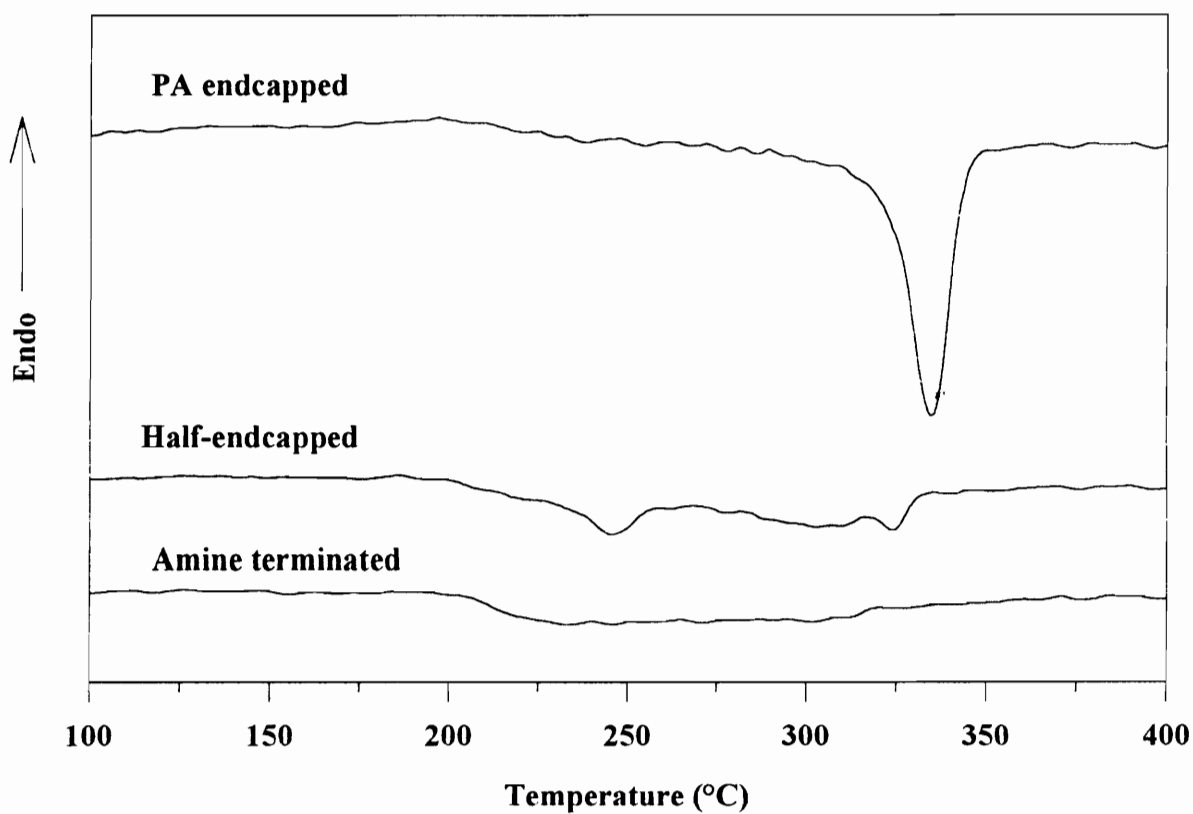


**Figure 5.20** DSC cooling scans for TPER 30K polyimide samples with different endgroups after a melt history of 430 °C, 30 min.

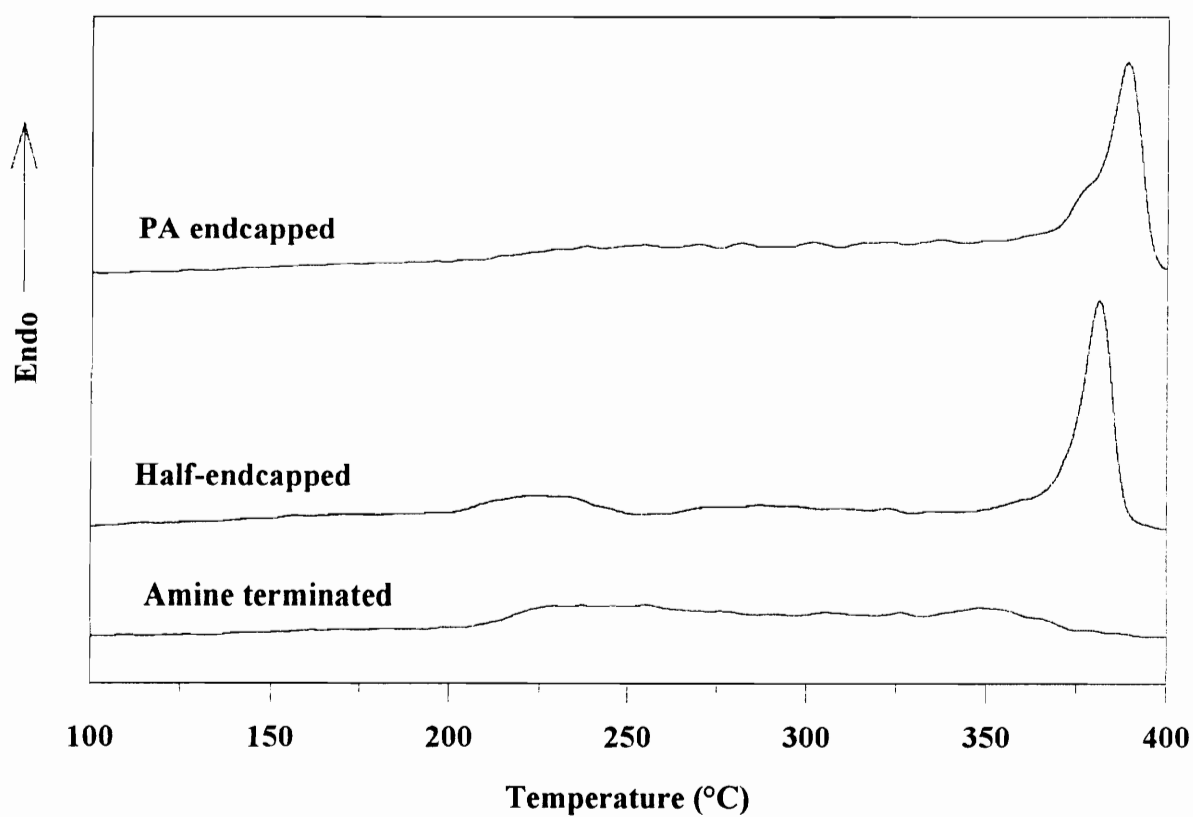


**Figure 5.21** DSC heating scans for TPER 30K polyimide samples with different endgroups after cooling as shown in Figure 5.20.

crystallization exotherm, and followed finally by a melting endotherm. Note that the melting temperature of the half-encapped sample is lower than that of the PA encapped sample. The amine terminated sample displayed a prominent glass transition, showed no evidence of any prominent exothermic event, and finally a weak melting endotherm, the position of which is lower compared to the other two samples. The data indicates the pronounced effect the endgroup nature has on the crystallization response after a melt treatment. The data discussed earlier in this section indicated that the PA encapped samples were not affected by a melt treatment of 430 °C for 30 min. The half-encapped sample was clearly affected by the melt state treatment as shown in Figures 5.20 & 5.21. The ability of the material to crystallize during the cooling scan was suppressed due to the melt treatment, resulting from a decrease in crystal growth rate. This is caused by an increase in the polymer molecular weight as evidenced by a rapid increase in melt viscosity as discussed in the next section. During the subsequent reheat, however, the polymer could crystallize due to the increased nucleation density, which resulted in a melting endotherm observed in the DSC scan. The depression of the melting temperature compared to the PA encapped polymer possibly results from the more imperfect crystals formed due to the chemical changes such as transimidization in the material. The melt treatment resulted in the almost complete suppression of the crystallizability of the amine terminated sample, again due to an increase in polymer molecular weight, to a greater extent than for the half-encapped sample, as shown by a greater increase in the melt viscosity. This increase in molecular weight not only prevented the polyimide from

crystallizing during the cooling scan, but also during the subsequent reheat as well. The few crystals that were formed were very imperfect which resulted in a minor endotherm observed at relatively low temperatures.

The fact that no crystallization is observed in the time scale allowed in the DSC scans could arise from either loss of nucleation or as a result of chemical changes discussed earlier. Reduction of the nucleation density would cause slower bulk crystallization kinetics, which could prevent crystallization from occurring in the time scale of the experiment, which is observed under some conditions in this study. The significant decrease in the melting temperature cannot however be the result of the destruction of residual nuclei. Chemical changes occurring in the material, like chain branching/crosslinking would all lead to an increase in the melt viscosity, and cause not only slower crystallization kinetics, but a reduction in melting temperature as well.

The endgroup study shows that effective endcapping of polyimides by phthalic anhydride (PA) groups greatly improves the thermal stability of the polymer. Amine endgroups are most susceptible to chain branching/crosslinking reactions leading to an increase in molecular weight and lower crystallizability. The half-endcapped polymer displays behavior that is intermediate to that of the PA endcapped polymer and the amine terminated system.

#### 5.4.6 *Rheological Studies*

The studies on the thermal stability of the polyimides indicated that under harsh melt conditions, the ability of the material to crystallize was hindered, this phenomenon having been attributed to chemical changes in the material leading to an increase in molecular weight. This hypothesis can be probed by utilizing rheological techniques since the melt state viscosity is critically dependent on the molecular weight of the system. Figure 5.22 shows the frequency dependence of the complex viscosity for the PA endcapped TPER 30K polyimide (420 °C, 3% strain). It can be seen from the figure that this polymer exhibited non-Newtonian shear thinning behavior in the range of frequencies studied. There seemed to be no Newtonian region even at frequencies as low as 0.1 Hz. From the figure, it can be seen that the complex viscosity decreased by a factor of ca. 150 (2 orders of magnitude) on increasing the frequency from 0.1 Hz to 100 Hz, i.e. over 3 decades in frequency. The second run denotes a frequency sweep experiment carried out on the sample at the end of the first run. As can be seen from the figure, the second run viscosities were higher than those observed during the first run, a result of chemical changes leading to an increase in molecular weight.

Isothermal viscosity sweeps were carried out on PA endcapped TPER 20K film, TPER 30K film, and TPER 30K powder (imidized in solution as discussed earlier), as well as New TPI film. Figure 5.23 shows the complex viscosity changes for the different samples as a function of time in the melt. Curves A represent the viscosity of the TPER 30K powder sample, with the open circles denoting the isothermal behavior at 430 °C, and

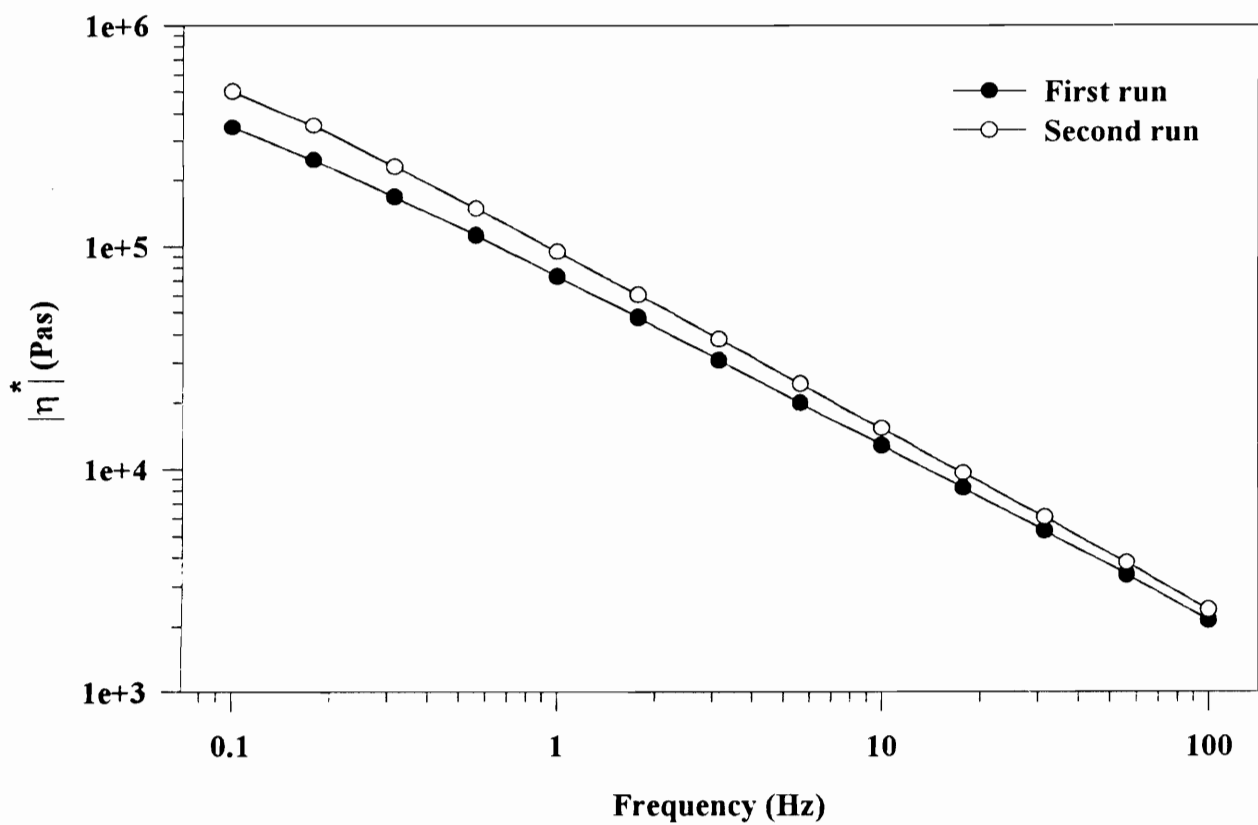


**Figure 5.22** Frequency dependence of complex viscosity for PA endcapped TPER 30K polyimide at 420 °C and 3% strain.

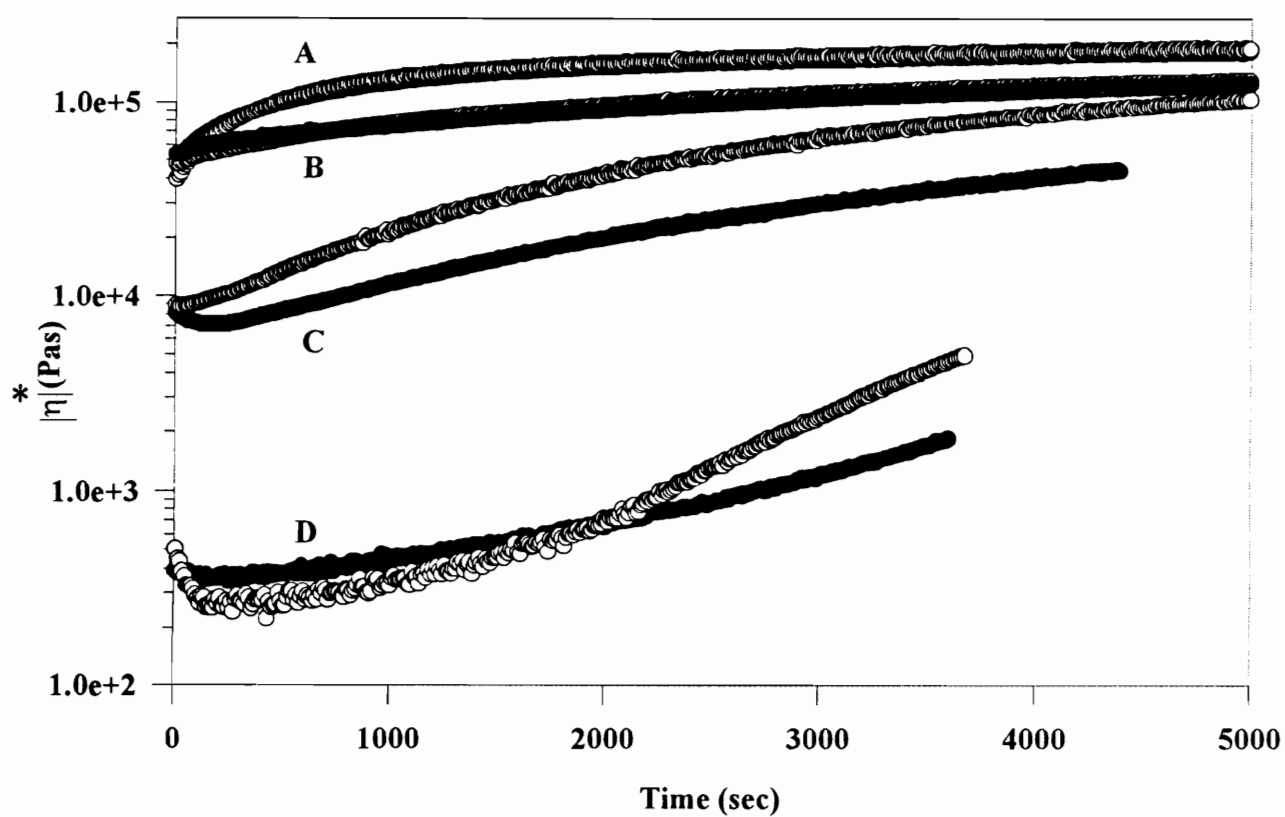


**Figure 5.23** Isothermal viscosity sweeps for PA endcapped TPER samples and New TPI at different temperatures.

the solid circles denoting the isothermal response at 420 °C. Curves B represent the viscosity dependence for the TPER 30K film, with the open circle representing the behavior at 430 °C, and the solid circles the behavior at 420 °C. Curves C are the viscosity dependence of the TPER 20K film (open circles- 426 °C, solid circles- 418 °C). Curves D are the viscosity response of New TPI (open circles- 430 °C, solid circles- 420 °C). It can be seen that the viscosity increased with time for all the samples studied here implying an increase in the polymer molecular weight as a function of time. This is speculated to occur due to chain branching/crosslinking reactions in the melt. At present it is only possible to speculate as to the causes behind the viscosity differences between the TPER 30K powder and the TPER 30K film. Since the starting viscosities of the TPER 30K powder and film are essentially identical, it can be reasonably assumed that their molecular weights were essentially identical prior to the melt treatment. After residence in the melt, however, the viscosity of the powder sample increase more rapidly and attains a higher value compared to the film sample after a long residence time in the melt, as can be seen in the figure. This implies that the powder sample undergoes chemical reactions like crosslinking/branching more rapidly than the film sample. As discussed later, amine endgroups are more susceptible to crosslinking reactions than phthalic anhydride endgroups. It can therefore be speculated that the powder samples, which were imidized in solution at low temperatures contains a larger fraction of amine endgroups compared to the film sample which had undergone thermal imidization at higher temperatures. For both these samples, there is no appreciable difference in the viscosity change with time for

melt temperatures of 420 °C and at 430 °C, on the log scale displayed in the figure. However, when plotted on an expanded scale, it was obvious that the viscosity increase was more prominent for a melt temperature of 430 °C, as compared to a melt temperature of 420 °C, implying that residence at higher melt temperatures caused an increase in the rate of the chemical changes giving rise to the branching/cross-linking reactions as would be expected. From the data it is obvious that the early time viscosity was lower at a melt temperature of 430 °C as compared to 420 °C and increased to a higher value after 30 min in the melt, again implying that, not surprisingly, higher melt temperatures caused an increase in the rate of branching/cross-linking reactions in the system. For the case of the TPER powder samples, the viscosity increased by almost a factor of 3 after 30 min at a melt temperature of 420 °C. For the case of the TPER film samples, the viscosity increased only by ca. 65% after 30 min at a melt temperature of 420 °C. At a melt temperature of 430 °C, however, the viscosity almost doubled after 30 min for the case of the TPER 30K film. For the case of the TPER 20K sample, at a melt temperature of 418 °C, the viscosity increased by a factor of 2 after 30 min in the melt. At a melt temperature of 426 °C, the viscosity increased to almost 4 times the original value over the same time period. A point worth noting is the much lower starting viscosity of the 20K polyimide as compared to the 30K polymer, which is to be expected. The rate of increase in viscosity as a function of melt time was greater for the 20K polymer as compared to the 30 K system, especially at higher temperatures. This could perhaps be attributed to the presence of a larger fraction of endgroups in the lower molecular system, which could

imply that any chemical changes occurring in the melt could involve the endgroups. It can be seen that for the case of New TPI, the viscosity did not show any appreciable increase for times up to 30 minutes at melt temperatures of 420 °C and 430 °C, implying no appreciable molecular weight changes occurred in the system. Recall that in this same time range, the DSC results indicated a major decrease in the crystallizability of the New TPI system. This decrease in crystallizability cannot thus be attributed to any appreciable changes in molecular weight. The drop in crystallizability can thus be at least partially attributed to changes in nucleation density of the polymer due to the melt treatment. The decrease in the melting temperature of the New TPI polyimide with increasing melt time and temperature, however, indicates some chemical changes occurring in the system. These chemical changes could occur without any substantial increase in molecular weight, and are possibly the cause of the drastic reduction in crystallizability of this polymer with increasing melt time/temperature.

A point worth mentioning here is that the TPER system utilized in this study was a relatively high molecular weight system which was received in the form of creasable films. Mechanical properties studies (not shown here) carried out at room temperature indicated that the semicrystalline films of the TPER system exhibited considerable toughness as evidenced by the high strain to break. The New TPI material was, however, of lower molecular weight as evidenced not only by the lower melt viscosities, but also by the fact that once crystallized, the films were extremely brittle, i.e. showed very low strain to break resulting in poor creasability. In spite of this difference in molecular weight, the TPER

polyimide showed very fast rates of bulk crystallization, whereas the New TPI system could easily be quenched into an amorphous form.

In the earlier section on thermal stability it was shown that the nature of endgroups played a critical role in determining the thermal stability as evidenced by changes in crystallizability. The isothermal viscosities for samples with different endgroups as a function of time in the melt at 430 °C are shown in Figure 5.24. It can be seen from the figure that the rate of increase in viscosity increased in the order: amine endcapped > half-endcapped > PA endcapped. This figure clearly emphasizes the importance of endgroups in determining the high temperature stability of polyimides. Amine endgroups seem to be much more susceptible to chain extension/branching/cross-linking than phthalimide endgroups which is consistent with basic considerations. The viscosity increase explains the decrease in crystallizability of the amine terminated and half-endcapped polyimides as compared to the completely endcapped system after residence in the melt.

## 5.5 Conclusions

The synthesis and characterization of a reasonably high molecular weight, thermally stable polyimide displaying high transition temperatures ( $T_g$  and  $T_m$ ) has been reported here. This polyimide is based on phthalimide endcapped 1,3-bis(4-aminophenoxy)benzene (TPER diamine) and 3,3', 4,4'-biphenyl tetracarboxylic dianhydride (BPDA). The excellent thermal stability of this system is evidenced by the

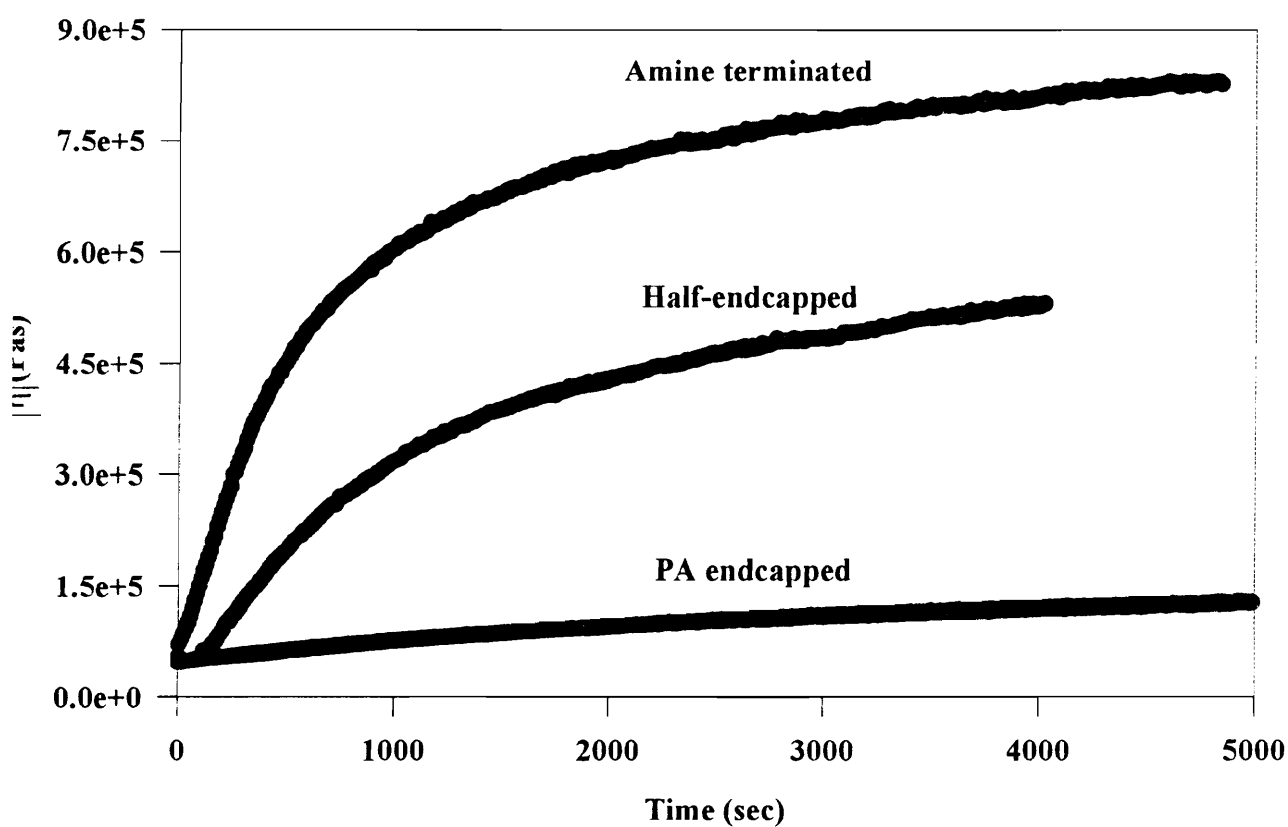


**Figure 5.24** Isothermal viscosity sweeps for TPER 30K polyimide with different endgroups at 430 °C.

results of TGA studies, melt time and temperature studies on the DSC as well as rheological studies. Rheological as well as crystallization studies showed that the nature of the endgroups played a critical role in determining the thermal stability of these polyimides. Polyimide samples with no non-reactive endcapping (amine endgroups) and half-endcapped with phthalic anhydride exhibited distinctly lower thermal stability in the melt compared to a PA endcapped system, as evidenced by large viscosity increases causing a dramatic decrease in the crystallizability. In spite of the reasonably high molecular weight and high melt viscosity of this polymer, this system displayed extremely fast crystallization kinetics, evidenced by the inability to quench this polymer into the fully amorphous state. The lower molecular weight New TPI material displayed a lower melt viscosity but showed much slower crystallization kinetics, as evidenced by the ease with which this material could be quenched into the amorphous state. The apparent lower molecular weight of the New TPI studied here also resulted in a very brittle, low toughness behavior, of the crystallized sample, which was in contrast to the TPER films which showed non-brittle behavior resulting in very good creasability. Even though the TGA results indicated the superior thermal stability of New TPI as compared to the TPER polyimide, a more detailed investigation based on melt time/temperature studies showed the superior stability characteristics of the TPER polyimide with respect to the crystallization and melting behavior.

The melting behavior of this polymer showed some unique features which included the sharp melting endotherm after non-isothermal as well as isothermal crystallization.

The melting endotherm of the as-received sample was, however, observed to be broad. This behavior of the melting endotherms has been attributed to a broad distribution of crystal thicknesses for the as-received sample, and a narrow distribution of crystal thicknesses for a slow cooled sample as shown by SAXS results. This distribution of crystal thicknesses has also been shown to have an effect on the amorphous phase properties causing different relaxation responses during dynamic mechanical studies. The melting behavior of this polymer included multiple melting endotherms (Peaks I, II and III) which have been assigned to a  $T_c+10$  °C type endotherm (Peak I), the melting of the crystals present in the sample before the DSC scan (Peak II), their subsequent recrystallization followed by melting to yield the highest temperature endotherm (Peak III). Imperfect crystals and thin crystals have been shown to be more susceptible to melting/ recrystallization than thicker and more perfect crystals.

## **Acknowledgments**

The authors would like to acknowledge the NSF Science and Technology Center for High Performance Polymeric Adhesives and Composites for full support of this study under contract number DMR 9120004. The assistance of Ravi Verma in collecting the SAXS data at the Du Pont Experimental Station is acknowledged. The assistance of Robert Young in collecting some rheological data is also acknowledged.

## References

1. Feger, C. J.; Khojasteh, M. M.; McGrath, J. E., Eds., *Polyimides: Materials, Chemistry and Characterization*; Elsevier Science Publishers B. V.: Amsterdam, 1989.
2. Mittal, K. L., Ed., *Polyimides: Synthesis, Characterization and Applications Vols. 1 & 2*; Plenum: New York, 1984.
3. Wilson, D.; Stenzenberger, H. D.; Hergenrother, P. M., Eds., *Polyimides*; Blackie & Son Ltd.: Glasgow and London, 1990.
4. Muellerleile, J. T.; Risch, B. G.; Rodrigues, D. E.; Wilkes, G. L.; Jones, D. M. *Polymer* **1992**, *34*, 789.
5. Bandom, D. K.; Wilkes, G. L. *Polymer* **1995**, *36*, 4083.
6. Srinivas, S.; Graham, M.; Brink, M. H.; Gardner, S.; Davis, R. M.; McGrath, J. E.; Wilkes, G. L. Accepted for publication in *Polym. Eng. and Sci.*
7. Rogers, M. E.; Brink, M. H.; Brennan, A.; McGrath, J. E. *Polymer* **1993**, *34*, 849.
8. Kim, Y. J.; Glass, T. E.; Lyle, G. D.; McGrath, J. E. *Macromolecules* **1993**, *26*, 1344.
9. Brink, M. H.; Bandom, D. K.; Wilkes, G. L.; McGrath, J. E. *Polymer* **1994**, *35*, 5018.
10. Hergenrother, P. M.; Wakelyn, N. T.; Havens, S. J. *J. Polym. Sci., Polym. Chem. Ed.* **1987**, *25*, 1093.

11. Hergenrother, P. M.; Havens, S. J. *J. Polym. Sci., Polym. Chem. Ed.* **1989**, *27*, 1161.
12. Hergenrother, P. M.; Beltz, M. W.; Havens, S. J. *J. Polym. Sci.: Part A: Polym. Chem.* **1991**, *29*, 1483.
13. Heberer, D. P.; Cheng, S. Z. D.; Barley, J. S.; Lien, H. S.; Bryant, R. G.; Harris, F. W. *Macromolecules* **1991**, *24*, 1890.
14. Cheng, S. Z. D.; Heberer, D. P.; Lien, H. S.; Harris, F. W. *J. Polym. Sci.: Part B: Polym. Phys.* **1990**, *28*, 655.
15. Cella, J. A. *Polym. Degrad. Stab.* **1992**, *36*, 99.
16. Kreuz, J. A.; Hsiao, B. S.; Renner, C. A.; Goff, D. L. *Macromolecules* **1995**, *28*, 6926.
17. Hsiao, B. S.; Kreuz, J. A.; Cheng, S. Z. D. *Macromolecules* **1996**, *29*, 135.
18. Friler, J. B.; Cebe, P. *Polym. Eng. and Sci.* **1993**, *33*, 587.
19. Huo, P. P.; Cebe, P. *Polymer* **1993**, *34*, 696.
20. Huo, P. P.; Friler, J. B.; Cebe, P. *Polymer* **1993**, *34*, 4387.
21. Brillhart, M. V.; Cebe, P. *J. Polym. Sci.: Part B: Polym. Phys.* **1995**, *33*, 927.
22. Lu, S. X.; Cebe, P.; Capel, M. *J. Appl. Polym. Sci.* **1995**, *57*, 1359.
23. Hsiao, B. S.; Sauer, B. B.; Biswas, A. *J. Polym. Sci.: Part B: Polym. Phys.* **1994**, *32*, 737

24. Konas, M.; Moy, T. M.; Rogers, M. E.; Shultz, A. R.; Ward, T. C.; McGrath, J. E. *J. Polym. Sci.: Part B: Polym Phys.* **1995**, *33*, 1429.
25. Konas, M.; Moy, T. M.; Rogers, M. E.; Shultz, A. R.; Ward, T. C.; McGrath, J. E. *J. Polym. Sci.: Part B: Polym Phys.* **1995**, *33*, 1441.
26. Bell, V. L.; Stump, B. L.; Gager, H. *J. Polym. Sci.* **1976**, *14*, 2275.
27. Chung, J. S.; Cebe, P. *Polymer* **1992**, *33*, 2312.
28. Chung, J. S.; Cebe, P. *Polymer* **1992**, *33*, 2325.
29. Cheng, S. Z. D.; Cao, M. Y.; Wunderlich, B. *Macromolecules* **1986**, *19*, 1868.
30. Bandom, D. K.; Wilkes, G. L. *Polymer* **1994**, *35*, 5672.
31. Hsiao, B. S.; Sauer, B. B.; Verma, R. K.; Zachmann, H. G.; Seifert, S.; Chu, B.; Harney, P. *Macromolecules* **1995**, *28*, 6931.
32. Blundell, D. J.; Osborn, B. N. *Polymer* **1983**, *24*, 953.
33. Lee, Y.; Porter, R. S. *Macromolecules* **1987**, *20*, 1336.
34. Lee, Y.; Porter, R. S.; Lin, J. S. *Macromolecules* **1989**, *22*, 1756.
35. Bassett, D. C.; Olley, R. H.; Al Raheil, I. A. M. *Polymer* **1988**, *29*, 1745.
36. Lattimer, M. P.; Hobbs, J. K.; Hill, M. J.; Barham, P. J. *Polymer* **1992**, *33*, 3971.
37. Cebe, P.; Hong, S. *Polymer* **1986**, *27*, 1183.
38. Verma, R. K.; Kander, R. G.; Velikov, V.; Marand, H.; Hsiao, B. S.; Chu, B. *Bull. Am. Phys. Soc.* **1994**, *39*, 109.
39. Jonas, A. M.; Russell, T. P.; Yoon, D. Y. *Macromolecules* **1995**, *28*, 8491.

40. Hoffman, J. D.; Davis, G. T.; Lauritzen, J. L. *Treatise on Solid State Chemistry Vol. 3*; Hannay, N. B., Ed.; Plenum: New York, 1976.
41. McCrum, N. G.; Read, B. E.; Williams, G. *Anelastic and Dielectric Effects in Polymeric Solids*; Dover: New York, 1967.
42. Jonas, A.; Legras, R. *Macromolecules* **1993**, *26*, 813.
43. Krishnaswamy, R. K.; Kalika, D.S. *Polymer* **1994**, *35*, 1157.
44. Coburn, J. C.; Boyd, R. H. *Macromolecules* **1986**, *19*, 2238
45. Sauer, B. B.; Hsiao, B. S. *Polym. Mater. Sci. Eng.* **1993**, *69*, 35.
46. Lovinger, A. J.; Hudson, S. D.; Davis, D. D. *Macromolecules* **1992**, *25*, 1752.
47. Santa-Cruz, C.; Stribeck, N.; Zachmann, H. G.; Baltá Calleja, F. J. *Macromolecules* **1991**, *24*, 5980.
48. Verma, R. K.; Biswas, A.; Marand, H.; Hsiao, B. S. *J. Appl. Crystallography*, submitted for publication.
49. Sukuki, H.; Wunderlich, B. *Makromol. Chem.* **1985**, *189*, 1109.
50. Cheng, S. Z. D.; Wu, Z. Q.; Wunderlich, B. *Macromolecules* **1987**, *20*, 2802.
51. D. W. van Krevelen, *Chimia*, **32**, 279 (1978).

## Chapter - 6

### Structural and Crystallization Studies of New TPI Polyimide

#### 6.1 Abstract

The effect of crystallization time and temperature on the crystallization, melting and relaxation behavior has been studied for a series of cold-crystallized samples of a commercial polyimide, Mitsui Toatsu's New TPI. Dynamic mechanical studies showed a representative amorphous sample (crystallized at 300 °C for 2.2 min) to display a  $\tan \delta$  glass transition temperature of 271 °C at 1 Hz; DSC studies on the same sample yielded a  $T_g$  of 249 °C. The glass transition temperature as measured by both DSC and dynamic mechanical experiments decreased with increasing crystallization temperature; the degree of crystallinity, however, was shown to increase with increasing crystallization temperature. An interesting feature noted was that the  $T_g$ 's, as measured by DSC for samples crystallized at various temperatures, were shifted upward at most by only 2 °C above that of a fully amorphous sample. Dynamic mechanical experiments, however, showed that the  $T_g$ 's of the same samples were shifted upward by ca. 10 °C relative to a representative amorphous sample. SAXS results showed that both the average lamellar and amorphous layer thicknesses increased with increasing crystallization temperature. Increasing crystallization time at a given crystallization temperature produced an increase in  $T_g$  as measured by both DSC as well as dynamic mechanical experiments, with the

increase following a log time dependence. An interesting feature observed from the dynamic mechanical studies was that for low crystallization times, the dependence of  $T_g$  on crystallization time was different than for higher crystallization times. WAXS studies showed the degree of crystallinity to increase with increasing crystallization time; at lower crystallization times a prominent increase was observed due to a primary crystallization process, following which a further gradual increase in crystallinity was observed corresponding to a secondary crystallization process. This was accompanied by a decrease in the average lamellar thickness as shown by SAXS studies; the average amorphous layer thickness, however, remained unchanged with increasing crystallization time. This has been explained on the basis of a secondary crystallization process leading to the formation of thinner lamellae in the amorphous regions between different lamellar stacks, which gives rise to the lower melting endotherm ( $T_c+10$ ) observed in DSC scans. The results discussed here suggest that a bimodal distribution of lamellar thicknesses are formed as a result of the primary followed by secondary crystallization processes.

## **6.2 Introduction**

Recent interest in the development of polymeric materials for use in engineering applications has led to extensive research in the area of high temperature/high performance polymers. A basic requirement for a high temperature, high performance polymer is that it should have mechanical and structural integrity at elevated temperatures. This implies that the

polymer should have a glass transition temperature ( $T_g$ ) above the maximum use temperature. The advantage of using semicrystalline thermoplastics is that they can be used at temperatures above their glass transition temperature if sufficient crystallinity exists, since the crystallites act as physical crosslinks which maintains dimensional stability of the polymer, i.e. minimizes the degree of softening. High performance semicrystalline thermoplastics also display greater solvent and water resistance, and improved thermal and radiation stability as compared to their amorphous counterparts.

Perhaps the most important category of high performance thermoplastic polymers are the aromatic polyimide based systems. These polymers, if of reasonable molecular weight, are tough, rigid and thermo-oxidatively stable polymers and possess excellent mechanical properties, and chemical and radiation resistance. These properties have made them suitable for use in a variety of engineering applications such as electrical and electronic applications, aerospace applications, adhesives, and as composite matrix materials<sup>1-4</sup>. The increasing importance of this polymer system has resulted in a variety of studies on polyimides by various research groups<sup>5-21</sup>. The aromatic rings in the backbone of these polymers impart high stiffness often resulting in high glass transition ( $>200$  °C) and melting temperatures ( $\sim 400$  °C). These high transition temperatures can often be detrimental as the temperatures needed to process these polymers have to be well above the transition temperatures, which may, depending on the chemistry and atmosphere, possibly result in some chemical changes (degradation) of these polymers. Efforts have therefore concentrated in improving the thermal stability of these polymers as well as reducing the transition

temperatures by increasing the flexibility of the polymer molecule by introducing meta linkages, and ether and carbonyl groups in the backbone of the chain.

A recent commercially available crystallizable polyimide is Mitsui Toatsu's "New TPI", which has been the subject of considerable study over the past few years<sup>9,22-32</sup>. New TPI, the structure of which is shown in Figure 6.1, is based on pyromellitic dianhydride (PMDA) and 3,3'-bis(4-aminophenoxy) biphenyl diamine (BAPB). At present, there is no information on the nature of the endgroups of this polymer; as reported recently, the nature of the endgroups can play a significant role in influencing the thermal stability of high temperature polyimides<sup>9</sup>. The structure shows the presence of flexible ether linkages and meta substituted phenyl groups, resulting in an observed glass transition of ca. 250 °C (DSC) and an observed melting temperature of 385 °C<sup>9</sup>. This system exhibits good thermal stability as evidenced by the high values of 2% weight loss temperatures (545 °C) in air as well as nitrogen, by TGA studies<sup>9</sup>. Earlier work discussed in the previous chapter, addressed the effect of thermal history on the subsequent crystallization and melting behavior of New TPI, which showed that the loss of crystallizability of the polyimide with increasing melt time/temperature was caused due to a drop in the nucleation density as well as chemical changes occurring in the material<sup>9</sup>. Rheological studies also showed the shear thinning behavior of this system with increasing frequency (unpublished data), while isothermal rheological studies showed an increase in complex viscosity with increasing time in the melt<sup>9</sup>.

The unit cell crystal structure of New TPI as shown by Okuyama et al.<sup>29</sup> is orthorhombic with dimensions  $a=7.89 \text{ \AA}$ ,  $b=6.29 \text{ \AA}$ , and  $c=25.11 \text{ \AA}$ , with the chain axis along

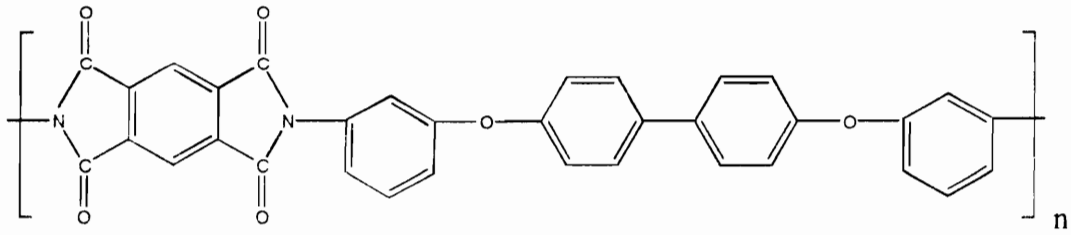


**Figure 6.1** Chemical structure of New TPI.

the  $c$  axis. Based on a two chain based unit cell, this results in a crystal density of  $1.47 \text{ gm/cm}^3$ , while the amorphous density has been reported<sup>32</sup> to be  $1.33 \text{ gm/cm}^3$ . Crystalline samples have been shown to exhibit a stacked lamellar morphology as shown by small angle x-ray scattering (SAXS) studies<sup>22,23,25,27</sup>. Based on a Hoffman-Weeks extrapolation, the equilibrium melting temperature was reported to be  $406 \text{ }^\circ\text{C}$  by Hsiao et al.<sup>22</sup>,  $400 \text{ }^\circ\text{C}$  by Cebe et al.<sup>25</sup>, and  $399 \text{ }^\circ\text{C}$  by Maffezzoli et al.<sup>28</sup>. Melt crystallized samples exhibited negatively birefringent spherulites with Maltese cross patterns, with the crystal  $b$  axis oriented along the radial growth direction<sup>22</sup>. Isothermal crystallization kinetic studies were carried out by Hsiao et al.<sup>22</sup>, Cebe et al.<sup>25</sup>, and Maffezzoli et al.<sup>28</sup> and analyzed using the Avrami approach. Hsiao et al.<sup>22</sup> observed that isothermal crystallization from the melt occurred with an Avrami exponent of 4, whereas, in contrast, Maffezzoli<sup>28</sup> reported Avrami exponents of 2 during isothermal crystallization from the melt. Isothermal crystallization from the glass yielded Avrami exponents ranging from 2.8 to 3.5 depending on the crystallization temperature<sup>25</sup>. The non-isothermal crystallization kinetic studies were studied and analyzed using the Ozawa approach<sup>23</sup>. Spherulitic growth rate studies were carried out by Hsiao et al.<sup>22</sup>, and the data analyzed using the Hoffman-Lauritzen approach. The product of the surface energies  $\sigma\sigma_e$  (fold surface and lateral surface) for the lamellar crystals was calculated from the spherulitic growth rate data using the Hoffman-Lauritzen approach and the value was found to be  $1176 \text{ erg}^2/\text{cm}^4$ . The heat of fusion for a 100 % crystalline material reported by the manufacturer is  $139 \text{ J/gm}^3$ <sup>32</sup>.

The effect of crystallization time and temperature on the crystallization, melting and relaxation behavior of a series of cold-crystallized samples of Aurum™ New TPI has been

investigated in this study. The crystallization and melting behavior have been studied utilizing differential scanning calorimetry (DSC) in conjunction with wide angle x-ray scattering (WAXS). Structural changes occurring in the polymer have been investigated using small angle x-ray scattering (SAXS) in conjunction with dynamic mechanical analysis (DMS). By combining these results, along with previous work by others, it is hoped that a more comprehensive picture of the crystallization process in New TPI will emerge.

## **6.3 Experimental**

### *6.3.1 Sample preparation*

The New TPI used in this study was in the form of amorphous extruded film. Samples of this film were sandwiched between Teflon sheets and annealed at 265 °C for 10 min in a preheated hot press in order to remove any orientational/residual stresses in the film which may have arisen as a result of processing. No pressure was applied while the platens of the hot press were kept in contact with the samples. No shrinkage of the films was observed after this annealing step, indicating no appreciable orientation in the as-received films. After the annealing step, the films were crystallized at different temperatures for various times in a hot press that was already maintained at the required temperature. Again, no pressure was applied to the samples. At the end of the crystallization step, the hot press was switched off and the samples allowed to slow cool below  $T_g$ .

### 6.3.2 Characterization techniques

DSC experiments were carried out on a Perkin Elmer DSC 7, under a nitrogen purge, using heating rates of 10 °C/min. Temperature and heat flow were calibrated using indium and zinc as the standards. The weight of all samples were kept as consistent as possible (ca. 9.5 mg). The DSC traces shown here have been normalized to a 1 mg sample mass.

Dynamic mechanical experiments were carried out on a Seiko DMS 210 under a nitrogen purge. The heating rate used in all experiments was 1 °C/min. Sample lengths of 10 mm and cross-section area of ca. 0.3 mm<sup>2</sup> were tested at frequencies ranging from 0.01 Hz to 20 Hz.

Small angle x-ray scattering (SAXS) experiments were performed on a Kratky camera using Ni filtered CuK<sub>α</sub> radiation ( $\lambda=1.54 \text{ \AA}$ ) and equipped with a M Braun position sensitive detector. The methods used for the data analysis are described along with the results.

Wide angle x-ray scattering (WAXS) experiments were conducted on a Nicolet diffractometer equipped with a STOE Bragg-Brentano type goniometer. CuK<sub>α</sub> radiation of wavelength 1.54 Å was used after monochromatization through a graphite monochromator. Data were collected at 0.05° increments at angles between 5-70°. The theory and methods used to analyze the WAXS data are also described along with the results.

## 6.4 Results And Discussion

### 6.4.1 WAXS studies

The determination of the degree of crystallinity in polymers using WAXS relies on the ability to deconvolute the scattering occurring due to the crystalline and amorphous regions from the total scattering. The crystalline fraction in a polymer is therefore the ratio of the integrated scattering arising from the crystalline domains to the total integrated scattering arising from the entire sample.

The total integrated scattering from a semicrystalline polymer over all reciprocal space can be written as<sup>33</sup>

$$4\pi \int_0^{\infty} s^2 I(s) ds = 4\pi \int_0^{\infty} s^2 \bar{f}^2 ds \quad (1)$$

where

$$\bar{f}^2 = \frac{\sum N_i f_i^2}{\sum N_i} \quad (2)$$

is the mean-square atomic scattering factor of the polymer, and  $s$  is the angular variable defined as  $2\sin\theta/\lambda$ , where  $2\theta$  is the radial scattering angle.

The scattering from the crystalline regions over all reciprocal space can similarly be written as

$$4\pi \int_0^{\infty} s^2 I_c(s) ds = 4\pi X_c \int_0^{\infty} s^2 \bar{f}^2 ds \quad (3)$$

where  $X_c$  is the degree of crystallinity

The degree of crystallinity can hence be determined by the following equation

$$X_c = \frac{\int_0^{\infty} s^2 I_c(s) ds}{\int_0^{\infty} s^2 I(s) ds} \quad (4)$$

However, the above equation underestimates the degree of crystallinity due to the fact that part of the scattering from the crystalline regions does not contribute to the crystalline peaks, but appears as diffuse scattering, thereby contributing to the amorphous scattering. This diffuse scattering contribution from the crystalline regions is due to two reasons: atomic thermal vibrations and lattice imperfections. The methods most commonly used to determine the degree of crystallinity do not take into account the diffuse scattering from the crystalline regions (e.g. the Hermans and Weidinger method). These methods could hence yield degree of crystallinity values that are smaller than the actual values. Perhaps the only method that takes into account the diffuse scattering arising from thermal vibrations and lattice imperfections, is the method due to Ruland<sup>34,35</sup>. This method takes into account the loss of intensity of the crystalline peaks due to the diffuse scattering by including a lattice imperfection factor  $D$ , in the intensity expression, where  $D$  is given as

$$D = \exp(-ks^2) \quad (5)$$

and  $k = k_T + k_I + k_{II}$  is the sum of the three terms corresponding to thermal vibrations ( $k_T$ ), lattice imperfections of the first kind ( $k_I$ ), and of the second kind ( $k_{II}$ ) respectively<sup>33</sup>. This factor allows for a loss of intensity of the crystalline reflections due to all departures of the

lattice motifs (atoms or molecules or segments of molecules) from their ideal positions, either due to thermal vibrations or due to lattice imperfections.

The scattering from the crystalline domains can therefore be written as

$$4\pi \int_0^{\infty} s^2 I_c(s) ds = 4\pi X_c \int_0^{\infty} s^2 \bar{f}^2 D ds \quad (6)$$

The degree of crystallinity  $X_c$  can hence be written as

$$X_c = \frac{\int_0^{\infty} s^2 I_c(s) ds}{\int_0^{\infty} s^2 I(s) ds} = \frac{\int_0^{\infty} s^2 \bar{f}^2 ds}{\int_0^{\infty} s^2 \bar{f}^2 D ds} \quad (7)$$

Based on the above equations, the degree of crystallinity of an isotropic semicrystalline polymer of known chemistry can be estimated. In this study, the degree of crystallinity of the various samples were estimated using the method outlined by Ruland, and later simplified by Vonk<sup>36</sup>.

Figure 6.2 shows the scattering profiles of samples isothermally cold-crystallized for 135 min at various temperatures. It can be seen from the figure that as the crystallization temperature increases, the degree of crystallinity appears to increase as can be seen from the increase in the crystalline peak intensities. The degree of crystallinity values for these samples estimated using the Ruland method are given in Table 6.1. It can be seen that the degree of crystallinity increases by ca. 9% on increasing the crystallization temperature from 280 °C to 320 °C. However, the samples crystallized at 310 °C and 320 °C, displayed essentially identical crystallinities.

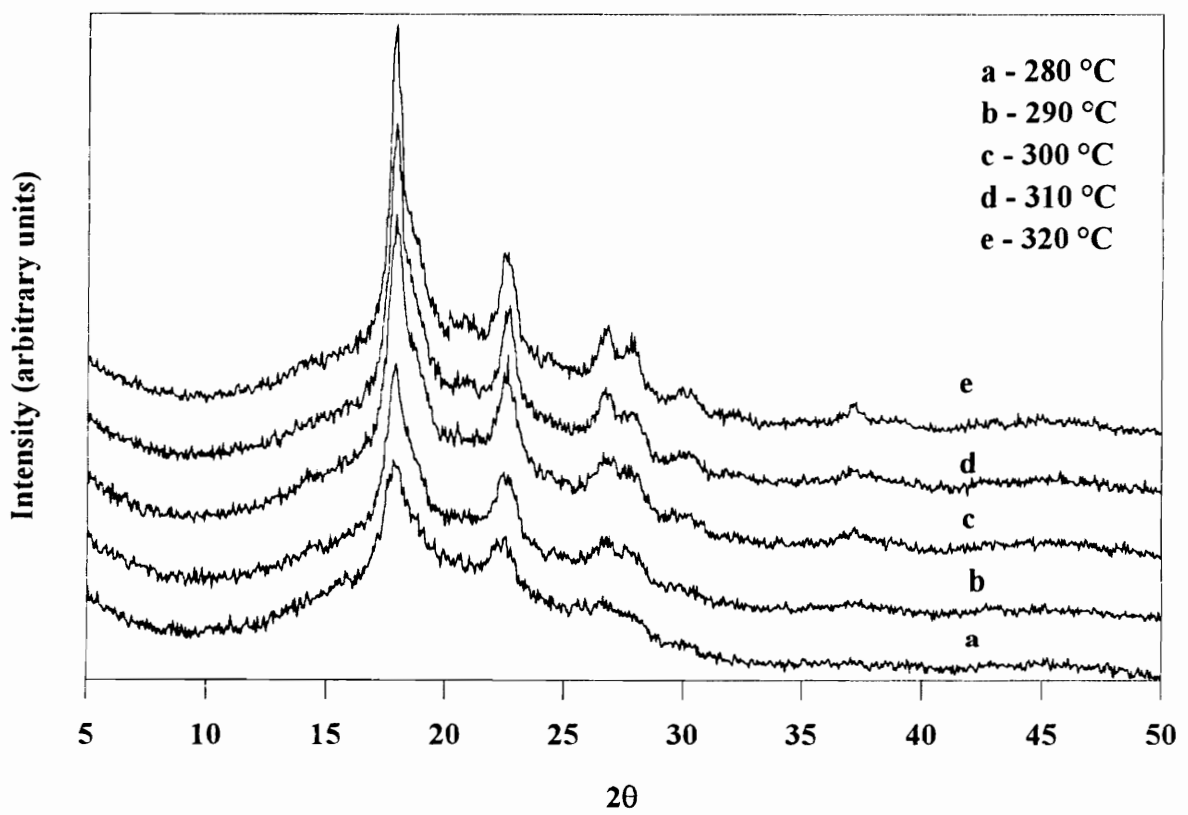


**Figure 6.2** X-ray profiles for samples crystallized at different temperatures.

**Table 6.1** Degree of crystallinity from WAXS measurements for samples isothermally cold-crystallized for 135 min at various temperatures.

<b>Crystallization temperature (°C)</b>	<b>Degree of crystallinity (%)</b>
280	17
290	22
300	24
310	26
320	26

Figure 6.3 shows the scattering profiles of samples crystallized for various times at 300 °C, compared to the scattering profile of a completely amorphous sample. The sample crystallized for 2.2 min at 300 °C shows the presence of a small amount of crystallinity as is evident by the appearance of a crystalline reflection of low intensity at a scattering angle of ca.  $2\theta = 18^\circ$ . Samples crystallized for 6 min and higher, however, show the presence of a substantial fraction of crystallinity. The degree of crystallinity dependence on crystallization time for samples crystallized at 300 °C is shown in Figure 6.4. As can be seen in the figure, the degree of crystallinity increases rapidly to a value of ca. 20 %, in the first 15 min; for longer times, the degree of crystallinity shows a gradual increase with the log of crystallization time, and increases to a value of ca. 30% at ca. 7000 min. Isothermal cold-crystallization experiments showed that the primary crystallization process was complete within 15 min at this temperature. The further increase in the degree of crystallinity with time after 15 min can therefore be attributed to a secondary crystallization process, which causes the formation of new lamellae accompanied perhaps by perfection of the existing lamellae. Based on the Avrami analysis of isothermal cold-crystallization, Cebe et al.<sup>25</sup> had hypothesized that the development of crystallinity in New TPI takes place mostly during primary crystallization, and had suggested the absence of a secondary crystallization process. Based on the results presented in Figure 6.4, it seems clear that a substantial fraction of crystallinity during isothermal cold-crystallization develops as a result of secondary crystallization. At a temperature of 300 °C, the sample attains ca. 20% crystallinity during primary

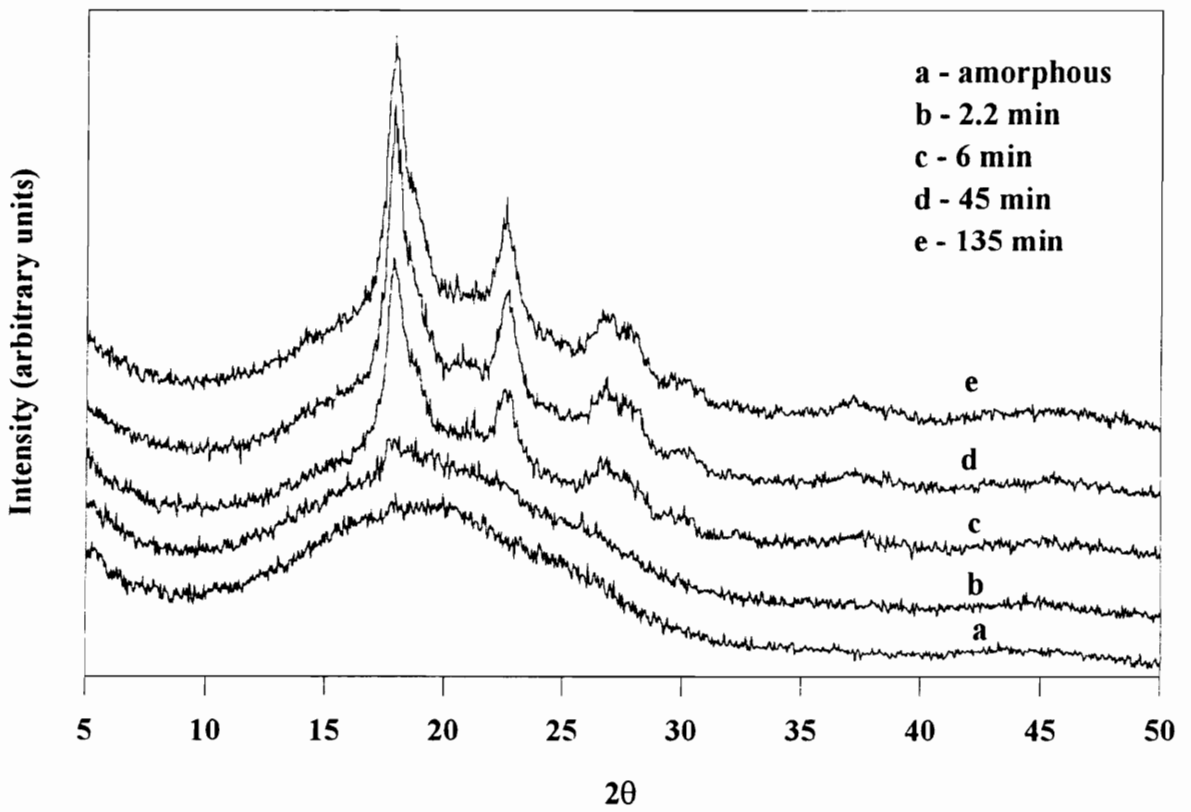


**Figure 6.3** X-ray profiles for samples crystallized at 300 °C for different times.

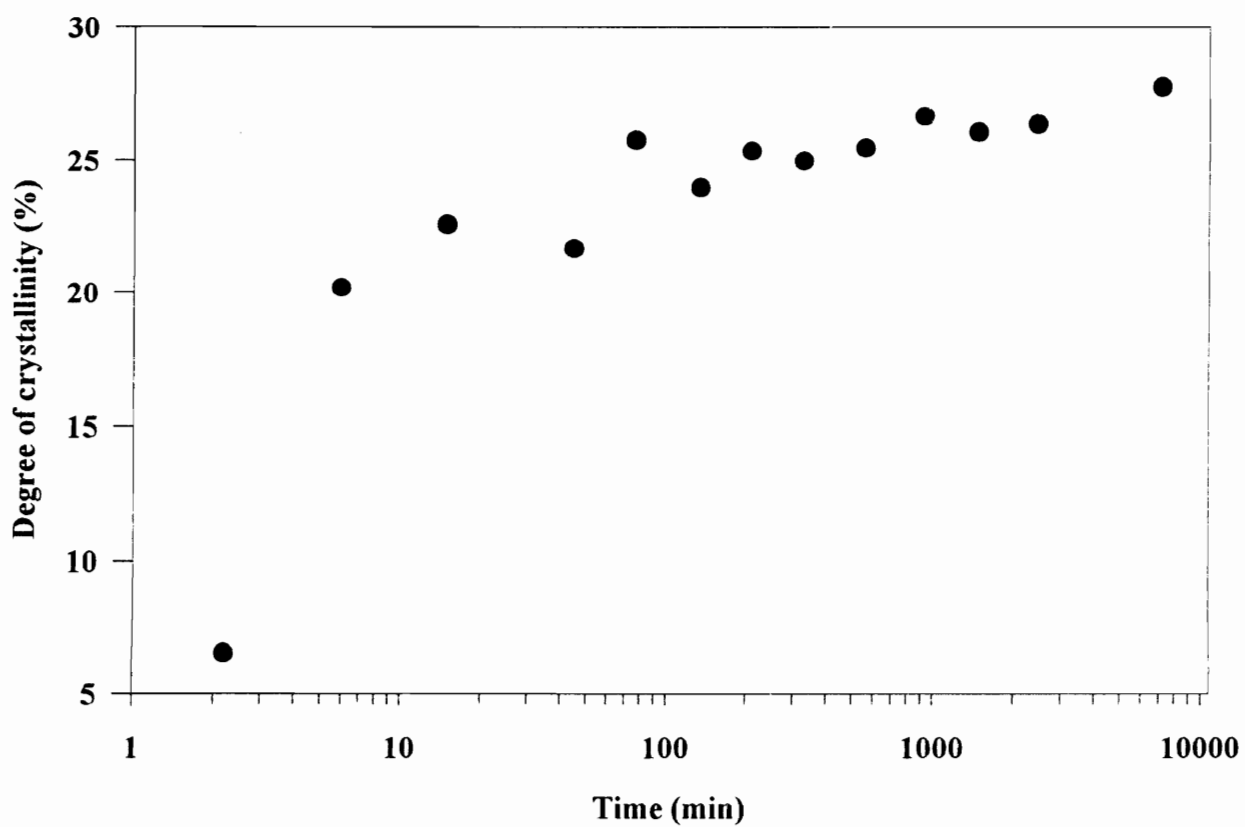


**Figure 6.4** Degree of crystallinity as a function of crystallization time at 300 °C.

crystallization, however, after annealing at this temperature for extended periods of time, the degree of crystallinity increases to ca. 30% due to a secondary crystallization process.

#### 6.4.2 DSC studies

Systematic studies of the crystallization and melting behavior of New TPI under isothermal and non-isothermal conditions have been carried out by Cebe et al.<sup>23,25</sup>. The effect of time and temperature of crystallization on the melting behavior and glass transition of New TPI has also been discussed in detail by Cebe et al.<sup>25</sup>. All details of the DSC studies will not be discussed, but some results which pertain to the dynamic mechanical and SAXS data will be presented.

Figure 6.5 shows the DSC traces of amorphous New TPI, a sample cold-crystallized at 300 °C for 2.2 min, and a sample cold-crystallized at 300 °C for 135 min. As can be seen from the figure, the amorphous sample exhibited a prominent  $T_g$ , followed by a crystallization exotherm, and finally by a melting endotherm. The sample crystallized at 300 °C for 2.2 min also displayed a prominent  $T_g$ , followed by a crystallization exotherm and finally by a melting endotherm. It can be seen in the figure that the maximum crystallization temperature of the sample crystallized for 2.2 min was lower than that of the amorphous sample, clearly implying that some crystallization had occurred as a result of residence at 300 °C for 2.2 min. From a calculation of the areas under the crystallization exotherm and the melting endotherm, one can conclude that the amorphous sample was essentially amorphous before the DSC scan, whereas the sample crystallized

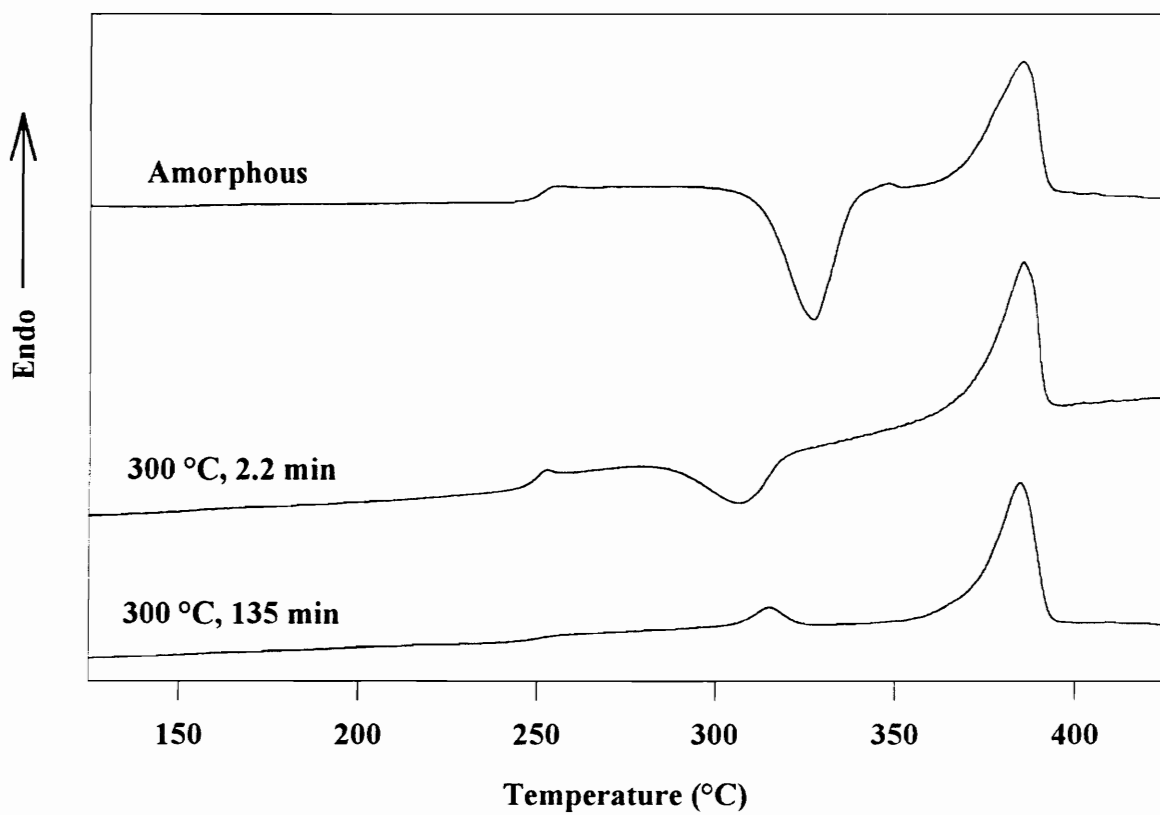


**Figure 6.5** DSC traces of amorphous and semicrystalline samples of New TPI.

for 2.2 min had a small degree of crystallinity (<7%), based on  $\Delta H_f^\circ = 139 \text{ J/gm}$ , which is consistent with the WAXS results discussed earlier which yielded a value of ca. 6% (it should be recognized that in calculating the degree of crystallinity by DSC, it is implicitly assumed that the enthalpy of melting and crystallization are independent of temperature). The sample crystallized at 300 °C for 135 min displayed a weak  $T_g$ , followed by a melting endotherm at 315 °C, and is followed by a prominent melting endotherm at 385 °C. Most semicrystalline polymers exhibit multiple melting endotherms when crystallized/annealed at temperatures between  $T_m$  and  $T_g$ <sup>9,37-42</sup>. The lower melting endotherm is usually observed at a temperature 10-20 °C above the crystallization temperature, corresponding to the melting of thin crystals believed to be formed as the result of a secondary crystallization process, following the formation of the dominant lamellae, at the crystallization temperature. The higher melting endotherm is relatively insensitive to crystallization conditions and is observed at temperatures corresponding to the melting of thicker crystals. The lower melting endotherm for the sample crystallized at 300 °C, observed at 315 °C can therefore be attributed to the  $T_c+10 \text{ °C}$  endotherm. All samples studied here except the amorphous sample, sample crystallized at 300 °C for 2.2 min, and the sample crystallized at 300 °C for 6 min, displayed a double endothermic behavior in the DSC scan.

No attempt has been made in this study to calculate the heats of melting from the DSC traces due to the common problems associated with constructing a reliable baseline. The glass transition temperature was estimated from the mid-point of the specific heat

transition accompanying the glass transition. Figure 6.6 shows the glass transition temperatures of samples crystallized for 135 min at various temperatures. *The glass transition temperature was found to decrease with increasing crystallization temperature.* The possible causes for this observed behavior will be discussed in the later section concerning the dynamic mechanical studies. The decrease in  $T_g$  on increasing the crystallization temperature from 280 °C to 320 °C was ca. 3 °C, which is consistent with the findings by dynamic mechanical analysis. An important difference between the DSC results and the dynamic mechanical results is that the  $T_g$  (determined from DSC) of the sample crystallized at 280 °C was shifted by only ca. 2 °C relative to the fully amorphous sample, a shift much smaller than that reported for cold-crystallized samples of other stiff chain polymers like PEEK<sup>38</sup> and PPS<sup>39</sup>. The dynamic mechanical results, however, showed that the sample crystallized at 280 °C displayed a  $T_g$  (determined from the  $\tan\delta$  peak) that was ca. 10 °C above a representative amorphous sample (crystallized at 300 °C, 2.2 min). The samples crystallized at 300 °C or higher seemed to display a DSC  $T_g$  that was lower than that of the fully amorphous sample. Such behavior was also reported by Cebe et al.<sup>25</sup> from their DSC studies. This is likely the result of the considerable broadening of the glass transition region and reduction in the specific heat jump at  $T_g$  due to the presence of crystallinity, thus introducing some uncertainties in the determination of the  $T_g$  from the mid-point of the specific heat jump at the glass transition.

The melting temperatures of the lower melting endotherm and upper melting endotherm as a function of crystallization temperature are shown in Figure 6.7. It can be

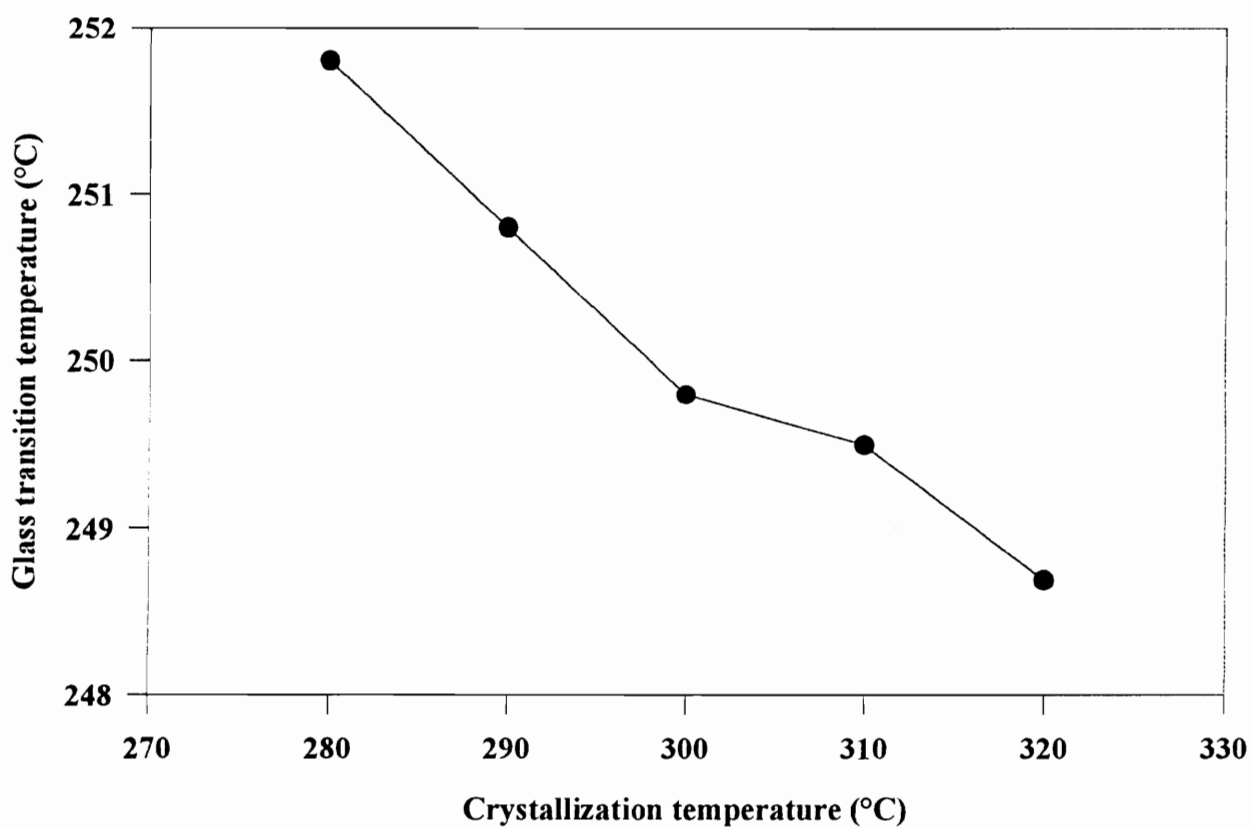


**Figure 6.6** Glass transition temperatures determined from DSC as a function of crystallization temperature.

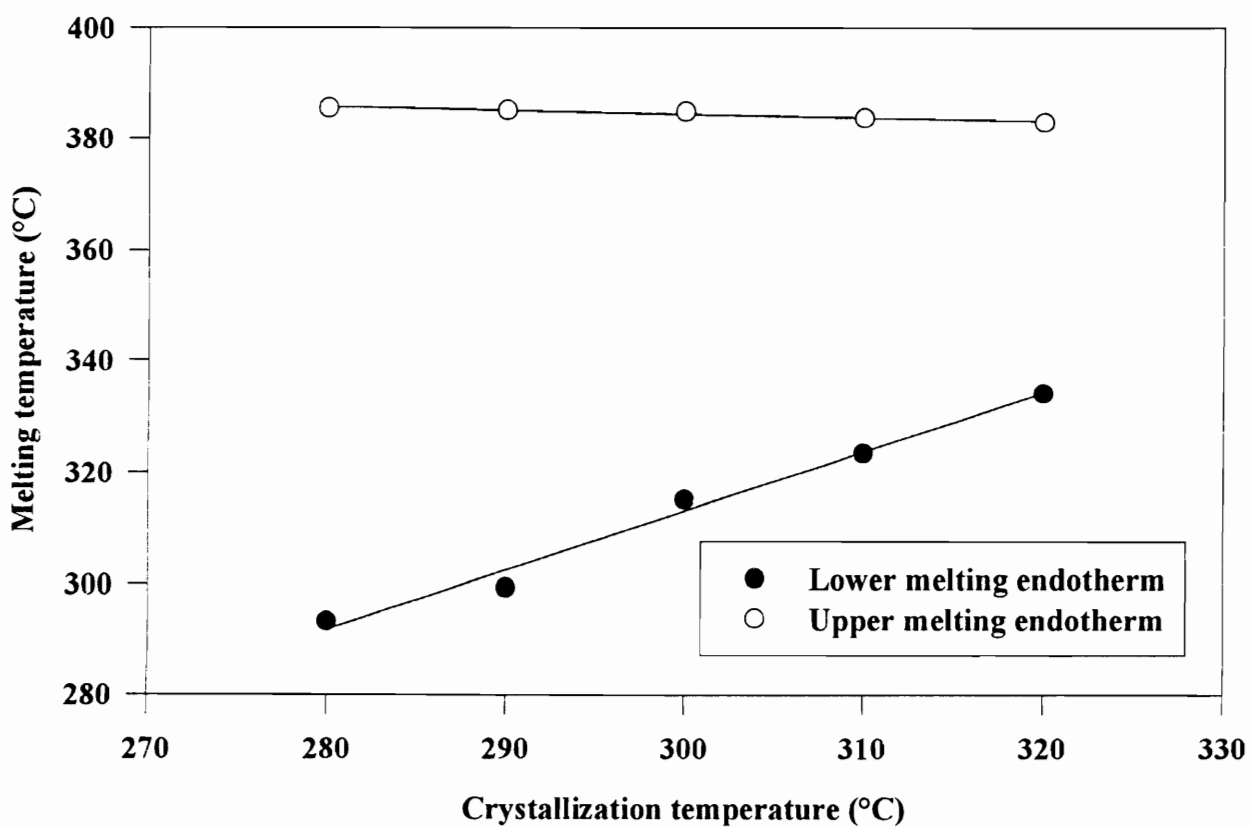


**Figure 6.7** Melting temperatures determined from DSC as a function of crystallization temperature.

seen that the lower melting endotherm increases with increasing crystallization temperature which is consistent with the  $T_c+10\text{ }^\circ\text{C}$  behavior of this endotherm. The upper melting endotherm was independent of crystallization temperature in the range of temperatures studied here. It is to be expected that the melting temperature would, in general, increase with increasing crystallization temperature. However, under conditions of high undercooling, such as those employed in this study, the observed melting temperature of polymers is typically independent of crystallization temperature<sup>25,38,39</sup>.

The DSC glass transition temperature is shown as a function of crystallization time at  $300\text{ }^\circ\text{C}$  in Figure 6.8. It can be seen that  $T_g$  increases with crystallization time, which again, is consistent with the results of the dynamic mechanical studies discussed later. For the case of samples crystallized for lower times, the  $T_g$  appeared to be lower than that of the fully amorphous polymer. At higher crystallization times, the  $T_g$  increased above that of a fully amorphous sample showing a log time dependence. The melting temperatures corresponding to the peaks of the lower melting and upper melting endotherms are shown as a function of crystallization time in Figure 6.9. It can be seen that initially, the upper melting endotherm temperature is essentially independent of crystallization time but then decreases at the higher crystallization times. The peak position of the lower melting endotherm, however, increases monotonically with the log of crystallization time, which is consistent with earlier reports on the behavior of the low endotherm<sup>25,42</sup>. At the highest crystallization time utilized in this study, the low endotherm appears as a shoulder on the low temperature side of the main melting endotherm. At the very early crystallization

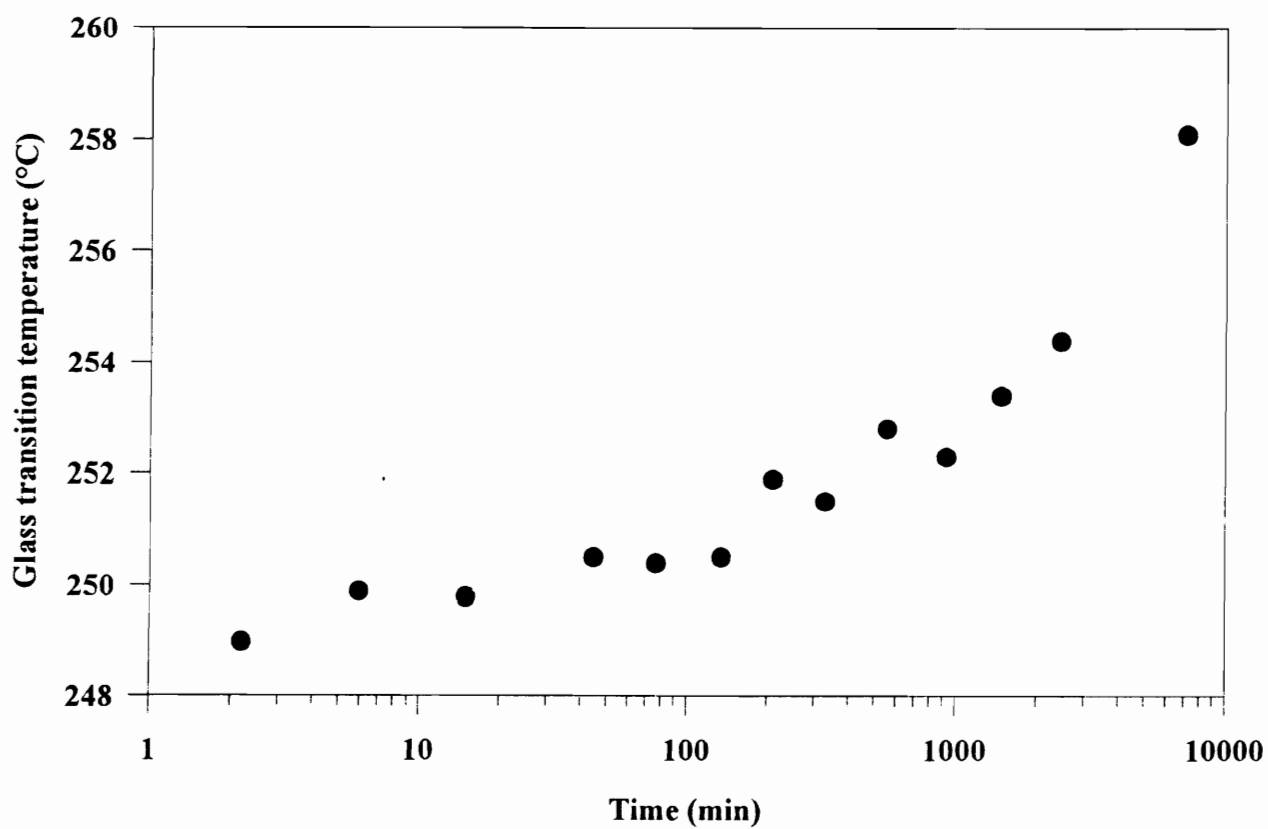


**Figure 6.8** Glass transition temperatures determined from DSC as a function of crystallization time.

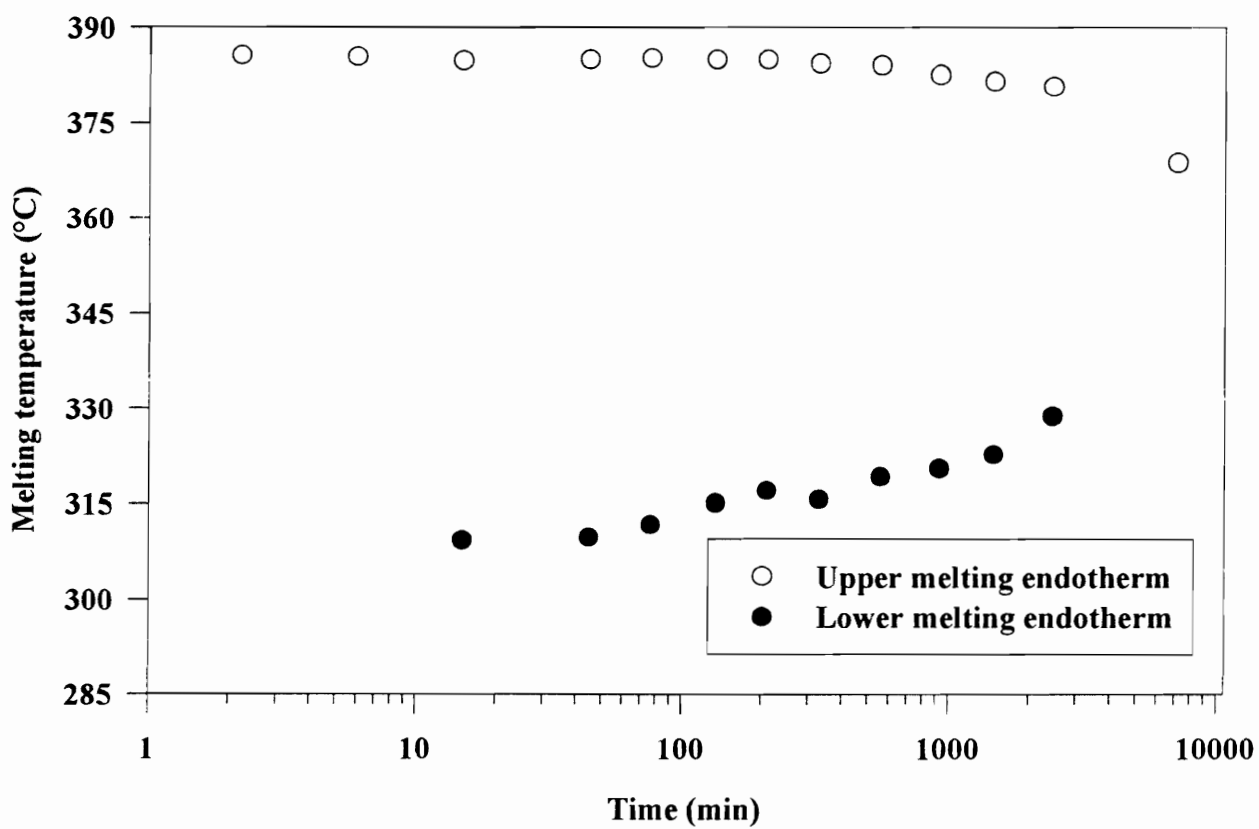


**Figure 6.9** Melting temperatures determined from DSC as a function of crystallization time.

times, the lower endotherm was not observed. The decrease in melting temperature of the upper endotherm is believed to be the result of chemical changes occurring in the material as a result of residence at high temperatures for extended periods of time. Indeed, it was shown in the previous chapter that the viscosity of New TPI increased with increasing time in the melt, indicating that some chemical changes like chain branching/cross-linking occur in the melt at high temperatures<sup>9</sup>. Since 300 °C is well above the glass transition temperature of New TPI, it is likely that residence at this temperature for extended times induced some chain branching/cross-linking in the amorphous regions of the sample, thereby resulting in a decrease in the melting temperature.

#### 6.4.3 *Dynamic mechanical studies*

It was not possible to obtain a dynamic mechanical spectrum of a fully amorphous sample due to the large extension of the sample in the instrument close to  $T_g$ . *Therefore, the sample crystallized at 300 °C for 2.2 min has been chosen as a representative amorphous sample.* Recall that the DSC and WAXS results discussed earlier showed that this sample indeed had a small fraction of crystallinity present. Figure 6.10 shows the storage modulus ( $E'$ ) as a function of temperature for a sample that had been crystallized at 300 °C for 2.2 min. A prominent  $\alpha$  relaxation is evident in the mechanical spectrum corresponding to the glass transition temperature. The storage modulus exhibits a dramatic decrease on going through the glass transition. The decrease in storage modulus is followed by an increase, which occurs as a result of cold-crystallization. Figure 6.11

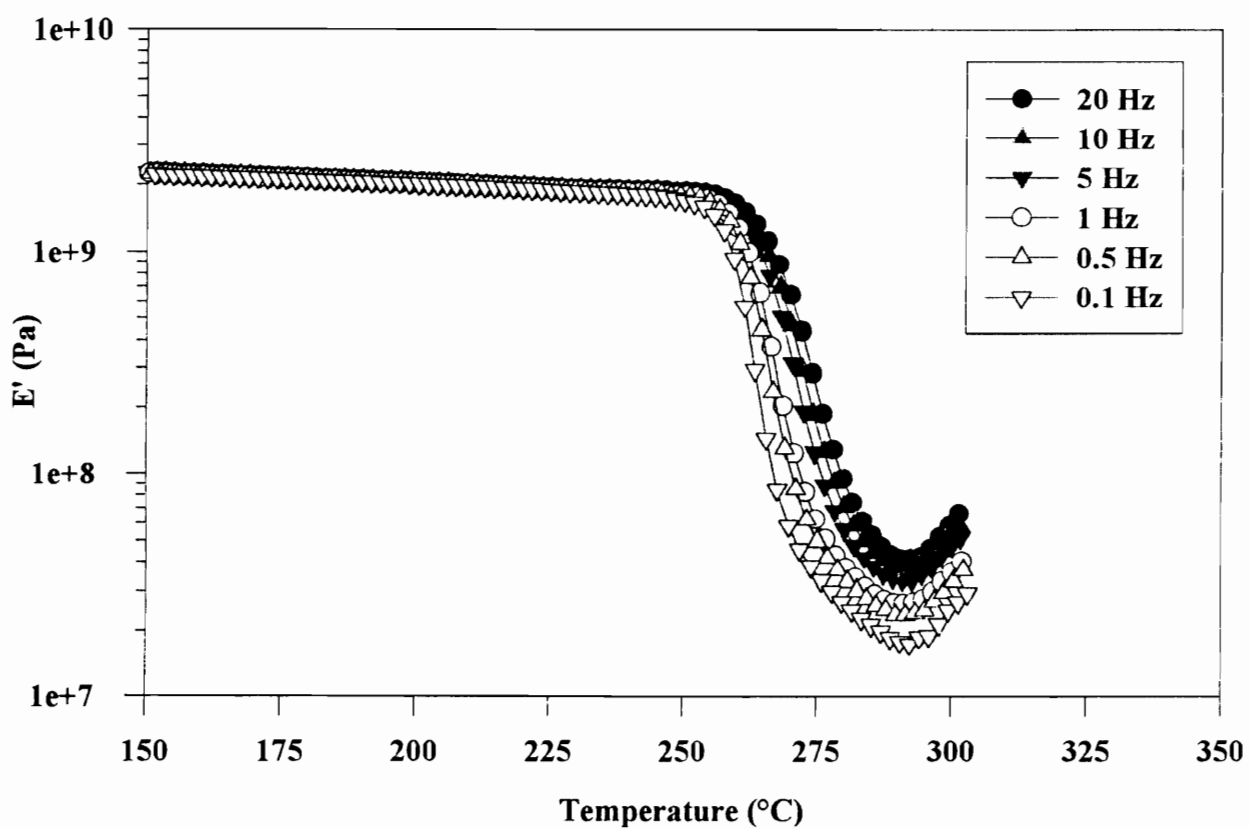


**Figure 6.10** Dynamic mechanical storage modulus for representative amorphous sample (crystallized at 300  $^{\circ}\text{C}$  for 2.2 min).

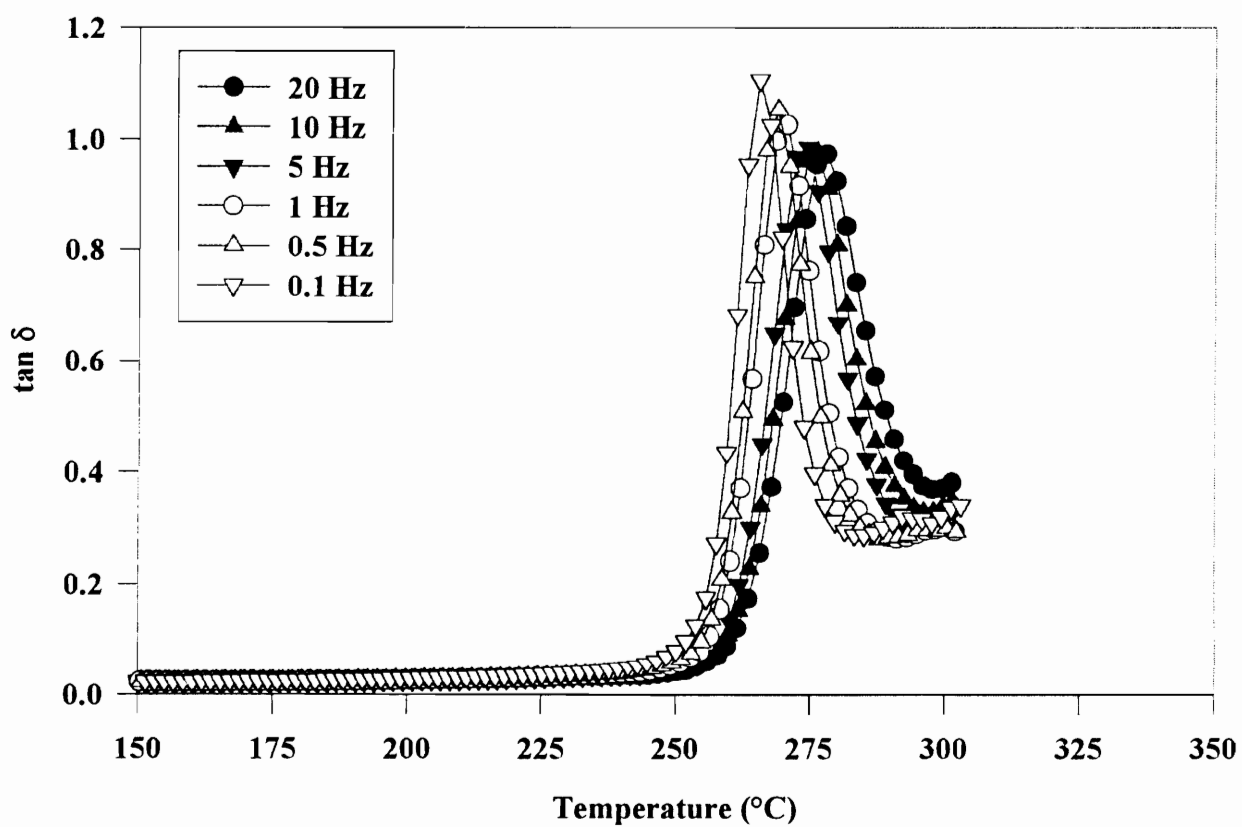


**Figure 6.11** Dynamic mechanical loss factor for representative amorphous sample (crystallized at 300 °C for 2.2 min).

shows the loss tangent of the same sample. The  $\alpha$  relaxation is characterized by a sharp narrow  $\tan \delta$  peak, with the position of the peak increasing with increasing frequency. The sharp  $\tan \delta$  peak indicates the narrow distribution of amorphous phase motions, causing a narrow distribution of relaxation times, accompanying the glass transition. Interestingly, the magnitude of the  $\alpha$  relaxation decreases with increasing frequency suggesting thermorheological complexity.

The dynamic mechanical data ( $E'$  and  $\tan \delta$ ) for a semicrystalline sample which was crystallized at 300 °C for 135 min, is shown in Figures 6.12 & 6.13. The figures clearly illustrate the effect crystallinity has on the  $\alpha$  relaxation, in that the  $\tan \delta$  peak is broadened considerably compared to the representative amorphous sample (300 °C, 2.2 min); the position of the  $\tan \delta$  peak is also shifted by as much as 11 °C to higher temperatures. The storage modulus value drops across the glass transition, with the decrease being less than that observed for the case of the representative amorphous sample, this being due to the smaller fraction of amorphous material available for undergoing the glass to rubber transition. The relaxation intensity of the semicrystalline sample is also significantly reduced compared to that observed for the representative amorphous sample, due also to the smaller fraction of the amorphous phase in the semicrystalline sample. The shift of the  $\tan \delta$  peak to higher temperatures indicates the constraining influence of the crystallites on the cooperative long range amorphous chain motions that give rise to the glass transition. The increase in the breadth of the relaxation

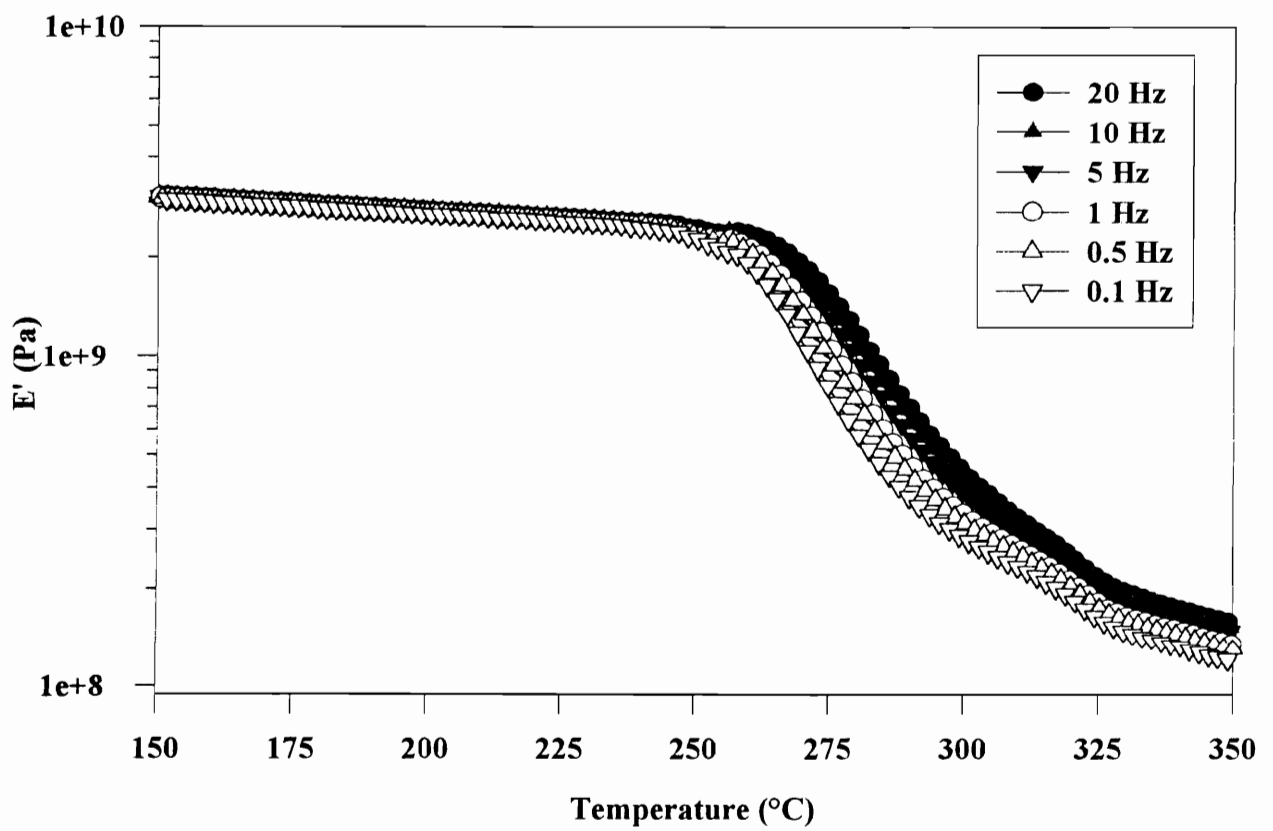


**Figure 6.12** Dynamic mechanical storage modulus for sample crystallized at 300  $^{\circ}\text{C}$  for 135 min.

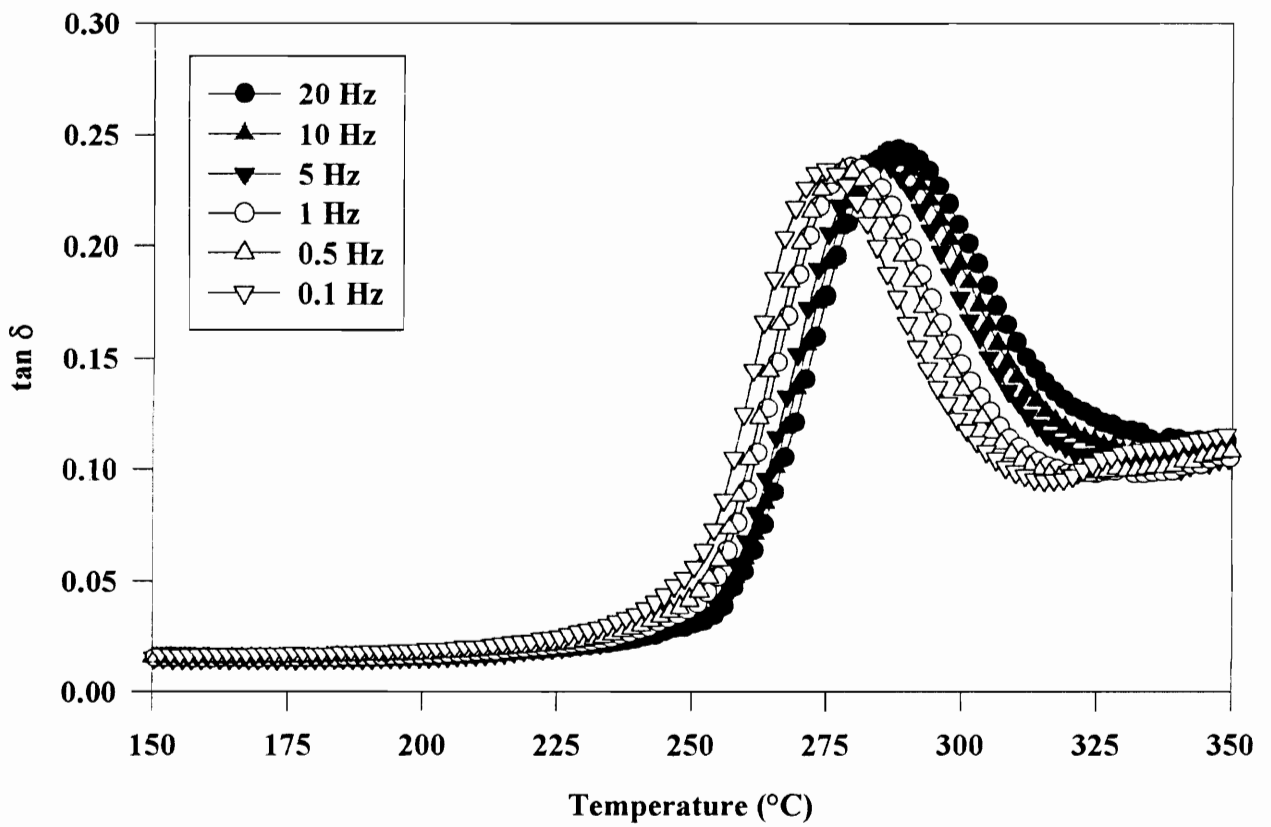


**Figure 6.13** Dynamic mechanical loss factor for sample crystallized at 300 °C for 135 min.

peak implies that a broader range of motions of the amorphous phase give rise to the glass transition, due to the broad range of constraints placed on the amorphous phase by the crystallites, thereby resulting in a broad distribution of relaxation times. As was observed for the representative amorphous sample, the peak temperature of the loss tangent ( $\tan \delta$ ) increased with increasing frequency. However, in contrast to the representative amorphous sample, the magnitude of the  $\alpha$  relaxation peak increased with increasing frequency. Such behavior has also been observed in dynamic mechanical relaxation studies on PEEK<sup>43</sup> and dielectric relaxation experiments on New TPI<sup>24</sup>. After the initial drop in storage modulus, there is a sudden change in the rate of decrease in modulus at ca. 315 °C. This can be attributed to the melting of crystals corresponding to the lower melting endotherm ( $T_c+10$  °C) that was observed in the same temperature range by DSC studies as shown in Figure 6.5.

Figure 6.14 shows the  $\tan \delta$  curves (1Hz) for samples that had been cold-crystallized isothermally at various temperatures. The peaks of the  $\tan \delta$  curves for all the samples were higher by at least 8 °C, compared to the representative amorphous sample. It can be seen from the figure that the magnitude of the relaxation intensity decreases with increasing crystallization temperature, this occurring due to an increase in the degree of crystallinity with increasing crystallization temperature. Such behavior could also result from an increase in the fraction of the rigid amorphous phase (RAP) with increasing crystallization temperature. This, however, seems unlikely since the fraction of the RAP

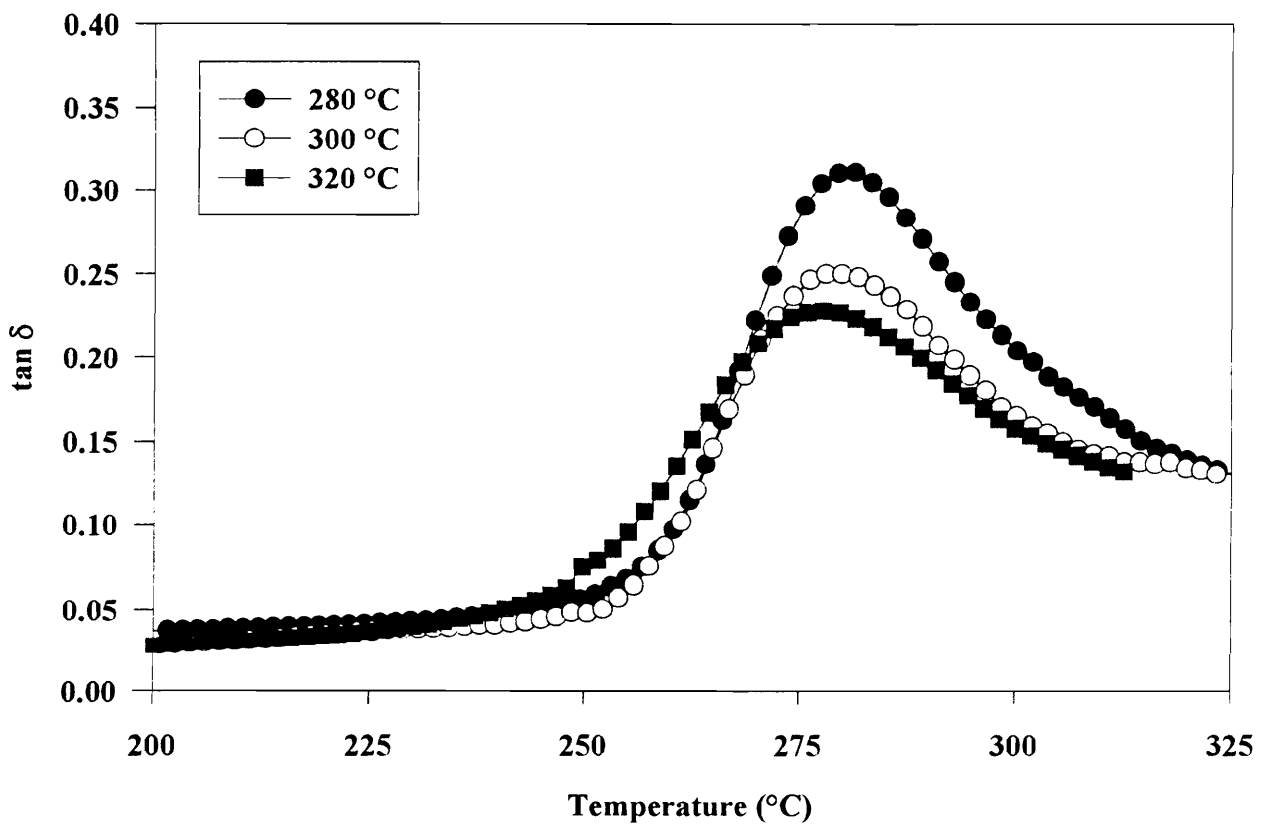


**Figure 6.14** Dynamic mechanical loss factor for samples crystallized for 135 min at various temperatures.

would be expected to decrease with increasing crystallization temperature (less restrictive crystallization conditions) as has been shown previously for the case of other stiff chain polymers<sup>38,39</sup>. *From Figure 6.14 it can be seen that the position of the peak of the  $\tan \delta$  curve decreases with increasing crystallization temperature.* Indeed, at a frequency of 1 Hz, the peak of the  $\tan \delta$  decreased by ca. 3 °C on increasing the crystallization temperature from 280 °C to 320 °C. This behavior is not surprising in itself and has been previously reported by Cheng et al.<sup>38</sup> from their DSC work on PEEK, Kalika et al.<sup>43</sup> from dynamic mechanical experiments on PEEK, and by Cebe et al.<sup>25</sup> from DSC studies on New TPI. The glass transition temperature (peak of  $\tan \delta$ ) decreases with increasing crystallization temperature in spite of an increase in the degree of crystallinity. This indicates that the relative constraint on the amorphous phase decreases with increasing isothermal crystallization temperature. An explanation offered by Cheng et al.<sup>38</sup> is that, at lower crystallization temperatures, crystallization occurs under more restrictive conditions, which gives rise to thinner and less perfect lamellae. This could increase the fraction of the amorphous phase that is associated with the crystal/amorphous interphase, accompanied by an increase in the strain at the interphase. The greater constraints on the amorphous phase could thus give rise to a higher and/or a broader glass transition behavior than for the case of samples crystallized at higher temperatures, i.e. less restrictive conditions. Another explanation for this behavior has been offered by Jonas et al.<sup>44</sup> who observed that for the case of PEEK, this decrease in the glass transition could be

correlated with the increase in the thickness of the amorphous layer between lamellae. Indeed, such a behavior was observed in this study as well, the results of which are discussed in the following section. The difference between the study of Jonas et al.<sup>44</sup> and this study is the assignment of the amorphous layer thickness and crystal layer thickness from SAXS data, as will be discussed later in the paper.

Under quiescent conditions of crystallization, semicrystalline polymers typically display a spherulitic superstructure. Each spherulite consists of outwardly radiating fibrils, which consist of stacks of chain folded lamellae, each lamella being separated from the other by an inter-lamellar amorphous layer. In the case of polymers displaying low degrees of crystallinity, the different lamellar stacks are also separated from each other by larger amorphous regions. For the case of polymers like PET and PEEK, this has been verified among others by Lovinger et al.<sup>45</sup>, Santa Cruz et al.<sup>46</sup>, and Hsiao et al.<sup>47</sup>. This leads to the conclusion that in polymers displaying low degrees of crystallinity, there are two distinct amorphous regions. The inter-lamellar amorphous phase can be visualized as being more constrained than the amorphous regions between different lamellar stacks, which more closely resembles the free amorphous phase. If one were to believe that the inter-lamellar amorphous layers do not contribute significantly to the observed glass transition, the observed behavior of the glass transition decrease with increasing crystallization temperature could be correlated with the size of the amorphous regions between different lamellar stacks and the number of constraints associated with these amorphous regions. However, if one were to assume that the inter-lamellar amorphous

layers do indeed contribute to the glass transition, then the hypothesis of Jonas et al. as well as the explanation of Cheng et al. can be invoked to explain the decrease in glass transition with increasing crystallization temperature. As described in more detail in the next section, the experimentally determined average amorphous layer thickness in this study increases from 47 Å to 56 Å as the crystallization temperature increases from 280 °C to 320 °C. Since the repeat unit length of New TPI has been shown to be of the order of 25 Å<sup>29</sup>, the amorphous layer thickness is approximately twice the repeat unit length. If the persistence length of New TPI is of the order of 50 Å, it would be difficult to visualize the inter-lamellar amorphous material contributing to the observed glass transition. The observed decrease in the glass transition with increasing crystallization temperature would, in this case, arise mainly from the decreased constraints on the amorphous regions between lamellar stacks due to the presence of the crystallites. However, if the persistence length of New TPI is significantly smaller than 50 Å, then the inter-lamellar amorphous layer could also contribute to the observed glass transition. In this case, the decrease in the glass transition temperature with increasing crystallization temperature could occur due to both above reasons, i.e. increasing amorphous layer thickness as well as decreased constraints on the amorphous regions between different lamellar stacks.

The activation energy for the  $\alpha$  relaxation was determined by plotting the log (frequency) as a function of the reciprocal temperature corresponding to the peak of the  $\tan \delta$  curve at each frequency; the slope of the line yields the activation energy. The results of this Arrhenius plot for samples isothermally crystallized at different

temperatures, compared to the representative amorphous sample (300 °C, 2.2 min) are shown in Figure 6.15. The cold-crystallized samples are shifted to the left of the graph, i.e. towards higher temperatures compared to the representative amorphous sample. As can be seen in the figure, the Arrhenius relation is quite adequate in describing this relaxation process. It can be seen that the activation energies of the  $\alpha$  relaxations are essentially independent of the crystallization temperature, with the activation energy values being ca. 900 kJ/mol. This value is, however, slightly lower than that observed for the amorphous sample which had an activation energy of 1041 kJ/mol. Such behavior has been previously observed for the case of cold-crystallized samples of PEEK, which showed lower values of activation energy compared to that of the amorphous counterpart<sup>43</sup>. This high value of the activation energy is indicative of the multi-segmental cooperative motion involved in the glass transition, and is close to the values of activation energies reported for other stiff chain polymers as well<sup>9,43</sup>. Since the glass transition involves multi-segmental cooperative motions, the difference in the activation energies between the amorphous system and the semicrystalline systems could imply that the motions corresponding to the  $T_g$  of the semicrystalline samples may involve fewer segments, owing perhaps to the constraints placed on the amorphous phase by the crystallites.

Figures 6.16 & 6.17 show the dynamic mechanical spectra (1Hz) for a series of samples isothermally crystallized for various times at 300 °C. Recall that the sample

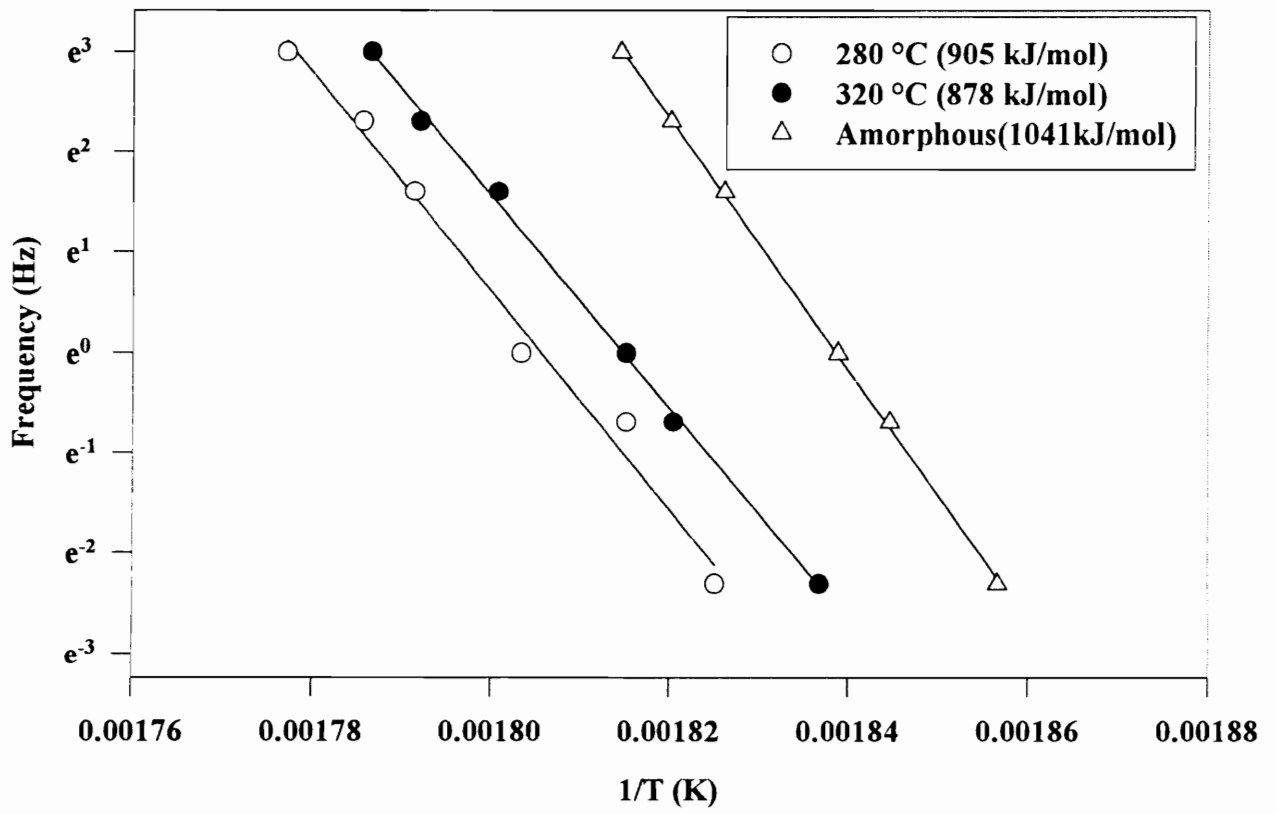


**Figure 6.15** Arrhenius plot of frequency vs.  $1/T$  from dynamic mechanical experiments for samples crystallized for 135 min at various temperatures.

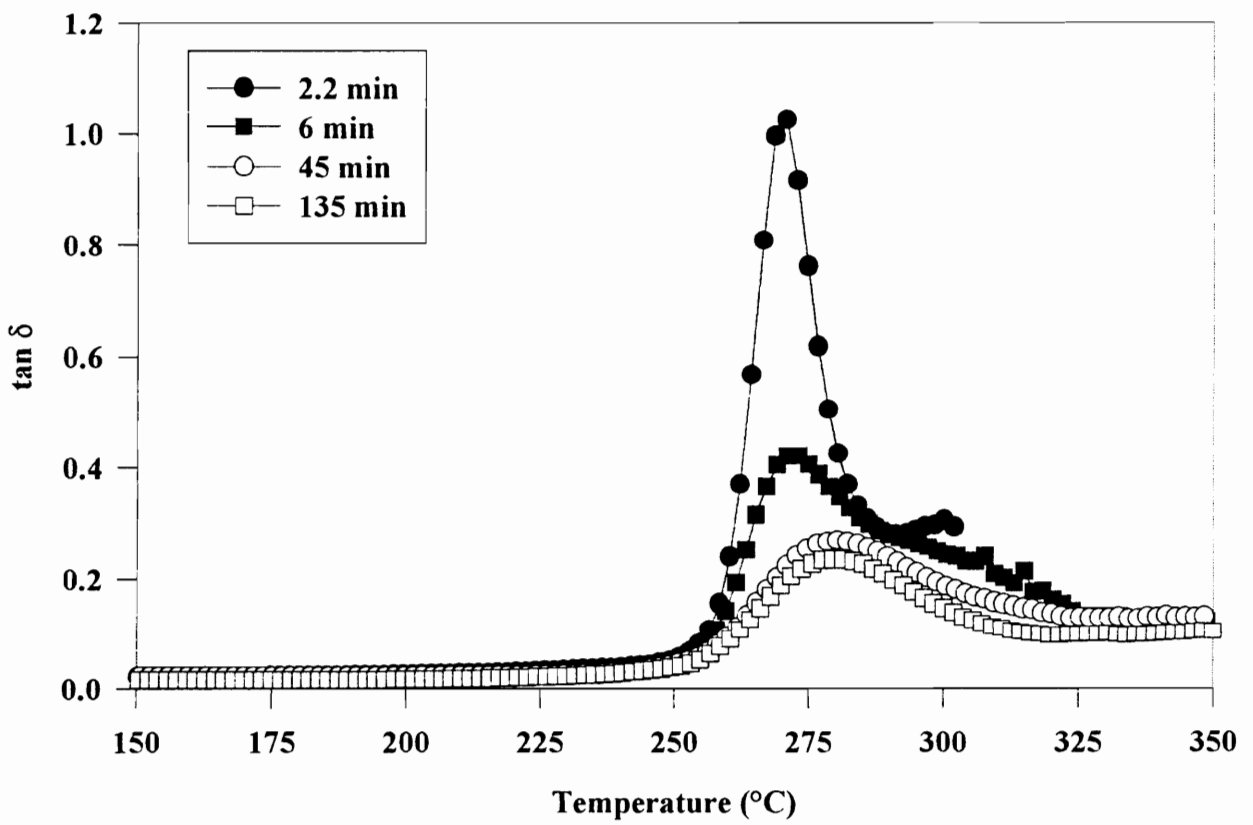


**Figure 6.16** Dynamic mechanical loss factor for samples crystallized at 300 °C for various times

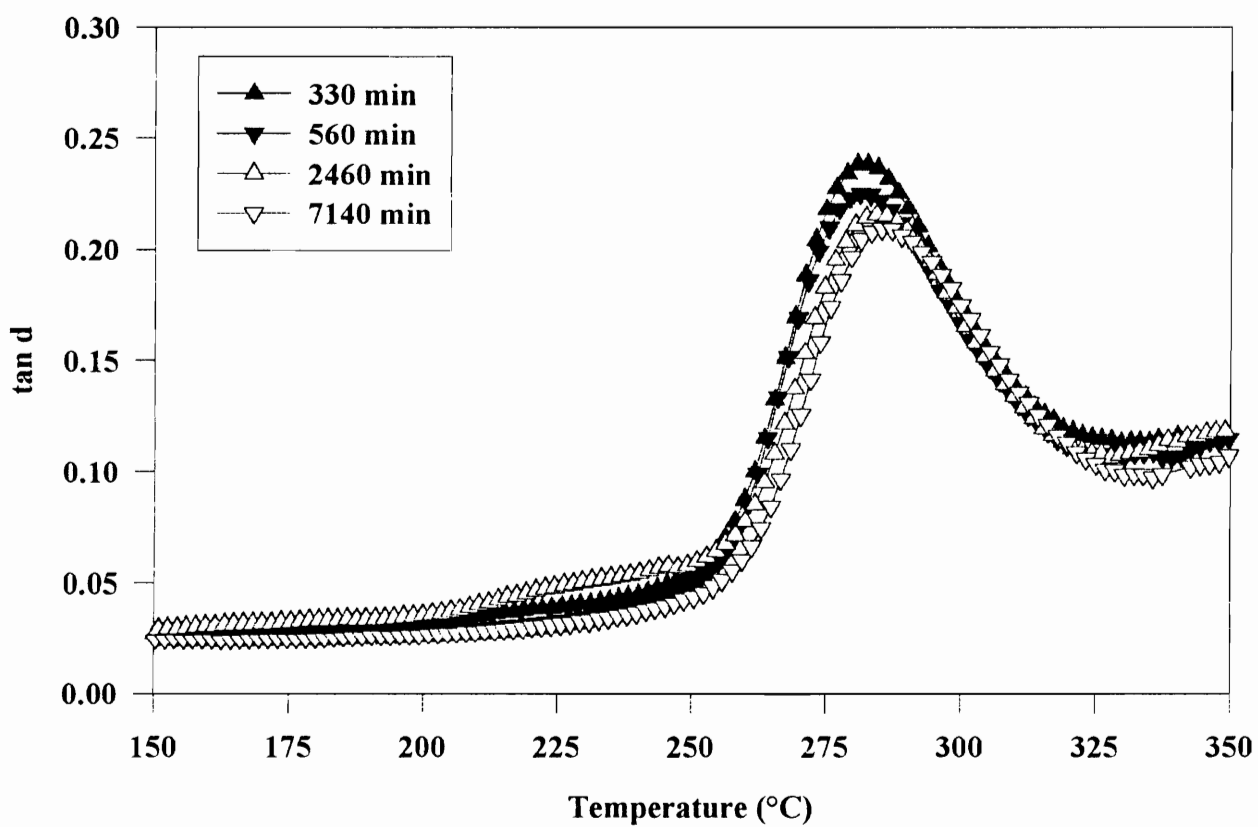


**Figure 6.17** Dynamic mechanical loss factor for samples crystallized at 300 °C for various times.

crystallized for 2.2 min is assumed to approximate the behavior of an amorphous sample. The sample crystallized for 6 min shows a reduced relaxation intensity, an increase in the breadth of the relaxation peak, and an increase in the peak temperature indicating an increase in the glass transition temperature. The relaxation curve corresponding to a crystallization time of 45 min is further broadened and shifted to higher temperatures; the relaxation intensity is also reduced compared to the sample crystallized for 6 min. The dynamic mechanical spectra of the samples crystallized for times higher than 45 min shift to higher temperatures and exhibit decreased relaxation intensities, but do not show any further broadening.

The increase in the peak relaxation temperature with crystallization time indicates an increase in the constraints placed on the amorphous phase by the presence of the crystallites. Note that at this point no assumption has been made regarding the contributions of the inter-lamellar amorphous layers and the amorphous regions between different lamellar stacks to the observed glass transition. The increase in glass transition, as defined by the peak temperature in  $\tan\delta$ , with crystallization time is shown in Figure 6.18 for three frequencies, 0.1 Hz, 1 Hz and 10 Hz. As can be seen in the figure, for low crystallization times (2.2 min, 6 min), the glass transition temperature falls significantly below the straight line fits obtained for the case of the higher crystallization times (>15 min). For times above 15 min, the glass transition displays a log time dependence on the crystallization (annealing) time. DSC cold-crystallization kinetic studies revealed that the peak crystallization time (time required to reach the peak of the crystallization exotherm)

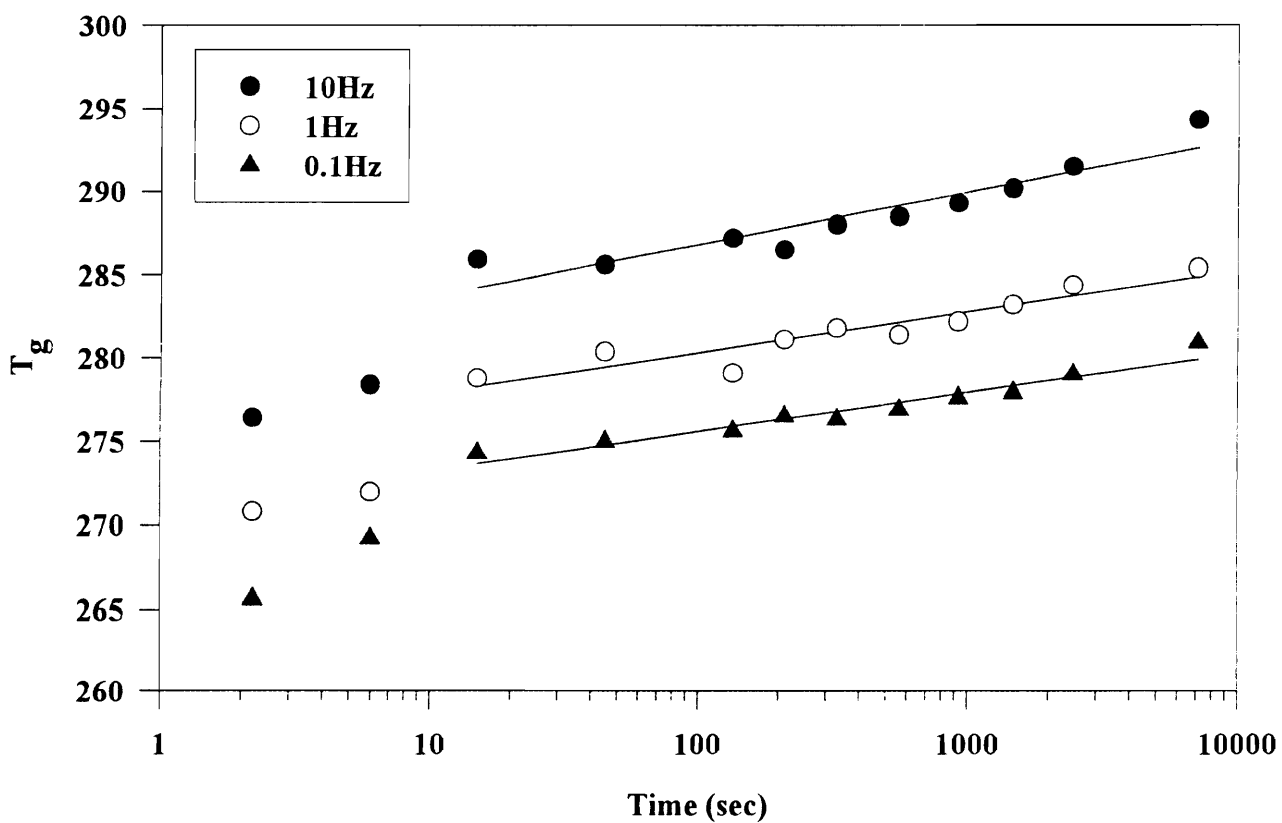


**Figure 6.18** Glass transition temperatures determined from peak of  $\tan \delta$  as a function of crystallization time at 300 °C.

was ca. 6 min. The peak crystallization time has generally been correlated with the time for spherulitic impingement in the sample. If one were therefore to assume that for crystallization times below 6 min, spherulitic impingement does not yet take place, then the morphology of the sample can be visualized as isolated spherulites dispersed in an amorphous matrix. Since the molecules in the amorphous matrix do not form part of any spherulite and hence do not feel the constraints of crystallites, they would be expected to display a lower glass transition than those molecules that are influenced by the presence of crystallites. For times greater than that required for full impingement, all molecules in the amorphous phase would be influenced by the crystallites and would hence display higher glass transitions as well as a different dependence on crystallization time. Recall that the degree of crystallinity from WAXS measurements showed an increase with increasing crystallization time. Recall also that the melting temperature from DSC measurements decreased at the higher crystallization times; this was attributed this to chemical changes like cross-linking/branching in the amorphous phase. Both cross-linking as well as an increase in the degree of crystallinity would lead to an increase in the constraints on the amorphous phase. The decrease in relaxation intensity with increasing crystallization time for low crystallization times, can therefore be attributed to an increase in the degree of crystallinity; for the case of higher crystallization times, the decrease in relaxation intensity can be attributed to an increase in the degree of crystallinity accompanied perhaps by the effect of some cross-linking within the amorphous phase. As stated earlier, an increase in the breadth of the relaxation peak indicates an increase in the breadth of relaxation times

owing to the broad distribution of constraints placed on the amorphous phase by the crystallites. For crystallization times higher than 45 min, there is no further increase in the breadth of the relaxation peak; this implies that the distribution of amorphous phase motions remains essentially identical.

Activation energies for samples crystallized for different times were not estimated since the Arrhenius relation did not yield adequate straight line fits to the data, which showed considerable curvature (different activation energies for different frequency ranges).

#### 6.4.4 SAXS studies

The SAXS data for New TPI has been analyzed using the correlation function approach of Vonk<sup>48</sup>, and using the methods described by Strobl and Schneider<sup>49</sup> with reference to some of the terminology adopted by Santa Cruz et al.<sup>46</sup>.

The correlation function is calculated from the Fourier-Bessel transform of the Lorentz corrected scattering profile. Before the Fourier transform can be carried out, the intensity has to be extrapolated to  $q = 0$  and  $q = \infty$ , where  $q$  is the scattering vector defined as  $q = 2\pi s$ . The extrapolation to  $q = 0$  was performed by an extrapolation between the first usable data point and the origin in the Lorentz corrected plot. The liquid scattering profile and the finite width of the crystal-amorphous interface were estimated

using a modified form of Porod's Law<sup>47,50</sup>, which was also used in the extrapolation of  $q = \infty$ .

The correlation function is then given by

$$\gamma(r) = \int_0^{\infty} [\tilde{I}(q) - I_b(q)] q e^{-\sigma^2 q^2} [J_0(qr) - qr J_1(qr)] dq \quad (8)$$

where  $\tilde{I}(q)$  is the smeared intensity obtained from the Kratky measurement,  $J_0$  and  $J_1$  are Bessel functions of order 0 and 1 respectively,  $I_b$  is the background scattering arising from local electron density fluctuations, and  $\sigma$  is the standard deviation of a gaussian distribution characterizing the phase boundary between the crystalline and amorphous regions. The above correlation function corresponds to the scattering arising from the corresponding system with sharp phase boundaries. Since the correlation function has been normalized by the invariant  $Q$ , the value of the correlation function  $\gamma(r)$  at the origin ( $r = 0$ ) is 1, where  $Q$  is given by

$$Q = \int_0^{\infty} q \tilde{I}(q) dq \quad (9)$$

The lamellar variables obtained from the data are the long period ( $L$ ), the linear degree of crystallinity in the lamellar stacks ( $X_{cl}$ ), the lamellar thickness ( $l_c$ ) and the amorphous layer thickness ( $l_a$ ). Using the terminology adopted by Santa Cruz et al.<sup>46</sup>, two long periods can be determined from the correlation function: the position of the first maximum ( $L_c^M$ ) and twice the value of the first minimum ( $L_c^m$ ). For the case of an *ideal two-phase model*, the two long periods obtained from the correlation function should yield

identical values. The average linear degree of crystallinity in the lamellar stacks can be determined from the following equation

$$x_1 x_2 L_c^M = B \quad (10)$$

where  $B$  is the first intercept of  $\gamma(r)$  with the abscissa, and  $x_1$  and  $x_2$  are the volume fractions of the two phases respectively in the lamellar stacks ( $x_1 + x_2 = 1$ ). The assignment of either  $x_1$  or  $x_2$  to the crystalline phase is not so straightforward however. There has been some controversy in literature with regards to the assignment of  $x_1$  and  $x_2$  to the crystalline and interlamellar amorphous phases<sup>50,51</sup>. Regardless of the assignment of the two phases to either the crystal or amorphous fractions, the thicknesses of the two phases can be calculated by

$$l_1 = x_1 L_c^M \quad (11)$$

$$l_2 = x_2 L_c^M \quad (12)$$

Figure 6.19 shows the smeared SAXS profiles of a fully amorphous sample of New TPI and a semicrystalline sample that had been crystallized at 300 °C for 135 min. The semicrystalline sample shows a prominent scattering peak at low angles corresponding to 240 Å, and a weaker scattering peak corresponding to ca. 27 Å. As will be discussed later, the prominent scattering peak was a function of crystallization time and temperature, however, the weaker maxima was found to be independent of crystallization conditions. Recall that Okuyama et al.<sup>29</sup> had proposed a unit cell with  $c=25.11$  Å. The weaker maxima can thus be attributed to the (001) reflection<sup>22,23</sup>. Note that the

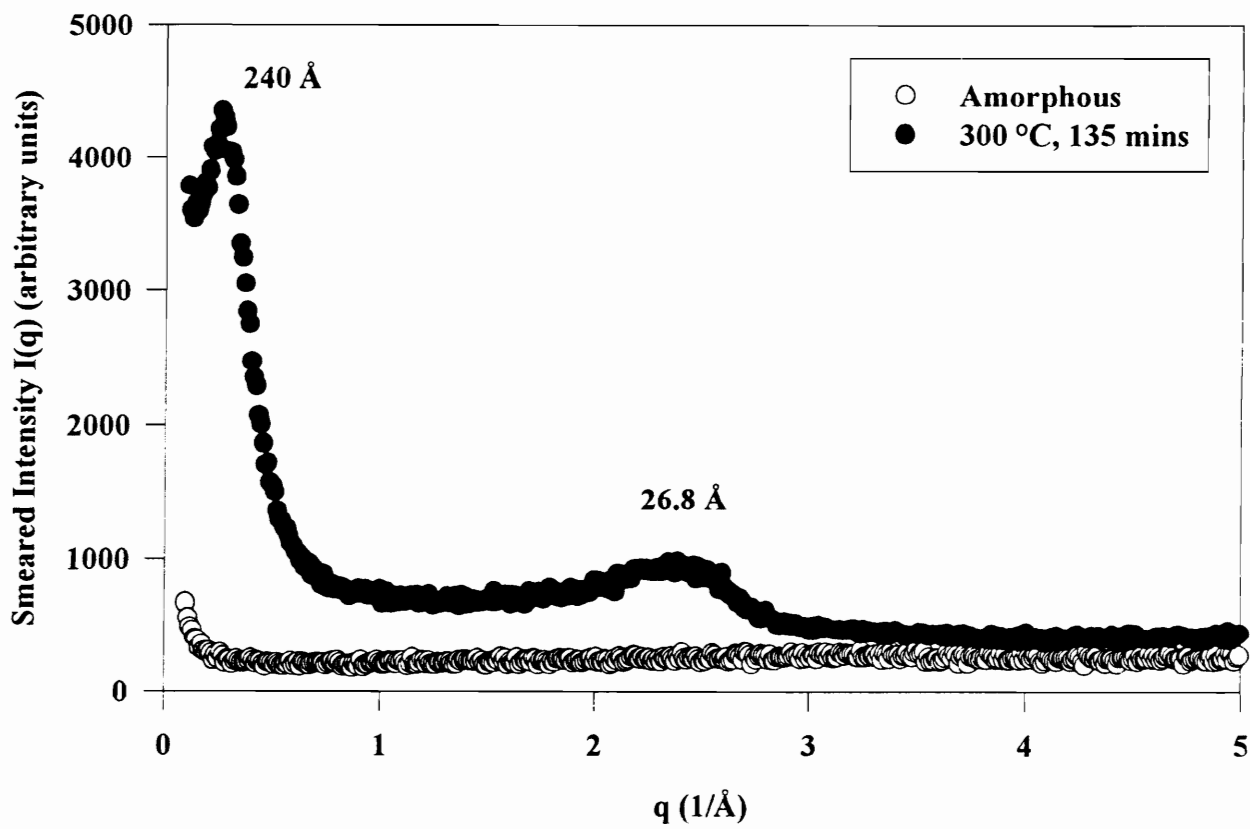


**Figure 6.19** Smeared SAXS data for an amorphous and a semicrystalline sample.

amorphous sample does not exhibit either a strong maxima or the weaker scattering peak corresponding to the (001) reflection. Cebe et al.<sup>23</sup> observed a weak scattering peak in their *unrelaxed amorphous sample* of New TPI processed film corresponding to a d-spacing of ca. 24 Å. This had been attributed by them to the (001) reflection. They explained this as being due to some amorphous phase orientation induced by the film processing operation. Similar effects have been noted earlier in the case of amorphous polyimide films subjected to tensile drawing, and attributed to lateral chain alignment<sup>52</sup>, or described as smectic-like ordering<sup>53</sup>. The absence of the peak corresponding to the (001) reflection in the amorphous film used in this study strongly suggests that the samples did not possess any appreciable local range order that could give rise to a scattering peak.

Figure 6.20 shows the Lorentz corrected curves, as a function of the scattering vector  $q$  for a series of samples cold-crystallized for 135 min at different temperatures. From the figure it is obvious that as the cold crystallization temperature increases, the long spacing corresponding to the peak position of the scattering maximum ( $L_B$ ) increases, i.e. the peak systematically shifts to lower values of  $q$ . Since the long spacing is the sum of the amorphous layer and lamellar thicknesses, this increase in long spacing could be the result of an increase in the amorphous layer thickness, the lamellar thickness or both. In order to estimate the thickness of the lamellar phase and the amorphous phase, the correlation function approach was utilized to treat the data. Figure 6.21 shows the correlation functions of various samples whose intensity versus  $q$  curves are shown in Figure 6.20. From the figure it is obvious that as the crystallization temperature increases,

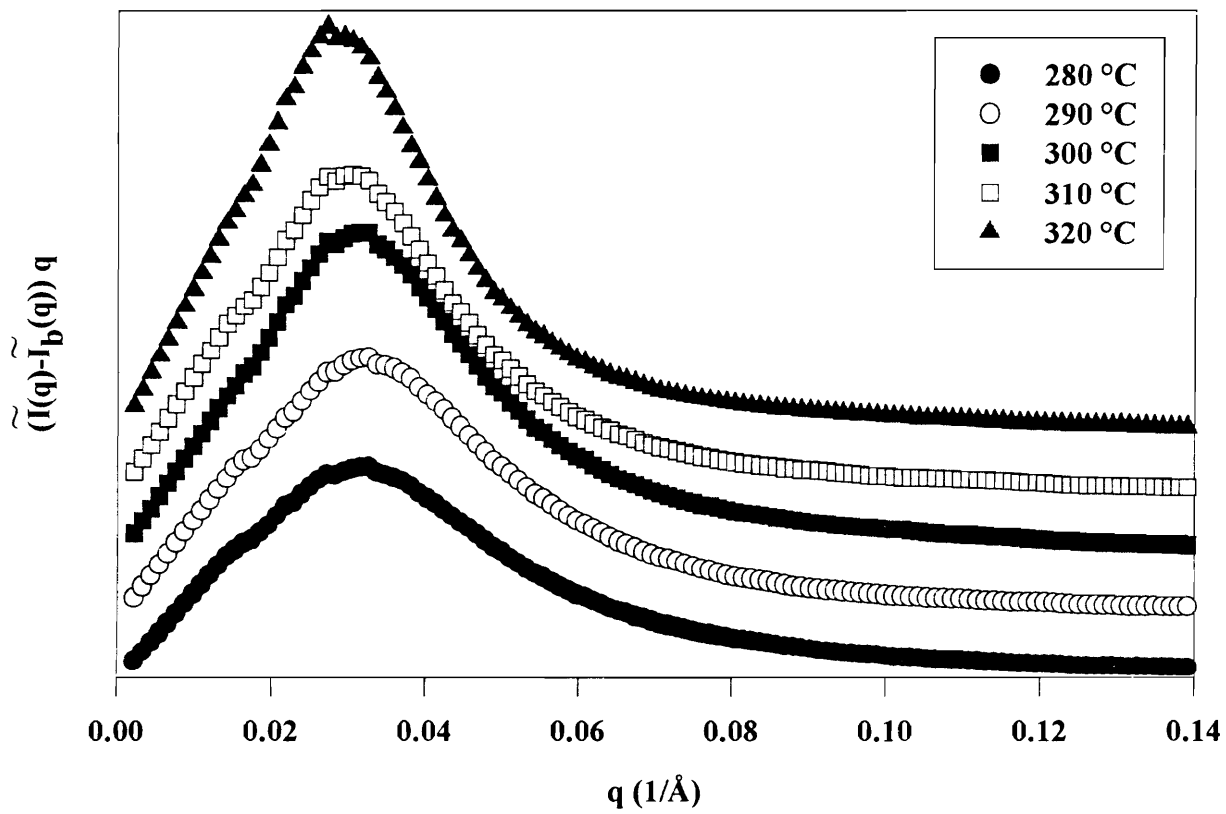


**Figure 6.20** Lorentz corrected plots for samples crystallized for 135 min at various temperatures.

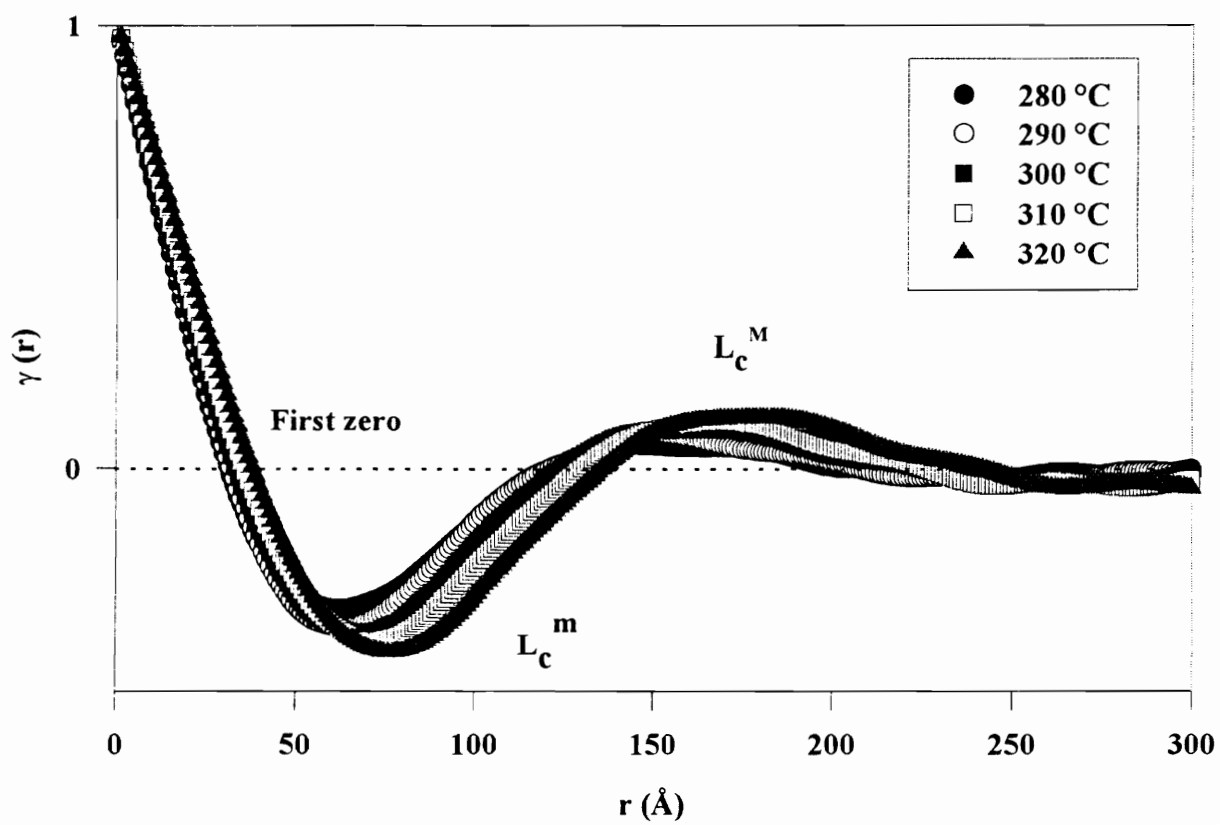


**Figure 6.21** Correlation functions for samples crystallized for 135 min at various temperatures.

the long spacing increases to higher values of  $r$ . Figure 6.22 shows the increase in long spacing estimated three different ways, for samples crystallized at different temperatures. From the figure, it can be seen that the value of the long period estimated from the Bragg spacing of the Lorentz corrected curve, yields higher values as compared to those estimated from the correlation function. The value of  $L_c^M$  changes from 148 Å at a crystallization temperature of 280 °C, to a value of 183 Å at a crystallization temperature of 320 °C, i.e. a change of 35 Å. The first intercept of the correlation function with the abscissa,  $B$ , also increases with increasing crystallization temperature as shown in Figure 6.21. The value of the intercept was used in conjunction with the long spacing ( $L_c^M$ ) in order to calculate the linear degree of crystallinity in the lamellar stacks; the values of  $x_1$  and  $x_2$  calculated from Eqn.10 yielded values of ca. 70% and 30%. Interestingly, there was no dependence of  $x_1$  or  $x_2$  on the crystallization temperature, whereas the bulk degree of crystallinity increased with increasing crystallization temperature.

As mentioned earlier, there is no way a priori to assign either of these values to either the crystalline phase or the amorphous phase. Since the high angle weak reflection shown in Figure 6.19 has been attributed to the (001) reflection, the thickness of the lamella can be estimated using the Scherrer analysis<sup>33</sup> on the width of the smeared (001) reflection. The Scherrer equation is given by

$$l_{hkl} = \frac{K\lambda}{\beta_0 \cos \theta} \quad (13)$$

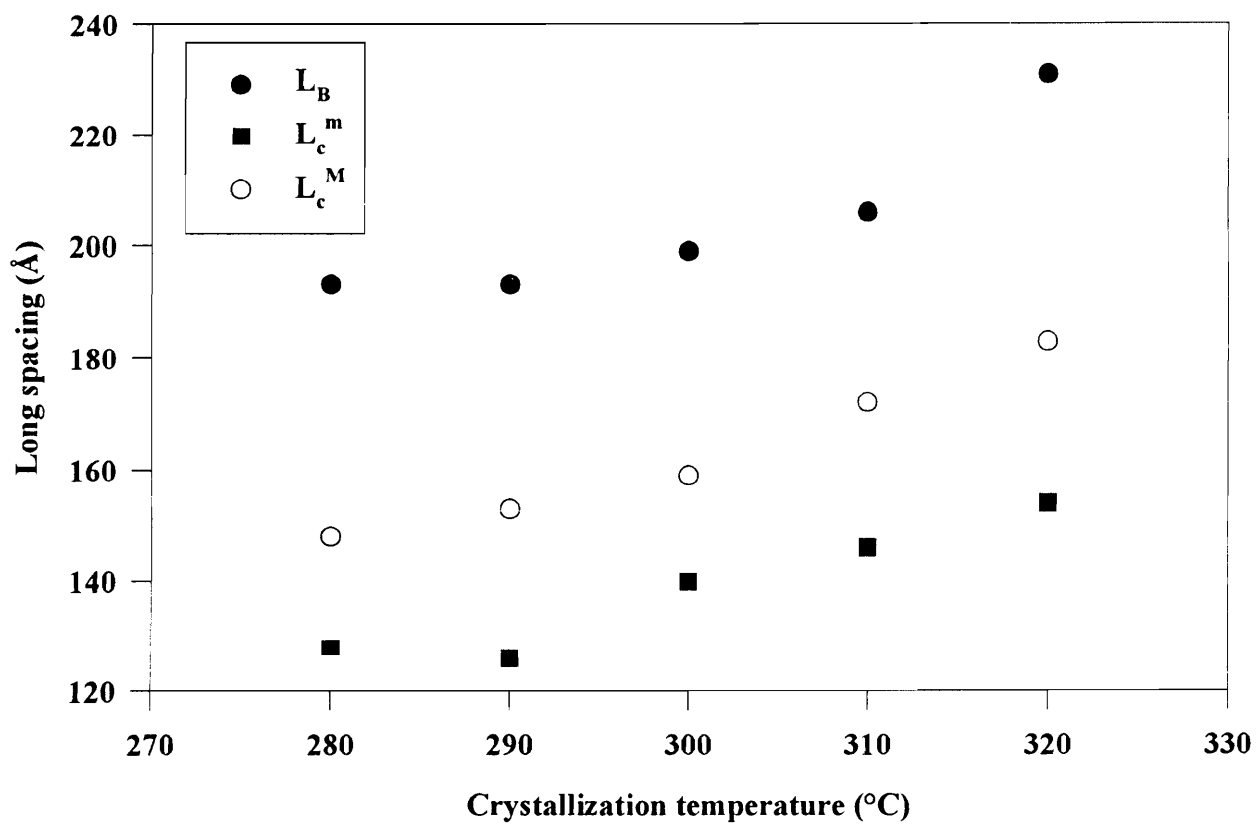


**Figure 6.22** Long spacings as a function of crystallization temperature.

where  $l_{hkl}$  is the thickness in a direction perpendicular to the (hkl) plane,  $\beta_o$  is the breadth at half maximum of the (hkl) reflection in radians,  $K$  is a constant assumed to be unity,  $\theta$  is half the radial scattering angle ( $2\theta$ ) corresponding to the maximum of the reflection, and  $\lambda$  is the wavelength of the x-ray used. Two points regarding this analysis must be emphasized; the first is that the line width analysis was carried out on raw data (smeared), and the second point is that this simple analysis ignores any effects of the presence of lattice defects, which could also cause line broadening. Nevertheless, the estimates of the lamellar thicknesses are shown in Table 6.2 along with the lamellar thicknesses and amorphous layer thicknesses estimated from the correlation function, by assigning the thicker phase as the crystalline phase. It is obvious that the estimates from the Scherrer analysis are close to the lamellar thickness values obtained from the correlation function. A similar analysis was carried out by Hsiao et al.<sup>22</sup>, who arrived at the same conclusion that the thicker phase value from the correlation function was close to the Scherrer analysis estimate. Therefore the larger value of  $l$  obtained from the correlation function has been assigned to the lamellar phase. It should be mentioned here that the reverse assignment was made by Cebe et al.<sup>25,27</sup>, whereas Hsiao<sup>22</sup> assigned the larger value to the lamellar phase, as was done here.

Figure 6.23 shows the change in lamellar thickness and amorphous layer thickness with crystallization temperature. It can be seen that both the lamellar thickness as well as the amorphous layer thickness increase with increasing crystallization temperature, with

**Table 6.2** Average lamellar and amorphous layer thickness obtained from the correlation function and minimum lamellar thickness determined from the Scherrer analysis.

<b>Crystallization temp</b>	<b><math>l_c</math> (Å)</b>	<b><math>l_a</math> (Å)</b>	<b><math>l</math> (Scherrer) (Å)</b>
280 °C	101	47	106
290 °C	105	48	110
300 °C	110	49	115
310 °C	121	51	118
320 °C	127	56	123

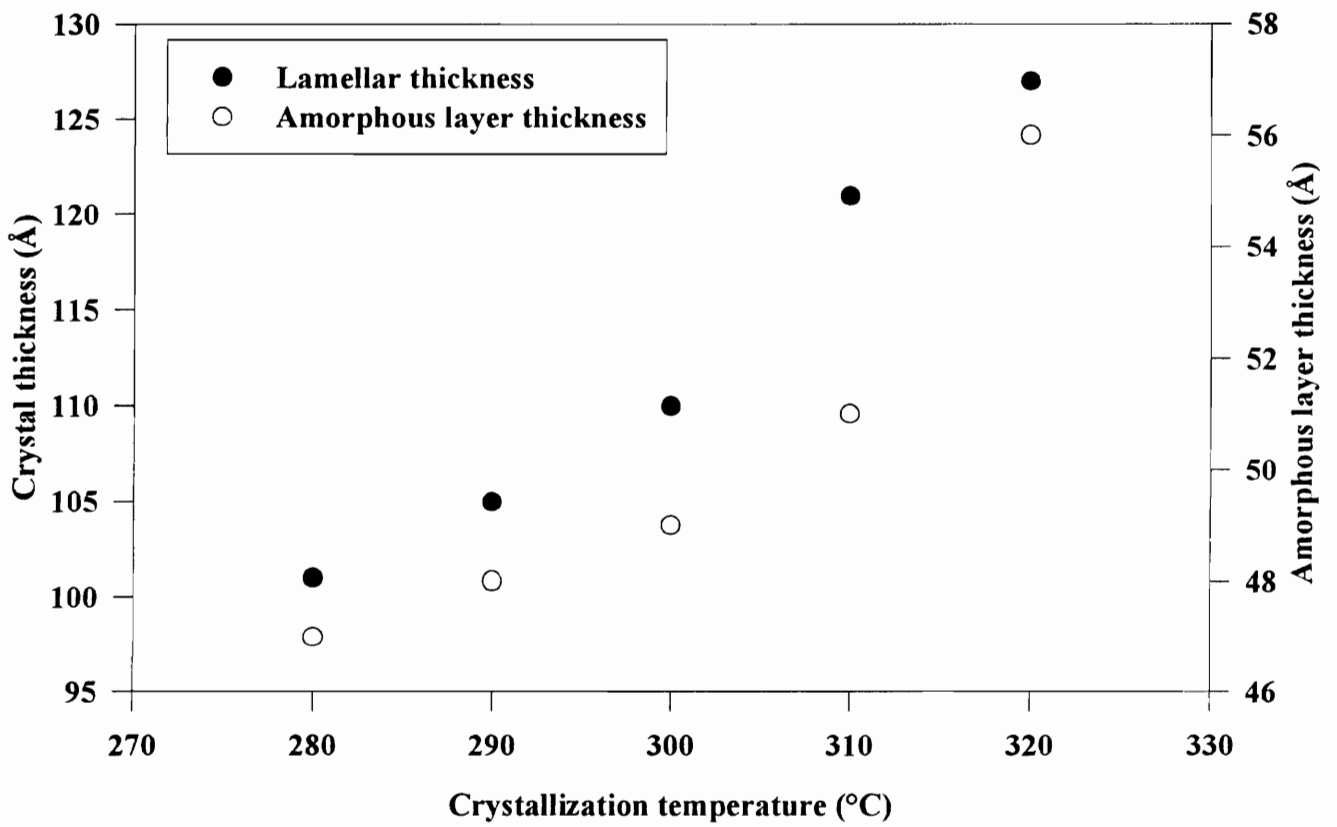


**Figure 6.23** Lamellar thickness and inter-lamellar amorphous layer thickness as a function of crystallization temperature.

the lamellar thickness changing from 101 Å to 127 Å, i.e. by the length of one repeat unit, and the amorphous layer thickness changing from 47 Å to 56 Å. Thus it is clear that the increase in long spacing observed was due to an increase in both amorphous layer thickness as well as lamellar thickness. The increase in lamellar thickness with increasing crystallization temperature is to be expected on theoretical grounds since the thickness of a crystal formed at a lower undercooling ( $T_m^\circ - T_c$ ) would be expected to be greater than a crystal grown at larger undercoolings. The increase in amorphous layer thickness with increasing crystallization temperature provides support for the explanation of Jonas et al.<sup>44</sup> regarding the dynamic mechanical results, which showed the glass transition temperature decrease with increasing crystallization temperature. Note, however, that the reverse assignment was made by Jonas et al., i.e. the thicker phase was assigned to the amorphous phase and the thinner phase was assigned to be the lamellar thickness.

Figure 6.24 shows the Lorentz corrected plots for samples cold crystallized at 300 °C for different times. The long spacings as determined from the first minimum and the first maximum of the correlation function, and the Bragg period of the Lorentz corrected plot, were all found to decrease systematically with increasing crystallization time, with this decrease being more prominent for lower times; for longer times, this decrease was less pronounced, as shown in Figure 6.25. As was the case earlier, the long spacings corresponding to the Bragg peak of the Lorentz corrected plot were higher than those values determined from the correlation function. At early times of crystallization, very few lamellae are formed with large distances between them. This leads to a large initial value

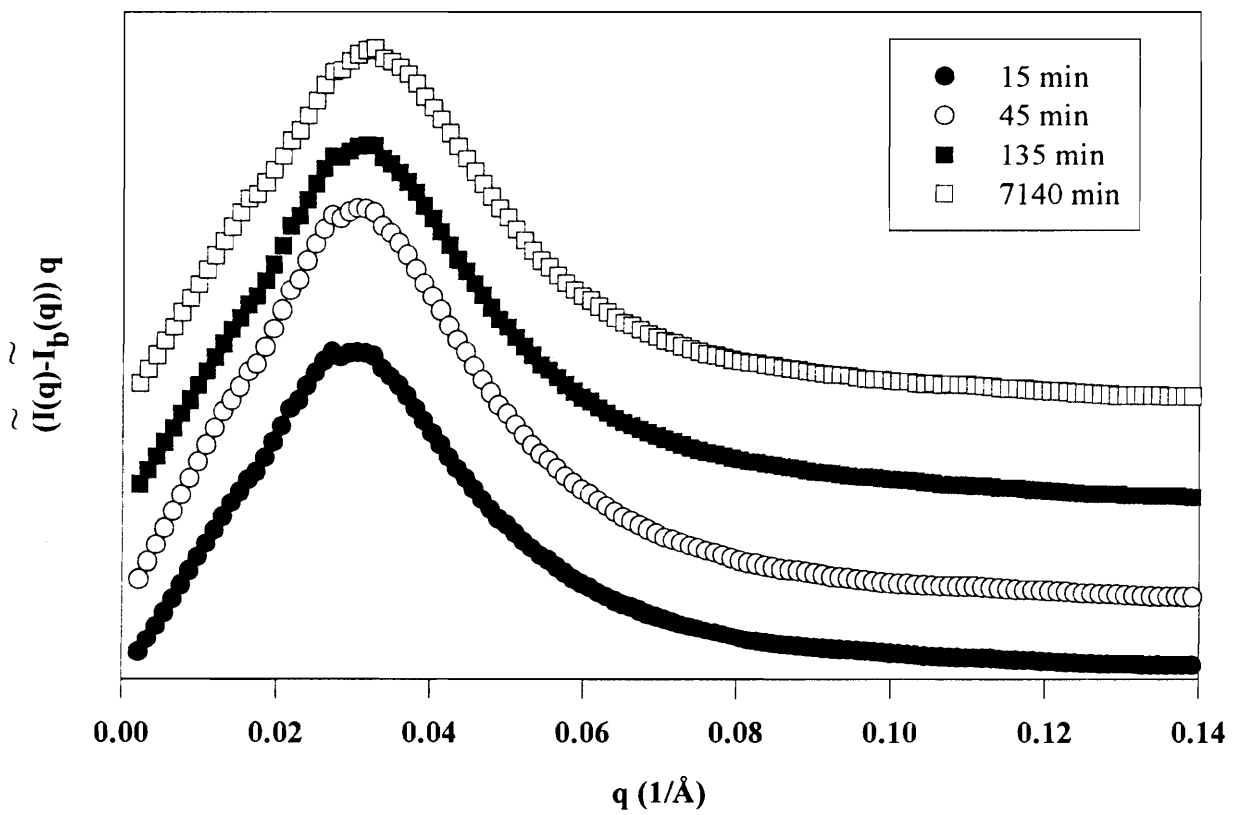


**Figure 6.24** Lorentz corrected plots for samples crystallized at 300 °C for various times.

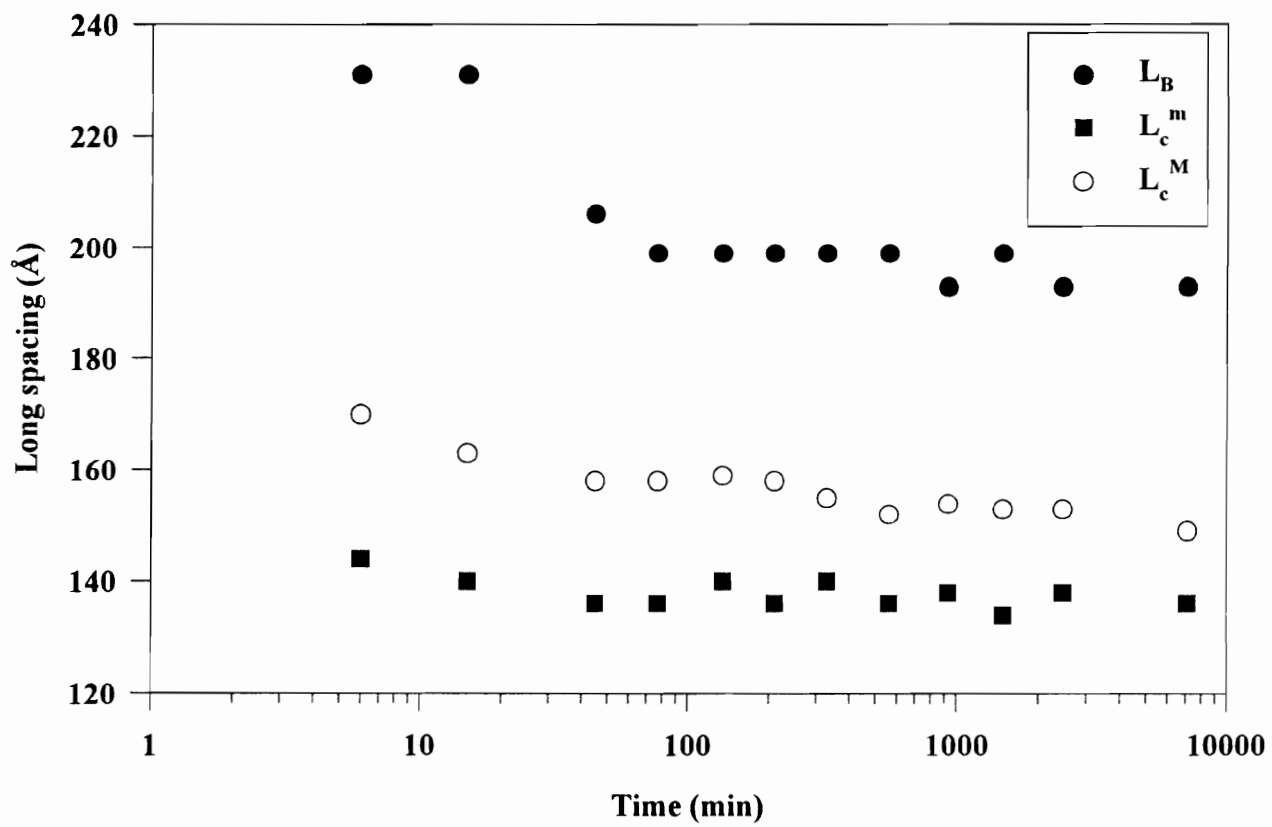


**Figure 6.25** Long spacings as a function of crystallization time.

of the long period. However, with increasing time, the lamellae start to fill in a greater volume of the spherulites, which is accompanied by a decrease in the long period. This causes the initial drop in the long period with crystallization time. The steady decrease in the long period as a function of crystallization time can be attributed to a steady decrease in the average lamellar thickness as a function of crystallization time.

Figure 6.26 shows the lamellar thickness and amorphous layer thickness as a function of crystallization time. As can be seen from the figure, the amorphous thickness remains unchanged with crystallization time, however, the lamellar thickness decreases as a function of the log of crystallization time. At the early stages of crystallization, primary lamellae are formed, the thickness of which is determined by the undercooling ( $T_m^\circ - T_c$ ). At the end of the primary crystallization process, complete spherulitic impingement occurs, and the spherulites occupy the entire volume of the sample. There is, however, still a considerable fraction of amorphous material in the sample that could undergo crystallization. The WAXS results discussed earlier showed that a considerable fraction of the final crystallinity is generated during the secondary crystallization stage. Recall from the earlier discussion on the spherulitic morphology and the SAXS results presented here, that the lamellar stacks consist of bundles of lamellae separated by inter-lamellar amorphous layers of ca. 50 Å thickness. The rest of the amorphous phase is assumed to lie in larger amorphous regions between different lamellar stacks. The secondary crystallization process can continue in these amorphous regions, under more constrained conditions, following log time kinetics. These secondary lamellae are thinner than the

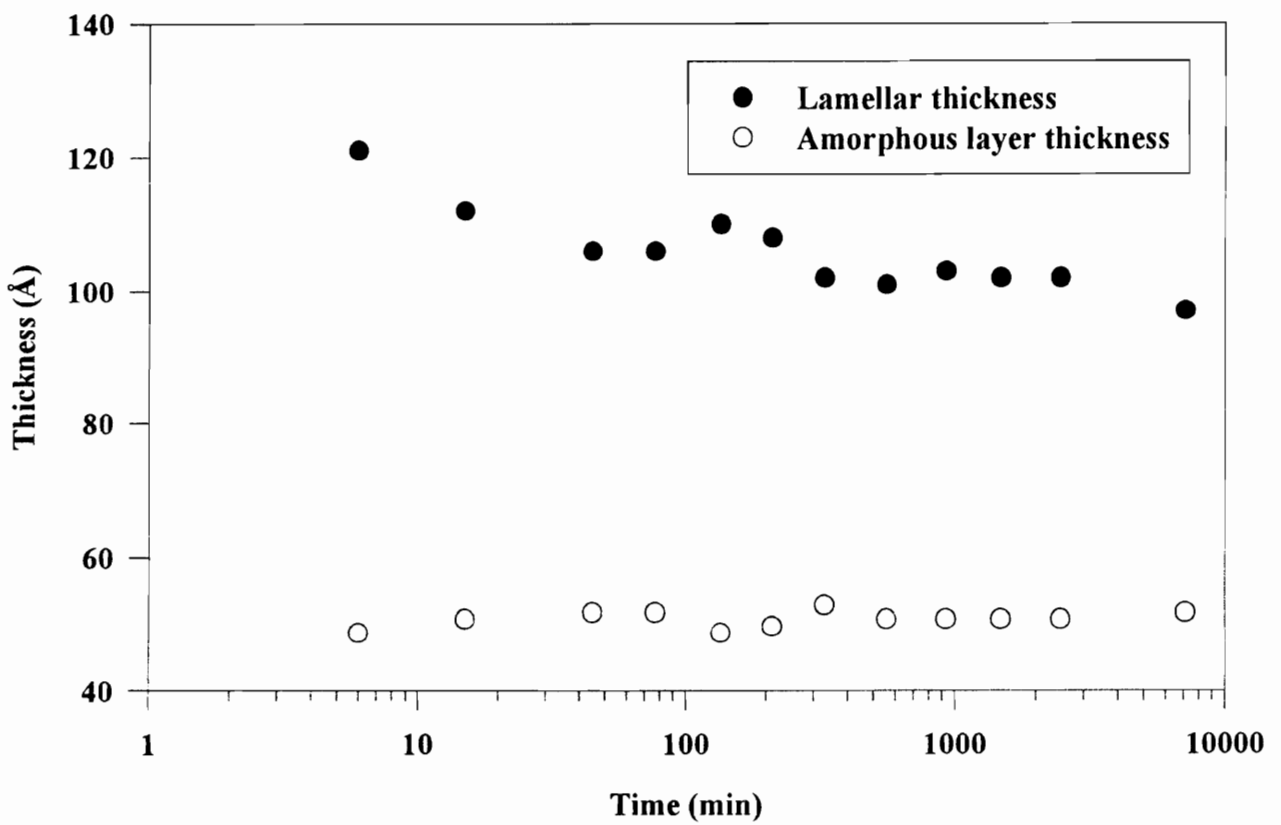


**Figure 6.26** Lamellar thickness and inter-lamellar amorphous layer thickness as a function of crystallization time.

lamellae formed during the primary crystallization process, and hence results in a net *decrease* in the average lamellar thickness detected by SAXS. This could lead to a bimodal distribution of lamellar thicknesses in the system at the end of both primary and secondary crystallization processes, as has also been suggested earlier<sup>50</sup>. Cebe et al.<sup>25</sup> had carried out a real time SAXS study of the cold crystallization of New TPI at 300 °C. The results presented here are consistent with their results in that prominent changes are observed in the first 10 min of crystallization, after which the changes are less pronounced. The results of this study, however, encompass a much higher range of crystallization times than the study of Cebe et al.<sup>25</sup>, which enabled the study of the effects of long time crystallization/annealing on the observed crystallization behavior of this system.

## **6.5 Conclusions**

The crystallization, melting and relaxation behavior of a commercial polyimide, Mitsui Toatsu's Aurum™ New TPI has been the focus of investigation in this study. Cold-crystallized samples with varying thermal histories were prepared in order to study the effect of crystallization history (time and temperature) on the structural, crystallization, melting and relaxation behavior of this system. Since this polyimide has been the focus of considerable study over the recent years, a comprehensive picture of the crystallization behavior has just begun to emerge.

The effect of varying crystallization temperature was investigated by crystallizing samples for 135 min at various temperatures. It was found that the degree of crystallinity increased with increasing crystallization temperature, as evidenced by the WAXS results and a decrease in the relaxation intensity as shown by the dynamic mechanical results. Increasing the crystallization temperature also resulted in a decrease in the glass transition temperature observed both by DSC as well as dynamic mechanical analysis. Small angle x-ray results showed that increasing crystallization temperature resulted in an increase in both lamellar as well as the inter-lamellar amorphous layer thicknesses. The decrease in  $T_g$  with increasing crystallization temperature is the result of a decrease in the number of constraints on the amorphous phase due to the presence of the crystallites. At this point, it is not considered very probable that the inter-lamellar amorphous regions contribute to the observed glass transition, based on the fact that the inter-lamellar amorphous layer was of the order of 50 Å, which is ca. only twice the repeat unit length of New TPI. The glass transition is speculated to arise only from the amorphous phase in the regions between different lamellar stacks. The melting behavior of New TPI crystallized at different temperatures exhibited dual melting endotherms, an endotherm corresponding to  $T_c+10$  °C, and a prominent higher melting endotherm at ca. 385 °C that was relatively insensitive to the prior crystallization history.

The effect of increasing crystallization time at 300 °C, was to increase the degree of crystallinity. This increase was prominent at low crystallization times, corresponding to a primary crystallization process, and was gradual, exhibiting log time kinetics at longer

crystallization (annealing) times. A substantial fraction of the final crystallinity develops in this latter stage, as shown by the WAXS results, due to a secondary crystallization process that results in a decrease in the average lamellar thickness as observed by SAXS, due to the formation of thinner lamellae in the amorphous regions between different lamellar stacks. This is accompanied by an increase in  $T_g$  as evidenced by the DSC and dynamic mechanical results. This increase in  $T_g$  was observed to follow log time kinetics as well for longer crystallization times. For extremely short crystallization times, i.e. times shorter than that required for spherulitic impingement, the glass transition exhibits lower values than would be predicted from a straight line fit of  $T_g$  with crystallization time. This behavior has been attributed to the presence of a “dual population” of amorphous phase in the sample.

## **Acknowledgments**

The authors would like to thank the NSF Science and Technology Center for High Performance Polymeric Adhesives and Composites for full funding of this study under contract number DMR 9120004. Useful discussions with Dr. Ravi Verma regarding the SAXS and WAXS results is also acknowledged. Dr. Kent Blizard is acknowledged for donating the New TPI film used in this study.

## References

1. C. J. Feger, M. M. Khojasteh, and J. E. McGrath, Eds. *Polyimides: Materials, Chemistry and Characterization*, Elsevier Science Publishers, Amsterdam, 1989.
2. D. Wilson, H. D. Stenzenberger, and P. M. Hergenrother, Eds. *Polyimides*, Blackie and Son Ltd., London, 1990.
3. P. M. Hergenrother, Heat Resistant Polymers in *Encycl. Polym. Sci. Eng. (2nd ed)*, 7, 639, 1987.
4. K. L. Mittal, Ed. *Polyimides, Synthesis, Characterization and Applications, Vols 1 & 2*, Plenum Press, New York, 1984.
5. J. T. Muellerleile, B. G. Risch, D. E. Rodrigues, and G. L. Wilkes, *Polymer*, **34**, 789 (1992).
6. D. K. Bandom and G. L. Wilkes, *Polymer*, **35**, 5672 (1994).
7. D. K. Bandom and G. L. Wilkes, *Polymer*, **36**, 4083 (1995).
8. S. Srinivas, M. Graham, M. H. Brink, S. Gardner, R. M. Davis, J. E. McGrath, and G. L. Wilkes, *Polymer Eng. and Sci*, in press.
9. S. Srinivas, F. E. Caputo, M. Graham, S. Gardner, R. M. Davis, J. E. McGrath, and G. L. Wilkes, submitted for publication.
10. M. H. Brink, D. K. Bandom, G. L. Wilkes, and J. E. McGrath, *Polymer*, **35**, 5018 (1994).

11. M. E. Rogers, M. H. Brink, A. Brennan, and J. E. McGrath, *Polymer*, **34**, 849 (1993).
12. Kim, Y. J.; Glass, T. E.; Lyle, G. D.; McGrath, J. E. *Macromolecules* **1993**, *26*, 1344.
13. P. M. Hergenrother, *Polymer Journal*, **19**, 73 (1987).
14. P. M. Hergenrother, N. T. Wakelyn, and S. J. Havens, *J. Polym. Sci., Polym. Chem. Ed.*, **25**, 1093 (1987).
15. P. M. Hergenrother and S. J. Havens, *J. Polym. Sci., Polym. Chem. Ed.*, **27**, 1161 (1989).
16. P. M. Hergenrother, M. W. Beltz, and S. J. Havens, *J. Polym. Sci., Polym. Chem. Ed.*, **29**, 1483 (1991).
17. S. J. Havens and P. M. Hergenrother, *J. Polym. Sci., Polym. Chem. Ed.*, **30**, 1209 (1992).
18. D. P. Heberer, S. Z. D. Cheng, J. S. Barley, H. S. Lien, R. G. Bryant, and F. W. Harris, *Macromolecules*, **24**, 1890 (1991).
19. S. Z. D. Cheng, D. P. Heberer, H. S. Lien, and F. W. Harris, *J. Polym. Sci.: Part B: Polym Phys.*, **28**, 655 (1990).
20. J. A. Kreuz, B. S. Hsiao, C. A. Renner, and D. L. Goff, *Macromolecules*, **28**, 6926 (1995).
21. B. S. Hsiao, J. A. Kreuz, and S. Z. D. Cheng, *Macromolecules*, **29**, 135 (1996).

22. B. S. Hsiao, B. B. Sauer, and A. Biswas, *J. Polym. Sci.: Part B: Polym. Phys.*, **32**, 737 (1994).
23. J. B. Friler and P. Cebe, *Polym. Eng. and Sci.*, **33**, 587 (1993).
24. P. P. Huo and P. Cebe, *Polymer*, **34**, 696 (1993).
25. P. P. Huo, J. B. Friler, and P. Cebe, *Polymer*, **34**, 4387 (1993).
26. M. V. Brillhart and P. Cebe, *J. Polym. Sci.: Part B: Polym. Phys.*, **33**, 927 (1995).
27. S. X. Lu, P. Cebe, and M. Capel, *J. Appl. Polym. Sci.*, **57**, 1359 (1995).
28. L. Torre, A. Maffezzoli, and J. M. Kenny, *J. Appl. Polym. Sci.*, **56**, 985 (1995).
29. K. Okuyama, H. Sakaitani, and H. Arikawa, *Macromolecules*, **25**, 7261 (1992).
30. T. H. Hou and R. M. Reddy, *SAMPE Q.*, January, 38 (1991).
31. T. Hirade, Y. Hama, T. Sasuga, and T. Seguchi, *Polymer*, **32**, 2499 (1991).
32. Technical data sheet, Aurum™ Polyimide, Mitsui Toatsu Chemicals Inc.
33. L. E. Alexander, *X-Ray Diffraction Methods in Polymer Science*, Wiley-Interscience, New York, 1969.
34. W. Ruland, *Acta Cryst.*, **14**, 1180 (1961).
35. W. Ruland, *Polymer*, **5**, 89 (1964).
36. C. G. Vonk, *J. Appl. Cryst.*, **6**, 148 (1973).
37. B. Wunderlich, *Macromolecular Physics Vol.3*, Academic Press, New York, 1980.
38. S. Z. D. Cheng, M. Y. Cao, and B. Wunderlich, *Macromolecules*, **19**, 1868 (1986).

39. S. Z. D. Cheng, Z. Q. Wu, and B. Wunderlich, *Macromolecules*, **20**, 2802 (1987).
40. J. S. Chung and P. Cebe, *Polymer*, **33**, 2312 (1992).
41. J. S. Chung and P. Cebe, *Polymer*, **33**, 2325 (1992).
42. V. Velikov, J. Vivirito, and H. Marand, *Bull. Am. Phys. Soc.*, **39(1)**, 168 (1994).
43. R. K. Krishnaswamy and D. S. Kalika, *Polymer*, **35**, 1157 (1994).
44. A. Jonas and R. Legras, *Macromolecules*, **26**, 813 (1993).
45. A. J. Lovinger, S. D. Hudson, and D. D. Davis, *Macromolecules*, **25**, 1752 (1992).
46. C. Santa-Cruz, N. Stribeck, H. G. Zachmann, and F. J. Baltá Calleja, *Macromolecules*, **24**, 5980 (1991).
47. B. S. Hsiao, B. B. Sauer, R. K. Verma, H. G. Zachmann, S. Seifert, S. B. Chu, P. Harney, *Macromolecules*, **28**, 6931 (1995).
48. C. G. Vonk and G. Kortleve, *Kolloid-Z.*, **220**, 19 (1967).
49. G. R. Strobl and M. Schneider, *J. Polym. Sci. Polym. Phys. Ed.*, **18**, 1343 (1980).
50. R. K. Verma, A. Biswas, H. Marand, and B. S. Hsiao, *J. Appl. Crystallography*, submitted for publication.
51. A. M. Jonas, T. P. Russell and D. Y. Yoon, *Macromolecules*, **28**, 8491 (1995).
52. T. P. Russell, H. R. Brown, and D. T. Grubb, *J. Polym. Sci., Polym. Phys. Ed.*, **25**, 1129 (1988).
53. N. Takahashi, D. Y. Yoon, and W. Parrish, *Macromolecules*, **17**, 2583 (1984).

## Chapter-7

### Summary and Future Work

This dissertation has dealt with the structure-property studies on high performance poly(arylene ether) based polymers with an emphasis on their crystallization, morphological and melting characteristics. These studies have concentrated on novel material systems developed at the NSF Center at Virginia Tech, and could lead to their further evaluation for various high performance applications. In addition, some of the results discussed here suggest further avenues of research in the area of crystallization and morphology of these polymers.

The first part of this dissertation dealt with the characterization and crystallization studies of a series of novel poly(arylene ether ether sulfide) polymers. These polymers were synthesized by the nucleophilic aromatic substitution reactions between difluorodiphenyl sulfoxides and biphenols. The resulting amorphous poly(arylene ether ether sulfide)s were then reduced to yield the semicrystalline poly(arylene ether ether sulfide)s. The polymers based on hydroquinone (referred to as phenyl sulfide) exhibited a glass transition temperature of 100 °C, a melting temperature of 245 °C and an equilibrium melting temperature of 292 °C, as determined from a Hoffman-Weeks extrapolation. The polymers based on biphenol (referred to as biphenyl sulfide) exhibited a glass transition temperature of 150 °C, a melting temperature of 350 °C and an equilibrium melting temperature of 371 °C. It should be emphasized that for the case of

the phenyl sulfide polymer, the equilibrium melting temperature determined from a Hoffman-Weeks approach was found to be independent of molecular weight. This is contrary to the findings in literature where the equilibrium melting temperature of poly(phenylene sulfide) (PPS) was found to increase with increasing molecular weight. The transition temperatures as well as the chemical structure of the hydroquinone based polymer is quite similar to PPS; indeed the phenyl sulfide polymer can be considered a copolymer of PPS and poly(*p*-phenylene oxide). This led to comparisons of the crystallization behavior of these polymers.

Isothermal crystallization kinetics of the poly(ether sulfide) polymers were studied, and the data analyzed using the Avrami approach. The Avrami rate constants of the phenyl sulfide and biphenyl sulfide polymers determined in this study were compared with the results available in literature for PPS and PEEK respectively. Even though it was not always possible to make a comparison for identical molecular weights, this approach yielded some interesting information. At equivalent undercoolings, the rate constants of the phenyl sulfide and biphenyl sulfide were at least 2 orders of magnitude (6 orders of magnitude in some cases) lower than that of PPS and PEEK for similar molecular weights. For the case of phenyl sulfide and PPS, the nucleation densities were found to be equivalent at all undercoolings; the differences in the rate constants were therefore attributed to differences in spherulitic growth rates, which is also consistent with the comparison of the phenyl sulfide growth rate data with the values available in literature for PPS. In contrast to the reported behavior for PPS, the nucleation densities calculated

from the rate constant and growth rate data for the phenyl sulfide polymer, were essentially independent of undercooling. Since the chemical structure as well as the crystallization windows of the phenyl sulfide polymer and PPS are very similar, it is quite interesting that the crystallization rates of the polymers are significantly different.

After the completion of the work described in chapters 1-3, molecular modeling calculations were carried out by Dr. Venkat Vasudevan to determine the rotational energy barriers in the case of the phenyl sulfide polymer and PPS. Even though the results of these studies are not described in this dissertation, it would be useful at this stage to mention and use some of the results. The energy barrier for rotation about the phenyl-oxygen-phenyl bond (4.5 kcal/mol) was found to be ca. 3 times greater than the energy barrier for rotation about the phenyl-sulfur-phenyl bond (1.5 kcal/mol), which was attributed to the shorter bond length of the phenyl-oxygen linkage leading perhaps to greater steric hindrances (unpublished data). This increased barrier could result in a greater melt viscosity for the case of the phenyl sulfide polymer investigated here compared to PPS, which would result in a reduced spherulitic growth rate. The melt state viscosities of the two systems can be determined from rheological studies, which would provide evidence for this hypothesis. The growth rate at a given temperature can be influenced by other parameters as well. The growth rate could also be decreased by lowering the rate of secondary nucleation on the crystal substrate, which would slow down the lamellar growth rate. All other factors remaining a constant, this decrease can result from an increase in the fold surface energy ( $\sigma_e$ ) and/or the lateral surface free energy

( $\sigma$ ). It can be hypothesized that since the rotational energy barrier for phenyl sulfide is greater than for PPS, the work of chain folding would be greater, leading to an increase in the fold surface energy ( $\sigma_e$ ). This would cause a lower growth rate at a given undercooling for the phenyl sulfide polymer as compared to PPS. This hypothesis can be investigated by determining the fold surface energies for the phenyl sulfide polymer and PPS via a Gibbs-Thomson procedure. It has been shown by Hoffman and co-workers that the lateral surface energy ( $\sigma$ ) is often inversely proportional to the characteristic ratio ( $C_\infty$ ) for a number of polymers. Assuming such a relationship holds in the case of the polymers under study here, it can be hypothesized that since the rotational barrier for the phenyl sulfide polymer is greater than PPS, this would lead to a “stiffer” molecule for the case of the phenyl sulfide polymer. This would lead to a higher  $C_\infty$ , and therefore a lower  $\sigma$ , which would lead to increased growth rate of the phenyl sulfide polymer. Since such behavior is not observed here, it is clear that the other factors discussed here are more prominent in influencing the growth rate compared to the lateral surface energy term. It is still unclear which of the above discussed factors dominate the growth kinetics of the phenyl sulfide polymer. Clearly further work could be carried out to investigate this issue.

Non-isothermal crystallization kinetics from the melt on the poly(ether sulfide)s were studied at cooling rates from 2 °C/min to 70 °C/min. Since the Ozawa approach was not successful in describing the kinetics of crystallization in all cases studied here, the conventional form of the Avrami equation was used to analyze the non-isothermal

crystallization data. In contrast to the application of the Avrami equation to model isothermal crystallization, in the case of non-isothermal crystallization, the Avrami parameters do not have the same physical significance; they are merely fitting parameters. In spite of this limitation with this kind of analysis, a reduced rate constant has been defined here which could serve as a useful means of comparison of crystallization rates under varied conditions, without, however, the ability to explain the mechanisms of the crystallization process.

In addition to the bulk crystallization studies, spherulitic crystallization in thin films of the phenyl sulfide 19.9K polymer were carried out in this study. Similar studies on the other molecular weight phenyl sulfide polymers and the biphenyl sulfide polymers could not be carried out due to experimental difficulties associated with obtaining samples with low enough nucleation densities to resolve individual spherulites. At all temperatures studied here, a dual population of spherulites were observed with different morphological textures and growth rates, which have been designated Type I and Type II spherulites. This behavior was attributed to differences in film thicknesses; specifically when the film thickness was lower than the spherulitic diameters, disc-like structures were observed to grow at a faster rate compared to spherical superstructures which grew in samples with film thicknesses of the order of the spherulitic diameters. Such behavior was also shown to be independent of the nature of the substrate on which crystallization was carried out. Though there have been numerous studies investigating the influence of various molecular and processing parameters on the spherulitic growth rate, there seems to be no study

reported in literature investigating systematically the effects of film thickness on the spherulitic growth rates. This again would be a possible avenue for further research, in light of the findings reported in this study. It is possible that the growth rate depends systematically on the film thickness up to a point when the film thickness becomes greater than the spherulitic diameter, then becomes independent of the film thickness. This would have important implications for the area of polymer crystallization, since there is no theoretical basis for explaining such a phenomenon. As stated earlier in the dissertation, different unit cell structures could potentially cause different spherulitic growth rates at a given temperature. It would be useful to carry out micro-beam x-ray diffraction experiments to study the unit cell structures of the two kinds of spherulites, as well as the orientation of the chains in the spherulites. From a consideration of the Lauritzen-Hoffman approach for describing crystallization, a few other possible causes for the observed behavior can be considered. Since there is no way to determine the fold surface and lateral surface energies, one can assume that these values are similar for the two kinds of spherulites. If this is indeed the case, then the thermodynamic driving force for crystallization at a given undercooling, would be the same for the two kinds of spherulites. The other factor that could influence the growth rate is the mobility term which is dominated by the parameters  $U^*$ , which is the activation energy for chain mobility, and  $(T_c - T_\infty)$ , where  $T_\infty$  is similar to a glass transition term. The thickness of the film on which the crystallites are growing could influence either one of these parameters.

Another interesting finding of this study was the disappearance/shift of the maximum of the growth rate curves of the disc-like structures to lower temperatures compared to the spherulitic growth rate curve. Since the maximum of the growth rate curve signifies the shift from a nucleation controlled crystallization process to a diffusion controlled crystallization process, it is obvious that this observation indicates a different mechanism of crystallization for disc-like structures as compared to spherulitic structures, i.e. a shift of the mobility controlled regime to lower temperatures.

Another topic addressed in this dissertation was the thermal stability and preliminary crystallization studies that were carried out on a series of molecular weights of novel semicrystalline polyimides based on PA endcapped TPEQ/ODPA as well as TPER/BPDA. The use of the all-para based diamine (TPEQ) monomer resulted in a polymer with high transition temperatures as well as extremely slow crystallization kinetics. The TPER based polyimide, though not identical to the TPEQ based polymer, however is quite similar in that the para links in the TPEQ diamine unit are replaced by meta linkages. This resulted in a polymer with a tremendously improved crystallizability; indeed, it was not possible to quench this polymer (30K molecular weight) into a completely amorphous material even at cooling rates of ca. 200 °C/min! The thermal stability of this polymer also showed a dramatic improvement over the TPEQ based polyimide. Another interesting feature of the TPER based polyimide is that the very fast crystallization kinetics of the polymer are also accompanied by sharp melting behavior indicative of a narrow distribution of lamellar thicknesses. This stiff chain polymer also

exhibited melting/recrystallization phenomena on heating isothermally as well as non-isothermally crystallized samples. Such phenomena occurring in stiff-chain polymers have been reported by other researchers as well, but is still surprising and definitely warrants further study. The melting/recrystallization could be studied with a combination of DSC heating rate studies, in conjunction with real time small angle and wide angle x-ray studies to detect any changes in structure during heating. Another possibility is the investigation of samples with a known crystallization history through linear or volume dilatometry, in order to study volume changes during heating.

The effect of non-reactive endcapping on the thermal stability of the TPER polyimides has been demonstrated with a combination of crystallization/melting and rheological studies, emphasizing the need to control the nature of the endgroups in order to maintain high temperature stability. Samples with no non-reactive endcapping (amine endgroups) and half-endcapped with phthalic anhydride (PA) exhibited distinctly lower thermal stability in the melt compared to a PA endcapped system, as evidenced by a substantial increase in viscosity resulting in a decrease in the crystallizability.

Based on the information available on the unique features of the TPER polyimide, which includes the excellent thermal stability and crystallizability, continued work in this area seems warranted. This polymer is a promising candidate as a matrix material for composites and possibly as an adhesive as well. The availability of this polymer in the form of fine powder can be utilized to manufacture composites using the powder-

prepregging method. Aqueous powder prepregging could be attempted, in which polyamic acid salts of the TPER polyimide could also be evaluated as stabilizing agents.

The effect of chain structure on the observed crystallization behavior of the TPER system could be investigated by suitably changing the backbone, e.g. investigating the para linked diamine analogues while keeping the same dianhydride (BPDA). One of the features that could make the system a fast crystallizing polymer could possibly be the meta linked diamine. Copolymers of this system with the same dianhydride (BPDA) but with varying amounts of meta linked diamines (TPER) and para linked diamines (TPEQ) could be synthesized. This possibly could give more control over the crystallization kinetics of this system, and also indicate the effect meta linkages have on the kinetics. A possible problem with this approach, however, would be the fact that random sequences of para and meta linkages would probably destroy the chain backbone symmetry, and therefore influence the crystallization behavior.

The final topic in this dissertation addressed the structural changes accompanying cold crystallization in a commercial polyimide, Mitsui Toatsu's Aurum™ New TPI as studied by a variety of techniques. The changes in both the crystalline and amorphous phases were investigated as a function of crystallization time and temperature. Increasing the crystallization temperatures resulted in increasing the degree of crystallinity, lowered  $T_g$ , decreased relaxation intensities, and increasing lamellar and amorphous inter-layer thicknesses. Increasing crystallization times at a given crystallization temperature resulted in increasing the degree of crystallinity, slightly raising the  $T_g$ , decreasing the relaxation

intensities, and decreasing the lamellar thickness. However, a constant inter-lamellar amorphous layer thickness suggests the formation of stacks of thinner lamellae in separate regions from the primary lamellar stacks, in the amorphous regions between primary lamellar stacks.

Based on the fact that the inter-lamellar amorphous layer thickness is ca. 50 Å, which is about twice the repeat unit length, the inter-lamellar amorphous layer thickness has been postulated not to contribute significantly to the glass transition; rather only the amorphous regions between different lamellar stacks are hypothesized to contribute to the observed glass transition. An interesting feature noted during the study was that the  $T_g$ 's of semicrystalline samples measured by DSC (inflection point) were almost the same as the  $T_g$  of the purely amorphous sample, indicating a weak influence of the crystalline regions on the amorphous phase. Dynamic mechanical experiments, however, showed that the  $T_g$  of the semicrystalline samples were significantly higher than a representative amorphous sample.

For extremely short crystallization times, i.e. times shorter than that required for spherulitic impingement, the glass transition exhibited values that were lower than would be predicted from a straight line fit of  $T_g$  with crystallization time. It has been suggested that this behavior occurs due to the presence of a “dual population” of amorphous phase in the sample, i.e. an amorphous phase that is unaffected by the presence of spherulites in the sample, and an amorphous phase that is contained in the spherulite. Due to the slow crystallization kinetics of New TPI, this polymer could be used as a model system to

further study the influence of crystallites on the amorphous phase, since the crystallization conditions and resulting morphology of this polymer can easily be controlled in order to systematically vary the crystallinity and morphology of the polymer. The dependence of the glass transition on crystallization time could be studied for samples crystallized at various temperatures. This could be correlated with the times for spherulitic impingement at these different crystallization temperatures, which can be estimated from isothermal cold-crystallization kinetic studies. Such a study would confirm the earlier hypothesis of a dual amorphous phase in samples crystallized for low times.

## Vita

Srivatsan Srinivas was born to Vatsala and M.Srinivasan on August 14 1967 in Rourkela, India. He joined the Indian Institute of Technology Madras in 1986 and graduated in 1990 with a Bachelor of Technology in Chemical Engineering. He joined the Chemical Engineering department at Virginia Tech in August 1990 for graduate studies. He received an MS in 1992, following which he joined the Materials Engineering and Science Doctoral program. After graduation he plans to carry out post-doctoral research with Dr. Hervé Marand in the Dept. of Chemistry at Virginia Tech.

